Università degli Studi di Cagliari

PHD DEGREE

Physics

Cycle XXXIV

TITLE OF THE PHD THESIS

Low-energy signatures in DarkSide-50 experiment

and neutrino scattering processes

Scientific Disciplinary Sector(s)

FIS/01

PhD Student: Emmanuele Picciau

Supervisor Dr. Walter Marcello Bonivento
Dr. Matteo Cadeddu

Final exam. Academic Year 2020/2021
Thesis defence: February 2022 Session

Low-energy signatures in DarkSide-50 experiment and neutrino scattering processes

THESIS FOR THE DEGREE OF DOCTOR OF PHILOSOPHY

Emmanuele Picciau

The PhD School of Physics
Università Degli Studi di Cagliari
Cycle: XXXIV

Academic advisors:
Dr. Walter Marcello Bonivento and Dr. Matteo Cadeddu

Department of Physics
Faculty of Science
Università degli Studi di Cagliari
Istituto Nazionale di Fisica Nucleare

Single-electron background in DarkSide-50 experiment and neutrino physics exploiting coherent elastic scattering

Short abstract:

Dark matter is one of the greatest unsolved mysteries in cosmology nowadays. About 80% of the gravitating matter in the Universe is non-luminous, and its nature and distribution are for the most part unknown. Many experiments around the world and in space are trying to discover dark matter interactions and properties. Among them, the DarkSide project aims to see dark matter signatures inside of time projection chamber filled with liquid argon. In order to reach such a goal the detector features along with the background must be studied and well understood. This thesis presents the so-called single-electron background of DarkSide-50 experiment, with the perspective of informing the community on the backgrounds which may affect future experiments, especially those looking for low-mass dark matter particles. Another important and irreducible background to be considered in the future regards the coherent neutrino-nucleus scattering in the detector. This process is supposed to mimic in very similar way the dark matter interaction, making its discovery even harder. For this reason it is crucial to increase the knowledge of the electroweak and nuclear parameters which are involved in the neutrino scattering process. In this thesis several phenomenological studies regarding the recent discovery of coherent neutrino-nucleus scattering are presented, along with the determination of quantities accessible through this channel.

Keywords: Dark Matter, Particle Physics, DarkSide, Liquid Argon, Neutrinos

CONTENTS

INTRODUCTION

The concept of dark matter was introduced more than 80 years ago to explain anomalous phenomena observed in the universe and nowadays turned out to be one of the most fascinating and intriguing problems that modern physics is trying to solve. Indeed, observations of rotation curves of galaxies and mass distributions of galaxy clusters, that are estimated through gravitational lensing effects, strongly suggest that a large part of the universe is composed by a kind of matter that interacts mainly (or even only) through gravity. At the time of writing, the most promising candidate for dark matter is the so-called Weakly Interacting Massive Particle (WIMP). Many models predict dark matter WIMP masses near the electroweak scale. The experimental direct search of WIMPs is based on the detection of the energy released after a scattering with target nuclei in the detector. Nowadays, the phase space available for the different dark matter models has been significantly constrained leading to an increasing interest in developing and fielding novel detector technologies with sensitivity to a broad range of well-motivated candidates, complementing the many existing and planned large-exposure searches for weakly interacting massive particles.

Two recent results from the DarkSide-50 detector, a dual-phase liquid argon time projection chamber operating at the Laboratori Nazionali del Gran Sasso, demonstrate the ability to extend the reach of a liquid argon time projection chamber to WIMPs with masses below 10 GeV/c^2 that scatter on nuclei (low-mass WIMPs), and to dark matter particles that scatter on electrons with masses down to 20 GeV/c^2 (electron-scattering DM). To this end, a tonne-scale liquid argon detector designed specifically to maximize sensitivity in this mass range could realistically explore the low-mass dark matter parameter spaces.

The main limitation for these low-mass searches with DarkSide-50 has been found to be the so-called single-electron background, affecting the sensitivity for WIMP masses below $\sim$1 GeV/c^2. Indeed, DarkSide-50 data showed an unexplained abundance of events reconstructed to be generated by very low-energy signals. In order to relate this abundance to a dark matter interaction, it is necessary to know and estimate the background expected in the same region of interest. At the moment of writing, this abundance is not yet completely understood, so that the conservative choice is not to consider the low-energy region for the analysis. For this purpose, an effort to reduce and simulate the single-electron background is needed, and the studies in this thesis are the first investigation of this background from a quantitative point of view.

Another limitation in both low and high-mass searches is due to the indelible presence of neutrinos in the Universe. The "ultimate limit" in absence of directional sensitivity, that is widely called as *neutrino floor* is related to the fact that, at large exposures, neutrino backgrounds would mask any potential dark matter signal. Neutrinos in the Standard Model have the possibility to interact with nuclei through the process called Coherent Elastic Neutrino Nucleus Scattering (CEνNS) which releases a recoil of the nucleus that mimics in a very similar way the predicted recoil induced by WIMPs. The prediction of this physical limit is, however, affected by the uncertainties related to the poor knowledge of CEνNS interaction from the experimental point of view. It has eluded detection for 40 years from its prediction and it was detected for the first time in 2017 by COHERENT collaboration with a cesium-iodine (CsI) detector. The detection has been confirmed in 2020 with the observation of the process in a liquid argon detector and with the improved statistics with CsI. The analyses of COHERENT data allowed us to investigate in detail many neutrino properties, to explore the nuclear structure of the target used, to test the electroweak theory of the Standard Model at very low energy, and to limit possibilities beyond the Standard Model by setting constraints on the presence of new mediators.

By pushing the concept of low-energy search even further, we propose a future experiment exploiting superfluid ^{4}He evaporation, that would allow the observation of Coherent Elastic Neutrino Atom Scattering (CEνAS) processes. We investigate its sensitivity and we show the potentialities of such a detector to perform the lowest-energy measurement of parameters in the electroweak sector, and to reveal a magnetic moment of the electron neutrino largely below the current experimental limit.

This thesis is organized into two different parts. The first part has four chapters and focuses on the studies related to dark matter detection, which are part of several works of the DarkSide Collaboration. The second part has three chapters which consist of studies and analyses related to neutrino coherent scattering from a phenomenological point of view. The first chapter is a review of the dark matter paradigm and the state of the art of experimental sector. In the second chapter, the DarkSide-50 experiment is described and the most recent results are reported and discussed. The third chapter focuses on the study of the single-electron background present in the DarkSide-50 data, with the aim of characterizing and know better how to deal with such a background. In the fourth chapter, the preliminary ideas and sensitivities for a low-mass dedicated experiment are presented. The fifth chapter reviews the theory beyond the CEνNS process and presents the analyses performed by us with the first data-sets of CsI and argon released by COHERENT Collaboration. In the sixth chapter, physics beyond the Standard Model is explored by using

the information obtained by the observation of CEνNS. Moreover, we also improved some of the results presented in the fifth chapter by combining the new and last data taken by COHERENT with CsI and the measurement performed by atomic parity violation experiments. The seventh chapter focuses on neutrino scattering in the case of energy scale as low as that the neutrino scatters with the whole target atom elastically, highlighting the power of low-energy signals in current searches of particle physics.

Part I

Low energy Dark-Matter Direct Detection with DarkSide experiment

1

THE PROBLEM OF THE DARK MATTER IN THE UNIVERSE

The first chapter reviews the dark matter problem: the evidences for the missing mass, the most popular dark matter candidates, the current detection experiments and their results.

Contents

One of the main problems for the scientific community regards the knowledge of the Universe and its properties. For millennia, we have experienced the latter through electromagnetic observations. For example, the development of cosmology started with Galileo's observations of the sky, through his telescope, understanding the behavior of the motion of the Earth around the Sun. In the following centuries, scientists improved their observational methods through new instruments which could collect electromagnetic radiation for several photon wavelengths, from the radio regime to the very high energy gamma radiation. Several large-scale detectors to study charged particles and neutrinos coming from outside of our planet have been built, too. Most recently, a so-far quiet window on our Universe was revealed with the measurement of gravitational waves from two black hole mergers and black hole and neutron star mergers, the latter accompanied by observations in almost all wavelengths of light kicking off the multi-messenger studies of the Universe.

1.1 Dark Matter Evidence

Despite the recent discoveries, there is still a yet-to-be-solved problem, the so-called missing mass problem. This one comes from the calculations for which many galaxies would fly apart instead of rotating, or would not have formed or move as they do if they did not contain a large amount of unseen matter. An other evidence includes observations through gravitational lensing, from the Cosmic Microwave Background (CMB), from astronomical observations of the observable current structure of the Universe, from the formation and evolution of galaxies, from the mass location during galactic collisions, and from the motion of galaxies within galaxy clusters. Nowadays, the referenced cosmological model is the ΛCDM (Lambda Cold Dark Matter) [1]. It is frequently referred to as the standard model of the Big Bang cosmology because it is the simplest model that provides a reasonably good account of the following properties of the cosmos. For example, the features of the CMB, the large-scale structure in the distribution of galaxies, the abundances of hydrogen, and the accelerating expansion of the Universe are well-described by ΛCDM. In this one, the Universe is composed of three main components as presented in Fig. 1.1. The first one is the well-known baryonic matter, in which abundance is about 5% of the total mass-energy contribution of the Universe, another 25% is composed of a mysterious form of matter called Dark Matter (DM). This one has not been directly observed, but it is present in a variety of astrophysical observations, generating gravitational effects that are not explainable with the

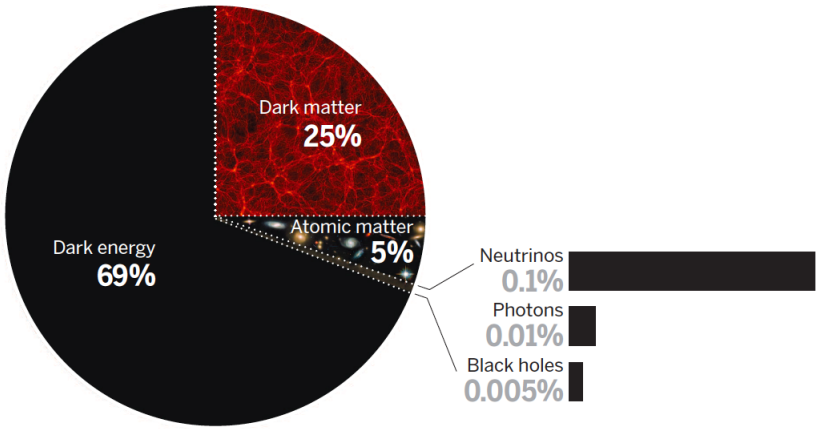

Figure 1.1: The multiple components that compose our Universe in the ΛCDM model. Dark energy composes 69% of the mass-energy density of the Universe, dark matter comprises 25%, and "ordinary" atomic matter makes up 5%. There are other visible subdominant components: three different types of neutrinos comprise at least 0.1%, the cosmic background radiation makes up 0.01%, and black holes comprise at least 0.005%. Figure taken from ref. [1].

amount of luminous matter. The DM presence played a fundamental role both in the structure formation and evolution of the Universe. The other important component is a form of unknown energy which answers the question "Why is the Universe accelerating?". It is called Dark Energy [2] and makes up about 70% of the mass-energy density of the Universe.

The existence of dark matter was discussed and debated since the beginning of the 20^{th} century. Indeed, Lord Kelvin was among the firsts to attempt a dynamic estimate of the amount of dark matter in the Milky Way. His argument was simple yet powerful: if stars in the Milky Way can be described as a gas of particles, acting under the influence of gravity, then one can establish a relationship between the size of the system and the velocity dispersion of the stars [3]. Indeed, he mentioned "Many of our stars, perhaps a great majority of them, may be dark bodies".

1.1.1 Galaxy Clusters

During the 20^{th} century, many scientists started studying the sky with the aim to understand the Universe but the Swiss-American astronomer Fritz Zwicky is arguably the most famous and widely cited pioneer in the field of dark matter. In 1933, he studied the red-shifts of various galaxy clusters, as published by Edwin Hubble and Milton Humason [4], and noticed a large

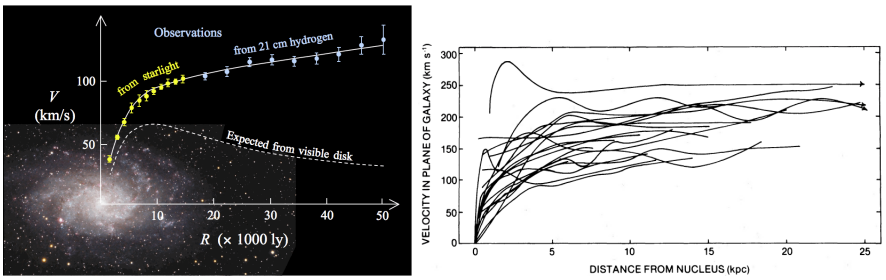

Figure 1.2: *Left*: Rotation curve of spiral galaxy M33 (yellow and blue points with error bars), and a predicted one from distribution of the visible matter (white line). The discrepancy between the two curves can be accounted for by adding a dark matter halo surrounding the galaxy. *Right*: Superposition of all rotation curves measured by V. Rubin et al. in ref. [8].

scatter in the apparent velocities of eight galaxies within the Coma Cluster, 99 Mpc away from our galaxy, with velocity dispersion of 1019 ± 360 km s^{-1} [5]. This had actually already been noticed by Hubble and Humason, but Zwicky went a step further, applying the virial theorem to the cluster in order to estimate its mass. In 1937, by assuming then an average absolute luminosity for cluster galaxies of 8.5×10^7 times that of the Sun, Zwicky showed that this led to a surprisingly high mass-to-light ratio of about 500 [6]. His work relied on the value of the Hubble constant known at that time, which was $H_0 = 558$ km s^{-1}Mpc^{-1}, with a $\sim 20\%$ uncertainty. By re-scaling the result applying the modern value of $H_0 = 73.3^{+1.7}_{-1.8}$ km s^{-1}Mpc^{-1} [7], we see that Zwicky overestimated the mass-to-light ratio by a factor of $\sim 558/73.3 = 7.6$. Despite this substantial correction, Coma's velocity dispersion still implies a very high mass-to-light ratio and points to the existence of dark matter in some form. This was the first evidence of the presence of dark matter, followed by several more within that century so that, from the 1980s, dark matter has become an accepted part of the cosmological paradigm.

1.1.2 Galactic Rotation Curves

One of the strongest pieces of evidence of DM is the measurement of the rotation velocities of stars and gas in many galaxies. The motion of collisionless rotating stars is governed by gravitational attraction, making galaxies a very good approximation of a virialized system. Under this hypothesis, the linear velocity of the stars is given by the formula

$$v = \sqrt{\frac{GM(r)}{r}}, \tag{1.1}$$

where G is the gravitational constant, r represents the distance from the galactic center, and $M(r)$ the total mass enclosed within the distance r. Since spiral galaxies are composed of a central dense bulk and a thin disk in the outer region, a great amount of the mass is located in the central bulk. Assuming a constant density in the bulk, for $r < R_{bulk}$ the mass increases as the volume ($\propto r^3$) and the velocity should increase as $v \propto r$, whereas for large distances $r > R_{bulk}$ the velocity should fall off as $v \propto r^{-1/2}$. However, the observed rotation curves are flat at large r, at least for values of r comparable with the disk radius, implying a total mass that grows linearly as the radius ($M(r) \propto r$) [9]. The behaviors of the rotation curves are reported in Fig. 1.2. These phenomena have been observed for the first time by Vera Rubin [8] and confirmed by the measurement of hydrogen 21 cm emission [10]. In order to explain the observations, several options are available. Among them, one could assume the existence of a halo of dark matter which interacts only by gravity. The density profile of this halo can be obtained exploiting the behavior of the mass which induces the measured rotation curve, getting

$$\rho_{\mathrm{DM}} \propto \frac{M(r)}{r^3} \propto \frac{1}{r^2}. \tag{1.2}$$

It would correspond to a spherically symmetric halo about the center of the Galaxy. On the contrary, the visible mass, constituted by stars and gases which can absorb and emit light, is concentrated in the disk. This behavior is the result of baryons dissipating energy through collisions and electromagnetic and strong interactions, which leads to collapse into a disk [11]. The rotation curve of the Milky Way itself has also been studied and found to be almost flat [12].

1.1.3 Gravitational lensing

The rotation curve observations allow for the possibility of having dark matter at galactic scale whereas the so-called gravitational lensing effect gives evidence of DM at galaxy cluster scale. This effect was theorized by Einstein in the framework of General Relativity. The effect of gravitational lensing occurs in presence of a gravitational field strong enough to bend the light rays trajectories [14], as represented in Fig. 1.3. Gravitational fields are generated by massive objects, and the greater is the mass, the greater is the space-time curvature. In particular, the strength of the deflection is proportional to the square root of object mass. By measuring the lensing distortions it is possible to reconstruct the profile of the mass that affected these deformations. Under the

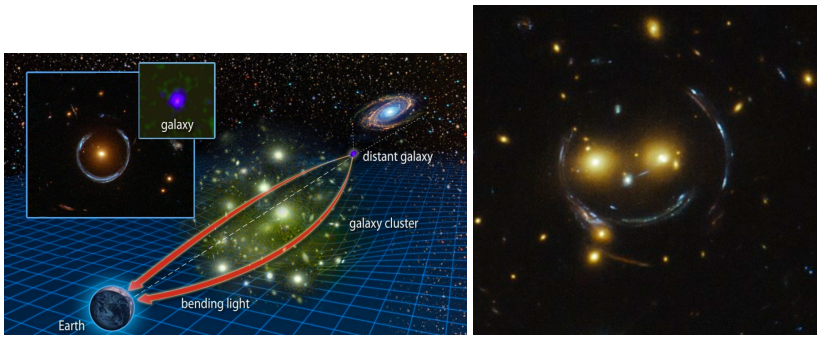

Figure 1.3: *Left*: Illustrated effect of gravitational lensing, where the bending of light around a massive object from a distant source is shown. *Right*: Example of a gravitational lens. The blue object is stretched and spread in a circular ring. Both images are taken from ref. [13].

hypothesis of point-like mass, the effect can be studied using the expression for the "Einstein radius" Θ_E

$$\Theta_E = \sqrt{\frac{4GM}{c^2}\frac{d_{LS}}{d_L d_S}}, \tag{1.3}$$

where c is the speed of light, d_{LS}, d_L and d_S are the distances between the lens and source, the distance to the lens, and the distance to the source, respectively. The estimation of the mass for several galaxy clusters was made by using such an effect. However, the result of many studies of gravitational lensing is that the baryonic matter is not enough to account for the lensing effects that are observed [15]. One of the hypotheses that may explain this discrepancy is based on the presence of non-luminous compact objects commonly referred to as Massive Compact Halo Objects (MaCHOs). Since this low number of MaCHOs candidates would only account for a small amount of non-luminous mass, these were ruled out as baryonic candidates for explaining dark matter. The lensing is also a good instrument to study the properties of DM, comparing its response with the one of the baryonic matter. This technique has been used during the observation of the so-called *Bullet Cluster*, the result of a sub-cluster colliding with the galaxy cluster 1E 0657-56 [16] shown in Fig. 1.4. During the collision, the galaxies between the cluster passed through each other without interacting. However, since the majority of the baryonic mass of the cluster is constituted by an extremely hot gas between galaxies, the collision compressed and shock-heated this gas, resulting in a huge amount of x-rays observed by NASA's Chandra x-ray observatory. In Fig. 1.4 the location of the dark matter in the cluster, which has been determined by measuring the lensing signal, is superimposed in blue. The offset between the position of the x-ray emission and the position of the lensing effect is thus a very strong indication for the presence of a far more weakly interacting form of matter than baryonic matter,

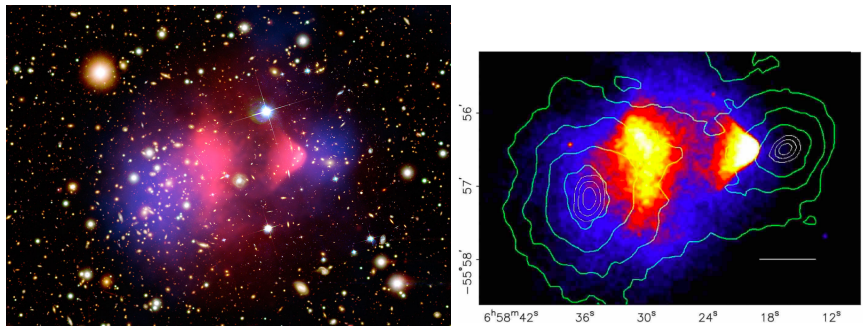

Figure 1.4: *Left*: Bullet cluster reconstruction in optical image data. The red part represents the hot x-ray emitting gas and the blue component shows the distribution of the majority of the mass in the cluster, clearly non-baryonic. The image is taken from ref. [13]. *Right*: X-ray emission from the "Bullet" cluster of galaxies observed by ground and space telescopes. Colored features correspond to X-ray emission observed by the Chandra space telescope, while the green contours correspond to mass reconstruction from weak lensing observations. This image is taken from ref. [17].

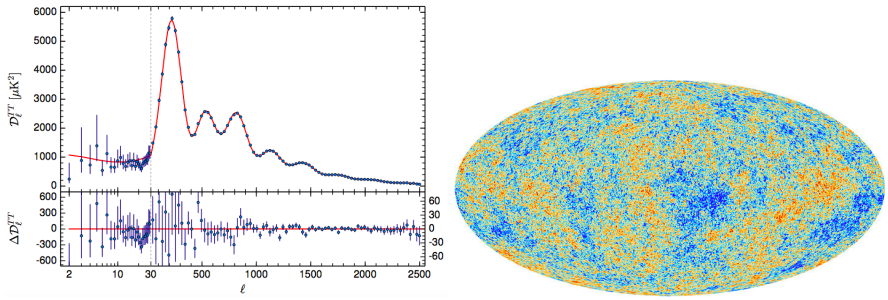

Figure 1.5: *Left*: Planck 2015 temperature power spectrum data in blue and the best-fit base ΛCDM theoretical spectrum in red. Figure from ref. [18]. *Right*: The anisotropies of the Cosmic microwave background (CMB) as observed by Planck. The CMB is a snapshot of the oldest light in our Universe, imprinted on the sky when the Universe was just 380000 years old. Credits: ref. [19].

with a total mass that by far exceeds the baryonic mass.

1.1.4 Cosmological evidences

The dark matter evidence at the cosmological scale is encased in the anisotropies of the CMB. In the ΛCDM model the structures that emerged in the early Universe are caused by the clustering of a non-interacting, slow-moving and yet undetected matter component called cold dark matter. Since dark matter interacts only (or almost) by gravity it begins to collapse gravitationally earlier than baryonic matter and after the decoupling between matter

and radiation, the baryonic matter falls into the gravitational wells forming the structures known nowadays. The direct measurements of the CMB spectrum from the WMAP satellite and most recently from the space observatory PLANCK allow for the determination of the CMB temperature anisotropies by analyzing the angular power spectrum. See Fig. 1.5. The power spectrum is simply a measurement of the amount that each point in the universe deviates from the mean temperature, decomposed to spherical harmonics. From the best-fit based on ΛCDM the parameters related to the density of the total matter, of the baryonic component, and the cold dark matter one [18] were extracted. These results, constrained with an accuracy of less than 2%, point to the conclusion that $\sim$84% of the matter content of the Universe is dark. A widely cited theory developed as an alternative to dark matter is the so-called MOdified Newtonian Dynamics (MOND), which is a framework for modified gravity on galactic scales [20]. A specific relativistic theory is needed to obtain predictions during the early universe. Assuming no additional matter content, popular candidates such as TeVeS [21] give a notably worse fit to CMB and large-scale structure data compared to cold dark matter [22, 23]. A recent analysis of the Milky Way rotation curve and stellar kinematics data is also in tension with MOND [24].

1.2 Dark Matter candidates

Any dark matter candidate must be consistent with a broad range of observations on astrophysical and cosmological scales [25], while also satisfying laboratory bounds. Several hypotheses about the main constituent of dark matter are broadly studied, keeping into account the evolution of the Universe and so the information about the clustering of dark matter encoded in the *matter power spectrum*. The matter power spectrum represents the variance in density perturbations. For large density fluctuations, gravitational collapse into halos will occur. Combining our knowledge of the matter power spectrum with other cosmological information, one can make general and quantitative statements about general dark matter properties. Dark matter has to be

- **Dark**, meaning that its interaction is not included in the Standard Model (SM) framework. Astrophysical observations imply that dark matter is not luminous and cosmological evidence requires that a matter component interacting only by gravity must be present.

- **Cold**, or better say non-relativistic, otherwise, the matter fluctuations would have been washed out due to the dark matter motion, leading to

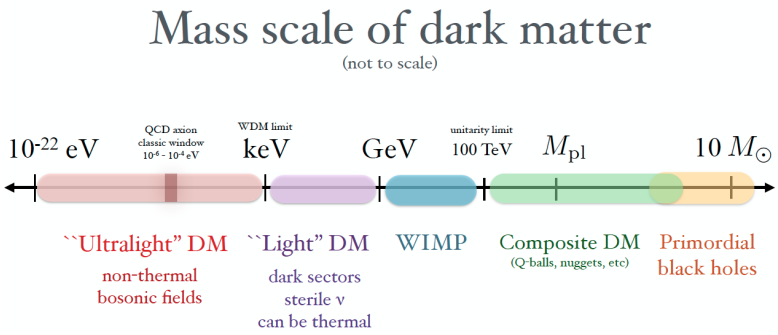

Figure 1.6: The mass range of possible DM candidates, including both particle candidates and primordial black holes. Mass ranges are only approximate and meant to indicate general considerations. Figure taken from [26].

a damping of the power spectrum. In other words, if DM is too light, and which therefore travels too quickly after decoupling, small-scale structures can not form and can not match the distribution of structures we see today.

- **Stable**, or almost stable, since its lifetime should be much greater than the age of the Universe or they would have decayed by now.

In the next paragraph the most studied and accredited candidates are listed and described, using as a reference Fig. 1.6.

1.2.1 Ultralight dark matter

We will refer to the entire span of candidates below ∼keV as ultralight bosonic dark matter. The very low mass end of DM candidates is usually quoted as around $m_{\rm DM} \approx 10^{22}$ eV/c^2. If dark matter is light it behaves as a coherent field. This can be seen by estimating the dark matter occupation number N

$$N = \frac{\rho_{\rm DM}}{m_{\rm DM}} \times \lambda_{\rm DB}^3 \tag{1.4}$$

$$\lambda_{\rm DB} = \frac{h}{m_{\rm DM} v_{\rm DM}}, \tag{1.5}$$

where $\lambda_{\rm DB}$ is the De Broglie length and h the Planck constant. By using as dark matter density $\rho_{\rm DM} = 0.4\,{\rm GeV\,c^{-2}\,cm^{-3}}$ [27] and as dark matter velocity

$v_{\rm DM} = 10^{-3}c$ (being c the speed of light), one obtain a value of N that is

$$N = 75 \left(\frac{10 \text{ eV}}{m_{\rm DM}} \right)^4 , \tag{1.6}$$

reminding that if $N \gg 1$ means that DM can be described as a classical field. Studies of the Lyman α forest and dwarf galaxies generally require $m_{\rm DM} \gtrsim 10^{22}$ eV/c^2. The regime within an order of magnitude or so of 10^{22} eV/c^2 is known as Fuzzy DM [28]. Supposing the DM so light, it would be highly relativistic if it had been produced in thermal equilibrium, not respecting the cosmological observations. The abundance here is instead set by misalignment, which is just a generic term for a mechanism that makes the field behave like a cold dark matter in the late universe. For instance, a free scalar field having no interactions with the SM, and with an average value set by the *misalignment mechanism* [29], is indeed a perfectly valid DM candidate that is extremely difficult to test. However, the QCD axion is a specific example of bosonic field dark matter with tiny couplings to the SM, which gives a compelling reason to search for weakly-coupled bosons. The QCD axion is a pseudo-Nambu-Goldstone boson of an approximate $U(1)$ called a Peccei-Quinn symmetry, proposed to solve the strong CP problem. By applying various astrophysical constraints and requiring that the axion comprises the entire amount of dark matter, the mass window permitted narrows to $10^{-6} - 10^{-4}$ eV/c^2. Many experiments are currently trying to detect these particles via Primakoff effect [30] which implies the conversion of axions into photons in a magnetic field. The three classes of experiment consist in haloscopic like ADMX [31], helioscopic as CAST [32] and laboratory experiments like ALPS [33].

1.2.2 Light dark matter

Moving to heavier particles allows for an explanation of dark matter that is more consistent with the cosmological constraints without requiring particular mechanisms of production. A general and qualitative statement can be made about DM candidates with mass below keV scale. They are often related to the so-called *warm dark matter* bound, with the idea of suppression in the matter power spectrum for sufficiently low mass DM. Currently, the strongest bounds are from observations of the Lyman α forest, which is a tracer for the matter power spectrum [34]. If dark matter was in thermal equilibrium and had a similar temperature as the photons, its mass should be $\gtrsim$ keV/c^2. Of course, this is not a hard boundary and specific models can fit observational data

depending on the actual velocity of the DM in the early universe. One of the frameworks worth to explore is the *dark sector* or *hidden sector* [35]. Here we view the DM and mediator as part of a separate "Dark Standard Model", and where there is a portal link to the SM. The ingredients of the dark sector can be fairly minimal, consisting of a feebly coupled dark force and a dark fermion charged under that force. If the dark sector is thermally populated during the early universe, the portal link also allows for any excess of energy/entropy to be deposited back to the SM thermal bath. The portal may take various forms that can be classified by the type and dimension of its operators. The best motivated and most studied cases contain relevant operators taking different forms depending on the spin of the mediator: *Vector* (spin 1), *Neutrino* (spin 1/2), *Higgs* (scalar) and *Axion* (pseudo-scalar). Among these possible portals, the vector portal is the one for which the interaction takes place because of the kinetic mixing between one dark and one visible Abelian gauge boson (non-Abelian gauge bosons do not mix). The visible photon is taken to be the boson of the $U(1)$ gauge group of electromagnetism or, above the electroweak symmetry-breaking scale, of the hypercharge whereas the dark photon comes to be identified as the boson of an extra $U(1)$ symmetry.

Another option related to light DM with a mass on the order of keV consist of *sterile neutrinos*. A sterile neutrino could be either an additional flavor of a neutrino that does not couple to any other known leptons, except possibly indirectly by oscillating into another flavor, or a right-handed neutrino (or left-handed anti-neutrino) remaining invisible due to the lack of coupling with its lepton counterpart with the correct parity. In those cases, sterile neutrinos would be detectable through their tiny mixing with active neutrinos. Depending on their mass, such sterile neutrinos could be produced with a wide range of temperatures, and thus could constitute either a warm ($m_{\nu_s} \sim$ keV/c^2) or a cold ($m_{\nu_s} \gg$ keV/c^2) candidate for dark matter. No theory can predict their exact mass scale but high enough masses such that they are not-relativistic are not excluded by the evidence that, by looking at the level of small-scale structure formation observed in the universe, require them to be larger than $\sim$10 keV/c^2 [36]. With such feeble interactions, such particles would have never been in thermal equilibrium in the early Universe, but instead would have been produced through the oscillations of the other neutrino species.

1.2.3 Weakly Interacting Massive Particles

An array of arguments discussed at the beginning of the section have led to establishing a popular (and sensible) paradigm that the dominant fraction of DM is probably cold and that it should be not only (sub) weakly interacting but also non-relativistic and massive, or in short, it is made up of Weakly Interacting Massive Particles (WIMPs). The latter refers to a mass range of GeV/c^2 up to $\sim$ 100 TeV/c^2, but WIMPs are also commonly used to mean thermal DM candidates as a whole, including the light DM discussed above. With such thermal DM candidates, meaning those in thermal equilibrium with the SM thermal bath, it is possible to determine early universe density and relic density by only a few quantities. The most robust mechanism for the generation of relic abundance of dark matter is the so-called freeze-out mechanism [37]. In the very early and hot Universe, SM species and DM were in thermal equilibrium, with DM particle production and annihilations balancing each other out

$$\mathrm{DM\ DM} \leftrightarrow \mathrm{SM\ SM}. \tag{1.7}$$

In the next phase, precisely when the temperature decreased enough so that the energy available is kept below the mass of the DM particle, dark matter still has the possibility to annihilate but it can not be produced anymore,

$$\mathrm{DM\ DM} \rightarrow \mathrm{SM\ SM}. \tag{1.8}$$

In this regime, the abundance of DM falls exponentially until the Universe expanded and cooled down enough to freeze out of equilibrium with the thermal plasma. This decoupling happened when the WIMP annihilation rate became roughly less than the expansion rate of the universe. WIMPs are then left with the abundance they had when they decoupled. As the rate of the DM annihilation is defined as

$$\Gamma_{\mathrm{ann}} = n_{\mathrm{DM}} \langle \sigma_{\mathrm{ann}} v \rangle \tag{1.9}$$

where $n_{\mathrm{DM}} \propto \exp\left(-m_{\mathrm{DM}}c^2/kT\right)$ is the particle DM density that follows a Maxwell-Boltzmann distribution (m_{DM} is the DM mass, k the Boltzmann constant and T is the temperature), σ_{ann} is the annihilation cross-section and v is the relative velocity between particles in the process. If σ_{ann} is small, DM would decouple early when the temperature of the universe is still high, leading to a larger relic abundance. On the contrary, if the annihilation cross-section is large, DM would remain in equilibrium for longer, meaning that

the particles would become more and more diluted. For a GeV-scale DM particle, by requiring a relic abundance comparable with the result of the CMB fit with ΛCDM model, one can estimate the product between the annihilation cross-section and velocity

$$\langle \sigma_{\rm ann} v \rangle \approx 3 \times 10^{-26} {\rm cm}^2 {\rm s}^{-1}. \tag{1.10}$$

For typical velocities $v \approx 0.1\ c$ one obtains a cross-section which is near the strength of weak interaction. In the early days, this coincidence was found so remarkable that it was coined as the "WIMP miracle". This kind of WIMP, a particle beyond the standard model, is commonly thought of as the Lightest Supersymmetric Particle (LSP) in supersymmetry (SUSY) theory [38]. This is primarily because supersymmetry can cure the theoretical difficulty of fundamental scalar particles. It can render a theory stable through the radiative corrections which would otherwise force a fine-tuning of high-energy parameters as, for example, the naturalness problem [39]. In supersymmetry, each particle from one group would have an associated particle in the other, which is known as its superpartner, the spin of which differs by a half-integer. For example, there would be a particle called a "selectron" (electron superpartner), a bosonic partner of the electron. Since we expect to find these "superpartners" using present-day equipment, if supersymmetry exists then it consists of a spontaneously broken symmetry allowing superpartners to differ in mass [40]. One of the most popular SUSY particles is the lightest neutralino χ [41], defined as a superposition of the supersymmetric partners of the W, B and Higgs boson. SUSY provides that the neutralino mass has to be in the range between ${\rm GeV/c}^2 \lesssim m_\chi \lesssim {\rm TeV/c}^2$. In addition to the neutralino, the WIMP category includes a lot of particles, for example, Two Higgs Doublet Models (2HDM) [42], Little Higgs models [43], the Twin Higgs model [44] or Sneutrinos [45].

1.2.4 Heavy Dark Matter

What is the largest possible mass of a DM candidate? The least-massive known galaxies reside in DM halos with mass as low as $\sim 10^5 - 10^6 M_\odot$ within the half-light radius. This means that DM could be composed of objects with mass as high as $\sim 10^5 - 10^6 M_\odot$, and still be consistent with observations of galactic dynamics. Indeed, there exist models of scalar field DM where the field condenses into dense and compact massive objects, known as a boson star or an axion star in the case of axions. Due to the conventions of the field, this is not regarded as an independent DM candidate, since not all of the DM

energy density is necessarily stored in the boson stars. For instance, among the heaviest dark matter candidates, we find

- *Superheavy particles and composite objects:* In between the $\mathcal{O}(10)$ TeV scale and $\sim 10^{13}$kg, the theoretical landscape has not been explored as thoroughly in the literature. Up to the Planck mass $M_{\rm pl} = (\hbar c/G)^{1/2} = 1.22 \times 10^{19}$ GeV/c^2, the easier solution is to consider fundamental particles as DM. Such superheavy candidates are typically called *WIMPzillas*. They could not have been in thermal equilibrium and must have been produced non-thermally or through gravitational particle production at the end of inflation [46]. For masses larger than $M_{\rm pl}$, DM candidates are thought of as composite objects, namely bound states or nuggets of lighter fundamental particles. The boson stars mentioned above can populate this mass range. A related possibility is that of $Q\text{-}balls$, solitonic states that appear in SUSY models [47]. Clusters of baryons or other fermions have also been considered, where recent work has explored formation in phase transitions or by fusion processes [48].

- *Primordial Black Holes:* The high-density limit for dark matter is a black hole, and here the constraints are much stricter and more severe. Dark matter consisting of black holes is known as primordial black hole (PBH) DM since they must have been formed and present well before recombination. To the extent that we would like to consider any possible candidate that makes up $\mathcal{O}(10\%)$ of the total DM density, then PBHs are accessible up to masses of about $50M_\odot$. Massive PBHs can contribute to the accretion of matter in the early universe, leading to the emission of ionizing radiation which is strongly constrained by CMB observations [49].

1.3 Dark Matter Experiments

In the previous section, we described a large number of theoretical DM candidates, but the real challenge is to confirm, or to reject to some extent, the existence of one of these. Many experiments are currently working to detect one possible candidate. In order to detect DM particles, the interaction with SM particles is assumed. The diagram used to group all possible interactions between DM and SM particles is shown in Fig. 1.7. All of these processes lead to a distinct detection strategy. Collider search for the production of DM in an annihilation SM process; indirect detection looks at unexpected abundances of

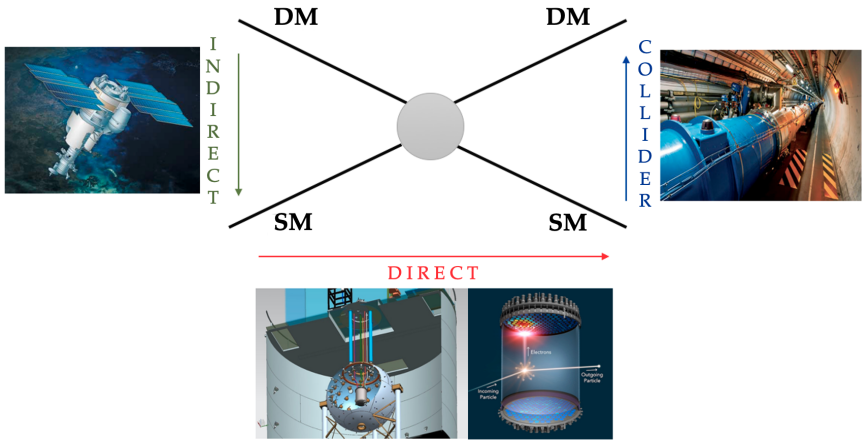

Figure 1.7: Schematic diagram of different strategies to detect a dark matter particle. The arrows point to the time order. *From top to bottom:* indirect detection aims to measure the products generated by DM annihilation; *from left to right:* direct detection looks at signals produced by scattering; *from bottom to top:* production of DM at colliders.

cosmic rays coming from DM annihilation while direction detection aims to measure a signal through the DM scattering off SM particles.

1.3.1 Direct Detection

Direct detection is the most common approach used in the dark matter search field. The idea is to detect a nuclear or an electron recoil into the detector due to the elastic scattering between the DM particle and the target

$$\mathrm{DM} + \mathrm{SM} \rightarrow \mathrm{DM} + \mathrm{SM}.$$

Goodman and Witten proposed this idea in 1985 [50] and it was developed by Drukier, Freese, and Spergel in 1986 [51]. The flux of DM particle that hits the Earth depends on the density of DM and the DM velocity with respect to the Earth frame. The DM speed distribution is obtained in the framework of the Standard Halo Model (SHM), where the DM in the Milky Way is modeled as an isothermal sphere with an isotropic and Maxwellian velocity distribution, truncated at the galactic escape speed $v_{\mathrm{esc}} \simeq 544$ km/s with a rms value of the velocity dispersion σ_v. This truncation takes into account the fact that WIMPs with sufficiently high velocities can escape the galaxy potential well and, thus, the high-velocity tail of the distribution is depleted. The DM escape velocity in the Milky Way is estimated from that of high-velocity stars. A

second assumption is that the DM halo rest frame is equal to the galactic rest frame (implying a non-rotating halo). We define the distribution in galactic rest frame as:

$$\widetilde{f}(\mathbf{v}) = \begin{cases} \frac{1}{N_{\rm esc}} \left(\frac{3}{2\pi\sigma_v^2}\right)^{3/2} e^{-3\mathbf{v}^2/2\sigma_v^2}, & \text{for } |\mathbf{v}| < v_{\rm esc} \\ 0, & \text{otherwise,} \end{cases} \tag{1.11}$$

where the factor $N_{\rm esc}$ is introduced to satisfy the normalization condition:

$$\int \widetilde{f}(\mathbf{v})\, d^3\mathbf{v} = 1, \tag{1.12}$$

which gives

$$N_{\rm esc} = \mathrm{erf}\left(\frac{v_{\rm esc}}{v_0}\right) - \frac{2}{\sqrt{\pi}} \frac{v_{\rm esc}}{v_0} e^{-(\frac{v_{\rm esc}}{v_0})^2} \tag{1.13}$$

with v_0 defined as the most probable speed of roughly 235 km/s [52]. The relation that links the most probable speed to the rms dispersion is $\sigma_v = \sqrt{3/2} \cdot v_0$. As the velocities are not relativistic, to obtain the DM speed distribution on Earth one has to perform a simple Galileian transformation

$$\mathbf{v}_{\substack{\rm DM \\ \rm Earth}} = \mathbf{v}_{\substack{\rm DM \\ \rm galaxy}} - \mathbf{v}_E \tag{1.14}$$

where $\mathbf{v}_E$ is the velocity of the Earth with respect to the galactic rest frame while $\mathbf{v}_{\substack{\rm DM \\ \rm Earth}}$ and $\mathbf{v}_{\substack{\rm DM \\ \rm galaxy}}$ represent the velocity of the DM with respect to the Earth and to the Milky Way, respectively. The Earth moves along with the solar system across the galaxy with the same velocity $v_\odot$ and it has a periodic orbital velocity $v_\oplus$ around the Sun

$$v_E = v_\odot + v_\oplus \cos\gamma \left(\frac{2\pi(t - t_0)}{T}\right). \tag{1.15}$$

where $\gamma \simeq 60°$ denotes the angle subtended by the orbital plane of the Earth and the galactic plane, $v_\odot \simeq 220$ km/s is the velocity of the solar system in the galactic rest frame, $v_\oplus \simeq 30$ km/s, $T = 1$ yr is the period of revolution of the Earth around the Sun and t_0 is a reference time in a year. Neglecting the seasonal motion of the Earth $\mathbf{v}_E$ gets constant the following frame reference invariance is allowed:

$$f(\mathbf{v}_{\substack{\rm DM \\ \rm galaxy}})\, d^3\mathbf{v}_{\substack{\rm DM \\ \rm galaxy}} = f(\mathbf{v}_{\substack{\rm DM \\ \rm Earth}})\, d^3\mathbf{v}_{\substack{\rm DM \\ \rm Earth}} = f(\mathbf{v}_{\substack{\rm DM \\ \rm Earth}} + \mathbf{v}_E)\, d^3\mathbf{v}_{\substack{\rm DM \\ \rm Earth}}. \tag{1.16}$$

Since we will focus on the velocity of the DM in the Earth reference frame, for simplicity we rename the variable $\mathbf{v}_{\substack{\rm DM \\ \rm Earth}} \equiv \mathbf{v}$. For a fixed v, integrating over the polar angle between $\mathbf{v}$ and $\mathbf{v}_E$ we obtain the one dimensional distribution

$f(v)$:

$$f(v)\,dv = \frac{1}{N_{\rm esc}}\frac{v}{\sqrt{\pi}v_E v_0}\left[e^{-(\min(v-v_E,v_{\rm esc}))^2/v_0^2} - e^{-(\min(v+v_E,v_{\rm esc}))^2/v_0^2}\right]\,dv. \tag{1.17}$$

Note that if $v > v_{\rm esc} + v_E$ then $f(v) = 0$. One of the DM detection techniques is based on the annual periodicity of Earth's motion around the Sun. Indeed, with respect to the motion of the Sun around the galaxy, in June the Earth moves in the same direction as the Sun while in December in the opposite one. This effect should cause a modulated WIMP wind during the year.

By using the SHM description, it is possible to estimate the expected DM flux assuming a local density of DM $\rho_{\rm DM} = 0.4\ {\rm GeV/cm^3}$, a DM mass of 100 GeV and DM static in the galactic rest frame. Under these assumption the flux $\phi_{\rm DM} \sim 10^6$ DM cm^{-2} s^{-1}. The detectable rate is given by

$$R = \phi_{\rm DM} \cdot \langle\sigma_{\rm DM-SM}\rangle \cdot N_T, \tag{1.18}$$

where $\langle\sigma_{\rm DM-SM}\rangle$ is the mean cross-section of the process and N_T is the available number of targets in the detector. In order to obtain a reference number, assuming an electroweak interaction for the estimation of $\langle\sigma_{\rm DM-SM}\rangle \simeq 10^{-40}\ {\rm cm}^2$ and a detector of about 10^{27} targets (relative, for example, to 50 kg argon detector), the total rate turns out to be roughly 10 events per year. With such a low event rate is very important to reduce the background abundance as much as possible. This is usually done using a different kinds of shields and veto systems surrounding the active detector. Moreover, assuming to control the background, a larger detector should maximize the total number of events observed.

In particular, it is interesting to describe in detail the energy dependence of the event rate in the case of a WIMP interacting with a detector target. The general formula is

$$\frac{dR}{dT_R} = \phi_{\rm DM} \cdot N_T \cdot \frac{d\sigma_{\rm DM-SM}}{dT_R}, \tag{1.19}$$

in which T_R represents the recoil energy of the target after the scattering. The DM flux for particles with speed in the range v and $v + dv$ in the laboratory frame is $\phi_{\rm DM} = (\rho_{\rm DM}/m_{\rm DM})vf(v)dv$.

In the standard hypothesis, the WIMP scatters off the whole nucleus of the target, given that the De Broglie wavelength of 10-100 GeV WIMP (in a non-relativistic regime) is

$$\lambda_{\rm DB}^{\rm WIMP} \simeq 10 - 100\ {\rm fm} \tag{1.20}$$

comparable or even larger than the typical nuclear sizes. [i] The most

[i] Under the assumption of the scattering off a nucleus the cross-section can be re-written by

generic WIMP-nucleus interaction has both Spin-Dependent (SD) and Spin-Independent (SI) contributions so that the total differential cross-section is the sum of the two

$$\frac{d\sigma_{\mathrm{DM}-\mathcal{N}}}{dT_{\mathrm{nr}}} = \frac{d\sigma_{\mathrm{SI}}}{dT_{\mathrm{nr}}} + \frac{d\sigma_{\mathrm{SD}}}{dT_{\mathrm{nr}}}, \tag{1.21}$$

where

$$\frac{d\sigma_{\mathrm{SI}}}{dT_R} = \frac{m_N \sigma_{\mathrm{SI}}}{2\mu_{\mathrm{DM}}^2 v^2} |Z + (f^n/f^p)(A-Z)|^2 |F(T_R)|^2, \tag{1.22}$$

$$\frac{d\sigma_{\mathrm{SD}}}{dT_R} = \frac{2m_N \sigma_{\mathrm{SD}}}{3\mu_{\mathrm{DM}}^2 v^2} \frac{J+1}{J} |a_p \langle S_p \rangle + a_n \langle S_n \rangle|^2 |F_{\mathrm{SD}}(T_R)|^2. \tag{1.23}$$

The parameters presented in the above differential cross-sections are the mass of the target nucleus m_N, the WIMP-proton reduced mass μ_{DM} and the velocity of the WIMP with respect to the target v. In SI cross-section, Z and A are respectively the atomic and mass number of the target, f^p and f^n are the coupling parameters with proton and neutron and $F(T_R)$ is the form factor corresponding to the Fourier transform of the nuclear density [53]. In SD cross-section, J is the total nuclear spin, $\langle S_{p,n} \rangle$ are the expectation values for the proton and neutron spin into the nucleus, $a_{p,n}$ are the spin coupling parameters, and $F_{SD}(T_R)$ is the form factor determined by the internal spin structure of the nucleus [54]. To see the derivation and details see ref. [55]. For a spin zero nuclus the SD term in eq. 1.23 vanishes, and assuming equal coupling to proton and neutron $f^p = f^n$ the differential rate of WIMPs, per unit of detector exposure, can be written as

$$\frac{dR}{dT_{\mathrm{nr}}} = \frac{\rho_{\mathrm{DM}}}{2\mu_{\mathrm{DM}}^2 m_{\mathrm{DM}}} \sigma_{\mathrm{SI}} A^2 |F(T_{\mathrm{nr}})|^2 \int_{v_{\mathrm{min}}}^{\infty} \frac{f(v)}{v} dv. \tag{1.24}$$

The shape of the differential event rate depends on a number of factors. First of all, the DM and target nuclear masses determine the kinematics of the process, such as the minimum WIMP velocity, v_{min}, needed to produce a nuclear recoil T_{nr}, and the WIMP flux. A less trivial dependence is encased in the nuclear form factor and in the shape of the DM speed distribution $f(v)$. From the experimental point of view, the events can be categorized depending on how the energy deposited is measured, which can be in the form of heat (phonons), ionization (electrons), scintillation (photons) or a combination of the three forms. In Fig. 1.8 several experiments using the mentioned techniques are listed. For example, crystal scintillator experiments such as DAMA/LIBRA [57,58] use crystals of Thallium-doped Sodium Iodide, NaI(Tl). When a nuclear recoil happens in the crystal, scintillation occurs. Cryogenic experiments, such as SuperCDMS [59], CRESST [60], CoGENT [61] and EDELWEISS [62] use cryogenic crystals such as germanium or silicon

specifying that the recoil is nuclear-type, so that $T_R \equiv T_{\mathrm{nr}}$ and $\frac{d\sigma_{\mathrm{DM}-\mathrm{SM}}}{dT_R} \equiv \frac{d\sigma_{\mathrm{DM}-\mathcal{N}}}{dT_{\mathrm{nr}}}$

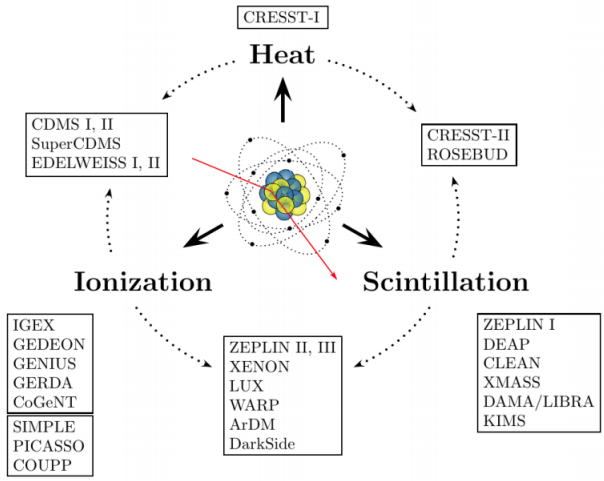

Figure 1.8: Different kind of signal detected in nowadays experimental direct detection projects. Figure taken from ref. [56].

as target materials. When a WIMP recoils off a target nucleus, phonons are generated in the crystal along with an ionization signal. Superheated liquid detectors such as COUPP [63], SIMPLE [64] and PICASSO [65] use a detector volume filled with droplets of superheated liquid, and when a WIMP deposits energy, it induces the nucleation of a bubble producing an acoustic signal which is detected by piezoelectric transducers. Noble liquid experiments use liquid (or two-phase gas-liquid) noble elements such as xenon and argon as target materials like DarkSide [66], DEAP [67], XENON [68], LUX [69], and PandaX [70]. When a WIMP interacts with the target in the noble liquid, a first scintillation signal is produced, together with the ionized electrons. For two-phase detectors, the extracted electrons get drifted towards the gas phase thanks to an electric field where they produce a second scintillation signal (S2). For a detailed review about the dark matter, experiments see ref. [71]. In Fig. 1.9 the updated results of the direct detection dark matter experiments are shown. The DAMA/LIBRA experiment operating at the LNGS laboratory in Italy, claims to see an annual modulated DM signal with a significance of 12.9σ [57, 58]. The mass of the dark matter particle compatible with such a signal falls in the range between 10 and 20 GeV/c^2 with a spin-independent WIMP-nucleon cross-section of $\sim 2 \times 10^{-40}$ cm^2 for sodium. For iodine, the mass is between 60 and 100 GeV/c^2 with a cross-section of about 5×10^{-41} cm^2. This result, however is not consistent with others experiments like XENON1T (2018) [72], LUX (2017) [73], PandaX-II (2017) [70], SuperCDMS (2018) [74] and DarkSide-50 experiment (2018) [75] since all of them excluded DAMA/LIBRA results. Nowadays, the worldwide most stringent upper limit

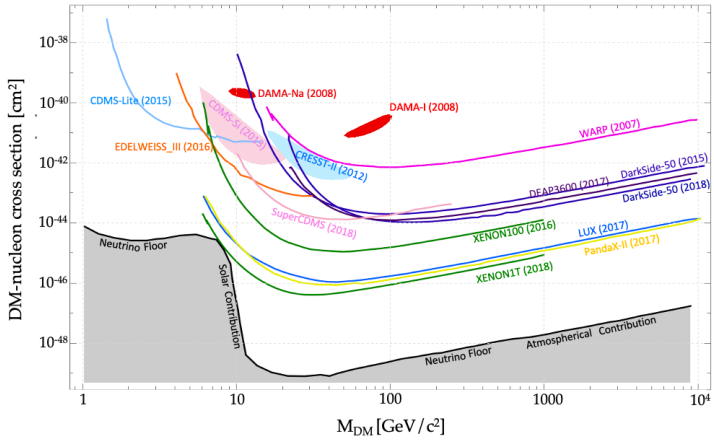

Figure 1.9: Current limits on DM direct detection spin-independent cross-section as a function of the WIMP mass. The shaded area below the black line on the bottom of the plot corresponds to the 3σ discovery limit for xenon in the presence of an irreducible neutrino background. See text for details.

is given by XENON1T excluding a spin-independent WIMP-nucleon cross-section of 4.1×10^{-47} cm^2 for a WIMP mass of 30 GeV/c^2. A general rule is that by increasing the exposure of the experiment, and maintaining the same level of background, it is possible to exclude lower cross-sections. Candidates for the next generation of multi-ton Ar and Xe detectors are XENONnT [76], DARWIN [77], and DarkSide-20k [78]. Finally, it is important to underline that next-generation experiments have to take into account the Coherent Elastic Neutrino Nucleus Scattering (CEνNS) background. This effect will be deeply investigated in the second part of this thesis. For next-generation dark matter experiments, CEνNS will be an irreducible background [79, 80], and the limit to the sensitivity due to this background is typically called "neutrino floor", roughly identified by the black region in Fig. 1.9. At this point, it will be important to evaluate new techniques to elude the neutrino limit, for example, directional detection of dark matter [81].

1.3.2 Indirect Detection

The indirect detection is based on the DM annihilation process

$$\mathrm{DM} + \mathrm{DM} \rightarrow \mathrm{SM} + \mathrm{SM}.$$

This type of detection looks at unexpected excess of standard model particles coming from space. In order to maximize the probability to detect the DM annihilation, it is important to look at over-dense regions of dark matter. The typical approach is to observe SM particles as γ-rays, charged leptons, and neutrinos produced by the annihilation of WIMPs. For gamma rays and neutrinos, which essentially travel through space undisturbed, the resulting flux is given by:

$$\frac{d\phi}{dE} = \frac{\langle \sigma_{\rm ann} v \rangle}{2m^2_{\rm DM}} \times \sum_i BR_i \times \frac{dN^i_{\gamma,\nu}}{dE} \cdot \int_{\Delta\Omega} d\Omega' \int_{\substack{\text{line of} \\ \text{sight}}} dl \; \rho^2_{\rm DM}(l), \qquad (1.25)$$

with $\langle \sigma_{\rm ann} v \rangle$ being the annihilation cross-section averaged over the velocity distribution of DM, $m_{\rm DM}$ is the DM mass, BR_i represents the branching fraction to different channels depending on the DM model, $dN^i_{\gamma,\nu}/dE$ is the yield of particles as function of their energy E. The remaining part represents the astrophysical contribution when $\rho_{\rm DM}$ is the DM density along the line of sight, $\Delta\Omega$ the solid angle element considered in the observation. For charged particles, since they interact along the path toward the Earth, the flux has to be calculated solving a diffusion equation. The measure of background diffuse γ-rays are made typically by satellite telescope such as Fermi-LAT. The latter put a limit on DM detection [82]. Current experiments have also the possibility to detect charged products. The main signature for DM in charged cosmic rays is in the anti-proton and positron channels. Experiments such as PAMELA [83], launched in 2006, on a Russian satellite and AMS [84], launched in 2011, on the International Space Station are operating to measure particle-antiparticle abundance in cosmic rays.

The results of the PAMELA experiment, presented in 2008, have induced a lot of interest among the community. Indeed, a rising positron fraction [85] together with a hard (electron+positron) spectrum presented by the Fermi-LAT [86] strongly suggests an additional source of positrons. AMS confirmed the rise of the positron fraction with much-improved event statistics at energy above 10 GeV. If the positron excess is interpreted as of WIMP origin, the result prefers relatively large particle masses ($\sim$TeV). This feature has been interpreted as tentative for the evidence of dark matter annihilation. The fact that there is an unexplained excess is of course exciting, but there are well motivated conventional sources that could provide the extra positron like pulsars [87] or supernova remnants effects [88, 89].

1.3.3 Collider Detection

The search of DM in hadron colliders such as Large Hadron Collider (LHC) is based on the possible process

$$\mathrm{SM} + \mathrm{SM} \rightarrow \mathrm{DM} + \mathrm{DM}.$$

Although such production is possible, the unknown DM mass means that we do not know whether the center-of-mass energy available in present experiments is sufficient for the production of DM. The DM particles would be invisible to any detector in the vicinity of the collision point and would hence reveal their presence only via an apparent imbalance in the total transverse momentum (so-called missing transverse momentum or, more colloquially, missing energy). This leads to the question of how to build DM models for predicting missing energy signals at the LHC. One approach is to look at the predicted effect of SUSY. Nevertheless, in models such as SUSY, DM particles are typically produced together with a significant number of additional SM particles from the decay chain, implying that there is no direct connection between the annihilation and the production process.

A different idea is based on the deviations from SM expectations to put limits on the Effective Field Theory (EFT) of DM coupling. This limit can also be used to constrain the parameter region of direct and indirect detection [90]. Despite the numerous searches that are currently pursued at the LHC, there have been no DM signals observed [91]. Future upgrades of LHC should give more information about SUSY and should put more stringent constraints in the DM parameter region.

2

THE DARKSIDE-50 EXPERIMENT

The second chapter is dedicated to the description of the DarkSide setup, in particular emphazising the pros and cons of using liquid argon as an active target for dark matter searches. The latest results obtained by DarkSide Collaboration are also presented and discussed.

Contents

Noble liquids such as liquid argon (LAr) and liquid xenon (LXe) are excellent scintillators and very good ionizers in response to the passage of radiation. The possibility of simultaneous detection of scintillation and ionization signals is a unique feature of these liquids compared with other detection techniques. This feature, combined with the ease of scaling up to large mass at moderated cost, has made LXe and LAr popular targets and detectors for rare physics including dark matter, solar neutrinos, and neutrinoless double beta decay interactions. The DarkSide program employs LAr as a target, exploiting the technology of a dual-phase Time Projection Chamber (TPC).

2.1 Liquid argon for dark matter searches

The benefit of liquid argon is that it is quite abundant in Earth's atmosphere and it is easy to purify by removing electro-negative impurities, making it less expensive with respect to other noble liquids. This characteristic makes more feasible the idea of building large detectors. The most abundant component in natural argon is the stable isotope ^{40}Ar, produced by the electron capture of ^{40}K [92]. The production rate is proportional to the number of ^{40}K, thus the majority of the production occurs underground and from there ^{40}Ar diffuses into the atmosphere. Unfortunately, this is not the end of the story, otherwise, argon would have been the best candidate for rare physics searches. Indeed, due to interactions of cosmic rays, atmospheric argon also contains three long-lived radioactive isotopes: ^{39}Ar, ^{37}Ar and ^{42}Ar. Among these three isotopes, the pure β-emitter ^{39}Ar is often the dominant source of background at low energies for argon-based detectors, limiting the sensitivity to rare events and creating difficulties through signal pile-up and high data acquisition rates. It has an activity of (1.01 ± 0.08) Bq kg^{-1} [93], an endpoint of 565 keV, and a half-life of 269 years. The production of ^{39}Ar in the atmosphere is primarily due to cosmic rays. Several of the production channels do not have measured cross-sections but it is estimated that interactions with fast neutrons account for more than 94% of the total ^{39}Ar production in the atmosphere [94]. More details regarding the recently measured production rate can be found in [95]. Finding a way to get rid of the radioactive component would be the key to enhance the sensitivity of future argon-based dark matter detectors. A solution to mitigate the effects caused by ^{39}Ar is to use argon extracted by underground natural gas reservoirs [96]. Indeed, argon from natural gas wells is a promising source of ^{39}Ar-depleted argon because ^{39}Ar production induced by cosmic rays is strongly suppressed underground. The DarkSide-50 collaboration has

demonstrated that underground argon (UAr) used as their dark matter target has an ^{39}Ar rate of 7.3×10^{-4} Bq kg^{-1} [97], almost a factor 1400 below atmospheric levels. The use of UAr rather than atmospheric argon (AAr) has allowed for a reduction in energy threshold and increase in nuclear recoil acceptance while maintaining a background-free WIMP dark matter search [75]. Additionally, the use of low radioactivity UAr is critical for low-mass dark matter searches which extend to lower energy thresholds than the standard WIMP search [98]. A new production chain was recently set up to significantly increase the production of UAr. This new production needs to meet the target requirements of the Global Argon Dark Matter Collaboration (GADMC), a worldwide effort that unifies the DarkSide, DEAP-3600, MiniCLEAN, and ArDM experimental groups, for the construction of new experiments for argon dark-matter searches. The argon procurement for this new production chain starts from the Urania plant, now in the construction phase in Cortez, CO, USA, that will extract and purify UAr at a maximum production rate of about 330 kg d^{-1}. In order to further reduce the abundance of ^{39}Ar for the experimental program lead by GADMC, the Aria project [99] is under development and will play a crucial role for the next steps of rare physics searches. The Aria project consists of a plant, hosting a 350 m cryogenic isotopic distillation column, the tallest ever built, which is currently in the installation phase in a mine shaft at Carbosulcis S.p.A., Nuraxi-Figus (SU), Italy. The reduction of the ^{39}Ar isotopic fraction of the UAr is estimated to be a factor 10 per pass through the column, with a production rate of several kg d^{-1}.

The other two radioactive isotopes ^{37}Ar and ^{42}Ar are less problematic than ^{39}Ar due to the short half-life and the low abundance, respectively. Indeed, ^{37}Ar, which is produced in the atmosphere by neutron interaction on argon, decays purely through electron capture, producing low energy x-rays and Auger electrons, with a relatively short half-life of 35.01 days [100]. Since low background experiments are typically operated deep underground, shielded from cosmic rays, the ^{37}Ar activity typically decays below measurable levels within a few months, though the x-ray peak can be used as a low energy calibration source during early data-taking [98]. The long-lived isotope of argon, ^{42}Ar, is a potential background source in argon-based low background detectors. The half-life of this isotope is 32.9 years, a Q-value of 599 keV, and the beta decay of its daughter isotope, ^{42}K, has the maximum electron energy of 3.52 MeV. ^{42}Ar could be formed in the Earth's atmosphere due to nuclear bomb tests in the upper atmosphere carried out at the end of the 1950th - the beginning of the 1960th. The specific activity of this isotope has been measured in Gran Sasso Underground Laboratory and it turns out to be 92^{+22}_{-46} µBq kg^{-1} [101].

Under the reasonable assumption that these background sources can be kept

under control, the sensitivity of argon to dark matter particle interaction depends on how the energy deposited by an incoming particle is transferred to atoms and molecules of the medium. When a particle interacts in liquid argon, the energy can be deposited through excitation, ionization, and non-radiative transition (e.g. heat). These processes, in argon, lead to a luminescence which is called scintillation when occurring in liquids or solids. Scintillation from noble liquids arises in two distinct ways involving de-excitation and recombination:

- The excited atoms form within a few ps weakly bound excited dimers, called excimers [102], which radiatively de-excite producing vacuum-ultraviolet (VUV) photons

$$\begin{aligned} \mathrm{Ar}^* + \mathrm{Ar} &\rightarrow \mathrm{Ar}_2^*, \\ \mathrm{Ar}_2^* &\rightarrow 2\mathrm{Ar} + \gamma, \end{aligned} \tag{2.1}$$

- The ionized atoms couple forming ionized dimers, which recombine with electrons. After relaxations through non-radiative processes, the de-excitation chain releases a VUV photon

$$\begin{aligned} \mathrm{Ar}^+ + \mathrm{Ar} &\rightarrow \mathrm{Ar}_2^+, \\ \mathrm{Ar}_2^+ + e^- &\rightarrow \mathrm{Ar}^{**} + \mathrm{Ar}, \\ \mathrm{Ar}^{**} &\rightarrow \mathrm{Ar}^* + \mathrm{heat}, \\ \mathrm{Ar}^* + \mathrm{Ar} &\rightarrow \mathrm{Ar}_2^*, \\ \mathrm{Ar}_2^* &\rightarrow 2\mathrm{Ar} + \gamma. \end{aligned} \tag{2.2}$$

For liquid argon, the wavelength of the VUV photon is $\lambda \simeq 128$ nm. For both channels, the excimer Ar_2^*, at its lowest excited level is de-excited to the dissociative ground state by the emission of a single photon, due to the large energy gap which forbids other decay channels. It has been measured that in liquid argon the number of scintillation photons produced per 1 MeV electron is about 4×10^4 [103]. In general, ionizing radiation in noble liquids will lead to the formation of excimer in either singlet or triplet states, which are affected by different decay times. For the dimer Ar_2^* the singlet and the triplet state have a lifetime of $\tau_1 = (7.0 \pm 1.0)$ ns and $\tau_3 = (1.6 \pm 0.1)$ µs, respectively. The type of particle producing the recoil does not affect the two decay times, but it changes drastically the ratio of singlet to triplet states. Indeed, the intensity ratio of the fast component to the slow component measured with particle producing nuclear recoils (NRs) as α's, neutron, and WIMP interactions (under the hypothesis of WIMPs inducing only NRs) is different from the same ratio produced by γ's and electrons which give interaction called electron recoils

(ERs). This ratio has been measured to be about 0.3 for ERs and in the range 1.3-3.3 for NRs [104]. This difference is a very powerful tool to distinguish between NRs and ERs, based on the comparison of the shape of the scintillation time profile. This is often referred to as pulse shape discrimination (PSD) and for liquid argon, it allows to reject about 10^7 ERs events for every event that is improperly cataloged as NR [66]. PSD is the main strength of liquid argon with respect to other noble liquids. For instance, xenon can also use the pulse shape discrimination technique, but it is intrinsically less effective given that the lifetime of xenon singlet and triplet states have much closer values ($\tau_1^{\mathrm{Xe}} = 4.3$ ns and $\tau_3^{\mathrm{Xe}} = 22$ ns). Apart from PSD, also the observed ionization-scintillation ratio depends on the NR or ER nature of the event and this observable can be used, together with 3D event position reconstruction, as an additional tool to discriminate between these two types of event, thus improving the discrimination power.

2.2 The DarkSide-50 detector

The DarkSide-50 detector has operated at Laboratori Nazionali del Gran Sasso (LNGS) in Italy. It is located about 1400 m under the rock, at a depth of 3800 m.w.e. [105]. The apparatus is composed of three nested detectors as shown in Fig. 2.1. The outermost one is a tank called water Cherenkov detector (WCD) veto, used as a shield and as anti-coincidence to reject events caused by residual fluxes of cosmic muons. The WCD is a cylindrical tank with a diameter of 11 m and a height of 10 m filled with high purity water. More internally there is the liquid scintillator veto (LSV) which is a 4 m-diameter stainless steel sphere filled with 30 tons of liquid scintillator. LSV serves as a shield and is useful to discriminate radiogenic and cosmogenic neutrons, γ-rays, and cosmic muons. At the center of the LSV is located the DarkSide-50 TPC, containing (46.4 $\pm$ 0.7) kg active mass of UAr. The TPC contains a thin layer ($\sim$ 1 cm) of gaseous argon above a larger monolithic cylindrical body of liquid. LAr is maintained at a temperature of T$\sim$85 K by using an external circulation loop connected with the cryostat. The cryogenic and purification system is located on the top of the water tank, in the radon-suppressed clean room, which contains all equipment that interfaces directly to the detectors.

A typical interaction in the TPC yields a prompt scintillation signal called S1, together with one or more clouds of ionization electrons, depending on the interaction being single- or multi-scatter. In the DarkSide-50 LAr TPC, the electrons which escape recombination drift upwards under a uniform electric field and are extracted into the thin layer of gas where they induce one or

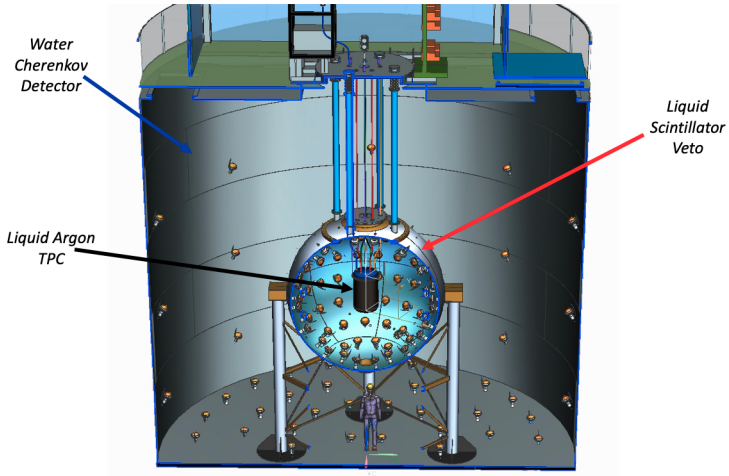

Figure 2.1: DarkSide-50 detector apparatus. The water tank WCD, the LSV sphere, and the liquid argon TPC are shown. The figure has been taken from ref. [106].

more electroluminescence signals, S2. The electron drift system consists of the cathode and anode planes, respectively on the bottom and on the top of the TPC, a field cage, and a grid that separates the drift region from the extraction region. The grid is situated 5 mm below the liquid surface and for this reason, we can distinguish three different field intensities. The drift field between the cathode and the grid has an intensity of 200 V/cm, the extraction field, between the grid and the liquid surface, of 2.8 kV/cm, and the electroluminescence field in the gas pocket, of 4.2 kV/cm. At this extraction field, the efficiency for extracting ionization electrons into the gas layer is estimated to be $> 99.9\%$ [107]. The drift time, i.e. the time difference $\Delta t_{\mathrm{S2-S1}}$ between the S2 and S1 signals, has its maximum value at 376 µs, with the drift speed of (0.93 ± 0.01) mm µs^{-1}.

The S1 and S2 signals have different pulse shapes. The S1 signal has a rise-time of few ns and falls as a double exponential depending on the state of the de-excited dimer. The S2 signal has ~ 1 µs rise-time and a ~ 3 µs fall-time. Detecting both the S1 and S2 pulses allows for three-dimensional reconstruction of the interaction position and a background rejection by multiple interactions detection and by fiducialization. The DarkSide-50 LAr TPC detects light from both S1 and S2 signals using the same array of photomultipliers (PMT). It has 38 3″ PMTs, 19 above the anode and 19 below the cathode. The PMTs are submerged in liquid argon and view the active volume through fused silica windows, which are coated on both faces with transparent conductive indium tin oxide (ITO) films 15 nm thick. This coating allows the inner window faces to serve as the grounded anode (top) and high-voltage cathode (bottom) of

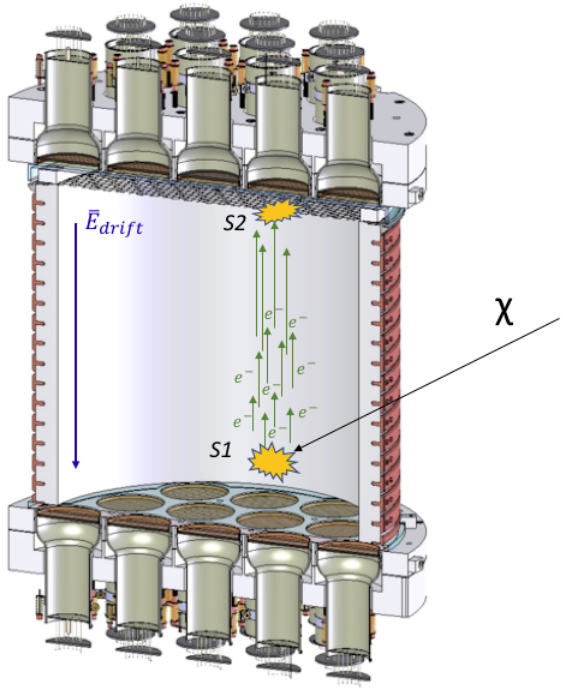

Figure 2.2: Sketch of the DarkSide-50 LAr TPC in which it is shown the production mechanism of S1 and S2 signals.

the TPC while maintaining their outer faces at the average photo-cathode potential of the 19 PMTs at each face. The cylindrical wall is a 2.54 cm-thick polytetrafluoroethylene (PTFE) reflector fabricated with a modified annealing cycle to increase its reflectivity. The reflector and the windows at the top and bottom of the cylinder are coated with a wavelength shifter, tetraphenyl butadiene (TPB), which absorbs the 128 nm scintillation photons emitted by liquid argon and re-emits visible photons with a peak wavelength of 420 nm. Under normal running conditions for the WIMP search, all three detectors are read out upon a trigger from the TPC that requires at least two PMTs above a threshold of 0.6 photo-electrons (PE) within a 100 ns window [75]. Subsequent triggers are inhibited for 800 µs and waveform data are recorded from all 38 PMTs for 440 µs starting $\sim$ 10 µs before the trigger. Software pulse-finding algorithms are then applied to the digitized data, including the pre-trigger data.

In order to reconstruct whether an event is a suitable candidate for dark matter interaction, the liquid argon discrimination potentialities are exploited. The technique used to identify the nature of a given event in the detector is a parameter related to the PSD, called f_{90}, defined as the fraction of S1 light

detected in the first 90 ns of a pulse. Indeed, NR-like pulses correspond to a very rapid scintillation signal. On the contrary, ER-like signals have a slower decay of the pulse. For this reason, very roughly, one can think about low values of f_{90} ($\lesssim 0.5$) corresponding to ER signals [108] and high values ($\gtrsim 0.5$) corresponding to NR signals. The z-fiducialization, by using drift time information, and the radial fiducialization, by using transverse (x-y) reconstruction, are also used in the latest DarkSide-50 analysis [75, 98, 109]. The position resolution is estimated to be about 0.6 cm for the S2 signal of $\sim 10^3$ PE of intensity.

A crucial procedure needed to understand the behavior of the detector is calibration. In DarkSide-50 the main protagonists of the calibration procedure are ^{83m}Kr, ^{241}Am-^{11}Be and ^{241}Am-^{13}C. The ^{83m}Kr source is introduced into the recirculating argon and it decays through two sequential transitions, where the second transition has a mean-life of 222 ns and thus is usually reconstructed as part of S1. This provides a monoenergetic signal of 41.5 keV in the TPC. ^{241}Am-^{11}Be and ^{241}Am-^{13}C are neutron sources located outside the TPC and are used to determine the f_{90} response and distribution of NR signals. Concerning the ER signal calibration, initial operations of DarkSide-50 with AAr provided a large sample of ^{39}Ar β decays and have been used for primary calibration of f_{90}. Another calibration method exploits ^{60}Co, that decays releasing two γ-rays in the cryostat steel are used to determine the LSV light yield. Regarding the ionization yield calibration, also ^{37}Ar present in the first 100 days of the latest data taking has been considered. Indeed, the decay branches of ^{37}Ar from the electron capture on K and L1 atomic shells lead to emission lines of 2.82 keV and 0.27 keV, respectively.

2.2.1 Background in DarkSide-50

In a direct detection dark matter experiment, and, more in general, in each experiment searching for rare events, it is fundamental to calculate the number of background events expected in the detector. In the DarkSide-50 experiment all background events can be gathered in two different groups. The first one is composed of the NR-like events, strongly resembling DM-nucleus scattering. ER-like signals belong to the second group.

In this first category, α particles and neutrons are included. For α decays in the TPC, the events induced by the α scattering or due to the recoil of daughter nuclide, give a signal with f_{90} in the rough range of $0.6 < f_{90} < 0.8$, at energy above ~ 50 keV. The material composing the TPC is highly radiopure and the α-emitters are likely radon daughters deposited on the detector surfaces at the

moment when the detector was assembled. The main surface backgrounds are ^{210}Pb and ^{210}Po decays. These contaminations are strongly suppressed through software analyses in addition to the radial fiducialization [75]. The other NR-like background is induced by neutrons. These particles can scatter off the nucleus in LAr with a process that is indistinguishable from DM-nucleus interactions, making neutrons a critical background source. Most of the neutrons are activated by cosmic-ray muons (cosmogenic) interacting in the rock and in the materials surrounding the detector, and by the radioactivity (radiogenic) of detector materials. Fortunately, as opposed to DM, neutrons typically produce multiple scattering, giving the possibility to reject part of this background. Another strong contribution to the rejection comes from fiducialization because of the short neutron interaction length in LAr. Moreover, neutrons likely leave a signal in the LSV and for cosmogenic neutrons, it is possible to study the coincidence in the WCV. Radiogenic neutrons come from the chain of ^{238}U. In DarkSide-50 the spontaneous fission events are easily rejected for two reasons: the respective high and moderate efficiency of LSV for neutrons and γ-rays, and the multiplicity of events during the fission process.

The second category of background sources includes ER-like backgrounds, represented by β-decays and γ-rays. The WCV and LSV provide efficient passive shielding against β and γ signals originating outside the TPC cryostat. So, the cryostat itself and TPC components (including the LAr) are considered the main sources of β/γ-induced background. The β sources in the TPC are the isotope ^{39}Ar and ^{85}Kr. As explained in the first part of the chapter, in UAr the activity of ^{39}Ar is 7.3×10^{-4} Bq kg^{-1}, in addition to the (1.9 ± 0.1) Bq kg^{-1} of ^{85}Kr found in the current DarkSide-50 UAr fill. These numbers make γ-rays Compton scattering the main source of ER-like background. When the statistics is high enough γ-ray signals can be rejected through the PSD. The main limitation of the PSD in removing single-sited ER scintillation events arises at low energies, for which low photo-electron statistic limits the rejection power.

At very low energy, a very insidious category of ER-like background arises, limiting the sensitivity in the low-mass DM region. Indeed, the latest DarkSide-50, called S2-only analyses, uses only the ionization signal. Given that S2 is generally much larger than S1, this technique gives access to smaller recoil energies at the price of the loss of the PSD and a cruder position reconstruction. The S2-only approach has been successfully applied to both DM-nucleus and DM-electron scattering searches [98, 109] and has been proposed for searches for supernovae neutrino bursts [110]. All S2-only analyses, with both argon xenon [111–114], have shown an excess of events at energies corresponding to one to two extracted electrons. This excess cannot be explained by radioactive

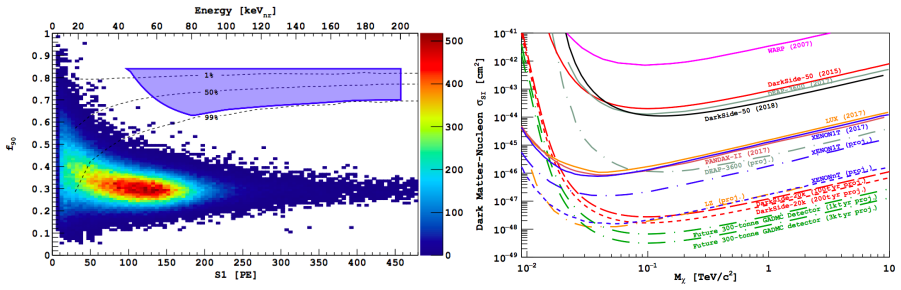

Figure 2.3: *Left*: WIMP search box in the region S1 vs f_{90} after all the cuts. *Right*: 90% CL limits on the spin independent cross section between WIMP and nucleons. The DarkSide-50 limit is represented by the black curve.

background. The origin of these events is not completely understood, and its presence limits the sensitivity of these experiments. For instance, for DarkSide-50 S2-only analyses, only events with more than four extracted electrons were accepted, thus restricting the sensitivity to WIMP masses above 1.8 GeV/c^2. Understanding the nature of these events is therefore the key to improve the sensitivity of low-mass DM searches. In this thesis, a detailed study regarding these events of this type is presented, by trying to explain their origin. This investigation will get useful for the design of next-generation detectors, in order to suppress this low-energy background as much as possible.

2.3 Latest result of DarkSide-50

In this part, a recap of the most recent analyses and results achieved by the DarkSide Collaboration is reported. In 2018, three different types of analysis have been performed. The so-called high mass analysis in the range between $\sim 10\,\mathrm{GeV/c^2}$ to $\sim 1000\,\mathrm{GeV/c^2}$ is discussed under the hypothesis of scattering between dark matter and Ar nuclei. The low-mass analysis, performed using the same hypothesis, extends the limit down to $\sim 1.8\ \mathrm{GeV/c^2}$. Through different hypothesis, that predicts dark matter scattering off the electrons inside of the Ar atom, it has been also possible to set limits for sub-GeV dark matter masses.

2.3.1 Standard WIMP search

The analysis of DarkSide-50 in the high mass range has been performed in a blind-mode on the 532.4-liveday data set [75]. This means that candidate selection/background rejection was designed, and the background surviving cuts was estimated, without knowledge of the number or properties of events in the final search region. The data are reported in the region f_{90} vs S1 (Fig. 2.3). During the analysis, the first operation consisted of opening sections of the blinded data outside of the WIMP search region to provide samples enriched in particular backgrounds for study, and later, when the background predictions were mature, to test the predictions. The expected background has been classified into three categories: surface events, neutrons (cosmogenic and radiogenic), and ERs. The number of surviving events expected using the entire statistics and after all the background rejection is 0.09 $\pm$ 0.04 while the total acceptance after the cuts has become $72.5 \pm 0.1(\mathrm{stat}) \pm^{0.5}_{0.4} (\mathrm{syst})$%, which impact is counted in considering the fiducial mass as (31.3 $\pm$ 0.5) kg. After the data unblinding, no events were observed in the defined WIMP search region, as shown in Fig. 2.3. The lack of events observed is consistent with up to 2.3 WIMP-nucleon scattering expected at 90% CL, which sets an upper limit on the spin independent scattering cross-section corresponding to 1.14×10^{44} cm^2 for a WIMP mass of 100 GeV/c^2 and 3.79×10^{44} cm^2 fora WIMP mass of 1 TeV/c^2, represented by the black curve shown in Fig.2.3. The minimum cross section excluded is 1.10×10^{44} cm^2 for a WIMP mass of 126 GeV/c^2. The limit is calculated assuming the standard halo model and using $v_{\mathrm{esc}} = 544$ km s^{-1}, $v_0 = 220$ km s^{-1}, $v_E = 232$ km s^{-1}, and ρ_{DM} = 0.3 GeV/c^{2}cm^{-3}.

2.3.2 Low-Mass WIMP search

The very important achievement reached by DarkSide consists of the background-free condition in the high mass regime. However, by relaxing the background-free requirement, it has been possible to exploit the DarkSide-50 detector to perform analysis at lower energies, associated to the search for lower masses of WIMPs [115]. In order to decrease the threshold, only the S2 signal has been used. On the other hand, not considering S1 means that PSD is therefore not available. The efficiency of the software pulse finding algorithm is essentially 100% for S2 signals larger than 30 PE. The energy threshold for this analysis has been set to 4 e^-, which correspond to $\sim$ 92 PE.

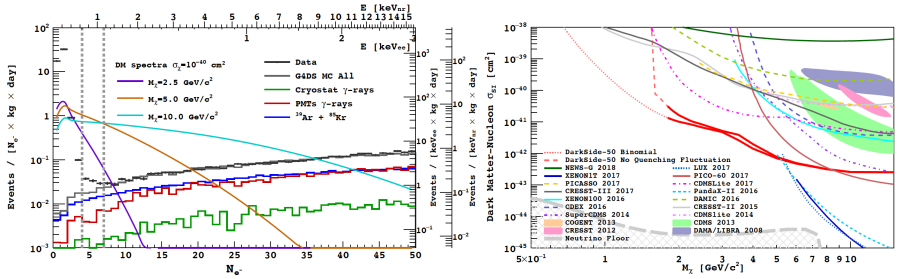

Figure 2.4: *Left*: Number of events after cuts as a function of the number of ionization electrons. On the top of the plot the energy scale is also shown. *Right*: The Darkside-50 90% CL limit (red lines) on the spin independent cross section between low mass WIMP and nucleons under two hypothesis of quenching behaviour.

Since S1 is not exploitable, neither the z-fiducialization is available. Moreover, at low energies the low statistic does not allow to use the xy algorithm for the radial fiducialization, thus the choice was to define a fiducial region only accepting events where the largest S2 signal is recorded in one of the seven central top-array PMTs. This means that the detector acceptance for this analysis is 0.42 ± 0.01, reducing the fiducial mass. The ionization yield has been determined using an *in situ* calibration data from ^{241}Am^{13}C and ^{241}AmBe neutron sources, combined with the data of SCENE and ARIS [116]. The events collected during the live-time of the detector and after the cuts are shown in the left plot of Fig.2.4. Precisely, three different ranges are defined. The first one is above 7 e^-, where the observed rate of events ($\sim 1.5/\mathrm{keV}_{ee}$ day kg) is very well reproduced by the MonteCarlo simulation used. This consistency validates the simulation in the range above 0.6 keV_{ee}. The second region to be considered is between 4 and 7 e^-, where there is a small excess of events with respect to the MonteCarlo predictions, which is not understood and it has been let for further studies. Finally in the region below 4 e^- a huge excess of events is observed. Setting the threshold at 4 e^-, the low energy excess is not taken into account, while the intermediate small excess limits the sensitivity in the WIMP mass region between 1.8 GeV/c^2 and 3 GeV/c^2. The uncertainty on the expected WIMP signal near the threshold is dominated by the average ionization yield, as extracted from calibrations, and its intrinsic fluctuations, modeled by applying binomial statistics to the ionization yield and the recombination processes. Upper limits on the WIMP-nucleon scattering cross-section are extracted from the observed e^- spectrum using a binned profile likelihood method. Nowadays, the DarkSide-50 limit remains world-leading only for the region below 3 GeV/c^2. The limit in the range above 3 GeV/c^2 has been improved by XENON1T [117] using the same approach for the analysis. Improved ionization yield measurement and assessment of a realistic ionization fluctuation model, may be used to determine the actual

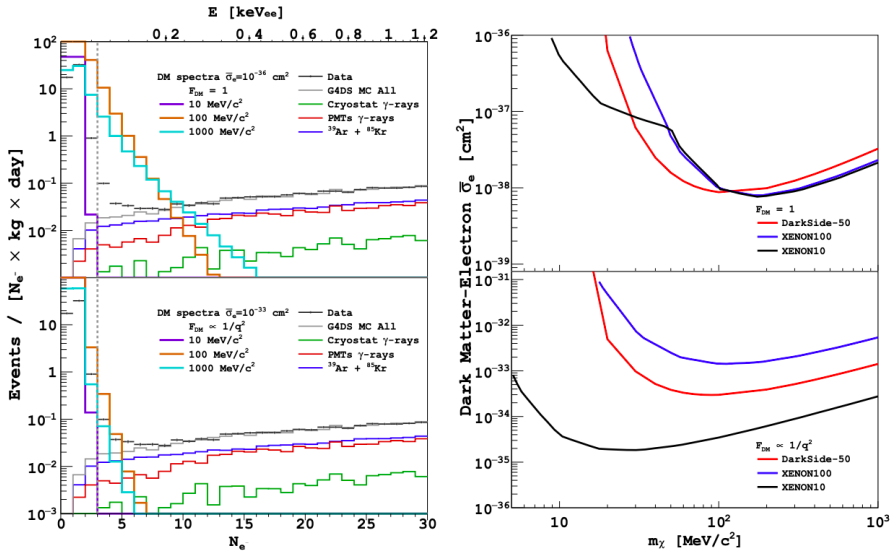

Figure 2.5: *Left*: Number of events obtained with the S2-only analysis compared with the spectra for the interaction DM-electron. *Right*: DarkSide-50 90% CL limit compared with XENON10 [118] and XENON100 [119] in two different regimes: heavy mediator on the top and light mediator on the bottom.

sensitivity of the present experiment within the range indicated.

2.3.3 Sub-GeV Dark Matter search

Nowadays, since the phase space available for the different WIMP models has been significantly constrained by the very precise limits set by the different experiments, physicists are led to explore new possibilities for dark matter. One of those is inside of the dark-sector framework, predicting sub-GeV particles with smaller coupling with respect to the weak-scale. For these models, a new mediator boson is assumed, and depending on its unknown mass, the predictions of the expected rate of events are different. In this analysis two opposite limits are discussed, very heavy and very light mediator [109]. Sub-GeV particles can not be detected by searching for elastic nuclear recoils, since their kinetic energy would be below the detection threshold. However, if dark matter scatters directly off the bound electrons of the target, the kinematics is more favorable and is sufficient to ionize the target atom and to produce a visible signal in detectors. The interaction induces an ER signal, whose response is therefore not subjected to the quenching uncertainty of the ionization signal induced by WIMP-nucleus interactions. The search for

these DM-electron interactions uses the same data selection described for the low-mass WIMP analysis but with a threshold set to 3 e^-, equivalent to 0.05 keV_{ee}. A very important goal regarding the energy calibration is achieved by exploiting the presence of the isotope ^{37}Ar. Indeed, this one disintegrates by 100% electron capture transition to the nuclear ground state of the nuclide ^{37}Cl. The recommended value for the ^{37}Ar half-life is 35.01 ± 0.02 days. The lines coming from the L-shell have an energy of 0.27 keV while those from K-shell have an energy of about 2.81 keV and most of those ($> 90\%$) are produced by Auger electrons. DarkSide-50 observed that the sample of ^{37}Ar was almost completely decayed after 100 days. The resulting ionization spectra, shown in Fig. 2.5 (left), are then smeared considering the ionization yield and recombination processes and convolving them with the detector response, measured from single-electron events. The resulting 90% C.L. limits are shown in Fig. 2.5 (right) for two different mediator assumptions. At the end of 2019, the same analysis has been performed by XENON Collaboration with XENON1T data [117], improving the limits presented here by almost two orders of magnitude for dark matter particles with a mass of 100 MeV/c^2.

3

THE DARKSIDE-50 SINGLE-ELECTRON BACKGROUND

In the third chapter the analyses regarding the single-electron background in DarkSide-50 are presented and discussed. The chapter is divided into two parts, exploring the characteristics of the single-electron background in events with three signals and with one isolated signal.

Contents

The single-electron background is the most tedious and bothering category of background in the S2-only analyses of DarkSide-50. Indeed, even though the efficiency of the software pulse finding algorithm is essentially 100% for S2 signals larger than 30 PE, the threshold for the S2-only analyses is set at $\sim$ 70 PE. This choice is due to the uncontrolled and unexpected abundance of events observed in the low energy range. In order to relate this abundance to a dark matter interaction it is necessary to know and estimate the background expected in the same region of interest (ROI). At the moment of writing, this abundance is not yet completely understood, so that the conservative choice is not to consider the low energy region in the ROI for the dark matter analyses. This choice leads to a limitation of the sensitivity. The low-energy ionization signal are believed to be due to electrons trapped and subsequently released by impurities. If this were true, that would be supported by a significant time correlation between these events and preceding large ionization events as well as an observed scaling in the single-electron event rate with argon purity. This effect has been observed in the S2-only analysis during the study of the ionization yield. S2 photo-electron yield per extracted ionization electron $\eta_e = (23 \pm 1)$ PE/e$^-$, was determined by studying single-electron events obtained during a short period of time in which the inline argon purification getter was turned off for maintenance purposes. These runs have a significantly enhanced single-electron event rate. The observation of strong time and space correlations between single-electron events and preceding large ionization events led the Collaboration to believe that these events comes from electrons captured by and subsequently released from trace impurities in the argon. However, quantitative explanations of these effects have not been given yet. With the studies proposed in this thesis we aim to improve our knowledge on the sources of this background, especially in view of the design of future DarkSide projects.

It is important to highlight that not only LAr detector showed this low-energy feature. Indeed, also LXe TPCs presented the issue and also for xenon detectors the most common explanation is the presence of electron capture by impurities or by liquid-gas surface [111–114, 120–124].

The two analyses described in this thesis focus on different categories. Indeed, the first one, named three-pulse analysis, selects a class of events with a low-charge pulse in the same acquisition window of a normal S1-S2 event. The second analysis requires the presence of a low-charge signal observed in isolation, separated in time from the preceding event, i.e. not accompanied by any other pulse in the acquisition window. These two categories likely come from a separate origin, and even if the three-pulse category is not part of the limiting background for dark matter searches, a deep study of its features could help in optimizing future S2-based analyses.

3.1 Analysis of three-pulse events

The starting point of the analysis is the extraction and selection of data. After reconstruction, DarkSide-50 data are stored in a ROOT format. This is summarized in a secondary output called SLAD (SLim Analysis Data), with event and pulse information for further study by analyzers. Separate SLAD are made for the TPC and veto data. These are then matched event-by-event using the timestamps in each data stream. The data reported here were acquired between July 2015 and October 2017.

The standard quality cuts are applied. We select only runs where data are present in all 38 PMTs, we require that baselines for the digitized waveforms are successfully found in all TPC channels, and we ask that the event occurs at least 400 µs after the end of the inhibit window of the previous trigger (that is, at least 1.21 ms after the previous trigger). This removes events that triggered on an S2 whose S1 occurred during the inhibit window. We then select three-pulse events, with the first one being an S1 signal, triggering the data acquisition, and the other two being S2 signals. We determine the nature of the pulse depending on the amount of charge, namely the value of the integral of the pulse, in units of PEs, and on the PSD parameter f_{90}. In particular, we define as S1-like any pulse that:

- has a pulse charge $> 10^{-3.3\times f_{90}+2.6}$ PE and $< 10^{4.35}$ PE,
- has a f_{90} value in the range $0.15 < f_{90} < 0.5$.

The complementary cuts define an S2-like pulse. The only additional cut is the requirement for an S2 to have a charge $< 10^5$ PE. To further strengthen the correct identification of the pulse sequence, we also require the ratio of S2 to S1 charges to be larger than 10, as expected when the two pulses come from the same interaction. This selection has not been decided a priori, indeed, by looking at the distribution of events we observed two main populations, as reported in Fig. 3.1. The one distributed around values of $f_{90} \sim 0.3$ and values of charge > 100 PE likely contains S1-like signals, according to the shape of the waveform of an S1 pulse. The population of S1-pulses for which $f_{90} \sim 0.3$ is also present in [75] and it is generated by ER interactions. We decided to restrain our selection to ER events removing NR events, that have a different ionization behavior, that includes electron recombination in the process. A dedicated treatment selecting NR events could be interesting, but this is beyond the purpose of this thesis. Among S2-like pulses, a big part has a charge smaller than 200 PE. Since this amount of charge corresponds

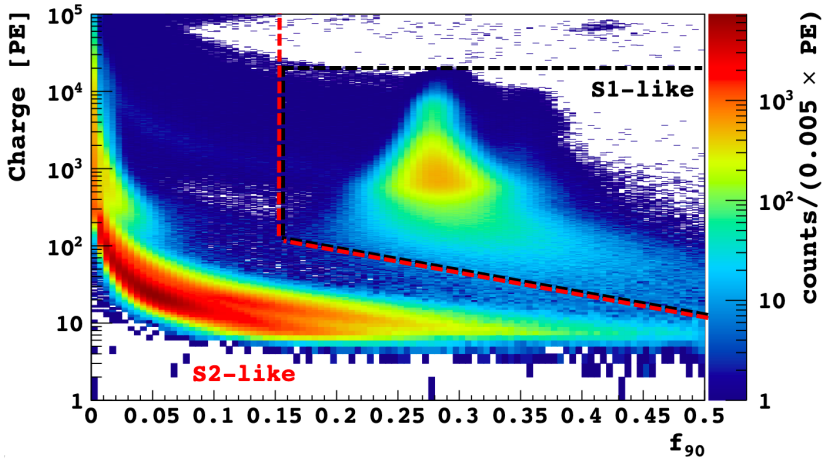

Figure 3.1: Pulse charge in photo-electrons, PE, as a function of the pulse shape discrimination parameter, f_{90}, for all pulses in events with three pulses. The S1-like pulse selection corresponds to the area to the right of the the black dashed line, while the S2-like pulse selection corresponds to the area to the left of the red dashed line.

to an electroluminescence signal produced by few electrons we call them single-electron candidates (SECs). Since the detector response of DarkSide-50 displays a radial dependence of the S2 light yield [98], we select only events where the maximum of the light produced by the SEC falls into the central PMT of the top array. As shown in the following, these three-pulse events have features allowing us to clearly distinguish them from multi-scatter background events with two S2 signals. Indeed, most of them have a clear time correlation with the S1 or S2 signals. Another peculiar feature of these events is that one of the S2 signals is consistent with being originated by one or two drifting electrons. We also provide a tentative interpretation for the observed event types. More studies, also possibly with other detectors, are needed to complete the picture. We classify the selected events in two groups, depending on the time sequence of the pulses: S1-S2-SEC, with the single-electron candidate occurring after the S2 signal, and S1-SEC-S2, with the SEC occurring between S1 and S2. In principle, is also possible to observe three-pulse events when the SEC triggers the events, being then uncorrelated to both S1 or S2. Looking at this case, we found only 2 events after the selection thus we are not able to perform any investigation and draw any conclusion. Other than the rarity of this sequence, the low abundance is probably due to the loss of efficiency in triggering an event with an SEC.

We remind that the declared time needed by an electron to travel across the total DarkSide-50 TPC with an electric field of 200 V/cm is $t_{\text{drift}}^{\text{max}} \sim 376$ µs. The single-electron origin could be different depending on where the signal comes

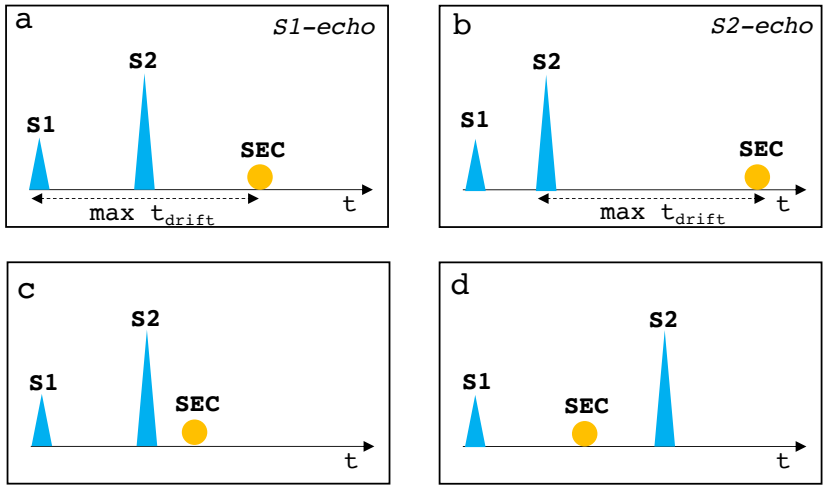

Figure 3.2: Event categories reported in the three-pulse analysis: *a*) the SEC occurs exactly after one maximum drift time from S1 signal, *b*) the SEC occurs exactly after one maximum drift time from S2 signal, *c*) the SEC occurs after S2 within one maximum drift time , and *d*) the SEC occurs in between S1 and S2.

from. In the case of SEC produced at the bottom the TPC, the probability to be produced would take into account to the characteristics of the materials forming the cathode and to the structure of the tank, whereas in the case of SEC produced in the TPC bulk it would involve only properties of LAr or any other impurity present in the liquid. For the latter reason, in the considered sequences we expect four different type of events, depending on how late the SEC occurs after S1 or S2, and in particular whether they come from the bottom or the bulk. In Fig. 3.2 the sketch of the expected categories is presented. In the case of single electrons coming from the bottom we expect either an SEC signal occurring exactly after one maximum drift time from S1 or exactly after one maximum drift time from S2. We name pulses of this kind as *S1-echoes* and *S2-echoes*, respectively. In the case of SEC occurring in between S1 and S2 and within one maximum drift time from S2 we call it *S1-liquid* and *S2-liquid* signals, respectively.

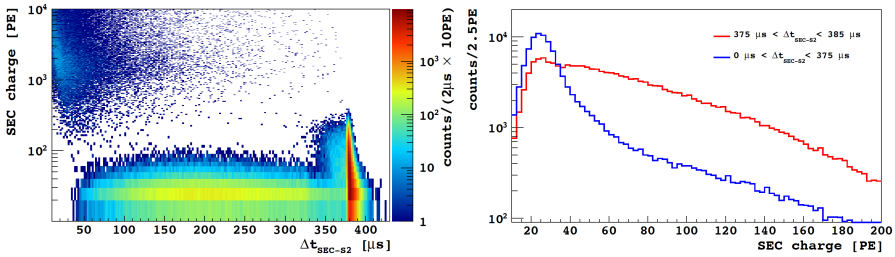

Figure 3.3: *Left*: SEC charge as a function of the time difference between the SEC and the preceding S2 pulse, $\Delta t_{\mathrm{SEC-S2}}$, distribution. *Right*: Distributions of SEC charge for the two low-charge populations on the left plot, see text for details.

3.1.1 S1-S2-SEC sequence

In the first part of the analysis we focus on the sequence S1-S2-SEC, where categories *a*), *b*), and *c*) of Fig. 3.2 appear. First of all, we decided to investigate the SEC signal as a function of its charge and its delay from S2. The left plot in Fig. 3.3 shows, for S1-S2-SEC events, the charge of the SEC pulse vs. the time difference, $\Delta t_{\mathrm{SEC-S2}}$, between the SEC and the preceding S2. The most abundant population of events is found for $\Delta t_{\mathrm{SEC-S2}} \sim 380$ µs, correspond to the category including S2-echoes. Their charge but extends up to few hundreds of PE, as visible from the red distribution in the right plot of Fig. 3.3, where the number of events as a function of the charge of the third pulse is shown. From this point on, the S2-echo is defined as an SEC which time delay from S2 is $375\ \mu\mathrm{s} < \Delta t_{\mathrm{SEC-S2}} < 385\ \mu\mathrm{s}$. Given that the time difference $\Delta t_{\mathrm{SEC-S2}}$ is approximately the maximum drift time, it is plausible that these events correspond to photoelectric extractions off the cathode by S2 VUV photons. The other clear population supposed in Fig. 3.2 is related to what we called *liquid* signals. It has a broad distribution in time, and the charge is mostly distributed around ~ 25 PE, identified by the blue line in Fig. 3.3. According to ionization yield measurements [98], this is the amount of charge corresponding to $\sim 1\ \mathrm{e}^-$. The last population to mention is the one present for large values of charge and small time difference. These events have a third pulse that is S2-like but above the value set to define it as an SEC. These events can easily be associated with so-called multi-scatter ER background events, namely those events induced by high-energy γ's and electrons scattering multiple times in the TPC producing ionization in different sites. Moreover, it is likely that the multiple ionization occurs with a small delay and this is why these events do not extend to large time differences. The first two populations have features that allow us to clearly distinguish them from multi-scatter background events

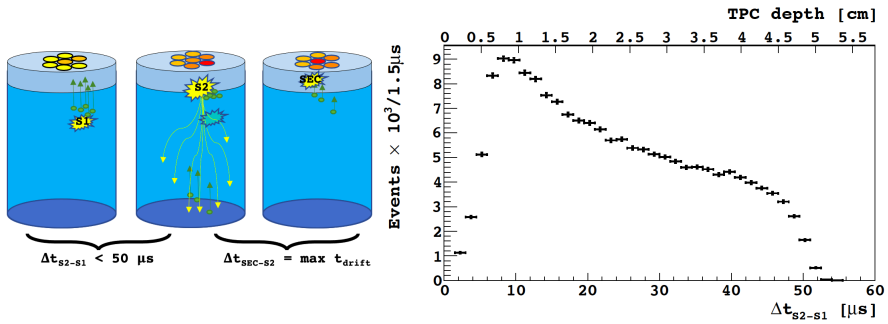

Figure 3.4: *Left*: Sketch of an S2-echo event, i.e. an S1 induces an S2 which induces itself an echo. *Right*: Drift time, $\Delta t_{\mathrm{S2-S1}}$, distribution of S2-echo events. The x-axis on the top represents the distance of the S1 scintillation from the top of the TPC, assuming a drift velocity of 0.93 mm/µs.

with two S2 signals, in particular, the requirement for the third pulse to have a charge < 200 PE is sufficient to select SECs in the event.

The number of detected S2-echo events is affected by the limited data acquisition time window, 430 µs after the trigger. This window is shorter than $2t_{\mathrm{drift}}^{\mathrm{max}}$, which would be needed to include all the S2-echoes. For example, in the case of an interaction occurring at the very bottom of the TPC, $\sim t_{\mathrm{drift}}^{\mathrm{max}}$ is needed to produce the S2 and another $t_{\mathrm{drift}}^{\mathrm{max}}$ to detect the S2-echo electrons. Therefore, the DarkSide-50 data acquisition only recorded S2-echoes for events with the particle interaction occurring in the top section of the chamber. This is confirmed by Fig. 3.4, which shows the number of events containing an S2-echo as a function of the drift time. The x-axis on the top represents the distance of the S1 scintillation from the top of the TPC, assuming a drift velocity of 0.93 mm/µs. The increase of the number of events up to ~ 10 µs is due to the inefficiency of the pulse-finder algorithm of reconstructing two different pulses when they occur very close in time and it is also observed in normal S1-S2 events. The drop of the number of events at later times, going to zero above 50 µs, is due to the limited data-acquisition time window. Indeed, the difference between the time window length, 430 µs, and the time that an echo needs to reach the gas layer, ~ 380 µs, is ~ 50 µs, which corresponds to the maximum allowed value for the time difference between S2 and S1 signals. This drift time can be translated into the distance from the liquid-gas surface. Assuming a drift velocity for the electrons of 0.93 mm/µs, it is possible to see S2-echoes produced by interaction occurring up to 5 cm from the surface. This limitation leads to the conclusion that DarkSide-50 is not sensitive to all the S2-echo events occurring in the TPC. Assuming that the probability to have an S2-echo pulse does not depend strongly on the position of the S1 signal, the limited time window induces a loss of $\sim 85\%$ of events with an S2-echo.

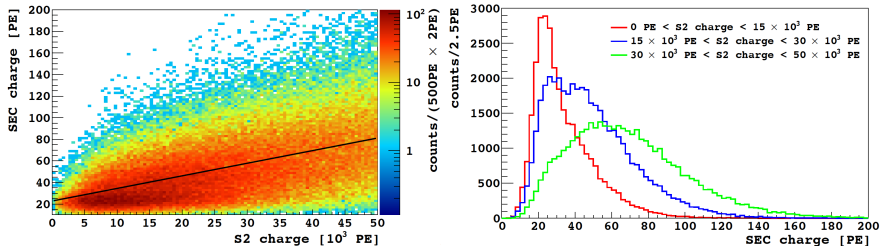

Figure 3.5: *Left*: SEC charge as a function of S2 charge for selected S2-echo events. The linear fit of the 2D histogram is also shown. *Right*: SEC charge distribution for S2-echo pulses generated by S2 with a charge in the ranges $[0-15]$, $[15-30]$, $[30-50]\times 10^3$ PE.

However, it is possible to study the dependence of the S2-echo charge as a function of the charge of the pulse that generated the echo. In the left plot of Fig. 3.5 we show the number of events as a function of the SEC charge and of the S2 charge. A correlation between these two variables appears and we performed a linear fit in the range $10^3\ \mathrm{PE} < \mathrm{S2-charge} < 50\times 10^3\ \mathrm{PE}$:

$$\mathrm{SEC} = a + b \times \mathrm{S2}. \tag{3.1}$$

The fitted parameter turned out as $a = 22.8 \pm 0.7$ PE and $b = 1.17 \pm 0.02$. These values could be affected by systematic effects induced by the pulse-finder algorithm, i.e. very low charge pulses not detected. For instance, the intercept should be, by definition of S2-echo, equal to zero. However, the value of the slope of the linear function highlights the correlation observed in the plot. The right plot of Fig. 3.5 shows the distributions of the charge of S2-echo pulses generated by S2 with a charge in the ranges $[0-15]$, $[15-30]$, $[30-50]\times 10^3$ PE. It is visible how the mean value of the distribution shifts towards higher values as the S2 charge increases, confirming the hypothesis of photoelectric extraction.

The photoelectric extraction from the cathode can be caused by the S2 light as well as the S1 light. It is interesting to look at the possibility of having an SEC occurring exactly one maximum drift time after S1. In this particular case, we do not expect any limitation due to the data acquisition window, since the echo caused by S1 light would appear $\sim$ 380 µs after the trigger. However, we expect a smaller absolute number of S1-echo events due to the fact that S1 is a smaller signal with respect to S2, meaning that the number of scintillation photons hitting the cathode would be smaller compared to the case of S2-echo events. In Fig. 3.6 the number of events as a function of the time difference of $\Delta t_{\mathrm{SEC-S2}}$ and $\Delta t_{\mathrm{SEC-S1}}$ is shown. A vertical band corresponding to $\Delta t_{\mathrm{SEC-S1}} \sim 380$ µs is clearly emerging in this distribution, exactly one maximum drift time after the S1 signal. We identify these events

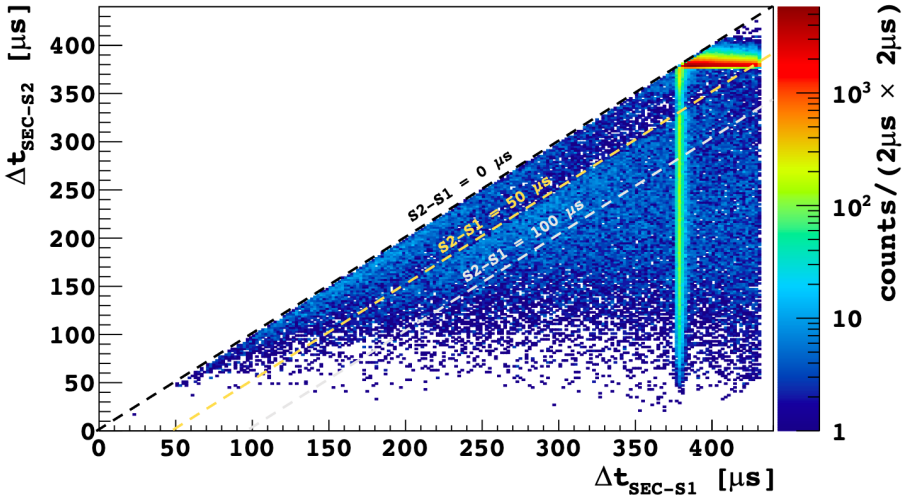

Figure 3.6: Time difference $\Delta t_{\mathrm{SEC-S2}}$ vs. time difference $\Delta t_{\mathrm{SEC-S1}}$ distribution. The diagonal dashed black, yellow, and gray lines represent different values of $\Delta t_{\mathrm{S2-S1}}$, namely 0, 50, and 100 µs, respectively.

as photoelectric extractions from the cathode from S1-emitted VUV photons and we associate them to the S1-echo category.

We decided to use the observation of S1-echo events in order to extract information from the material that the cathode is made of. First of all, we measured the average fraction of events containing an S1-echo with respect to the total number of events. For this purpose, both categories have been selected without limiting the selection to three pulses in the event. From the qualitative point of view, this different selection has a marginal effect on the distributions, but it allows to avoid the need for efficiency corrections in the calculation of the photoelectric emission probability from the cathode discussed below. We derive the photoelectric emission probability from the cathode, P_{ph}, at liquid argon emission wavelengths of around 128 nm, as:

$$P_{\mathrm{ph}} = \langle R_{\mathrm{S1-echo}} \rangle \times \frac{g_1}{\langle S1 \rangle \cdot \varepsilon_{\mathrm{geo}}}, \tag{3.2}$$

where $\langle R_{\mathrm{S1-echo}} \rangle = (6.4 \pm 0.1) \times 10^{-3}$ is the average fraction of events with an S1-echo over the total number of events, $\langle S1 \rangle$ = (1318 ± 1) PE is the average S1 charge and $g_1 = (0.157 \pm 0.001)$ PE/photon is the collection efficiency in DarkSide-50 [125]. The geometric acceptance $\varepsilon_{\mathrm{geo}}$ has been determined through a toy-MC assuming that the VUV photon, generated anywhere in the TPC, hits the cathode in the area corresponding to the central PMT, finding that $\varepsilon_{\mathrm{geo}} = (8.6 \pm 1.3) \times 10^{-3}$. Combining all uncertainties one obtains $P_{\mathrm{ph}} =$

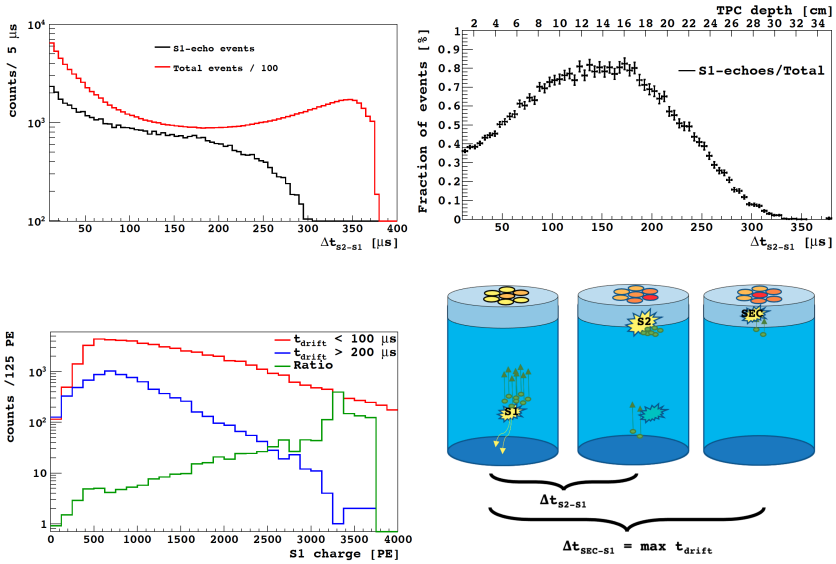

Figure 3.7: *Top left*: $\Delta t_{\mathrm{S2-S1}}$ distribution for events with one S1-echo signal (black) compared with the same distribution for generic events (red). The latter has been divided by 100 for representative purposes. *Top right*: Distribution obtained by the division of the black line and the red multiplied by a factor 100. It represents the fraction of events with echoes as a function of the drift time. *Bottom left*: Distributions of S1-charge for events with S1-echo signals requiring $\Delta t_{\mathrm{S2-S1}}$ <100 µs (red line) and $\Delta t_{\mathrm{S2-S1}}$ >200 µs (blue line). The ratio (green line) between the two histograms is also shown. *Bottom right*: Sketch of an S1-echo event, i.e. an S1 inducing an echo which is detected after S2.

$(1 \pm 0.15) \times 10^{-4}$. The dominant uncertainty on this quantity comes from photons hitting the cathode in an area between PMTs and it was evaluated by comparing the cathode surface covered by PMTs with the total area and dividing it by the number of the top array PMTs. Since the measured VUV absorption length is of about 400 nm [126] and given the TPB thickness on the cathode, discussed in Chap. 2, of few µm, most of VUV photons are expected to interact in the TPB. Therefore, P_{ph} is indeed a measurement of the photoelectric quantum efficiency of the tetraphenyl-butadiene, which has never been measured so far. In Fig. 3.7 (top plots) we analyze the S1-echo signals as a function of the drift time, which is also directly proportional to the depth of the chamber. We evaluated the ratio between the drift time distribution of events containing an S1-echo signal and the same without requiring the presence of the echo. The reason why we look at the ratio is that the drift time distribution of normal background events has more events closer to the cathode and the anode than in the middle of the chamber. We observe a rise in the event number until about 150 µs, as expected from acceptance effects, but contrary to the expectations, we observe a decrease at large drift times. This effect can be explained by the different energy distribution of

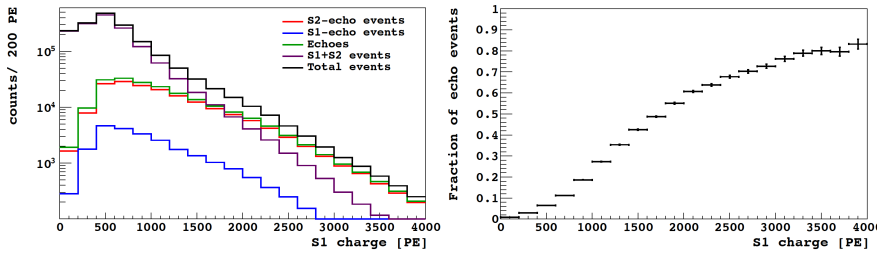

Figure 3.8: *Left*: Number of events for several categories and their total, as a function of the charge of the S1 that triggered the acquisition, requiring $\Delta t_{\mathrm{S2-S1}}$ <50 µs. *Right*: Fraction of echoes as a function of the S1 charge. The numerator of the ratio is the number of echoes, which corresponds to the green line in the left plot. The denominator corresponds to the black line in the left plot, i.e. the sum of S1+S2, S1-echo, and S2-echo category.

background events in the top part of the TPC compared to the bottom one, possibly due to the asymmetry in the material distribution and therefore in the radioactivity entering the chamber. This is visible on the bottom left plot in Fig. 3.7, where there is a clear indication that high-energy S1 signals tend to occur in the top part of the chamber. We also expect larger S1 pulses to have a larger probability to produce S1-echo and, being the S2 amplitude approximately proportional to the S1 one, S2-echo events too. We consider, for comparison, the sample of regular two pulse events with scintillation and ionization pulses, that we refer to as S1+S2 category. We, therefore, looked at the fraction of events with an echo as a function of the S1 charge, shown in Fig. 3.8. Since we showed that S2-echo events are strongly affected by the time acquisition window, we require $\Delta t_{\mathrm{S2-S1}} < 50$ µs, to compare the categories opportunely. As it is visible from the right plot in Fig. 3.8 the fraction of echoes increases with the S1 charge, confirming the hypothesis that is more likely to have an echo for higher energy events. Indeed, echoes occur in almost every event (above 80% of the cases) when an interaction with a charge $\gtrsim 3500$ PE occurs in the TPC.

In addition to echoes caused by the photoelectric effect on the cathode, we also observe in Fig. 3.6 events with time differences unrelated to the hypothesis of emission from the cathode. We make the hypothesis that these events are induced by photoelectric extraction from some species in the liquid, such as meta-stable argon anions or contaminants. We, therefore, call these events *S2-liquid*. There is also the possibility that part of these signals is produced by S1 light but we suppose that, in the sample S1-S2-SEC, its contribution is negligible, given that the SEC signals induced by S2 photons are dominant with respect to those induced by S1, as it occurs for echoes.

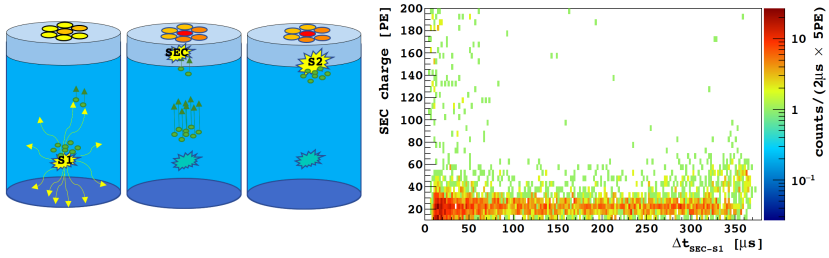

Figure 3.9: *Left*: Sketch of an S1-liquid event, i.e. an S1 inducing photoelectric extraction from the liquid above the scintillation site. *Right*: Two-dimensional distribution of SEC charge and the time difference between the SEC and the preceding S1 pulse, $\Delta t_{\mathrm{SEC-S1}}$.

3.1.2 S1-SEC-S2 sequence

To further study the hypothesis of photo-ionization in the liquid, it is interesting to investigate the category that we name *S1-liquid* by studying events requiring the time sequence S1-SEC-S2. By definition, the SEC signal occurs before S2, thus the only possibility is that S1 induces a photoelectric extraction from the liquid. Moreover, the extraction must occur above the scintillation site, otherwise, S2 would be detected before the SEC signal. In Fig. 3.9, we show the SEC charge vs. the time difference $\Delta t_{\mathrm{SEC-S1}}$ distribution. We notice that the events are almost evenly distributed in time and with an SEC charge consistent with single electrons (~ 25 PE). We also observe a cluster of events at low time difference, which can be related to some effect related to the liquid-gas interface or the grid, given that such an abundance is distributed at low values $\Delta t_{\mathrm{SEC-S1}} \lesssim 20$ µs.

To further investigate the hypothesis linking S-liquid signals to contaminants, we analyzed a set of data taken in a period of five days, during July 2015, when the getter was turned off for maintenance. During this period of time, we expect an increase of contaminants and, therefore, of S-liquid events. This is indeed observed, as the fraction of S-liquid events increased to $(11.0 \pm 0.6)\%$ compared to $(8.00 \pm 0.05)\%$, as for the standard data-taking period. This ∼40% increase of S-liquid fraction suggests that at least part of these events are due to the photoelectric extraction from contaminants that are normally trapped by the getter. The rest of them can possibly be due to photoelectric off impurities not trapped by the getter or meta-stable states of argon. The possibility that single electrons are remnants from the previous event and not originated from the photoelectric effect in the event itself, was tested by looking at correlations with the previous event in time. The time difference distribution, between

Category	Δt *cut*	*SEC cut*	F (%)
S1+S2	-	-	25.6 ± 0.1
S-echo signals	-	< 200 PE	65.6 ± 0.1
S2-echo	375 µs$< \Delta t_{\mathrm{SEC-S2}} <$ 385 µs	< 200 PE	63.9 ± 0.1
S1-echo	375 µs$< \Delta t_{\mathrm{SEC-S1}} <$ 385 µs	< 200 PE	1.69 ± 0.03
S-liquid signals	-	< 50 PE	8.00 ± 0.05
S2-liquid	$\Delta t_{\mathrm{SEC-S2}} > 0$ & not-echo	< 50 PE	7.96 ± 0.06
S1-liquid	$\Delta t_{\mathrm{SEC-S2}} < 0$ & not-echo	< 50 PE	0.04 ± 0.01

Table 3.1: Fraction (F) of selected events in two and three-pulse events in the various categories: S1+S2 are regular two pulse events with a scintillation and an ionization pulse, S-echo signals include both S1-echo and S2-echo pulses due to electron extraction from the cathode, and S-liquid signals represent S1 and S2 signals due to electron extraction from the liquid, as discussed thoroughly in this chapter. The selection $10 < \Delta t_{\mathrm{S2-S1}} < 50$ µs was applied. The number of standard S1-S2 events reported are divided by the number of PMTs in the top array. The denominator is defined as the sum of all categories with SEC<200 PE. For the S1-echo signal selection, it is also required that the event is not an S2-echo signal. In the table the sum is not exactly 100% because of the SEC cut in the S-liquid selection.

an S1-liquid or an S2-liquid event with any previous event in a time window of 10 s, did not display any significant time correlation. The hypothesis of photoelectric extraction off the liquid was also suggested by other authors using xenon detectors [122, 127, 128]. For instance, in Ref. [122], the authors claim as a possible origin of isolated electrons the photo-ionization of a *yet undetermined contaminant species*.

3.1.3 Summary of three-pulse analysis

In Tab. 3.1 we report a summary of the observed categories inducing single-electron signals in the TPC compared with the abundance of regular two pulse events with scintillation and ionization pulses. The latter category has been divided by the number of PMTs in the top array in order to compare its fraction with the other categories, given the request for SECs to have their maximum light detected in the top central PMT. It can be noticed that the fraction of events with an S-echo is large, above 65%, and about 2.5% of them are S1-echo signals. The most abundant category includes S2-echo events, which are low-charge S2-like pulses occurring after one maximum drift time from the previous S2. These signals are induced by VUV scintillation light reaching the cathode and extracting electrons from it. Given the limited data-acquisition time window, only S2-echo signals produced in events with interactions occurring in the upper ~ 5 cm of the chamber can be detected. Another category, not affected by the limited data-acquisition time window,

includes S1-echo events which are low-charge pulses occurring one maximum drift time after S1. The probability of such a process is linked to the photo-ionization efficiency of the DarkSide-50 cathode, which is made of fused silica and coated with ITO and TPB. We measured this efficiency at wavelengths of 128 nm, resulting to be around 0.1‰. Despite the small probability, the number of events with echoes turns out to be about twice as the standard two-pulse events S1-S2, used for WIMP dark matter searches, due to the large number of VUV photons associated to the S2 pulses. Being a definite time delay from S1 and S2 pulses, echo signals can easily be tagged and therefore they do not lead to inefficiencies in the dark matter searches. We also observed events possibly related to interactions of photons in the liquid. Indeed, VUV radiation can also interact with electro-negative impurities or meta-stable states along its path, inducing photo-ionization processes in the liquid. We also investigated their relative number in the period of maintenance of DarkSide-50, when the getter of the purification system was removed. During that period, the amount of S-liquid increased by $\sim 40\%$, suggesting that at least part of these events are due to the photoelectric extraction from contaminants that are typically trapped by the getter. The other part can possibly be due to photoelectric off impurities not trapped by the getter or meta-stable states of argon, for which a further investigation is needed.

The analysis described up to this point resulted in a collaboration paper titled "A study of events with photoelectric emission in the DarkSide-50 liquid argon Time Projection Chamber" [129], submitted to Astroparticle Physics and currently under review.

3.2 Study of isolated single-electron signals

After studying the set of three-pulse events and characterizing the behavior and the possible origin of single-electron signals, we are focusing on the particular category which limits the sensitivity in the low-mass dark matter searches, namely the single-electron signals in S2-only selection. For this purpose, in this section, the events are processed with the same low-level reconstruction software used in Ref. [98]. We show some preliminary studies of an ongoing analysis that includes several categories of events in order to compare their rate during the DarkSide-50 data-taking.

First of all, the event classification for this selection must be reported. Given an event in the TPC, if there is no pulse found by the pulse finder, the events are categorized as *No-pulse*. Those events in which at least one pulse is found

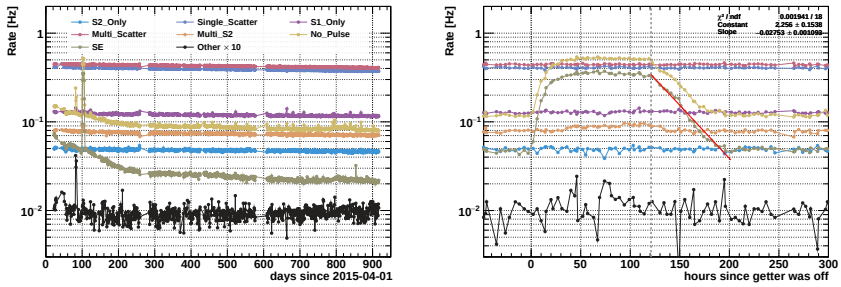

Figure 3.10: *Left*: Rate for each category of events as a function of the whole data taking of DarkSide-50. *Right*: Hourly rate change for each category of events from when the getter was removed from the system. The vertical dashed line marks the time when the getter was placed back in the system.

are then separated by either the first pulse is S1-like or S2-like. The events with a first S1-like pulse are further divided into three categories depending on how many pulses are found in the event: *S1-only* for only one pulse events, *Single-scatter* for two pulses events, and *Multiple-scatter* for more than two pulses events. The very particular case of events with more than one S1-like pulse in the event is called *Other*. Focusing on the events triggered by an S2-like pulse, we further divide them into three categories depending on how many S2-like pulses are present in the event: *Multi-S2* for more than one pulses events, *S2-only* for events with one S2-like pulse with a charge of ≥ 92 PE (corresponding to $\geq 4\ \mathrm{e}^-$), and *SE* for events with one S2-like pulse of < 92 PE (corresponding to $< 4\ \mathrm{e}^-$). The last category is the one that limits the sensitivity of DarkSide-50 to low-mass searches.

The possible cause of each event category is summarized as follows

- *No-pulse*: events are triggered, but the pulse finder can not find pulse including low charge events happening at the edge of the TPC.
- *S1-only*: events do not have S2 or is too small (Cherenkov, wall effect, events in holes).
- *Single-scatter*: standard S1+S2 events.
- *Multi-scatter*: gamma events, random pileups.
- *Other*: rare case of many S1-like pulses in the same event, 10^{-3} Hz ($< 0.1\%$ of all events).
- *Multi-S2*: multi-scatter events when only S2 pulses are present in the acquisition window.

- *S2-only*: events that do not have S1, or S1 is too small for pulse finder to be recognized.
- *SE*: possible single-electron events, corresponding to low charge S2-only events.

The time evolution of the rate of each event category from the UAr filling date in 2015 is presented in Fig. 3.10. Except for rates of *SE* and *No Pulse*, the rates of the other categories are relatively stable over the 900 days of operation, which reflects the stability of our TPC and cryogenic system. The gaps of data points are due to runs with different configurations such as different field runs and calibration source runs. In *SE* and *No Pulse*, there are two decreasing trends: until 200 days (time constant of 65 days) and rest (time constant of 8 years). There are notable spikes in *Other* at about 80 days, and in *SE* and *No Pulse* at around 100 days. The former spike was caused by an abnormal high rate in one of the PMTs and not discussed further in this paper. The latter spike was when the hot getter was removed from the gas circulation system for maintenance from 99 to 108 days. When we removed the hot getter from the gas circulation system for maintenance, there was a quick rise in event rates in the TPC. Those additional events had a short lifetime, which means they are triggered right after the previous events, and a small amount of light compared to average lights from normal events. The rate of each event category vs hours after the getter removal is plotted in Fig. 3.10 (*right*). The increases are seen only in *SE* and *No Pulse*, which means those events are one S2-like signal with a charge <4 e^-. Due to the radial dependency of the field in the gas pocket, if this event happened at the inner radius of TPC, the light is large enough to be found by pulse finder and categorized as *SE*. If an event happens at the outer radius of TPC, the amplification of the signal is not large enough and the pulse finder may not find the signal as a pulse and the event is categorized as *No Pulse*. We also saw the spatial correlation between preceding normal events and following small-signal events. From those observations, we concluded these additional events are caused by some impurity that delays electron drifting. The rate increased exponentially in 2 days and stabilized until the getter was re-installed. The decreasing rate of the extra events had a time constant of about 36 hours. The impurity introduced by the absence of the getter caused only *SE* events, removed by the getter within days.

Based on the fact we saw the sudden increase in *SE* events, the most likely hypothesis of the cause is induced by the presence of impurities: a trace amount of impurities captures the drifting electrons from normal events and release them later by some unknown mechanism. In order to check this hypothesis, we checked correlations of the *SE* events with previous events. If *SE* events are caused by, for example, spontaneous electron emission from the grid, correlation with previous events should be minimal. First of all we

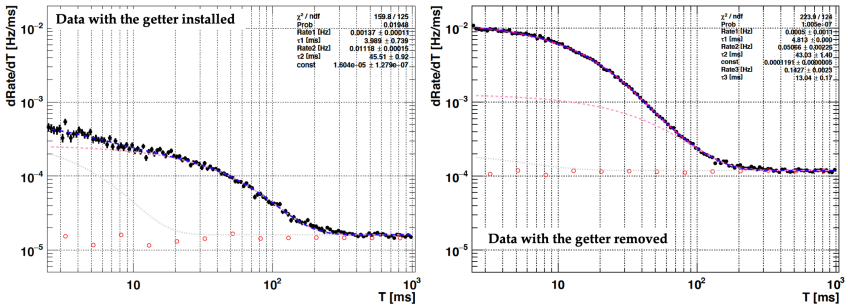

Figure 3.11: Rate per each time bin vs time difference of all the SE events from their parent events for during the period when the getter was installed (*left*) and removed (right). The blue dashed line is the total fit function. The red dashed line is the longer time constant component plus a constant component, which represents a flat uncorrelated pairs. The gray dot line is the shorter time constant component plus the same constant component. The red open circles are the uncorrelated pairs, which shows flat distribution as expected for uncorrelated distribution.

define what is called a "parent event", namely a *Single-scatter* event with an S1 with large charge ($\geq$ 1000 PE).

We register the trigger time for both the parent events and for *SE* events. For each identified *SE* events, the time differences dT from all the preceding parent events within 1 s from the *SE* events are calculated. Among these time difference, some of them include correlated components and some of them are just random coincidences (uncorrelated, which give a flat dT distribution). In order to check the uncorrelated time difference, for each identified parent event, the time difference from all preceding *SE* events within 1 s from the parent event is calculated. Indeed, by definition, a preceding *SE* can not be correlated to a future large-charge event.

Except for the getter off period (for which a third exponential component is needed), it turns out that the data demands to be fitted with two exponential functions

$$\frac{dR_{\mathrm{SE}}(t)}{dT} = \frac{R_1}{\tau_1} e^{-t/\tau_1} + \frac{R_2}{\tau_2} e^{-t/\tau_2} + c, \tag{3.3}$$

where R_1 and R_2 are total event rates of the two different time-constant components, and τ_1 and τ_2 are the shorter and longer time-constants, respectively. The c term is a flat component that represents the uncorrelated random coincidence pairs. For the getter-off period, as another middle time-constant component appeared, we need an additional exponential component to obtain reasonable fit results without drastically changed the short time constant. It is worth noticing that the time correlation distribution in LAr is not a power law unlike in some of the LXe TPCs [130].

In Fig. 3.11 the rate of *SE* events after a parent event, together with the fit

of the rate are shown. In the left plot data recorded from 26/01/2016 to 15/02/2016 (corresponding to a period when the getter in the detector was operating) are used. In the right plot data taken from 10/07/2015 to 20/07/2015 (corresponding to a period when the getter in the detector was removed for maintenance) are considered. By comparing the two plots is visible that there is a constant increase of the rate of almost an order of magnitude (indeed the uncorrelated component changes from $\sim 10^{-5}$ Hz/ms to $\sim 10^{-4}$ Hz/ms) whereas the correlated component (identified by the shoulder in the plots), increases of about one order of magnitude and a half (from $\sim 4 \times 10^{-4}$ Hz/ms to $\sim 10^{-2}$ Hz/ms).

There are at least three different sources with different time constants: the short ~ 4 ms, long ~ 45 ms, and the one in the getter-off runs ~ 13 ms. Based on the fact that in the getter-off runs, there is no degradation in the electron lifetime (related to the number of electronegative impurities which delay electrons across the TPC), the impurity causing *SE* events with the time constant of ~ 13 ms is different from the impurity causing the electron lifetime loss. Based on the faster reduction of the rate (~ 36 hours) after the reinstallation of the getter, the impurity causing *SE* event during the getter-off period is mainly present in the gas phase at the liquid argon temperature. One candidate is N_2, which has a boiling temperature of 77 K, and it could be the source. Even though the electron affinity of N_2 is negative (-0.07 eV), given that Ar has a lower electron affinity of -0.1 eV and in Ar media, the effective electron affinity of N_2 could be positive. Another component that affects both the electron lifetime and the *SE* rate could be O_2. Indeed, the electron affinity of O_2 is high.

All of the observation suggests the cause of *SE* events are related to some kind of impurities and even though the electron release mechanism is not known, it releases one electron at a time. At this stage, the cause of *SE* events is just speculations based on the observations. In order to confirm the hypothesis, the *SE* rate need to be studied with spiked impurities concentrations in a dedicated system.

The emission mechanism is still not clear. Spontaneous emission in case of resonance and no need for a separate emission mechanism. Thermal collision or IR radiation causes the release of trapped electrons. Understanding the emission process is quite important to mitigate this *SE* background in future dark matter search experiments.

More details regarding both spatial and energy correlation between parent and *SE* events will be discusses in the next future in a collaboration paper that is still in preparation.

4

TOWARDS LOW-MASS SEARCHES

In the fourth chapter a brief overview of future projects and developments towards the low-mass dark-matter searches is presented. These studies are very preliminary and still in a theoretical stage, so further progresses are expected in the near future.

Contents

As it has been described in the previous chapters, there is an increasing interest within the dark matter community in developing and fielding novel detector technologies with sensitivity to a broad range of well-motivated DM candidates, complementing the many existing and planned large-exposure searches for WIMPs. The two most recent results from the DarkSide-50 detector demonstrate the ability to extend the reach of a LAr TPC to WIMPs with masses below 10 GeV/c^2 that scatter on nuclei (low-mass WIMPs), and to DM particles that scatter on electrons with masses down to 20 MeV/c^2 (electron-scattering DM). A tonne-scale LAr TPC designed specifically to maximize sensitivity in this mass range could realistically explore the low-mass WIMP and electron-scattering DM parameter spaces down to interaction cross-sections at which the neutrino backgrounds would mask any potential signal.

There is currently a substantial experimental effort to search for low-mass DM through multiple techniques; see Refs. [131, 132] and references therein. Probing new parameter space for these DM candidates requires detectors with exceptionally low energy thresholds. A suite of dedicated, next-generation direct DM detection experiments will target the GeV/c^2 mass regime. Significant steps have been made to enhance sensitivity in this mass range over recent years, with several detector technologies capable of detecting single quanta. At these low energies, detectors lose the ability to discriminate against most backgrounds, necessitating more stringent radio-purity requirements. Given the small size and granular nature of many of these novel low-mass DM detectors, the challenge of maintaining negligible background rates will become particularly acute as experiments scale to larger target masses. While initially developed for TeV/c^2-scale WIMP searches, dual-phase TPCs are also excellent probes of low-mass DM, which can ionize atoms to create an electroluminescence signal (S2) even when the corresponding prompt scintillation signal (S1), typically used to identify NRs, is below the detector threshold. This technique was pioneered using data collected with the XENON-10 experiment and later expanded to use data from the larger XENON-100 experiment and XENON-1T experiment. As described in Chap. 2, DarkSide-50 TPC exploited the same technique obtaining very competitive results. A tonne-scale LAr TPC optimized to pursue low-mass DM could realistically push experimental sensitivity down to the level at which the irreducible background from coherent solar neutrino-nucleus scattering becomes dominant.

In this chapter, a description of the potentialities of a detector designed and built with the main focus on a low-mass search is presented and discussed. The studies discussed below have been produced in 2019 for a proposal to the National Science Foundation in collaboration with the University of Massachusetts, Amherst, MA, Princeton University, NJ, and Williams College, MA.

4.1 DarkSide Low-Mass project

The DarkSide-50 detector was designed to search for WIMPs with masses above 10 GeV/c^2 and suffered significant background rates at nuclear recoils energies below 1 keV$_{\rm nr}$, see Fig. 2.4. The sensitivity of DarkSide-50 was also limited by uncertainties in the response of LAr to low-energy NRs. The minimum energy calibration point directly measured in LAr is 7 keV$_{\rm nr}$ [133], so it was necessary to extrapolate a model to describe the detector response at lower energies. While these models were validated with *in situ* calibration data, significant systematic uncertainties were still present. These uncertainties can be reduced with a dedicated low-energy *ex situ* calibration. For the record, a very new calibration study of DarkSide-50 have been performed by the collaboration [134].

Fig. 2.4 is a 500 day S2-only spectrum collected with DarkSide-50 and used for the analyses in [98] and [109]. Several prominent background features are visible. First, a continuum of gamma-ray-induced events extends from high energy down to a single ionized electron. Monte Carlo simulations using the assayed component activities in DarkSide-50 show that the rate in this continuum is dominated by U, Th, K, and Co activity in the photomultiplier tubes (red) with a secondary contribution from events originating in the walls of the stainless steel DarkSide-50 cryostat (green). Second, two beta spectra (blue), due to the presence of ^{39}Ar and ^{85}Kr within the target argon volume, contribute a rate comparable to the Compton continuum, with ^{85}Kr contributing roughly twice the rate of ^{39}Ar. Third, there is a clear excess of events over the predicted background between 4 and 7 ionized electrons. The origin of this excess is not presently known, possible explanations include uncertainty in the ionization response of LAr or distortions in the ^{39}Ar and ^{85}Kr beta spectra due to an atomic exchange effect not included in the modeled beta spectral shapes. In the latter case, the GADMC collaboration is working with nuclear theorists to better model this spectral shape. Finally, there is a large rate increase below approximately five ionized electrons believed to be due to electrons trapped and subsequently released by impurities. This is supported by the significant time correlation between these events and preceding large ionization events as well as an observed scaling in the single electron event rate with argon purity, as already presented in Chap. 3.2.

Fig. 4.1 shows the projected sensitivities to low-mass WIMP-nucleon scattering and electron-scattering DM for a 1 tonne-year exposure with a future detector with backgrounds 4 orders of magnitude lower than what was observed in

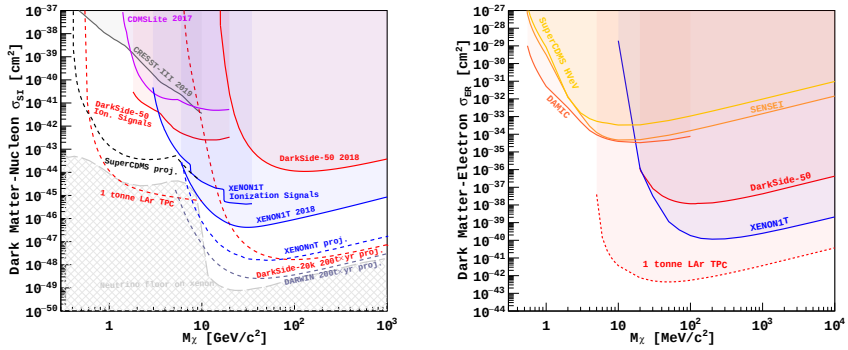

Figure 4.1: Projected exclusion sensitivity of a 1 tonne-year exposure with a LAr TPC (red dashed) with background levels 10^4 times lower than those measured in DarkSide-50 and a 2 electron analysis threshold compared to various existing and planned experiments. The projected exclusion sensitivity to low-mass WIMP-nucleon scattering is shown on the left. The projected exclusion sensitivity to electron-scattering DM in the case of a heavy mediator is shown on the right.

DarkSide-50 and with an analysis threshold of 2 extracted electrons. Achieving this background rate requires improvements on several fronts. First, the ^{39}Ar and ^{85}Kr rates measured in DarkSide-50 must be reduced to levels below 0.1 µBq. UAr sourced from the planned Urania plant, a higher throughput version of the argon extraction plant used for DarkSide-50, will be free from ^{85}Kr and likely much lower in ^{39}Ar (investigation into the source of these isotopes in DarkSide-50 revealed a probable point of air infiltration into the UAr following extraction, explaining the presence of both contaminants). Any residual ^{39}Ar in the Urania argon can be reduced by successive factors of 10 by utilizing the Aria cryogenic distillation column currently being commissioned in Sardinia, Italy. Second, the rate in the Compton continuum observed in DarkSide-50 must be reduced by a similar factor, which can be done by modifying the most significant contributors to the rate. The contribution from the PMTs can be reduced to the required levels by swapping them with much cleaner photo-sensors based on silicon photo-multipliers (SiPMs). Large-area SiPM-based modules designed for the next generation detector DarkSide-20k already show a factor of more than 10 improvement in overall activity compared to the DarkSide-50 PMTs, with almost all of the remaining activity originating in the photo-sensor substrate and pre-amplifier components, which can be replaced by fused silica or sapphire substrates and integrated electronics. This leaves the background contribution from the cryostat. Preliminary simulations indicate that replacing the stainless steel vacuum cryostat used in DarkSide-50 with a thin acrylic membrane with purity similar to values reported in [135] situated within a LAr gamma veto would reduce the cryostat contribution below the residual ^{39}Ar rate. The single electron

rate (and two and three electron pile-up rate) is assumed to scale with the overall background rate reduction in Fig. 4.1 but will be investigated within this proposal. Any remaining single-electron events can be reduced using a time and spatial correlation cut given an adequate calibration of the TPC event reconstruction at the relevant energies. Improved modeling of the ionization response of LAr for very low energy recoils will allow for a lower energy threshold, as will reducing the low-energy backgrounds. Additional improvements to the detector sensitivity are possible by increasing the electron yield of the detector by doping the argon with additives that increase ionization yield, improve the kinematical coupling of the target to light dark matter, or have both effects.

Some of the background reduction techniques addressed above also apply to a higher mass WIMP search, and as such are under active development within the DarkSide-20k collaboration, e.g. the extraction and purification of UAr and the development of an acrylic TPC vessel. This proposal aims to address several of the points that are specific to an argon TPC optimized for a low-mass dark matter search. Namely, the development of very low-background silicon-photomultiplier detectors, the investigation of argon doping methods to increase ionization yields, the exploration of methods to optimize electron extraction from the bulk argon target, and methods for reducing single-electron backgrounds. In addition, the need for an experiment to directly measure argon ionization yields is crucial, including the spread around the median ionization yield, at recoil energies down to 1 $\mathrm{keV_{nr}}$. This would be a necessary step for any serious experimental effort about investigating this part of the dark matter parameter space. This will pave the way for the design and construction of a dedicated low-mass argon TPC capable of exploring a broad swath of well-motivated dark matter parameter space.

4.2 Sensitivity optimization

Within the context of proposing and optimizing detectors for low-mass searches, measurements of the LAr response at low recoil energies, developments of techniques for doping LAr with additives and test their effects, methods for optimizing the design of a TPC, and methods of reducing low-energy backgrounds are essential.

4.2.1 LAr response measurement for low-energy recoils

The direct measurement of the mean ionization yield of LAr to low-energy NRs, as well as the spread around this mean due to intrinsic fluctuations in the ionization yield, is required to maximize the reach of a future dual-phase argon TPC. A possibility is to measure the response of LAr to low-energy NRs at 30-40 recoil energies, spanning 100 $\mathrm{eV_{nr}}$ to 50 $\mathrm{eV_{nr}}$. This range maintains overlap with existing measurements at higher energies while measuring previously unexplored low energies. Such a measurement could be achieved using, for instance, a pulsed neutron beam. Measurements of such low-energy recoils require careful control of the energy of the neutrons that scatter on the target and a strong understanding of the intrinsic detector systematics that may affect the measurements. These could be achieved by tuning the neutron beam to resonances in neutron scattering cross-section on argon and by calibrating the spatial dependence of the ionization yield. To reduce the spread in the energy of neutrons scattering, a possible technique is to tune the beam energy to match a resonance in the neutron-Ar scattering cross-section. The cross-section has significant resonances near 75 keV, 170 keV, and 220 keV. By selecting beam energies near these resonances and making the detector size comparable to the mean free path at one of these resonances, the energy distribution for neutrons that scatter in the detector can be narrowed. Any neutron in the tuned beam that loses a significant amount of energy before reaching the target will fall off-resonance and be less likely to scatter in the LAr, improving the purity of the data.

4.2.2 Doping liquid argon

Two factors limit the sensitivity of a low mass WIMP search: the kinematic coupling between the WIMP and the nucleus, which limits how large a recoil the WIMP can make, and nuclear recoil quenching, which causes energy to be lost as heat rather than as visible ionization. It is possible that doping LAr can enhance its response to recoils from low mass WIMPs by mitigating these factors. Furthermore, if WIMPs couple to nuclear spin they will not scatter on ^{40}Ar, doping LAr with additives that have unpaired nucleons would give sensitivity to spin-dependent interactions.

First, if the additive has lower ionization energy than Ar, energy from a recoiling nucleus that has slowed below the ionization threshold and would

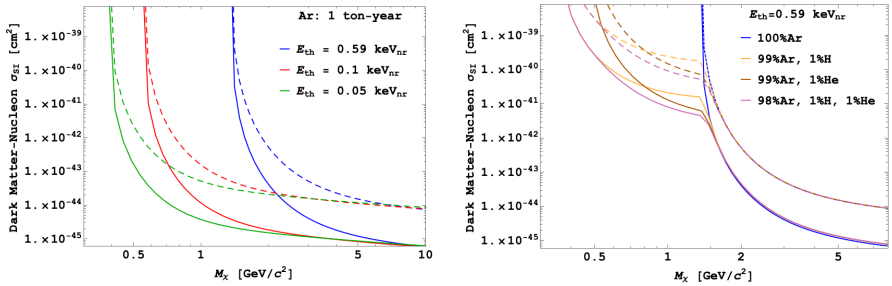

Figure 4.2: (Left) Impact of the energy threshold on the exclusion sensitivity curve of an argon detector with a 1 tonne-year exposure. (Right) Effect of kinematic matching with lighter targets on the experimental sensitivity, see text for details. Solid lines are calculated including background subtraction. Dashed lines are calculated assuming no knowledge of the underlying background spectrum.

otherwise be lost as heat can instead go into ionizing the additive, resulting in a larger S2 signal and a lower energy threshold, which in turn increases the sensitivity to lower dark matter masses. This phenomenon was described by Doke et al. [136] and has been observed in [137] at high energies where it was seen that doping LAr with xenon improved the energy resolution. Similar but stronger effects have been seen in studies that dope LAr with allene [138, 139]. In these studies, stronger effects are seen for NRs than for electronic recoils, consistent with the explanation that energy that would otherwise be dissipated by heat is being channeled into ionization, as described by Doke et al. Fig. 4.2 (left) illustrates how the effective value of the threshold impacts the sensitivity of a tonne-scale argon experiment. The sensitivity assumes the background rate is dominated by ^{39}Ar within the target volume at a level of 0.1 µBq/kg and an irreducible neutrino background. The exclusion curve calculation conservatively includes no binomial fluctuation of the quenching factor.

Second, while LAr has a favorable kinematic coupling to low-mass DM compared to other common targets, lower-mass additives (e.g. H or He) can significantly increase the kinematic coupling of a detector to lower dark matter masses, since the DM might recoil from the lighter target and produce a recoil above the energy threshold. The kinematic impact of several mixtures is illustrated in Fig. 4.2 (right) by assuming identical experiments with the same energy thresholds but different doping mixtures. With even 1% loading of a light element, it is possible to reach DM masses that were previously inaccessible. The most studied additives in LAr are allene (C_3H_4), Xe, H_2, and He. They are summarized in Tab. 4.1. Some of these dopants, like allene and Xe, are expected to affect the scintillation and ionization properties of the LAr in a way that can be easily measured at the concentrations of interest. In these cases, the uniform dissolution of the dopant in the LAr can be monitored by measuring the S1 and S2 signals and pulse shapes. To this end, a ^{210}Po

Additive	Ionization Energy [eV]
Allene	9.7
Xe	12.1
H_2	15.4
He	24.6

Table 4.1: Summary of the ionization energies of dopants being considered. For reference, Ar has an ionization energy of 15.8 eV.

source will be placed at the bottom of the TPC and the S1 and S2 responses will be monitored as a function of dopant concentration and time since the dopant was added. In the case of allene, which ionization energy is below 9.7 eV (128 nm), there is a risk that gaseous argon (GAr) scintillation produced in the S2 signal will ionize more electrons in the LAr, which will produce more S2 resulting in a breakdown. Other additives, like He and H_2, are being considered for their efficient kinematic coupling to low mass WIMPs rather than their effects on the scintillation signal. As such, their effects on the measured S1 and S2 signals may be too weak to use as a metric for their solubility. In these cases, we will sample the gas from the gas pocket as we increase the doping concentration. When the LAr has saturated with the dopant, the ratio of Ar to the dopant should increase more rapidly as the dopant concentration increases. Once a saturation curve has been established by this method, the LAr will be doped to the desired concentration and left to sit for a week. After a week, the gas pocket will be sampled to determine if the dopant fraction matches expectation, and then the LAr will be slowly boiled off and sampled to determine the total amount of dopant in the LAr.

4.2.3 TPC optimization

A set of TPC design optimizations aimed at improving the efficiency of detecting electrons and reducing the rate of single-electron backgrounds are discussed. Spuriously emitted electrons are the limiting background at low energy when performing an S2-only analysis [98, 117]. Three sources of these backgrounds have been identified: trapping and delayed re-emission of electrons on bulk LAr impurities, photo-ionization of detector inner surfaces by VUV S2 light, and trapped electrons on the LAr-GAr interface.

If electronegative impurities are absorbed in LAr at very low concentrations, they may capture ionized electrons and re-emit them later with a characteristic timescale ranging from microseconds to milliseconds. This phenomenon results in single electrons following large S2 events, contributing to the low

energy background rate. The LBECA collaboration has recently reported preliminary results showing that an infrared laser (λ =1550 nm) shining on a small LXe TPC enhances the number of electrons detected following ^{210}Po α-decays [140]. Their suggested explanation is that this may be due to the photo-detachment of trapped electrons, stimulated by the IR light. If this interpretation is correct, it may provide a technique for reducing single electron backgrounds from impurity trapping. As described in [141], the capture cross-section for electrons on electronegative impurities (in this case O_2 impurities in gaseous argon) may depend significantly on the electric field in which the electrons are drifting. At eV-scale energies, the cross-section may increase or decrease with the drift field due to the molecular properties of the impurity. However, measurements of thermalized electrons in LAr show that the electron capture dynamics are well-described by a constant kinematic factor [142], implying that the capture probability is proportional to the contaminant concentration and the electron's drift time, which can be reduced by increasing the drift field in the TPC. A very interesting study may include testing whether changing the drift field can be used as a method for reducing single electron backgrounds from impurity trapping.

A study of the optimal extraction and electroluminescence field in the detector is also necessary. This could be achieved by measuring the Compton edge of a γ-ray source placed outside of some TPC to infer the S2 yield for single scatter events while varying the grid potential between 1-10 kV/cm and varying the liquid level above the grid between 1-10 mm. By performing these measurements, the number of electrons extracted in the Compton edge is obtainable. If electrons are not trapped on the LAr surface, the number of extracted electrons should be constant. If electrons are trapped, increasing the extraction field will decrease the number of trapped electrons and increase the S2 signal. The effectiveness of this technique was demonstrated in [143]. These tests will also measure the relation between the extraction and electroluminescence fields and the S2 resolution.

Due to the strong amplification of the S2 signal, a large number of VUV photons are released from the gas pocket for each drifted electron. These photons pose two challenges: they may photo-ionize inner detector surfaces, inducing a single electron background, and they may prevent the operation of a TPC loaded with a dopant like allenes with ionization energy at or below 9.7 eV (the energy corresponding to the 128 nm LAr scintillation photons). The latter concern is that S2 photons may ionize the dopant, whose electrons will then drift to the gas pocket and produce additional S2 signals, resulting in a self-sustaining cascade. By optically decoupling the gas pocket from the LAr, we can prevent this effect and allow a broader array of possible dopant candidates.

Last but not least, a wise choice for the electronics front-end design and packaging would reduce the γ- background in the ROI. For instance, given that the S2 signal does not require the multi-stage pre-amplifiers in order to be detected, the number of electric components required can be reduced. In concert with this effort, one idea is to use parabolic light collectors made from high-purity copper and coated with a thin reflective layer of silver or aluminum. The use of light collectors has two advantages. First, it would increase the distance between the photo-sensors and the LAr target, reducing the background contribution of the device. Second, light collectors would allow us to shrink each photo-sensor without sacrificing the active area of the TPC, which in turn further simplifies the readout electronics.

Many of the ideas discussed in this chapter have applications beyond optimization of a LAr TPC for dark matter research. LAr, indeed, is a target used also in the COHERENT experiment and may have application in nuclear monitoring applications, both of which would benefit from the calibration of the nuclear recoil energy scale below $1\ \mathrm{keV_{nr}}$. The continued development of low-background large-area photo-sensors has broad application to liquid noble detectors used in both dark matter and neutrino experiments. Similarly, the development of tools to minimize the single electron background in a noble gas detector would be beneficial not just for LAr TPCs, but for any future liquid noble detectors hoping to make measurements at these energy scales.

Part II

Electroweak and nuclear phenomenology based on Coherent Elastic Neutrino Scattering

5

The Coherent Neutrino Nucleus Scattering in the Standard Model

The fifth chapter focuses on the Coherent Elastic Neutrino Nucleus Scattering process through two different point of view: first, as a very peculiar form of background in the dark matter sector, and second, as a probe for nuclear and electroweak physics. The studies presented in this thesis use public data of COHERENT experiment, which is the only experiment that has detected the process, so far. With those data, we have been able to measure and constraint parameters such as neutron radii, the Weinberg angle and some of the electromagnetic properties of neutrinos.

Contents

The Coherent Elastic Neutrino Nucleus Scattering (CEνNS) plays a fundamental role in the detection of dark matter for high-exposure or low-threshold detectors. Indeed, the signal released by this type of neutrino interaction will be very hard to distinguish from signal induced by WIMP-nucleus processes. So far, dark matter detectors have not seen any compatible signal with the WIMP hypothesis and this fact pushes the community to build new detectors with larger exposure, in order to explore smaller dark matter interaction cross-sections. The experimental challenge is to limit the effects of the CEνNS background to increase the sensitivity to WIMPs. The CEνNS process, according to the Standard Model prediction, should be considered and taken into account especially for large LAr and LXe dark matter detectors. In this chapter, we will describe the theoretical framework of CEνNS and its consequences for LAr and LXe experiments. We determine the so-called 1-neutrino event curve for the two targets in the parameter plane of WIMP cross-section vs. WIMP mass. We also provide a comparison between the exlusion limit at 90% of Confidence Level (C.L.) and 5σ discovery limit for the future LAr and LXe experiments.

In addition, the potentialities in exploring neutrino properties, nuclear and electroweak physics are emphasized by describing our two analyses performed with public data released by COHERENT Collaboration.

The observation of CEνNS in cesium-iodide performed in 2017 by the COHERENT experiment [144, 145] unlocked an innovative and powerful tool to study many and diverse physical phenomena [146–155]. This detection led to a very fruitful discovery period, recently enriched by the observation of CEνNS in liquid argon [156–158]. The experimental challenge behind the CEνNS analyses is the need to observe nuclear recoils with a very small kinetic energy $T_{\rm nr}$ of a few keV, and thus the need of a low NR energy threshold. The CEνNS process gives model-independent information on the neutron nuclear form factor, which is more difficult to obtain than the proton one. Form factors represent the Fourier transform of the corresponding nucleon distribution, necessary for obtaining in turn measurements of the neutron rms radius, R_n, which is a crucial ingredient of the nuclear matter equation of state (EOS). The latter plays an essential role in understanding nuclei in laboratory experiments and several processes, like heavy ion collisions, and the structure and evolution of compact astrophysical objects as neutron stars [159–162].

The CEνNS process can also give information on the weak mixing angle, usually referred to as $\sin^2\vartheta_W$, a fundamental parameter of the electroweak theory of the Standard Model. It is also possible to set bounds on neutrino electromagnetic properties, including neutrino magnetic moment, neutrino charge radii and neutrino electric charges. The CEνNS analyses presented in

this chapter are mainly reported in the paper published on Physical Review D in 2020 [157].

5.1 Overview on the CEνNS interaction

Coherent elastic neutrino-nucleus scattering is a neutral current process induced by the exchange of a Z boson. It was first theorized in 1974 by Freedman [163] not long after the discovery of the weak neutral current process in neutrino-nucleus interactions [164]. Generally, the interaction between a neutrino and the nucleus is complex given that the neutrino interacts with the individual nucleons within the nucleus. A very attractive feature of such processes is the enhancement of the cross-section and perhaps, more intriguingly, the fact that neutrinos can scatter coherently with the nucleons. This feature appears for $|\vec{q}|R \ll 1$ [165], where $|\vec{q}| \simeq \sqrt{2MT_{\rm nr}}$ is the three-momentum transfer, R is the nuclear radius of the order of few fm, and M is the nuclear mass of the target. For most nuclei the typical inverse sizes $1/R$ are in the range from 25 to 150 MeV. Therefore, the condition for full coherence in the neutrino-nuclei scattering is well satisfied for reactor neutrinos and also for solar, supernovae neutrinos and artificial neutrino sources. The purely quantum mechanical process leads to a coherent enhancement of the cross-section proportional to the number of neutrons in the target nucleus squared. As shown in the right plot of Fig. 5.1, this enhancement leads to a cross-section that is much larger for an $\mathcal{O}$(10 MeV) neutrino than other neutrino interactions such as inverse beta decay (IBD), electron scattering, and other charged/neutral current interactions.

The kinematics of the process is easily determined from elastic scattering formulas. From them it is possible to obtain the maximum recoil energy of the target nucleus and the minimum neutrino energy E (in the limit $M \gg E$)

$$T_{\rm nr}^{\rm max,CE\nu NS} = \frac{2ME^2}{(M+E)^2 - E^2} \quad \text{and} \quad E^{\rm min,CE\nu NS} = \sqrt{\frac{MT_{\rm nr}}{2}}\,. \tag{5.1}$$

For instance, the maximum Ar and Xe nuclear recoil given by a neutrino of 30 MeV has an energy of 48 and 15 keV, respectively. Despite the large cross-section, the experimental challenge consist of being able to detect such a small energy release.

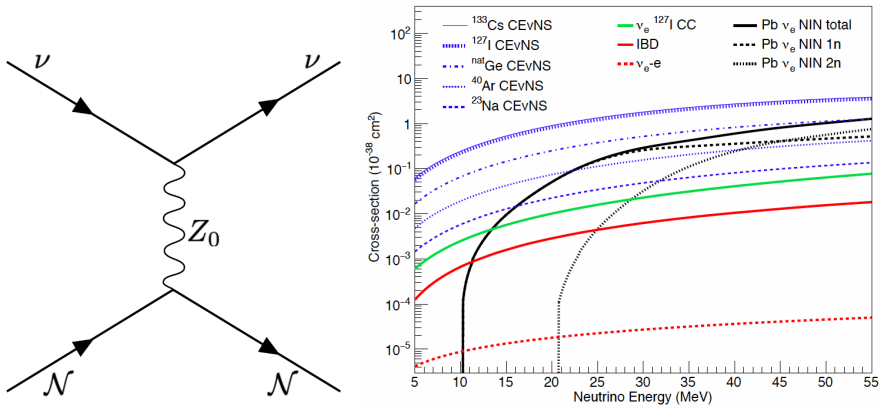

Figure 5.1: *Left*: Feynman diagram representing CEνNS interaction as a neutral current process mediated by a Z_0 boson. *Right*: Comparison of neutrino interaction cross-sections. CEνNS has an enhanced cross-section as a function of the neutrino energy for a given target nucleus when compared to other interaction channels such as charged/neutral current scattering and IBD. Figure taken from [144].

5.1.1 CEνNS cross-section

The SM weak-interaction differential cross-section as a function of the nuclear kinetic recoil energy $T_{\rm nr}$ of CEνNS processes with a spin-zero nucleus $\mathcal{N}$ with Z protons and N neutrons is given by [166–168]

$$\frac{d\sigma_{\nu_\ell\text{-}\mathcal{N}}}{dT_{\rm nr}}(E,T_{\rm nr}) = \frac{G_{\rm F}^2 M}{\pi}\left(1-\frac{MT_{\rm nr}}{2E^2}\right)Q_{\ell,\rm SM}^2, \tag{5.2}$$

where $Q_{\ell,\rm SM}$ is the electroweak charge defined as

$$Q_{\ell,\rm SM} = g_V^p Z F_Z(|\vec{q}|^2) + g_V^n N F_N(|\vec{q}|^2), \tag{5.3}$$

and where $G_{\rm F}$ is the Fermi constant, $\ell = e,\mu,\tau$ is the neutrino flavor, E is the neutrino energy. The well-known tree-level values of g_V^p and g_V^n are

$$g_V^p = \frac{1}{2} - 2\sin^2\vartheta_W, \qquad g_V^n = -\frac{1}{2}, \tag{5.4}$$

where $\vartheta_{\rm W}$ is the weak mixing angle, also known as the Weinberg angle. For the analyses presented in this chapter we consider the following more accurate

values that take into account radiative corrections in the $\overline{\text{MS}}$ scheme [169]:

$$g_V^p(\nu_\ell) = \rho\left(\frac{1}{2} - 2\sin^2\vartheta_W\right) - \frac{\hat{\alpha}_Z}{4\pi\hat{s}_Z^2}\left(1 - 2\,\frac{\hat{\alpha}_s(m_W)}{\pi}\right) + \frac{\alpha}{6\pi}\left(3 - 2\ln\frac{m_\ell^2}{m_W^2}\right), \tag{5.5}$$

$$g_V^n = -\frac{\rho}{2} - \frac{\hat{\alpha}_Z}{8\pi\hat{s}_Z^2}\left(7 - 5\,\frac{\hat{\alpha}_s(m_W)}{\pi}\right), \tag{5.6}$$

where

$$\sin^2\vartheta_W = 0.23857 \pm 0.00005 \text{ [170]} \tag{5.7}$$

is the low-energy value of the weak mixing angle, often denoted with $\hat{s}_0^2$ [169, 170], and

$$\rho = 1.00058 \text{ [170]}, \tag{5.8}$$
$$\hat{s}_Z^2 = 0.23122 \pm 0.00003 \text{ [170]}, \tag{5.9}$$
$$\hat{\alpha}_Z^{-1} = 127.955 \pm 0.010 \text{ [170]}, \tag{5.10}$$
$$\hat{\alpha}_s(m_W) = 0.123 \pm 0.018 \pm 0.017 \text{ [171]} \tag{5.11}$$

are, respectively, the ρ parameter of electroweak interactions, the value of $\sin^2\vartheta_W$ at the scale of the Z-boson mass, the value of the electromagnetic fine-structure constant at the scale of the Z-boson mass, and the value of the strong constant at the scale of the W-boson mass. The value of $\hat{\alpha}_s(m_W)$ in Eq. 5.11 is the only measured one that we found in the literature. It is in agreement with the PDG summary in Fig. 9.5 of Ref. [170]. In any case, a precise value of $\hat{\alpha}_s(m_W)$ is not needed, because its contribution is practically negligible. The terms in Eqs. 5.5 and 5.6 proportional to $\hat{\alpha}_Z/\hat{s}_Z^2$, which in turn is proportional to the square of the charged-current weak coupling constant, are due to box diagrams with W-boson propagators. The last term in Eq. 5.5 depends on the flavor ℓ of the interacting neutrino ν_ℓ through the corresponding charged lepton mass m_ℓ. This term can be interpreted as the contribution of the neutrino charge radius and is consistent with the expression of the neutrino charge radius calculated in Refs. [172–174]. Numerically, neglecting the small uncertainties, we obtain

$$g_V^p(\nu_e) = 0.0401, \tag{5.12}$$
$$g_V^p(\nu_\mu) = 0.0318, \tag{5.13}$$
$$g_V^n = -0.5094. \tag{5.14}$$

These values are different from the tree-level values $g_V^p = 0.0229$ and $g_V^n = -0.5$ obtained with Eq. 5.4, especially those of $g_V^p(\nu_e)$ and $g_V^p(\nu_\mu)$. Anyway, looking at Eq. 5.3 and given the absolute value of the vector coupling it is clear that neutrinos couple more intensively with neutrons than protons. This is the reason why the cross-section is naively proportional to N^2.

5.1.2 Form factors, nuclear and electroweak parameters

In Eq. 5.2 $F_Z(|\vec{q}|^2)$ and $F_N(|\vec{q}|^2)$ are, respectively, the form factors of the proton and neutron distributions in the nucleus. They are given by the Fourier transform of the corresponding nucleon distribution density in the nucleus and describe the loss of coherence for $|\vec{q}|R_p \gtrsim 1$ and $|\vec{q}|R_n \gtrsim 1$, where R_p and R_n are, respectively, the rms radii of the proton and neutron distributions. For the two form factors one can use different parameterizations. The three most popular ones are the symmetrized Fermi [175], Helm [53], and Klein-Nystrand [176] parameterizations that give practically identical results. Here, we briefly describe only the Helm parameterization (descriptions of the other parameterizations can be found in several papers, for example in Refs. [146, 175, 177, 178]), that is given by

$$F^{\text{Helm}}(q^2) = 3\,\frac{j_1(qR_0)}{qR_0}\,e^{-q^2s^2/2}, \tag{5.15}$$

where $j_1(x) = \sin(x)/x^2 - \cos(x)/x$ is the spherical Bessel function of order one and R_0 is the box (or diffraction) radius.

The rms radius R of the corresponding nucleon distribution is given by

$$R^2 = \frac{3}{5}\,R_0^2 + 3s^2. \tag{5.16}$$

For the parameter s, that quantifies the so-called surface thickness, we consider the value $s = 0.9\,\text{fm}$ which was determined for the proton form factor of similar nuclei [179]. The value of the rms proton distribution radius R_p is determined from the value of the charge radius R_c through the relation [180, 181][i]:

$$R_c^2 = (R_p^{\text{point}})^2 + \langle r_p^2\rangle + \frac{N}{Z}\,\langle r_n^2\rangle_c, \tag{5.17}$$

[i] Other contributions considered in Refs. [180, 181] are negligible. They are the Darwin-Foldy contribution $3/4M^2 \simeq 0.033\,\text{fm}^2$, and the spin-orbit charge density contribution $\langle r^2\rangle_{\text{so}} \simeq 0.002\,\text{fm}^2$.

where R_p^{point} is the point-proton distribution radius, $\langle r_p^2 \rangle^{1/2} = 0.8414 \pm 0.0019\,\text{fm}$ [182] is the charge radius of the proton and $\langle r_n^2 \rangle_c = -0.1161 \pm 0.0022\,\text{fm}^2$ is the squared charge radius of the neutron [170]. Since the proton form factor $F_Z(|\vec{q}|^2)$ in the cross-section in Eq. (5.2) describes only the interaction of the protons in the nucleus, the corresponding proton distribution radius R_p is given by

$$R_p^2 = (R_p^{\text{point}})^2 + \langle r_p^2 \rangle = R_c^2 - \frac{N}{Z} \langle r_n^2 \rangle_c \,. \tag{5.18}$$

Regarding the neutron distribution radius R_n, that determines the neutron form factor $F_N(|\vec{q}|^2)$ in the cross-section in Eq. 5.2, it will be determined experimentally from the fit of the COHERENT data.

It is also worth noticing that, when fitting COHERENT data, it is possible to let the parameter $\sin^2\vartheta_W$ free to vary. Indeed, the weak mixing angle is a fundamental parameter in the theory of the electroweak interactions and its experimental determination provides a direct probe of physics phenomena not included in the SM, usually referred to as new physics. In particular, low-energy determinations of ϑ_{W} offer a unique role, complementary to those at high-energy, being highly sensitive to extra Z (Z') bosons predicted in grand unified theories, technicolor models, supersymmetry and string theories [183]. This highlights the need for improved experimental determinations of ϑ_{W} in the low-energy regime.

5.1.3 Neutrino electromagnetic properties

Other interesting parameters that can be measured through CEνNS are the neutrino electromagnetic properties, namely the neutrino charge radii, neutrino electric charges and neutrino magnetic moments.

5.1.3.1 Neutrino charge radii

The neutrino charge radii are the only electromagnetic properties of neutrinos that are predicted as nonzero in the Standard Model of electroweak interactions. They are induced by radiative corrections, with the predicted

values [172–174]

$$\langle r^2_{\nu_\ell}\rangle_{\rm SM} = -\frac{G_{\rm F}}{2\sqrt{2}\pi^2}\left[3 - 2\ln\left(\frac{m_\ell^2}{m_W^2}\right)\right], \tag{5.19}$$

where m_W and m_ℓ are the W boson and charged lepton masses ($\ell = e, \mu, \tau$), and we use the conventions in Refs. [153,184,185]. The Standard Model charge radii of neutrinos are diagonal in the flavor basis, because in the Standard Model the generation lepton numbers are conserved. Numerically, the predicted values of $\langle r^2_{\nu_e}\rangle_{\rm SM}$ and $\langle r^2_{\nu_\mu}\rangle_{\rm SM}$, that can be probed with the data of the COHERENT experiment, are

$$\langle r^2_{\nu_e}\rangle_{\rm SM} = -0.83 \times 10^{-32}\,{\rm cm}^2, \tag{5.20}$$
$$\langle r^2_{\nu_\mu}\rangle_{\rm SM} = -0.48 \times 10^{-32}\,{\rm cm}^2. \tag{5.21}$$

The current 90% CL experimental bounds for $\langle r^2_{\nu_e}\rangle$ and $\langle r^2_{\nu_\mu}\rangle$ obtained in laboratory experiments that do not involve CEνNS are listed in Table I of Ref. [153]. Since they are only about one order of magnitude larger than the Standard Model predictions, they may be the first neutrino electromagnetic properties measured by new experiments in a near future.

As already discussed, the contribution of the Standard Model charge radius of ν_ℓ is taken into account by the last term in the expression in Eq. 5.5 of $g_V^p(\nu_\ell)$. In this treatment it is possible to study the effects of the neutrino charge radii in the CEνNS data of the COHERENT experiment independently of the origin of the charge radii, that can have contributions both from the Standard Model and from physics beyond the Standard Model. Therefore we consider the differential cross-section with a modified electroweak charge, named $Q_{\ell,{\rm CR}}$

$$\frac{d\sigma_{\nu_\ell\text{-}\mathcal{N}}}{dT_{\rm nr}}(E, T_{\rm nr}) = \frac{G_{\rm F}^2 M}{\pi}\left(1 - \frac{MT_{\rm nr}}{2E^2}\right) Q^2_{\ell,{\rm CR}}. \tag{5.22}$$

Here, the electroweak charge shows explicitly the presence of the contribution of diagonal charge radii and it is modified, with respect to the Standard Model prediction, by the presence of non-diagonal terms.

$$Q^2_{\ell,{\rm CR}} = \left[\left(\tilde{g}_V^p - \tilde{Q}_{\ell\ell}\right) ZF_Z(|\vec{q}|^2) + g_V^n NF_N(|\vec{q}|^2)\right]^2 + Z^2F_Z^2(|\vec{q}|^2)\sum_{\ell'\neq\ell}|\tilde{Q}_{\ell'\ell}|^2 \tag{5.23}$$

where $\tilde{g}_V^p = 0.0204$ is given by Eq. 5.5 without the last term that contains the contribution of the Standard Model charge radius. The effects of the charge

radii $\langle r^2_{\nu_{\ell\ell'}} \rangle$ in the cross-section are expressed through [186]

$$\tilde{Q}_{\ell\ell'} = \frac{\sqrt{2}\pi\alpha}{3G_{\rm F}} \langle r^2_{\nu_{\ell\ell'}} \rangle. \tag{5.24}$$

We consider the general case in which neutrinos can have both diagonal and off-diagonal charge radii in the flavor basis. The off-diagonal charge radii, as well as part of the diagonal charge radii, can be generated by physics beyond the Standard Model.

The effects of the charge radii in the cross-section are sometimes expressed through [187, 188]

$$\hat{Q}_{\ell\ell'} = \frac{2}{3}\, m^2_W \sin^2\vartheta_W \langle r^2_{\nu_{\ell\ell'}} \rangle, \tag{5.25}$$

that is considered equivalent to $\tilde{Q}_{\ell\ell'}$ in Eq. 5.24 [189] through the well-known relations $G_{\rm F}/\sqrt{2} = g^2/8m^2_W$ and $g^2 \sin^2\vartheta_W = e^2 = 4\pi\alpha$, where g is the weak charged-current coupling constant and e is the elementary electric charge (see, for example, Ref. [190]). The problem is that the equivalence holds only at tree level and radiative corrections induce a significant difference. Indeed, using the PDG values of all quantities [170] we obtain, neglecting the uncertainties, $\sqrt{2}\pi\alpha/3G_{\rm F} = 2.38 \times 10^{30}\,{\rm cm}^{-2}$ and $2m^2_W \sin^2\vartheta_W/3 = 2.64 \times 10^{30}\,{\rm cm}^{-2}$, that differ by about 10%. Therefore, the form in Eq. (5.25) overestimates the effect of the charge radius by about 10% with respect to the form in Eq. (5.24), that is the correct one for low-energy interactions because it depends only on measured low-energy quantities. Moreover, one can notice that the electromagnetic interaction due to the charge radius must be proportional to the electromagnetic fine-structure constant α and must be independent of the weak interaction constant $G_{\rm F}$. Indeed, the $G_{\rm F}$ in the denominator of Eq. 5.24 cancels the $G_{\rm F}$ in the cross-section (5.22).

The diagonal charge radii contribute to the cross-section coherently with the neutrino-proton neutral current interaction, generating an effective shift of $\sin^2\vartheta_W$. In the case of $\bar{\nu}_\ell$-$\mathcal{N}$ scattering, we have $g_V^{p,n} \to -g_V^{p,n}$ and $\langle r_{\nu_{\ell\ell'}} \rangle \to \langle r_{\bar{\nu}_{\ell\ell'}} \rangle = -\langle r_{\nu_{\ell\ell'}} \rangle$. Therefore, the charge radii of flavor neutrinos and antineutrinos contribute with the same sign to the shift of $\sin^2\vartheta_W$ in the CEνNS cross-section.

There are five charge radii that can be determined with the COHERENT CEνNS data: the two diagonal charge radii $\langle r^2_{\nu_{ee}} \rangle$ and $\langle r^2_{\nu_{\mu\mu}} \rangle$, that sometimes are denoted with the simpler notation $\langle r^2_{\nu_e} \rangle$ and $\langle r^2_{\nu_\mu} \rangle$ in connection to the Standard Model charge radii in Eqs. 5.19–5.21, and the absolute values of the three off-diagonal charge radii $\langle r^2_{\nu_{e\mu}} \rangle = \langle r^2_{\nu_{\mu e}} \rangle^*$, $\langle r^2_{\nu_{e\tau}} \rangle$, and $\langle r^2_{\nu_{\mu\tau}} \rangle$.

5.1.3.2 Neutrino electric charges

As discussed in Ref. [153], the CEνNS process is sensitive not only to the neutrino charge radii, but also to the neutrino electric charges. Usually neutrinos are considered as exactly neutral particles, but in theories beyond the SM they can have small electric charges (often called as milli-charges). This possibility was considered in many experimental and theoretical studies (see the review in Ref. [184]).

The differential CEνNS cross-section that takes into account the contribution of the neutrino electric charges in addition to Standard Model neutral-current weak interactions is written as a function of the modified electroweak charge $Q_{\ell,\mathrm{EC}}$

$$\frac{d\sigma_{\nu_\ell\text{-}\mathcal{N}}}{dT_{\mathrm{nr}}}(E,T_{\mathrm{nr}}) = \frac{G_{\mathrm{F}}^2 M}{\pi}\left(1-\frac{MT_{\mathrm{nr}}}{2E^2}\right)Q_{\ell,\mathrm{EC}}^2, \tag{5.26}$$

where

$$Q_{\ell,\mathrm{EC}}^2 = \left[(g_V^p - Q_{\ell\ell})\,ZF_Z(|\vec{q}|^2) + g_V^n NF_N(|\vec{q}|^2)\right]^2 + Z^2F_Z^2(|\vec{q}|^2)\sum_{\ell'\neq\ell}|Q_{\ell'\ell}|^2 \tag{5.27}$$

with g_V^p and g_V^n given, respectively, by Eqs. 5.5 and 5.6, with the numerical values in Eqs. 5.12–5.14. The neutrino electric charges $q_{\nu_{\ell\ell'}}$ contribute through [184, 186]

$$Q_{\ell\ell'} = \frac{2\sqrt{2}\pi\alpha}{G_{\mathrm{F}}q^2}\,q_{\nu_{\ell\ell'}}, \tag{5.28}$$

where $q^2 = -2MT_{\mathrm{nr}}$ is the squared three-momentum transfer. Although the electric charges of neutrinos and antineutrinos are opposite, neutrinos and antineutrinos contribute with the same sign to the shift of $\sin^2\vartheta_W$, as in the case of the charge radii, because also the weak neutral current couplings change sign from neutrinos to antineutrinos.

5.1.3.3 Neutrino magnetic moments

The neutrino magnetic moment is the electromagnetic neutrino property that is most studied and searched experimentally. The reason is that its existence is predicted by many models beyond the Standard Model, especially those that include right-handed neutrinos. It is also phenomenologically important for astrophysics because neutrinos with a magnetic moment can interact with astrophysical magnetic fields leading to several important effects (see the

reviews in Refs. [184, 191]). In the original SM with massless neutrinos the neutrino magnetic moments are vanishing, but the results of neutrino oscillation experiments have proved that the SM must be extended in order to give masses to the neutrinos. In the minimal extension of the SM in which neutrinos acquire Dirac masses through the introduction of right-handed neutrinos, the neutrino magnetic moment is given by [178, 185, 192–195]

$$\mu_\nu = \frac{3\, e\, G_F}{8\sqrt{2}\,\pi^2} m_\nu \simeq 3.2 \times 10^{-19} \left(\frac{m_\nu}{\mathrm{eV}}\right) \mu_B \,, \tag{5.29}$$

where μ_B is the Bohr magneton, m_ν is the neutrino mass and e is the electric charge. The CEνNS process is also sensitive to neutrino magnetic moments [150,177,178,185,194,195]. The existence of a neutrino magnetic moment could have a significant effect on the CEνNS cross-section, that acquires an additional term

$$\left.\frac{d\sigma_{\nu_\ell\text{-}\mathcal{N}}}{dT_{\mathrm{nr}}}(E, T_{\mathrm{nr}})\right|_{\mu_\nu \neq 0} = \frac{d\sigma_{\nu_\ell\text{-}\mathcal{N}}}{dT_{\mathrm{nr}}}(E, T_{\mathrm{nr}}) + \frac{d\sigma^{\mathrm{mag}}_{\nu_\ell\text{-}\mathcal{N}}}{dT_{\mathrm{nr}}}(E, T_{\mathrm{nr}}). \tag{5.30}$$

The additional term is

$$\frac{d\sigma^{\mathrm{mag}}_{\nu_\ell\text{-}\mathcal{N}}}{dT_{\mathrm{nr}}}(E, T_{\mathrm{nr}}) = \frac{\pi\alpha^2}{m_e^2}\left(\frac{1}{T_{\mathrm{nr}}} - \frac{1}{E}\right) Z^2 F_Z^2(|\vec{q}|^2) \left|\frac{\mu_{\nu_\ell}}{\mu_{\mathrm{B}}}\right|^2 , \tag{5.31}$$

where m_e is the electron neutrino mass and μ_{ν_ℓ} is the effective magnetic moment of the flavor neutrino ν_ℓ in elastic scattering (for a deeper and theoretical treatment see Ref. [184]).

5.2 Background for future dark matter detectors

The CEνNS process leads to the possibility of having neutrino interactions with nuclei producing a nuclear recoil in a very similar way with respect to what a WIMP would do. Indeed, next generation direct dark matter detectors will have the sensitivity to detect neutrinos from several sources, among which solar, atmospheric, and diffuse supernova neutrinos. On one side, dark matter experiments could exploit their large sensitivity to nuclear recoils in order to study CEνNS interaction by looking at these signals. On the other side, being CEνNS indistinguishable from WIMP scattering, the presence of neutrinos would limit the sensitivity to the dark matter searches, which is the main aim of these experiments.

The studies presented in this section have been used to write a document of the Global Argon Dark Matter Collaboration (GADMC) submitted to the European Strategy of Particle Physics in 2018.

5.2.1 CEνNS background prediction

In this paragraph the neutrino background in dark matter experiments is estimated. The starting point consists of the description of the neutrino flux components. The main neutrino fluxes on Earth could be divided into three categories: solar, atmospheric and diffuse supernovae neutrinos. Solar neutrinos are produced by the nuclear synthesis reactions in the Sun such as the proton proton (*pp*) or Carbon-Nitrogen-Oxygen (*CNO*) chains. These neutrino components are characterized by energies lower than $\sim$ 2 MeV. Two very crucial components of the pp chain consist of ^{8}B and hep neutrinos. The first ones arise from the decay $^8\text{B} \rightarrow ^7\text{Be}^* + e^+ + \nu_e$, which occurs in approximately 0.02% of the termination of the pp chain. The hep neutrinos come from the reaction $^3\text{He} + p \rightarrow ^4\text{He} + e^+ + \nu_e$. The total flux produced in the *pp* chain is 5.94×10^{10} cm^{-2} s^{-1}. Following Ref. [196], the theoretical uncertainties for solar fluxes are of the order of 10%. In particular, ^{8}B and hep components have an uncertainty of 16%. Another important flux is the Diffuse Supernova Neutrino Background (DSNB) which derives from all the past supernova explosions in the Universe. The neutrino spectrum of a core-collapse supernova is assumed to be a Fermi-Dirac spectrum with temperatures in the range 3-8 MeV. DSNB flux covers energies up to hundreds of MeV. Following Ref. [197], the DSNB flux strongly depends on the temperature spectrum and, for this reason, the assumed uncertainty is 50%. The last component consist of atmospheric neutrinos produced through cosmic ray collisions against the Earth atmosphere. The energy range is approximately 10-1000 MeV. For these energies, the uncertainty on the predicted atmospheric neutrino flux is approximately 20% [198]. Among the three types of source cited, the atmospheric one is the main responsable for neutrino-nucleus background in next generation dark matter experiments that aim to improve the limits in the high-mass WIMP region (20 GeV/c^2 - 1 TeV/c^2) . For low-mass WIMP searches (0.1-20 GeV/c^2) the main background comes from the solar component, in particular ^{8}B and hep. In the left plot of Fig. 5.2 all the neutrino flux components just mentioned are shown in details.

By combining the fluxes arriving on Earth with the CEνNS differential cross-section it is possible to estimate how many neutrino events are expected in the

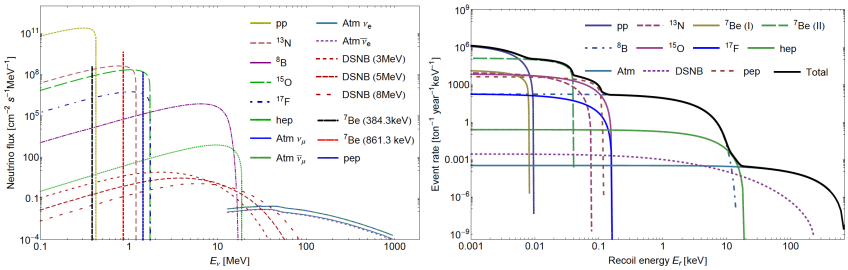

Figure 5.2: *Left*: Relevant neutrino fluxes on Earth for direct dark matter detection at LNGS as a function of the neutrino energy. From low to high energies: Solar, diffuse supernova and atmospheric neutrinos. *Right*: Event rate of neutrino background events per unit of tonne-year due the CEνNS as a function of nuclear recoil energy considering an argon target (continuous black line); partial contributions relative to specific neutrino fluxes are also shown.

detector per unit of NR energy and time

$$\frac{d^2N^{\mathrm{CE}\nu\mathrm{NS}}}{dt\,dT_{\mathrm{nr}}} = N_{\mathrm{target}} \int_{E_{\mathrm{min}}}^{E_{\mathrm{max}}} dE \sum_{\nu=\nu_e,\nu_\mu,\overline{\nu}_\mu} \frac{d\phi_\nu}{dE} \frac{d\sigma_{\nu\text{-}\mathcal{N}}}{dT_{\mathrm{nr}}}(E, T_{\mathrm{nr}})\,, \tag{5.32}$$

where N_{target} is the number of nuclei in the detector, E_{min} is the minimum neutrino energy producing a nuclear recoil T_{nr} (see Eq. 5.1), E_{max} is the largest neutrino energy among the neutrinos on Earth (looking at the left plot in Fig. 5.2 above 1 GeV the fluxes considered are negligible), and ϕ_ν are the number of incoming neutrinos per unit of time and area. In the right plot of Fig. 5.2 the event rate per unit of tonne-year is shown considering an argon detector. This represents the background prediction for future argon experiments as DarkSide-20k and Argo. Depending on the value of the detection threshold the number of neutrinos expected changes dramatically. In particular, with a threshold $T_{\mathrm{nr}} > 20$ keV, only DSNB and atmospheric neutrinos are expected, giving then a contribution of $\mathcal{O}(1)$ per 100 tonne-year. On the contrary, lowering the threshold at a level of $\sim$ 1 keV would include the ^{8}B flux in the background expected, making the neutrinos expected to be $\mathcal{O}(1000)$ with the same exposure.

5.2.2 1-neutrino event limit and future sensitivity

Since neutrinos might become the dominant background in future dark matter direct detection searches, it could be interesting set a limit in the parameter plane $\sigma^{\chi-n}$ vs m_χ. The community typically refers to the discovery limit obtained for xenon by Billard et al. [79]. Another neutrino curve more intuitive

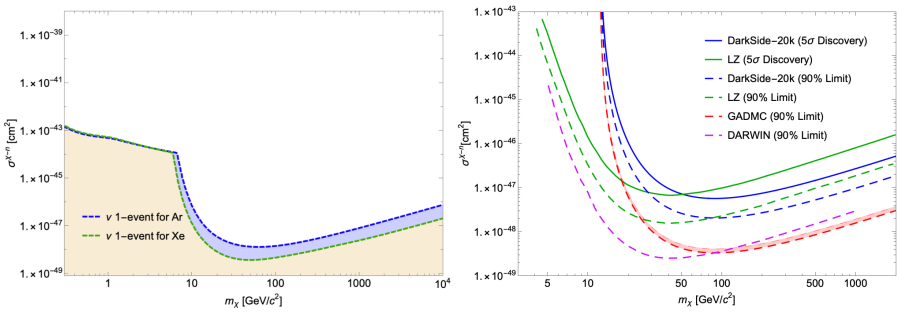

Figure 5.3: *Left:* 1-neutrino event limit for LAr and LXe in WIMP parameter plane. *Right:* Sensitivities curves for future direct detection dark matter experiments. Dashed curve represents upper limits at 90% C.L. while continuous lines 5σ discovery. The red band for GADMC represents a 20% of uncertanty for the neutrino background.

Experiment	Target	Threshold [keV]	Exposure	Sensitivity
DarkSide-20k	LAr	30	100 tonne-year	Calculated
LZ	LXe	4-5	15 tonne-year	[199]
Argo	LAr	30	1500 tonne-year	Calculated
DARWIN	LXe	6.6	200 tonne-year	[200]

Table 5.1: Future LAr and LXe direct detection dark matter experiments.

is represented by the 1-neutrino event limit. This neutrino limit is obtained by generating a set of 200 background-free exclusion limits (defined as 2.3 WIMP events at 90% C.L.) with varying thresholds from 1 eV to 500 keV and adjusting each curve's exposure such that a single neutrino event is expected. The minimum of these curves is what is defined as the 1-neutrino limit. In Fig. 5.3 (*left*), we show the difference between the 1 neutrino curve for Xe and Ar. In particular, above $m_\chi = 6\,\mathrm{GeV/c^2}$, the limit for Ar is higher of about a factor of 3 than the Xe curve. This is due to the higher event rate in the region above 10 keV of recoil energy. The interpretation of this curve is the following: if a background-free experiment sensitivity curve is below this limit, that experiment should expect at least one event of neutrino background during its data taking. Since this background is irreducible, to claim a discovery or to set an upper limit the experiment would need to observe more WIMPs, with respect to the background-free only case, and for this reason, the sensitivity of the detector, including neutrino events, will get worse. Moreover, considering that for a zero-background experiment the sensitivity increases proportionally to the exposure, once the 1-event limit is reached, the exposure will increase as the square root of the exposure. In this work, we calculate the sensitivity curves for future LAr experiments through the statistical counting approach, comparing the results with LXe results for future LZ [199] and DARWIN [200] detectors. Since the number of backround events considered is low enough,

the counting approach should give very similar results with respect to a more detailed analysis using, for instance, a profile likelihood ratio test. This statement will be deeper studied in future works. In Fig. 5.3 (*right*) we show the different upper limit at 90% of C.L. and the 5σ discovery potential for the experiments listed in Tab. 5.1. As it is visible in the plot, for large-scale experiment (Argo and DARWIN) LAr provides a weaker upper limit above masses of roughly 90 GeV/c^2, while below this value LXe experiment could better explore the parameter region for lighter WIMPs.

5.3 The COHERENT experiment

CEνNS events in a detector could also be considered as a signal rather than a background. This approach is the one that scientists use to study and characterize experimentally the interaction.

This section briefly describes the COHERENT experiment and its usage of the Spallation Neutron Source (SNS) as a neutrino source. Indeed, SNS generates a flux of neutrinos through proton collisions with mercury. The COHERENT experiment located at the SNS uses these neutrinos for CEνNS detection with multiple detectors. COHERENT is the only experiment in the world to have seen CEνNS, so far.

The SNS at Oak Ridge National Laboratory (ORNL), in Tennessee, USA, is a DOE Office of Science user facility and currently the most powerful pulsed-beam neutron source in the world [58]. Spallation neutrons are created from a ~ 1 GeV, 1.4 MW proton beam impinging on a liquid mercury target, producing 20-30 neutrons per each proton-Hg collision. The SNS produces $\sim 1 \times 10^{16}$ protons-on-target (POT) every second at its designed operating power of 1.4 MW. The proton beam is pulsed at 60 Hz with a full width at half maximum (FWHM) of ~ 350 ns. Knowledge of when the beam pulse occurs allows for the rejection of the steady-state (SS) backgrounds in a CEνNS experiment. The SNS is also the best stopped-pion neutrino source in the world with its combination of beam power and background rejection via the pulsed beam structure. Charged and neutral pions are created along with the spallation neutrons when the proton beam reaches the mercury target. About 99 % ff the π^- produced are captured within the mercury target. Neutrinos are produced from the decay of charged pions produced in the proton collisions with the mercury target. First, the π^+ decays into a μ^+ and a ν_μ. Then the mu^+ decays into a e^+, ν_e, and $\bar{\nu}_\mu$. Under this sequence three distinct neutrino flavors for each π^+ decay are produced. The energy spectrum of neutrinos

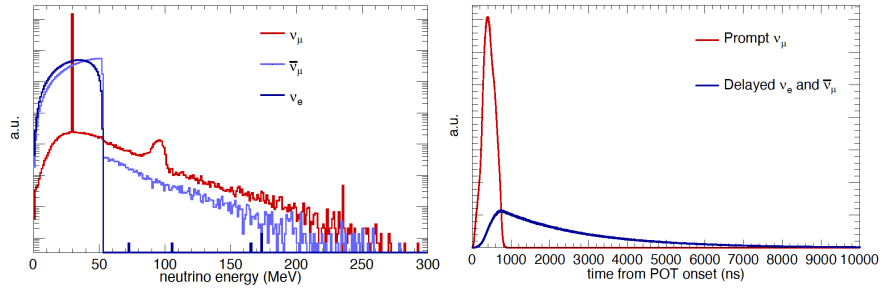

Figure 5.4: *Left:* Simulation of the neutrino energy distribution at SNS. Neutrinos above the endpoint of the Michel spectrum ($E < 52.8$ MeV) arise from decay-in-flight and muon capture, giving a negligible signal rate ($< 1\%$) signal rate. *Right:* Arrival time of SNS neutrinos to the COHERENT detector. The figures presented are taken from [144].

produced by the SNS represents a pion-decay-at-rest neutrino spectrum. The resulting neutrino energy for the ν_μ is mono-energetic from the resulting 2-body decay of the μ^+ and whereas the energy spectra for the ν_e and $\bar{\nu}_\mu$ are produced from the decay of the μ^+ and are described by the Michel spectrum [201], with a maximum neutrino energy $E^{\max} = m_\mu/2$. Neutrinos above the endpoint of the Michel spectrum ($E < 52.8$ MeV) arise from decay-in-flight and muon capture, giving a negligible signal rate ($< 1\%$) signal rate.

The CEνNS event rate in the COHERENT experiment [156] depends on the neutrino flux dN_ν/dE produced from the SNS. It is given by the sum of the three components

$$\frac{dN_{\nu_\mu}}{dE} = \eta\,\delta\left(E - \frac{m_\pi^2 - m_\mu^2}{2m_\pi}\right), \tag{5.33}$$

$$\frac{dN_{\nu_{\bar{\mu}}}}{dE} = \eta\,\frac{64E^2}{m_\mu^3}\left(\frac{3}{4} - \frac{E}{m_\mu}\right), \tag{5.34}$$

$$\frac{dN_{\nu_e}}{dE} = \eta\,\frac{192E^2}{m_\mu^3}\left(\frac{1}{2} - \frac{E}{m_\mu}\right), \tag{5.35}$$

with the normalization factor $\eta = rN_{\rm POT}/4\pi L^2$, where r is the number of neutrinos per flavor that are produced for each proton-on-target (POT), $N_{\rm POT}$ is the integrated number of proton on target and L is the distance between the source and the COHERENT detectors. The pions decay at rest ($\pi^+ \to \mu^+ + \nu_\mu$) producing ν_μ's which arrive at the COHERENT detector as a prompt signal within about $1.5\,\mu$s after protons-on-targets. The decay at rest of μ^+ ($\mu^+ \to e^+ + \nu_e + \bar{\nu}_\mu$) produces a delayed component of $\bar{\nu}_\mu$'s and ν_e's, since they arrive at the detector in a relatively longer time interval of about $10\,\mu$s. The time spectra are obtained by a integral parametrization according to the data releases in [202, 203]. The differential probability as a function of time are

calculated with the formulas

$$\frac{dP_{\nu_\mu}(t)}{dt} = \frac{1}{\sqrt{2\pi}\, b_{\rm POT}\, \tau_\pi} \int_0^t \exp\left[-\frac{(t' - a_{\rm POT})^2}{2b_{\rm POT}^2}\right] \exp\left[-\frac{(t-t')}{\tau_\pi}\right] dt', \quad (5.36)$$

$$\frac{dP_{\nu_e,\bar{\nu}_\mu}(t)}{dt} = \frac{1}{\tau_\mu} \int_0^t \frac{dP_{\nu_\mu}(t')}{dt'} \exp\left[-\frac{(t-t')}{\tau_\mu}\right] dt', \quad (5.37)$$

where $a_{\rm POT} = 0.44$ µs and $b_{\rm POT} = 0.15$ µs are protons-on-target trace parameters from the SNS. The trace is well approximated by a gaussian of mean $a_{\rm POT}$ and width $b_{\rm POT}$. This is convoluted with the τ_π and τ_μ neutrino decay lifetimes to estimate the CEνNS signal. Simulation of energy and time behavior of neutrinos can be seen in Fig. 5.4.

Not only neutrinos come out from the SNS, indeed prompt neutrons escaping the iron and steel shielding monolith surrounding the mercury target would swamp a CEνNS detector sited at the SNS instrument bay. Neutron-induced nuclear recoils would largely dominate over neutrino-induced recoils, making experimentation impossible. To overcome this problem, the detectors have been located in a basement corridor, called the "neutrino alley" which offers more than 12 m of additional void free neutron-moderating materials in the line-of-sight to the SNS target. An overburden of 8 meters of water equivalent (m.w.e.) provides an additional reduction in backgrounds associated with cosmic rays.

COHERENT plans to deploy several detectors to measure CEνNS on multiple nuclei. The CsI[Na] CEνNS detector and shielding were installed in the corridor location nearest to the SNS target and it gave the first and main result obtained by the COHERENT collaboration, derived from 15 months of accumulated live-time [144]. The latest 2020 CsI[Na] results with larger statistics on coherent elastic neutrino-nucleus scattering data have been recently presented [204] and they will be discussed more in details in the next chapter. The CsI[Na] detector was decommissioned in June 2019. Currently, the operations of a $\mathcal{O}$(20 kg) active mass liquid argon detector CENNS-10 are ongoing. A 185 kg NaI[Tl] crystal array not sensitive to a CEνNS measurement is deployed to measure the neutrino charged current interaction on ^{127}I [205]. The currently operating detectors neutrino alley is represented in Fig. 5.5. Deployments of a 16 kg p-type point contact HPGe crystal array and a tonne-scale NaI[Tl] crystal array are planned to explore the N^2 dependence of the CEνNS cross-section. The tonne-scale NaI[Tl] array will be both sensitive to CEνNS and the ^{127}I charged current interaction. A tonne-scale liquid argon detector and a tonne-scale heavy water detector [206] are planned further in the future to begin precision measurements using CEνNS. The well known neutrino-deuterium charged current interaction cross-section allows the heavy water detector to better constrain the SNS neutrino flux.

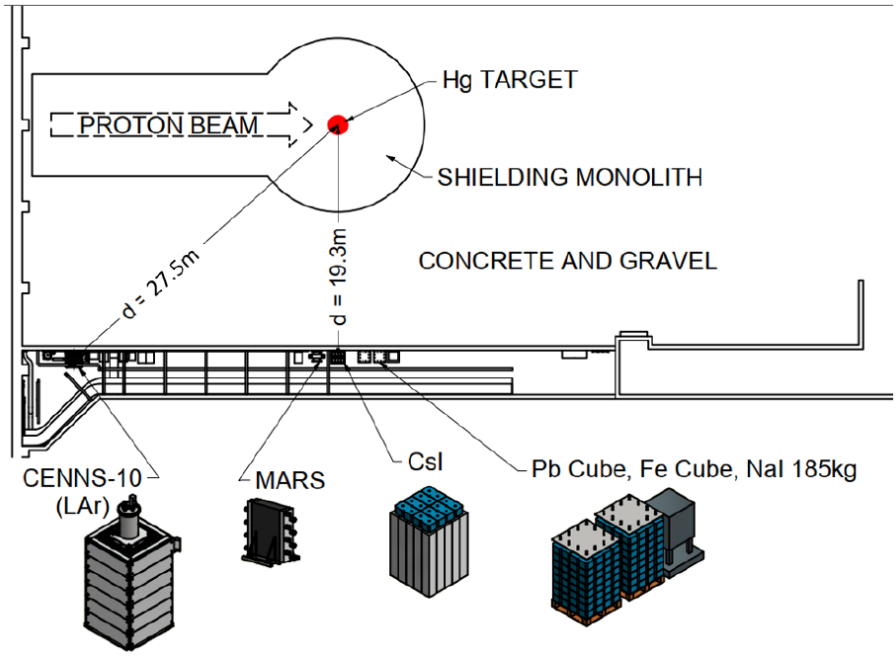

Figure 5.5: Current detector suite and siting in Neutrino Alley for the COHERENT experiment. The CsI[Na] detector was decommissioned in June 2019. CENNS-10 is sensitive to a CEνNS measurement. The 185 kg NaI[Tl] is not sensitive to CEνNS but to the charged current interaction on ^{127}I. MARS is a Gd-loaded plastic scintillator detector to measure beam-related neutron backgrounds.

5.4 Neutrino and nuclear physics in CsI and LAr

In this section we will briefly review the detection of CEνNS performed with CsI and LAr, by COHERENT Collaboration. In particular, we will describe the experimental ingredients needed for the analyses presented below.

5.4.1 First detection in CsI

The first result obtained by the COHERENT collaboration [144], which was also the one with larger impact among the community, derived from fifteen months of accumulated live-time. For the observation of CEνNS, COHERENT exploited two modalities of data taking: "Beam On" and "Beam Off". In

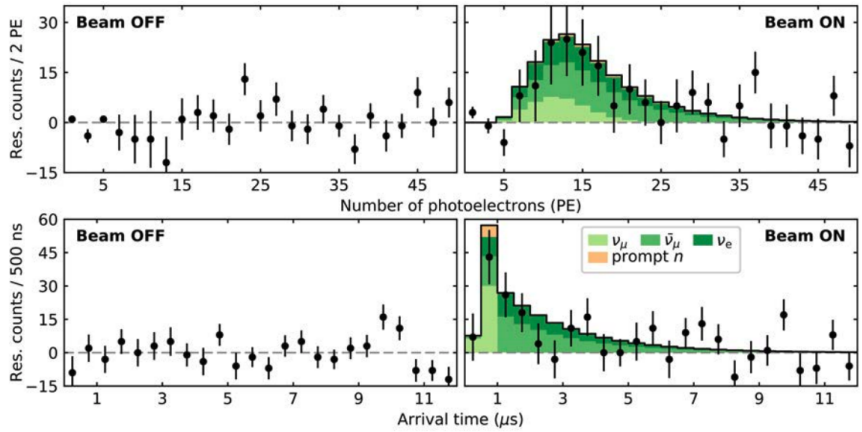

Figure 5.6: Residual difference between CsI[Na] signals in the 12 µs following POT triggers, and those in a 12-µs window before, as a function of their energy in the top panel, and of event arrival time in the bottom panel. Steady-state environmental backgrounds contribute to both groups of signals equally, vanishing in the subtraction. Error bars are statistical. These residuals are shown for 153.5 live-days of SNS inactivity ("Beam OFF") and 308.1 live-days of neutrino production ("Beam ON"), over which 7.48 GWhr of energy ($\sim 1.76 \times 10^{23}$ protons) was delivered to the mercury target. Approximately 1.17 PE are expected per keV of cesium or iodine nuclear recoil energy. Figure taken from [144].

the first scenario the protons are delivered to the Hg target at SNS and then neutrinos are produced. In the second one, the protons do not reach the target so that there is no production of neutrinos and it is possible to study the background unrelated to the beam with good accuracy. When comparing CsI[Na] signals occurring before POT triggers, and those taking place immediately after, the collaboration observes a high-significance excess in the second group of signals, visible in both the energy spectrum and the distribution of signal-arrival times. This excess appears only during times of neutrino production. The excess follows the expected CEνNS signature very closely, containing only a minimal contamination from beam-associated backgrounds. Neutrino-induced neutrons (NINs) have a negligible contribution, even smaller than that from prompt neutrons, which is shown in the figure. The formation of the excess is strongly correlated to the instantaneous power on target. All neutrino flavors emitted by the SNS contribute to reconstructing the excess, as expected from a neutral current process.

In Fig. 5.6 the CsI data-set compared to the Standard Model CEνNS predictions for prompt ν_μ and delayed ν_e and $\bar{\nu}_\mu$, is presented. Consistency with the Standard Model is observed at the one-sigma level with 134 ± 22 events observed and 173 ± 48 expected. Characteristic excesses closely following the Standard Model CEνNS prediction are observed for periods of neutrino production only, with a rate correlated to instantaneous beam power.

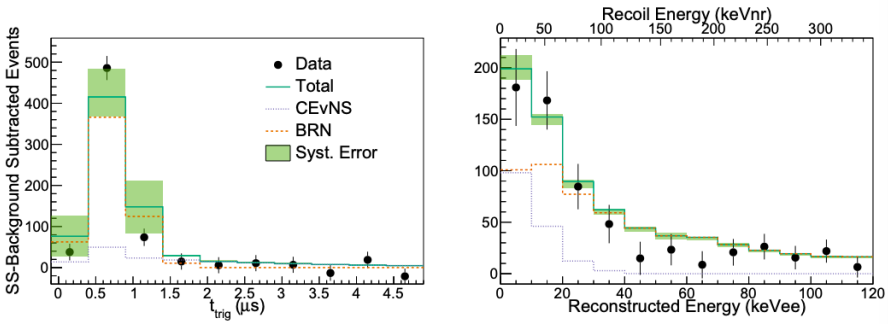

Figure 5.7: *Left:* Projection of the best-fit maximum likelihood probability density function (PDF) for LAr from Analysis A of [156] on the trigger time. *Right:* Same projection for the reconstructed energy. Both the plots show selected data and statistical errors. The steady-state background has been subtracted to better show the CEνNS component. The green band shows the envelope of fit results resulting from the $\pm 1\sigma$ systematic errors on the PDF.

In 2017, right after the observation performed by the COHERENT Collaboration, a novel technique has been developed by Cadeddu et al. [146] to investigate nuclear properties of Cs and I with the observation of CEνNS. This idea uses the fact that CEνNS measurements give information on the nuclear neutron form factor (Eq. 5.15), which is more difficult to obtain than the information on the proton nuclear form factor, that can be obtained with elastic electron-nucleus scattering and other electromagnetic processes. Indeed, before the COHERENT experiment, the only measurement of the nuclear neutron distribution with neutral-current weak interactions was done with parity-violating electron scattering on ^{208}Pb in the PREX experiment [207]. By fitting COHERENT data with the Standard Model prediction of CEνNS it is possible to measure the rms neutron radius R_n. At that time, the measurement of R_n

$$R_n^{\mathrm{CsI,2017}} = 5.5^{+0.9}_{-1.1}\mathrm{fm} \tag{5.38}$$

had a precision of about 20%. In the next chapter the analysis of the new COHERENT data with CsI[Na] is presented, together with the improvements on the rms neutron radii.

5.4.2 First detection in LAr

The CENNS-10 is a single-phase 24 kg LAr scintillation detector installed in the neutrino alley in late 2016 and ran for a short engineering run. This run was not sensitive to CEνNS due to the high detector threshold, but was still able to place a limit on the CEνNS cross-section and help constrain the beam-related

neutron backgrounds [208]. The experimental challenge behind this analysis is the need to observe nuclear recoils with a very small kinetic energy $T_{\rm nr}$ of a few keV, and thus the need of a low nuclear-recoil-energy threshold. In LAr COHERENT have to deal with the presence of a larger background, when compared to the cesium-iodide case. An upgrade to the CENNS-10 detector in the summer of 2017 improved the light collection efficiency of the detector and lowered the energy threshold to be sensitive to CEνNS. The upgrade allowed the collaboration to improve the light collection efficiency with respect to the engineering run and to lower the threshold from ~ 80 keV$_{\rm nr}$ to ~ 20 keV$_{\rm nr}$. Multiple calibration sources, confirm the improvement in the light collection efficiency and measure a linear detector response in the CEνNS region of interest. A 13.8×10^{22} POT sample of data taken with CENNS-10 over the period of July 2017-December 2018 provides the first detection of CEνNS in argon. A binned likelihood technique performed in two independent analyses (A and B) prefers CEνNS over the background-only null hypothesis with greater than $3\ \sigma$ significance. The measured flux-averaged cross-section of $(2.3 \pm 0.7) \times 10^{-39}\ {\rm cm}^2$ (corresponding to 159 ± 43 events) is consistent with the SM prediction of $1.8 \times 10^{-39}\ {\rm cm}^2$ which results in 128 expected events. In Fig. 5.7 the data-set of Analysis A along with the probability density functions for the arrival time (*left*) and the reconstructed energy (*right*) are shown. In both Analysis A and B of [156], also the information of the pulse shape of the signal is used in order to better recognize CEνNS from the background. Also in this LAr detector, as well as the DarkSide-50 detector, the f_{90} parameter is used as a pulse shape discriminator. However, most of the information and power of the analysis is contained in the energy distribution of events. For the sake of simplicity, our following LAr analyses contain only the reconstructed energy information.

5.4.2.1 Nuclear physics of LAr with CEνNS

In order to extract the physical parameter of interest, the first step is to simulate the CEνNS signal at CENNS-10 as a function of the nuclear recoil energy. The theoretical CEνNS event number $N_i^{\rm CE\nu NS}$ in each nuclear recoil energy bin i is given by

$$N_i^{\rm CE\nu NS} = N({\rm Ar}) \int_{T_{\rm nr}^i}^{T_{\rm nr}^{i+1}} dT_{\rm nr}\, A(T_{\rm nr}) \int_{E_{\rm min}}^{E_{\rm max}} dE \sum_{\nu=\nu_e,\nu_\mu,\overline{\nu}_\mu} \frac{dN_\nu}{dE} \frac{d\sigma_{\nu\text{-}\mathcal{N}}}{dT_{\rm nr}}(E, T_{\rm nr})\,, \tag{5.39}$$

where $A(T_{\rm nr})$ is the energy-dependent reconstruction efficiency given in Fig. 3 in Ref. [156], $E_{\rm min} = \sqrt{MT_{\rm nr}/2}$ and $E_{\rm max} = m_\mu/2 \sim 52.8$ MeV, m_μ being the

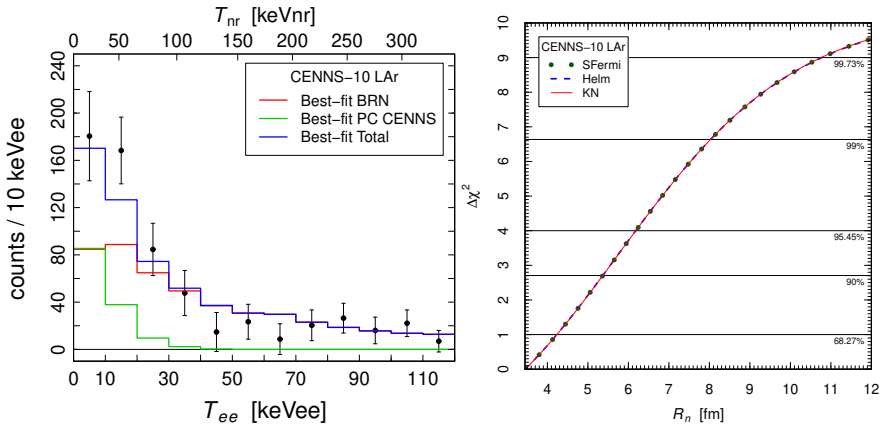

Figure 5.8: *Left:* Histograms representing the fits of the CENNS-10 data (black points with statistical error bars) in the case of partial coherence (PC), with the neutron form factor corresponding to the minimal neutron distribution radius $R_n = 3.45$ fm.*Right:*$\Delta\chi^2 = \chi^2_S - (\chi^2_S)_{\rm min}$ as a function of the rms neutron distribution radius R_n of ^{40}Ar obtained from the fit of the data of the CENNS-10 experiment. The three curves correspond to the symmetrized Fermi [175] (SFermi), Helm [53] (Helm), and Klein-Nystrand [176] (KN) form factor parameterizations..

muon mass, $N(\mathrm{Ar})$ is the number of Ar atoms in the detector, and $\frac{dN_\nu}{dE}$ is the neutrino flux integrated over the experiment lifetime. Concerning the former element, we digitalise the efficiency as a function of the electron-equivalent recoil energy T_{ee} [keV$_{ee}$], which is subsequently transformed as a function of the nuclear recoil energy $T_{\rm nr}$ [keV$_{\rm nr}$] thanks to the relation

$$T_{ee} = f_Q(T_{\rm nr}) T_{\rm nr}\,. \tag{5.40}$$

Here, f_Q is the quenching factor, which is the ratio between the scintillation light emitted in nuclear and electron recoils and determines the relation between the number of detected photoelectrons and the nuclear recoil kinetic energy. Following Ref. [156], the quenching factor is parameterized as

$$f_Q(T_{\rm nr}) = (0.246 \pm 0.006\,\mathrm{keV_{nr}}) + ((7.8 \pm 0.9) \times 10^{-4}) T_{\rm nr} \tag{5.41}$$

up to 125 keV$_{\rm nr}$, and kept constant for larger values. The value of $N(\mathrm{Ar})$ is given by $N_{\rm A}\, M_{\rm det}/M_{\rm Ar}$, where $N_{\rm A}$ is the Avogadro number, $M_{\rm det}$ is the detector active mass equal to 24 kg and $M_{\rm Ar} = 39.96$ g/mol is the molar mass of ^{40}Ar. Actually, one should consider that atmospheric argon is contaminated by a small percentage of ^{36}Ar and ^{38}Ar, namely $F(^{36}\mathrm{Ar}) = 0.334\%$ and $F(^{38}\mathrm{Ar}) = 0.063\%$. However, since the amount of ^{36}Ar and ^{38}Ar is very small and the uncertainties are large, in practice one gets the same results considering $F(^{40}\mathrm{Ar}) = 100\%$ and $F(^{36}\mathrm{Ar}) = F(^{38}\mathrm{Ar}) = 0$.

In Ref. [156] two independent analyses, labeled A and B, are described, that

differ mainly for the selection and the treatment of the background. In the following, we will use the data coming from the analysis A, whose range of interest of the nuclear recoil energy is [0, 120] keV_{ee} (corresponding to roughly [0, 350] $\mathrm{keV}_{\mathrm{nr}}$), with 12 energy bins of size equal to 10 keV_{ee}. In our analysis corresponding to analysis A of the COHERENT collaboration [156], we considered the least-squares function

$$\begin{aligned}\chi^2_{\mathrm{Ar}} &= \sum_{i=1}^{12}\left(\frac{N_i^{\mathrm{exp}} - \eta_{\mathrm{CE}\nu\mathrm{NS}} N_i^{\mathrm{CE}\nu\mathrm{NS}} - \eta_{\mathrm{PBRN}} B_i^{\mathrm{PBRN}} - \eta_{\mathrm{LBRN}} B_i^{\mathrm{LBRN}}}{\sigma_i}\right)^2 \\ &+ \left(\frac{\eta_{\mathrm{CE}\nu\mathrm{NS}}-1}{\sigma_{\mathrm{CE}\nu\mathrm{NS}}}\right)^2 + \left(\frac{\eta_{\mathrm{PBRN}}-1}{\sigma_{\mathrm{PBRN}}}\right)^2 + \left(\frac{\eta_{\mathrm{LBRN}}-1}{\sigma_{\mathrm{LBRN}}}\right)^2, \end{aligned} \tag{5.42}$$

where PBRN stands for Prompt Beam-Related Background, LBRN for Late Beam-Related Neutron Background and with

$$\sigma_i^2 = \left(\sigma_i^{\mathrm{exp}}\right)^2 + \left[\sigma_{\mathrm{BRNES}}\left(B_i^{\mathrm{PBRN}} + B_i^{\mathrm{LBRN}}\right)\right]^2, \tag{5.43}$$

$$\sigma_{\mathrm{BRNES}} = \sqrt{\frac{0.058^2}{12}} = 1.7\%, \tag{5.44}$$

$$\sigma_{\mathrm{CE}\nu\mathrm{NS}} = 13.4\% \text{ for fixed } R_n, \text{ or } 13.2\% \text{ for free } R_n, \tag{5.45}$$

$$\sigma_{\mathrm{PBRN}} = 32\%, \tag{5.46}$$

$$\sigma_{\mathrm{LBRN}} = 100\%. \tag{5.47}$$

For each energy bin i, N_i^{exp} is the experimental event number, $N_i^{\mathrm{CE}\nu\mathrm{NS}}$ is the theoretical event number that is calculated in Eq. 5.39, B_i^{PBRN} and B_i^{LBRN} are the estimated number of PBRN and LBRN background events, and σ_i is the total signal uncertainty. The Beam Related Neutron Energy Shape (BRNES) 5.8% uncertainty (σ_{BRNES}) is taken into account by distributing it over the 12 bins in an uncorrelated way. All the numbers are taken from Ref. [156]. In Eq. 5.42, $\eta_{\mathrm{CE}\nu\mathrm{NS}}$, η_{PBRN} and η_{LBRN} are nuisance parameters which quantify, respectively, the systematic uncertainty of the signal rate and the systematic uncertainty of the PBRN and LBRN background rate, with corresponding standard deviations $\sigma_{\mathrm{CE}\nu\mathrm{NS}}$, σ_{PBRN} and σ_{LBRN}. The COHERENT spectral data are shown in Fig. 5.8 (*left*) together with the best-fit histogram obtained with the CEνNS cross-section of Eq. 5.2 and the neutron form factor corresponding to the minimal neutron distribution radius $R_n = 3.45$ fm, that gives the larger CEνNS cross-section for R_n in the range of [3.45,4] fm. We obtained $(\chi^2_{\mathrm{Ar}})_{\mathrm{min}} = 8.8$ with 11 degrees of freedom, corresponding to an excellent 64% goodness of fit.

As we already mentioned, the observation of CEνNS scattering in argon can be used to probe the nuclear neutron distribution [146, 147, 147, 168, 209]. First of all, it is important to set a value for the proton distribution radius which

enters in the proton form factor in Eq. 5.3. From the experimental value of R_c in Eqs. 5.17 and 5.18, we obtain

$$R_p = 3.448 \pm 0.003\,\text{fm}\,. \tag{5.48}$$

This is the value of the rms radius R_p that we used in our calculations. Let us now consider the neutron distribution radius R_n that determines the neutron form factor $F_N(|\vec{q}|^2)$ in the cross-section in Eq. 5.2. Experimentally, the value of R_n is not known and we can get information on it from the fit of the COHERENT data. However, in our analysis it would be nonphysical to consider R_n as a completely free parameter, because it is very plausible that the neutron distribution radius is larger than the proton distribution radius R_p in Eq. 5.48, since the ^{40}Ar nucleus has 22 neutrons and only 18 protons. In order to check if this hypothesis is supported by the nuclear theory, we have calculated the proton and neutron radii with two publicly available numerical codes: the Sky3D code [210] of non-relativistic nuclear mean-field models based on Skyrme forces, and the DIRHB code [211] of relativistic self-consistent mean-field models. From the calculation of these models one can see that $R_n^{\text{point}} > R_p^{\text{point}}$ in all the nuclear models that we have considered and the excess is between 0.08 and 0.11 fm. Since

$$R_n^2 = (R_n^{\text{point}})^2 + \langle r_n^2 \rangle\,, \tag{5.49}$$

where $\langle r_n^2 \rangle^{1/2} \simeq \langle r_p^2 \rangle^{1/2}$ is the radius of the neutron (this approximation is supported by the measured value of the neutron magnetic radius $\langle r_n^2 \rangle_{\text{mag}}^{1/2} = 0.864^{+0.009}_{-0.008}$ fm [170], that is close to the measured value of the proton charge radius $\langle r_p^2 \rangle^{1/2} = 0.8414 \pm 0.0019$ fm [182]). Hence, from the nuclear model prediction $R_n^{\text{point}} \simeq R_p^{\text{point}} + 0.1$ fm we obtain the approximate relation

$$R_n \simeq R_p + 0.1\,\text{fm}\,. \tag{5.50}$$

Therefore, in our analyses of the COHERENT Argon data we consider two cases:

Fixed $\mathbf{R_n}$ where R_n is given by Eq. 5.50 with the value in Eq. 5.48 for R_p:

$$R_n = 3.55\,\text{fm}. \tag{5.51}$$

Free $\mathbf{R_n}$ where R_n is considered as a free parameter between R_p and 4 fm:

$$3.45 < R_n < 4\,\text{fm}. \tag{5.52}$$

We fitted the COHERENT data in order to determine the neutron rms radius

R_n of Ar, considering for R_n the lower bound in Eq. 5.52, without an upper bound. Fig. 5.8 (*right*) shows the comparison of $\Delta\chi^2 = \chi^2_{\rm Ar} - (\chi^2_{\rm Ar})_{\rm min}$ as a function of the rms neutron distribution radius R_n of ^{40}Ar using the three most popular form factor parameterizations: symmetrized Fermi [175], Helm [53], and Klein-Nystrand [176]. One can see that the three form factor parameterizations give practically the same result and the best fit is obtained for the minimal allowed value $R_n = 3.45\,$fm. Therefore, from the analysis of the COHERENT data we can only put the following upper bounds on the value of ^{40}Ar neutron distribution radius:

$$R_n(^{40}\mathrm{Ar}) < 4.2\,(1\sigma),\ 6.2\,(2\sigma),\ 10.2\,(3\sigma)\,\mathrm{fm}. \tag{5.53}$$

These bounds are in agreement with the nuclear model predictions cited before, which explicit calculation is reported in Tab. 1 of [157], but unfortunately they are too weak to allow us a selection of the models.

5.4.3 Combined analysis CsI+LAr

The detection of CEνNS in two different targets allows for the possibility of combining the results in order to obtain stronger constraints on the measurable parameters. For CsI the statistics is larger and the background is lower, resulting in a more precise determination of the parameters. The complementarity of LAr is due to the fact that it is very lighter compared to CsI, exploring features enhanced at low $T_{\rm nr}$. Following the approach used in Ref. [185], where the bounds on several physical quantities from the analysis of the COHERENT CsI data [144] have been improved considering the quenching factor in Ref. [212], we derive here the results for CsI considering the least-squares function

$$\begin{aligned}\chi^2_{\rm CsI} &= \sum_{i=4}^{15}\left(\frac{N_i^{\rm exp} - (1+\alpha_{\rm c})\,N_i^{\rm CE\nu NS} - (1+\beta_{\rm c})\,B_i}{\sigma_i}\right)^2 \\ &+ \left(\frac{\alpha_{\rm c}}{\sigma_{\alpha_{\rm c}}}\right)^2 + \left(\frac{\beta_{\rm c}}{\sigma_{\beta_{\rm c}}}\right)^2 + \left(\frac{\eta-1}{\sigma_\eta}\right)^2.\end{aligned} \tag{5.54}$$

For each energy bin i, $N_i^{\rm exp}$ is the experimental event number in Ref. [145], $N_i^{\rm CE\nu NS}$ is the theoretical event number, B_i is the estimated number of background events, and σ_i is the statistical uncertainty, both taken from Ref. [145]. As explained in Ref. [185], we employ only the 12 energy bins from $i = 4$ to $i = 15$ of the COHERENT spectrum, because they cover the recoil kinetic energy of the more recent Chicago-3 quenching factor measurement [212] that we use in this work. In Eq. 5.55, $\alpha_{\rm c}$ and $\beta_{\rm c}$ are nuisance parameters which

quantify, respectively, the systematic uncertainty of the signal rate and the systematic uncertainty of the background rate, with the corresponding standard deviations $\sigma_{\alpha_c} = 0.112$ and $\sigma_{\beta_c} = 0.25$ [144]. The uncertainty on the quenching factor is taken into account through a normalization factor η with σ_η= 0.051, that contributes to the least-squares function. The combined fit is performed with a least-squares function defined as the sum of the two

$$\chi^2_{\text{CsI+Ar}} = \chi^2_{\text{CsI}} + \chi^2_{\text{Ar}}. \tag{5.55}$$

5.4.3.1 Weak mixing angle measurement

The weak mixing angle is a fundamental parameter in the theory of the electroweak interactions and its experimental determination provides a direct probe of physics phenomena not included in the SM, usually referred to as new physics. In particular, low-energy determinations of ϑ_{W} offer a unique role, complementary to those at high-energy, being highly sensitive to extra Z (Z') bosons predicted in grand unified theories, technicolor models, supersymmetry and string theories [183]. This underscores the need for improved experimental determinations of ϑ_{W} in the low-energy regime.
We fitted the COHERENT CENNS-10 data in order to determine the value of $\sin^2\vartheta_{\text{W}}$ in Ar, considering R_n either fixed or free. The result for the weak mixing angle is independent on the assumption used for R_n and in both cases we get:

$$\sin^2\vartheta_{\text{W}}(\text{Ar}) = 0.31 \pm 0.06\,(1\sigma), ^{+0.11}_{-0.13}\,(2\sigma), ^{+0.18}_{-0.23}\,(3\sigma), \tag{5.56}$$

which is about 1.2σ above the SM prediction, $\sin^2\vartheta_{\text{W}}^{\text{SM}} = 0.23857(5)$ [170]. The reason of this small discrepancy is that a larger weak mixing angle increases the CEνNS cross-section and it allows a better fit of the low-energy bins of the Ar data. Given the independence of $\sin^2\vartheta_{\text{W}}$ on the value of R_n, in the following we will consider only the case with R_n fixed. Fig. 5.9 shows the comparison of $\Delta\chi^2 = \chi^2_{\text{Ar}} - (\chi^2_{\text{Ar}})_{\text{min}}$ as a function of $\sin^2\vartheta_{\text{W}}$ using the Helm parameterization for the neutron form factor.

Following again the approach used in Ref. [185], we derive here the result for the weak mixing angle also exploiting the COHERENT CsI dataset. Fixing $R_n(\text{Cs})$ and $R_n(\text{I})$ to 5.01 fm and 4.94 fm [219], respectively, we get

$$\sin^2\vartheta_{\text{W}}(\text{CsI}) = 0.24 \pm 0.04\,(1\sigma), \pm 0.09\,(2\sigma), ^{+0.13}_{-0.14}\,(3\sigma), \tag{5.57}$$

in very good agreement with the SM prediction. The corresponding $\Delta\chi^2$ is also shown in Fig. 5.9.

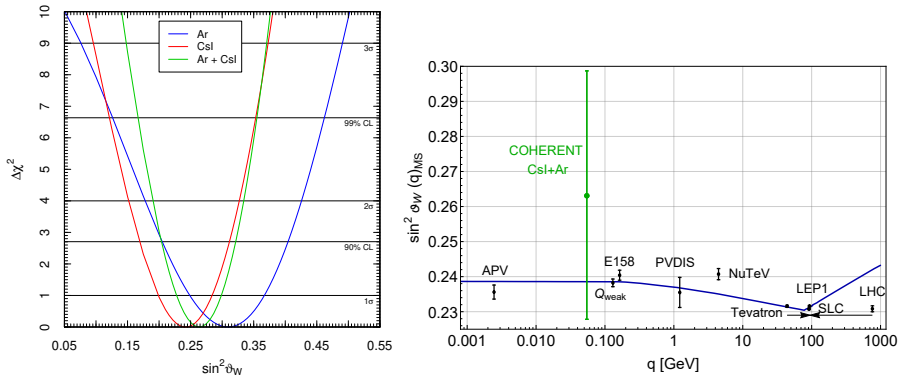

Figure 5.9: *Left:* $\Delta\chi^2 = \chi^2 - (\chi^2)_{\rm min}$ as a function $\sin^2\vartheta_{\rm W}$ obtained (blue) from the fit of the data of the Ar CENNS-10 experiment, (red) from the fit of the COHERENT CsI data and (green) from the combined fit . *Right:* Variation of $\sin^2\vartheta_{\rm W}$ with energy scale q. The SM prediction is shown as the solid curve, together with experimental determinations in black at the Z-pole [170] (Tevatron, LEP1, SLC, LHC), from APV on cesium [213, 214], which has a typical momentum transfer given by $\langle q\rangle \simeq 2.4$ MeV, Møller scattering [215] (E158), deep inelastic scattering of polarized electrons on deuterons [216] (e^2H PVDIS) and from neutrino-nucleus scattering [217] (NuTeV) and the new result from the proton's weak charge at $q = 0.158$ GeV [218] ($\rm Q_{weak}$). In green it is shown the result derived in this paper, obtained fitting the Ar and CsI COHERENT dataset. For clarity we displayed the Tevatron and LHC points horizontally to the left and to the right, respectively.

Finally, we performed a combined fit of the CsI and Ar data. The value found for the weak mixing angle is

$$\sin^2\vartheta_{\rm W}({\rm CsI}+{\rm Ar}) = 0.26^{+0.04}_{-0.03}\,(1\sigma), \pm 0.07\,(2\sigma), \pm 0.11\,(3\sigma), \tag{5.58}$$

which is slightly more precise than the CsI result alone and in agreement within 1σ with the SM prediction. Unfortunately, as it is possible to see in Fig. 5.9, the uncertainty obtained for the weak mixing angle from COHERENT is still very large when compared to the other determinations at low-momentum transfer. For the proton coupling coefficient g_V^p, we obtain

$$g_V^p(\nu_e; {\rm CsI}+{\rm Ar}) = -0.003^{+0.060}_{-0.080} \quad \text{and} \quad g_V^p(\nu_\mu; {\rm CsI}+{\rm Ar}) = -0.011^{+0.060}_{-0.080}. \tag{5.59}$$

These values differ from the SM predictions in Eqs. 5.12 and 5.13 by less than 1σ and confirm that the proton coupling is much smaller than the neutron coupling in the CEνNS process.

	Fixed R_n			Free R_n		
	1σ	2σ	3σ	1σ	2σ	3σ
			CsI			
$\langle r^2_{\nu_{ee}} \rangle$	[-55,-2]	[-67,11]	[-76,20]	[-54,1]	[-66,14]	[-76,24]
$\langle r^2_{\nu_{\mu\mu}} \rangle$	[-64,8]	[-68,8]	[-73,17]	[-64,10]	[-68,15]	[-72,20]
$\langle r^2_{\nu_{e\mu}} \rangle$	< 26	< 32	< 37	< 26	< 32	< 36
$\langle r^2_{\nu_{e\tau}} \rangle$	< 27	< 39	< 48	< 27	< 39	< 48
$\langle r^2_{\nu_{\mu\tau}} \rangle$	<36	<40	<45	<36	<40	<45
			Ar			
$\langle r^2_{\nu_{ee}} \rangle$	[-89,39]	[-98,48]	[-108,58]	[-89,38]	[-97,47]	[-107,57]
$\langle r^2_{\nu_{\mu\mu}} \rangle$	[-63,12]	[-73,22]	[-80,30]	[-63,9]	[-72,22]	[-80,29]
$\langle r^2_{\nu_{e\mu}} \rangle$	< 34	< 40	< 46	< 33	< 40	< 46
$\langle r^2_{\nu_{e\tau}} \rangle$	< 64	< 73	< 83	< 63	< 72	< 82
$\langle r^2_{\nu_{\mu\tau}} \rangle$	< 37	< 48	< 55	< 36	< 47	< 54
			CsI + Ar			
$\langle r^2_{\nu_{ee}} \rangle$	[-56,-2]	[-68,11]	[-78,22]	[-55,-4]	[-67,14]	[-77,25]
$\langle r^2_{\nu_{\mu\mu}} \rangle$	[-64,6]	[-68,12]	[-71,17]	[-64,9]	[-67,15]	[-71,19]
$\langle r^2_{\nu_{e\mu}} \rangle$	< 27	< 33	< 36	< 25	< 32	< 36
$\langle r^2_{\nu_{e\tau}} \rangle$	< 27	< 40	< 50	< 26	< 40	< 50
$\langle r^2_{\nu_{\mu\tau}} \rangle$	< 36	< 40	< 44	< 36	< 40	< 44

Table 5.2: Limits at 1σ, 2σ, and 3σ for the neutrino charge radii in units of 10^{-32} cm^2, obtained from the analysis of the COHERENT CsI and Ar data, and from the combined fit.

5.4.3.2 Neutrino charge radii measurement

In Ref. [153] the first bounds on the neutrino charge radii from the analysis of the COHERENT CsI data [144] were obtained. The bounds were improved in Ref. [185] considering the improved quenching factor in Ref. [212]. Here we present the bounds on the neutrino charge radii that we obtained from the analysis of the spectral Ar data of the COHERENT experiment [156] and those obtained with a combined fit of the CsI and Ar data. We also revise the CsI limits on the charge radii presented in Ref. [185] because they have been obtained through Eq. 5.25, that overestimates their contribution by about 10%, as discussed above.

The results of our fits for fixed and free R_n are given in Table 5.2. One can see that the bounds obtained with fixed and free R_n are similar. Therefore, our results are practically independent from the unknown value of R_n, and in the following, for simplicity, we discuss only the case of fixed R_n.

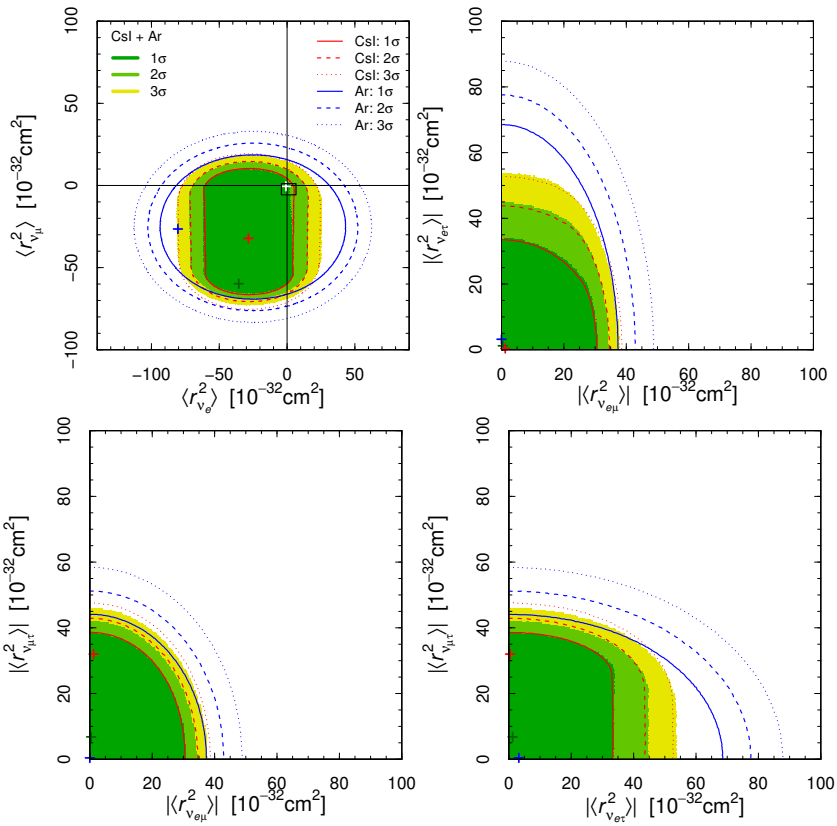

Figure 5.10: Contours of the allowed regions in different planes of the neutrino charge radii parameter space obtained with fixed R_n obtained from the analysis of COHERENT CsI data (red lines), from the analysis of COHERENT Ar data in this paper (blue lines), and from the combined fit (shaded green-yellow regions). The crosses with the corresponding colors indicate the best fit points. The white cross near the origin in the first panel indicates the Standard Model values in Eqs. 5.20 and 5.21. The black rectangle near the origin shows the 90% bounds on $\langle r^2_{\nu_e} \rangle$ and $\langle r^2_{\nu_\mu} \rangle$ obtained, respectively in the TEXONO [220] and BNL-E734 [221] experiments.

The bounds in Tab. 5.2 obtained from the COHERENT Ar data are compatible, but less stringent than those obtained from the CsI data, and the bounds of the combined fit are similar to those obtained with the CsI data only. This is illustrated by Fig. 5.10, that depicts the allowed regions in different planes of the parameter space of the neutrino charge radii. It is interesting, however, that the contribution of the argon data shrinks the allowed region in the vicinity of the Standard Model values of the diagonal charge radii given in Eqs. 5.20 and 5.21 and shown by the white cross near the origin in Fig. 5.10. In the combined fit, the point corresponding to the Standard Model values of the diagonal charge radii lies at the edge of the 1σ allowed region. The best fit of the COHERENT Ar data is obtained for relatively large values of the charge radii shown by the blue crosses in Fig. 5.10. As shown in Fig. 5.11, the resulting enhancement of the CEνNS cross-section with respect to the SM allows a better fit of the low-energy data, while the medium- and high-energy data are fitted better with a slightly lower background allowed by the uncertainties. The best-fit large values of $\langle r^2_{\nu_e} \rangle$ and $\langle r^2_{\nu_\mu} \rangle$ are, however, completely excluded by the bounds obtained by other experiments (see Table I of Ref. [153]). The black rectangle near the origin in Fig. 5.10 shows the most stringent 90% bounds on $\langle r^2_{\nu_e} \rangle$ and $\langle r^2_{\nu_\mu} \rangle$ obtained, respectively in the TEXONO [220] and BNL-E734 [221] experiments. Unfortunately the CEνNS data still do not allow us to limit the neutrino charge radii with such small precision, but it is interesting to see that they tend to favor negative values of the charge radii.

We considered also the case of absence of the neutrino transition charge radii, that is motivated by the attempt to probe the values of the neutrino charge radii in the Standard Model, where only the diagonal charge radii with the values in Eqs. 5.20 and 5.21 exist. It is also possible that the physics beyond the Standard Model generates off-diagonal neutrino charge radii that are much smaller than the diagonal charge radii and can be neglected in a first approximation. The right plot of Fig. 5.11 shows the allowed regions in the $(\langle r^2_{\nu_e} \rangle, \langle r^2_{\nu_\mu} \rangle)$ plane. One can see that the contribution of the Ar data leads to a restriction of the allowed regions. Although the combined fit tends to favor the allowed island at large negative values of $\langle r^2_{\nu_\mu} \rangle$, we cannot consider it as possible, because it lies well outside the black rectangle near the origin that shows the 90% bounds of the TEXONO [220] and BNL-E734 [221] experiments. The allowed island of the combined CsI and Ar analysis for values of $\langle r^2_{\nu_\mu} \rangle$ around zero is compatible at about 2σ with these bounds, as well as with the Standard Model values of the neutrino charge radii.

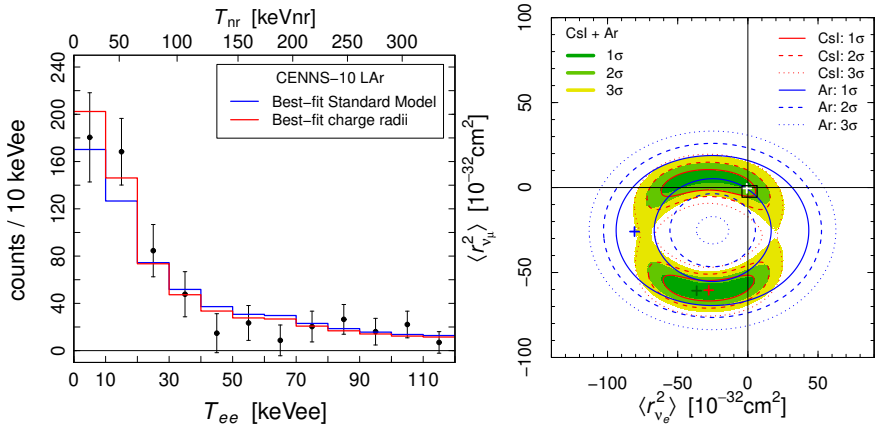

Figure 5.11: *Left:*Histogram representing the fits of the CENNS-10 data (black points with statistical error bars) with the Standard Model charge radii given in Eqs. 5.20 and 5.21 (blue histogram), and with the best-fit charge radii of the COHERENT Ar data analysis (red histogram).*Right:* Contours of the allowed regions in the $(\langle r^2_{\nu_e} \rangle, \langle r^2_{\nu_\mu} \rangle)$ plane obtained with fixed R_n obtained from the analysis of COHERENT CsI data (red lines), from the analysis of COHERENT Ar data in this paper (blue lines), and from the combined fit (shaded green-yellow regions), assuming the absence of transition charge radii. The crosses with the corresponding colors indicate the best fit points. The white cross near the origin indicates the Standard Model values in Eqs. 5.20 and 5.21. The black rectangle near the origin shows the 90% bounds on $\langle r^2_{\nu_e} \rangle$ and $\langle r^2_{\nu_\mu} \rangle$ obtained, respectively in the TEXONO [220] and BNL-E734 [221] experiments.

5.4.3.3 Neutrino electric charges measurement

In this part, we present the bounds on the neutrino electric charges that we obtained from the analysis of the spectral Ar data of the COHERENT experiment [156] and those obtained with a combined fit of the CsI and Ar data. We also revise the CsI limits on the electric charges presented in Ref. [185] because they have been obtained through an expression similar to that in Eq. 5.25 (see Eq. 30 of Ref. [185]), that overestimates their contribution by about 10%, as discussed in Sec. 5.1.3.1 for the charge radii.

There are five electric charges that can be determined with the COHERENT CEνNS data: the two diagonal electric charges $q_{\nu_{ee}}$ and $q_{\nu_{\mu\mu}}$, and the absolute values of the three transition electric charges $q_{\nu_{e\mu}} = q^*_{\nu_{\mu e}}$, $q_{\nu_{e\tau}}$, and $q_{\nu_{\mu\tau}}$.

The results of our fits for fixed and free R_n are given in Table 5.3. Since the bounds are similar in the two cases, in Figure 5.12 we show only the allowed regions in different planes of the neutrino electric charge parameter space obtained with fixed R_n.

From Tab. 5.3 and Fig. 5.12 one can see that the COHERENT Ar data allow us to

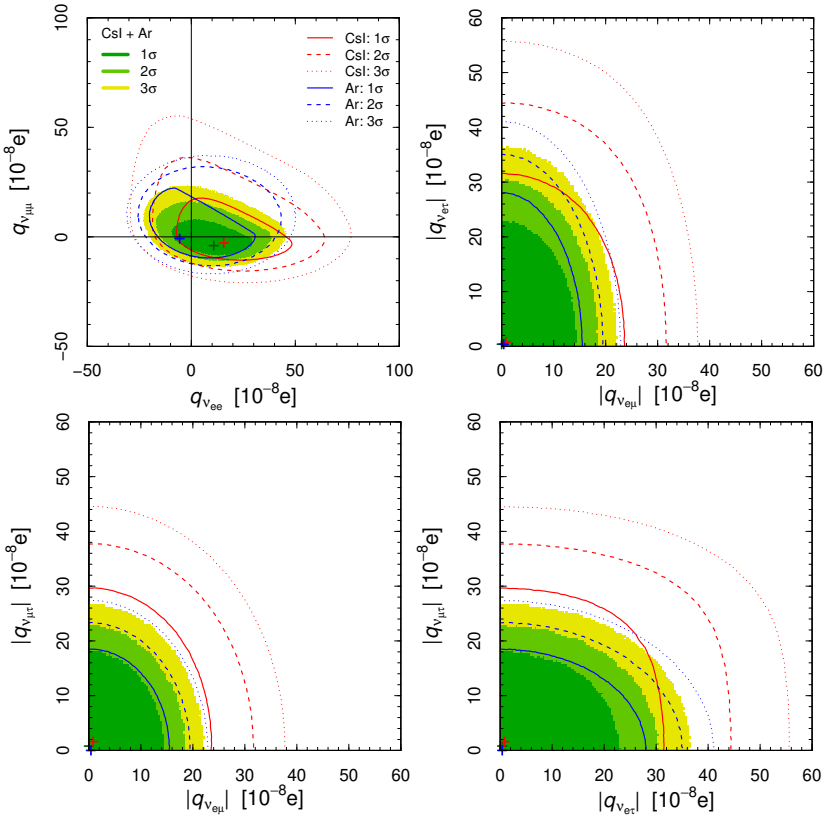

Figure 5.12: Contours of the allowed regions in different planes of the neutrino electric charge parameter space obtained with fixed R_n obtained from the analysis of COHERENT CsI data (red lines), from the analysis of COHERENT Ar data in this paper (blue lines), and from the combined fit (shaded green-yellow regions). The crosses with the corresponding colors indicate the best fit points.

	Fixed R_n			Free R_n		
	1σ	2σ	3σ	1σ	2σ	3σ
			CsI			
$q_{\nu_{ee}}$	[0,37]	[-13,57]	[-24,71]	[0,39]	[-15,57]	[-27,71]
$q_{\nu_{\mu\mu}}$	[-8,8]	[-13,27]	[-19,47]	[-8,9]	[-14,28]	[-20,47]
$\lvert q_{\nu_{e\mu}}\rvert$	< 17	< 28	< 35	< 18	< 28	< 35
$\lvert q_{\nu_{e\tau}}\rvert$	< 23	< 38	< 51	< 23	< 38	< 51
$\lvert q_{\nu_{\mu\tau}}\rvert$	< 23	< 34	< 41	< 24	< 34	< 41
			Ar			
$q_{\nu_{ee}}$	[-17,18]	[-23,38]	[-28,47]	[-16,18]	[-23,38]	[-28,47]
$q_{\nu_{\mu\mu}}$	[-8,14]	[-11,28]	[-15,35]	[-7,14]	[-11,28]	[-15,35]
$\lvert q_{\nu_{e\mu}}\rvert$	< 12	< 18	< 21	< 12	< 17	< 21
$\lvert q_{\nu_{e\tau}}\rvert$	< 22	< 32	< 38	< 21	< 32	< 38
$\lvert q_{\nu_{\mu\tau}}\rvert$	< 14	< 21	< 25	< 14	< 21	< 25
			CsI + Ar			
$q_{\nu_{ee}}$	[-4,24]	[-14,34]	[-20,42]	[-5,23]	[-14,34]	[-20,41]
$q_{\nu_{\mu\mu}}$	[-7,4]	[-10,12]	[-12,20]	[-7,3]	[-10,12]	[-13,20]
$\lvert q_{\nu_{e\mu}}\rvert$	< 11	< 17	< 20	< 11	< 16	< 20
$\lvert q_{\nu_{e\tau}}\rvert$	< 18	< 27	< 34	< 17	< 27	< 33
$\lvert q_{\nu_{\mu\tau}}\rvert$	< 14	< 20	< 25	< 14	< 20	< 24

Table 5.3: Limits at 1σ, 2σ, and 3σ for the neutrino electric charges in units of $10^{-8}\,e$, obtained from the analysis of the COHERENT CsI and Ar data, and from the combined fit.

put slightly more stringent limits on the neutrino electric charges than the CsI data, in spite of the larger uncertainties. The larger sensitivity of the Ar data to the electric charges is in contrast with the smaller sensitivity to the charge radii discussed in Section 5.1.3.1. It follows from the enhancement of the neutrino electric charge effect in CEνNS at low q^2, because of the denominator in Eq. 5.28. Since $q^2 = -2MT_{\rm nr}$, light nuclei are more sensitive than heavier ones at the neutrino electric charges for similar nuclear recoil kinetic energies $T_{\rm nr}$. The acceptance functions of both the CsI and Ar experiments have a threshold of about 5 $\mathrm{keV_{nr}}$. Since $M(^{40}\mathrm{Ar}) \simeq 37\,\mathrm{GeV}$, $M(^{133}\mathrm{Cs}) \simeq 123\,\mathrm{GeV}$, and $M(^{127}\mathrm{I}) \simeq 118\,\mathrm{GeV}$, the minimum value of $|q^2|$ can be about 3.2 times smaller in the Ar experiment than in the CsI experiment. However, this enhancement of a factor as large as 3.2 of the neutrino electric charge effect for nuclear recoil kinetic energies above the experimental threshold is mitigated by the different sizes of the energy bins: in the Ar experiment the first bin includes energies from the threshold to about 36 $\mathrm{keV_{nr}}$, whereas the CsI energy bins have a size of about 1.7 $\mathrm{keV_{nr}}$. Therefore, the enhancement of the electric charge effect occurs only in the first energy bin of the Ar experiment. Nevertheless, this enhancement is sufficient for achieving a slightly better performance of the Ar data in constraining the neutrino electric charges in spite of the larger

uncertainties, as can be seen in Table 5.3 and Figure 5.12.

The combined fit of the COHERENT CsI and Ar data leads to a significant restriction of the allowed values of the neutrino electric charges, especially the diagonal ones, because of the incomplete overlap of the CsI and Ar allowed regions that can be seen in Fig. 5.12. Although the best-fit values of $q_{\nu_{ee}}$ and $q_{\nu_{\mu\mu}}$ are visibly different from zero, the deviation is not significant, because the 1σ allowed region includes well the point $q_{\nu_{ee}} = q_{\nu_{\mu\mu}} = 0$. From Fig. 5.12, one can see that the best-fit values of the off-diagonal electric charges are close to zero and the values of the off-diagonal electric charges are well constrained.

As already noted in Ref. [185], the bounds of the order of $10^{-7}\,e$ that we obtained are not competitive with the bounds on the electron neutrino electric charges obtained in reactor neutrino experiments, that are at the level of $10^{-12}\,e$ [170, 184, 222, 223]. These limits are given in the literature for the diagonal electron neutrino charge $q_{\nu_{ee}}$, because the contribution of the off-diagonal charges was not considered. However, since the off-diagonal charges contribute to the cross-section in a quantitatively comparable way, we can consider them to be bounded at the same order of magnitude level of $10^{-12}\,e$. Therefore our bounds are not competitive with the reactor bounds for $q_{\nu_{ee}}$, $q_{\nu_{e\mu}}$, and $q_{\nu_{e\tau}}$. On the other hand, they are the only existing laboratory bounds for $q_{\nu_{\mu\mu}}$ and $q_{\nu_{\mu\tau}}$.

5.4.3.4 Neutrino magnetic moment measurement

For the analysis of neutrino magnetic moment with COHERENT data we used the least-squares function in Eq. 5.42, with the theoretical predictions $N_i^{\mathrm{CE}\nu\mathrm{NS}}$ calculated with the cross-section in Eq. 7.12. The results of the fits for fixed and free R_n are given in Tab. 5.4. Again, one can see that the bounds are robust with respect to our lack of knowledge of the value of R_n, because the bounds are similar for fixed and free R_n. For simplicity, in Figure 5.13 we show only the allowed regions in the $(|\mu_{\nu_e}|, |\mu_{\nu_\mu}|)$ plane obtained with fixed R_n.

From Fig. 5.13 one can see that the best fit of the Ar data is obtained for relatively large values of the neutrino magnetic moments. The reason is similar to that discussed in Sec. 5.1.3.1 for the neutrino charge radii: as illustrated in the left plot of Fig. 5.13, the enhancement of the CEνNS cross-section with a sizable neutrino magnetic moment contribution fits better the low-energy bins of the Ar data set than the SM cross-section and the medium- and high-energy bins are fitted better with a slightly smaller background allowed by the uncertainties. In the combined CsI and Ar analysis we find the best fit

	Fixed R_n			Free R_n		
	1σ	2σ	3σ	1σ	2σ	3σ
			CsI			
$\lvert\mu_{\nu_e}\rvert$	< 24	< 42	< 58	< 33	< 50	< 65
$\lvert\mu_{\nu_\mu}\rvert$	< 26	< 34	< 42	[3,31]	< 39	< 46
			Ar			
$\lvert\mu_{\nu_e}\rvert$	< 55	< 70	< 85	< 55	< 70	< 85
$\lvert\mu_{\nu_\mu}\rvert$	< 39	< 50	< 60	< 39	< 50	< 60
			CsI + Ar			
$\lvert\mu_{\nu_e}\rvert$	< 27	< 44	< 56	< 33	< 48	< 60
$\lvert\mu_{\nu_\mu}\rvert$	[5,27]	< 34	< 41	[12,31]	< 37	< 43

Table 5.4: Limits at 1σ, 2σ, and 3σ for the neutrino magnetic moments in units of $10^{-10}\,\mu_B$, obtained from the analysis of COHERENT CsI data in Ref. [185], from the analysis of COHERENT Ar data in this paper, and from the combined fit.

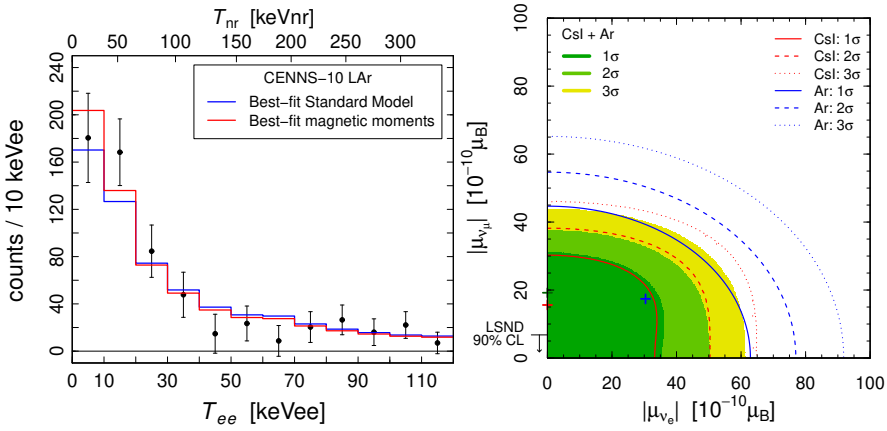

Figure 5.13: *Left:*Histograms representing the fits of the CENNS-10 data (black points with statistical error bars) with the Standard Model weak-interaction cross-section (blue histogram), and with the best-fit magnetic moment of the COHERENT Ar data analysis (red histogram). *Right:*Contours of the allowed regions in the $(|\mu_{\nu_e}|, |\mu_{\nu_\mu}|)$ plane obtained with fixed R_n obtained from the analysis of COHERENT CsI data in Ref. [185] (red lines), from the analysis of COHERENT Ar data in this paper (blue lines), and from the combined fit (shaded green-yellow regions). The crosses with the corresponding colors indicate the best fit points. The figure shows also the LSND 90% CL upper bound on $|\mu_{\nu_\mu}|$ [224].

for $|\mu_{\nu_e}| = 0$, but a best-fit value of $|\mu_{\nu_\mu}|$ that is relatively large. However, we cannot consider this as a valid indication in favor of a non-zero $|\mu_{\nu_\mu}|$ because the best-fit value is much larger than the bounds obtained in accelerator experiments with $\nu_\mu - e$ scattering (see Table IV of Ref. [184]). The most stringent of those bounds is the LSND bound $|\mu_{\nu_\mu}| < 6.8 \times 10^{-10}\ \mu_B$ at 90% CL [224] shown in the right plot of Fig. 5.13. Nevertheless, the 1σ allowed region of the combined fit is compatible with this bound, as well as with the stringent bounds on $|\mu_{\nu_e}|$ established in reactor neutrino experiments (the currently best one, $|\mu_{\nu_e}| < 2.9 \times 10^{-11}\ \mu_B$ [170, 184, 225], is not shown in Fig. 5.13 because it would not be distinguishable from the y axis).

6

BSM EXTENSION AND ELECTROWEAK PHYSICS WITH COHERENT AND APV

In the sixth chapter we present new constraints on different BSM models which predict a new light vector Z' mediator. These constraints are obtained analyzing the COHERENT LAr and CsI data, along with the combined analysis of these two datasets, using the same inputs described in the previous chapter. We also improved some of the results presented in the previous chapter by combining the new and last data taken by COHERENT with CsI and the measurement performed by atomic parity violation experiments.

Contents

Since the first observation of the coherent elastic neutrino-nucleus scattering process in cesium-iodide by the COHERENT experiment [144, 145], many intriguing physics results have been derived by a large community of physicists [146–155, 185, 226–228] on very diverse physical sectors. With the recent detection of CEνNS in a single-phase 24 kg liquid-argon scintillation detector [156] the COHERENT Collaboration has started to probe the CEνNS cross-section dependence on the square of the number of neutrons, N^2, and unrevealed a new way to test the Standard Model. Indeed, this new measurement allowed to gain additional and complementary information to the one provided by the CsI dataset on nuclear physics, neutrino properties, physics beyond the SM, and electroweak interactions [157]. Let us remind that CEνNS is a neutral current process induced by the exchange of a Z boson. It thus represents also a sensitive probe for non standard interactions (NSI) that are not included in the SM [229], induced by yet to be discovered neutral vector bosons [149], particularly if they are light.

Indeed, for sufficiently light vector mediator masses, the scattering rate grows as $1/|\vec{q}|^2$ as one goes to lower energies, so the low momentum transfer of CEνNS experiments makes them ideal laboratories for such searches. On average the momentum transfer for CEνNS is of the order of few tens of MeV, making CEνNS the perfect place to study scenarios including a new MeV-scale vector mediator. The nature of the boson depends on the details of the specific model assumed. In particular, we consider three models with different interactions of the light vector Z' mediator. The first one is the so-called universal model, in which the mediator couples universally to all the SM fermions [149, 230]. The second one is referred to as the $B - L$ model [230, 231], where the coupling of the mediator is different between quarks and leptons. Finally, the third one is the so-called $L_\mu - L_\tau$ model [232], in which the mediator only couples at tree level with SM particles of the muonic or tauonic flavor. All these models are theoretically well motivated to provide a coherent explanation to a series of emerging discrepancies in precision studies of low-energy observables. Among those, the anomalous measurement of the magnetic moment of the muon, referred to as $(g-2)_\mu$, performed by the E821 experiment at BNL [233] and more recently at FermiLab [234] represents since almost two-decades an intriguing puzzle. Indeed, the experimental value differs from the SM prediction by about 4.2σ [234, 235]. Thus, new constraints on this kind of models that incorporate new physics in the leptonic sector are very much awaited. In this context, the new COHERENT results provide a timely and stimulating opportunity to probe some of these models and improve the existing limits.

Our analyses regarding light vector have been published on JHEP in 2020 [236], so that the $(g-2)_\mu$ references presented in the plots of this chapter are obtained

to the BNL measurement.

After a fruitful discovery period, a new era of precision measurements has now begun, thanks to the new data recorded by the COHERENT experiment using a CsI target [204]. Indeed, the larger CEνNS statistics collected together with a refined quenching factor determination allow us to perform stringent tests of the Standard Model. However, in the low-energy sector, the most precise $\sin^2\vartheta_W$ measurement performed so far belongs to the so-called atomic parity violation (APV) experiment, using cesium atoms [213,237]. This latter measurement depends on the value of $R_n(^{133}\mathrm{Cs})$ that, at the time of Ref. [214], could only have been extrapolated from a compilation of antiprotonic atom x-rays data [238]. A combination of COHERENT and APV data is thus highly beneficial to determine simultaneously in a model-independent way these two fundamental parameters, keeping their correlations into account. In this chapter we determine a new measurement of the average neutron rms radius of ^{133}Cs and ^{127}I. In combination with the atomic parity violation (APV) experimental result, we derive the most precise measurement of the neutron rms radii of ^{133}Cs and ^{127}I, disentangling for the first time the contributions of the two nuclei. By exploiting these measurements we determine the corresponding neutron skin values for ^{133}Cs and ^{127}I. These results suggest a preference for models which predict large neutron skin values, as corroborated by the only other electroweak measurements of the neutron skin of ^{208}Pb performed by PREX experiments. Moreover, for the first time, we obtain a data-driven APV+COHERENT measurement of the low-energy weak mixing angle with a percent uncertainty, independent of the value of the average neutron rms radius of ^{133}Cs and ^{127}I, that is allowed to vary freely in the fit.

These very new results are the core of the paper "New insights into nuclear physics and weak mixing angle using electroweak probes", under review by APS [239].

6.1 Light vector Z' mediator in CEνNS

The SM cross-section for CEνNS interactions presented in the previous chapter is modified by the presence of a new massive vector mediator which couples to SM leptons and quarks. Considering a vector neutral-current neutrino non-standard interaction [240] and assuming that the neutrino does not change flavor, it is generically described by the effective four-fermion interaction Lagrangian (see Ref. [241] and references therein). In general, neutral-current neutrino non-standard interactions can have also axial components, but their

effect is negligible in coherent elastic scattering of neutrinos with heavy nuclei [167]. The effective neutral current NSI Largangian can be written as

$$\mathcal{L}_{\rm NSI}^{\rm NC} = -2\sqrt{2}G_{\rm F}\sum_{\ell=e,\mu}\left(\overline{\nu_{\ell L}}\gamma^{\rho}\nu_{\ell L}\right)\sum_{f=u,d}\varepsilon_{\ell\ell}^{fV}\left(\overline{f}\gamma_{\rho}f\right). \tag{6.1}$$

The parameters $\varepsilon_{\ell\ell}^{fV}$, where $f = u, d$ stands for the flavor of the quark and $\ell = e, \mu$ is the neutrino flavor[i], describe the size of non-standard interactions relative to standard neutral-current weak interactions. The full cross-section comes from coherently summing the contributions from the exchange of the SM and NSI mediators, which may interfere. In particular, the NSI mediator effectively induces an energy-dependent modification of the SM factor $Q^2_{\ell,\,\rm SM}$ in Eq. 5.2. To keep things as simple as possible, we assume that there is no $Z - Z'$ mixing and that the Z' has a purely vector interaction with the fermions of the SM, Indeed, considering the NSI scenario described before it becomes

$$Q_{\ell}^2 = \left[\left(g_V^p(\nu_\ell) + 2\varepsilon_{\ell\ell}^{uV} + \varepsilon_{\ell\ell}^{dV}\right)ZF_Z(|\vec{q}|^2) + \left(g_V^n + \varepsilon_{\ell\ell}^{uV} + 2\varepsilon_{\ell\ell}^{dV}\right)NF_N(|\vec{q}|^2)\right]^2. \tag{6.2}$$

In this paper, we focus on three simple models in which the vector neutral-current neutrino NSI is induced by a gauge boson Z' with mass $M_{Z'}$ and coupling $g_{Z'}$ associated with a new $U(1)'$ symmetry. In this scenario, the CEνNS cross-section can be determined by writing the parameter $\varepsilon_{\ell\ell}^{fV}$ in terms of the light Z' propagator as

$$\varepsilon_{\ell\ell}^{fV} = \frac{g_{Z'}^2\, Q'_{\ell} Q'_f}{\sqrt{2}G_F\left(|\vec{q}|^2 + M_{Z'}^2\right)}, \tag{6.3}$$

where Q' are the charges under the new gauge symmetry.

The first model that we consider describes a Z' boson which couples universally to all SM fermions [149, 230]. We set the charges to be $Q'_{\ell} \equiv Q'_f = 1$, and the coupling becomes the same for all the fermions. Under this model, the cross section in Eq. 5.2 becomes [149]

$$\left(\frac{d\sigma}{dT_{\rm nr}}\right)_{\rm univ}^{\nu_\ell\text{-}\mathcal{N}}(E, T_{\rm nr}) = \frac{G_F^2 M}{\pi}\left(1 - \frac{MT_{\rm nr}}{2E^2}\right)\times \left[Q_{\ell,\,\rm SM} + \frac{3(g_{Z'})^2}{\sqrt{2}G_F}\frac{ZF_Z(|\vec{q}|^2) + NF_N(|\vec{q}|^2)}{|\vec{q}|^2 + M_{Z'}^2}\right]^2. \tag{6.4}$$

The second model that we consider is the so-called $B - L$ (baryon number

[i] We consider only the first generation of quarks since they are the only ones contained in nuclei and only electronic and muonic neutrinos since they are the only species present at the SNS.

minus lepton number) extension of the SM [230, 231]. In this case the gauge charges are determined by imposing that the theory is anomaly free. In particular, in this model the boson couples universally to the quarks, as well as to the neutrinos, but with different charges, namely $Q'_\ell \neq Q'_f$. In particular, in the $B-L$ model the gauge charges are such that $Q'_\ell = 1$ and $Q'_f = -Q'_\ell/3$. Under these assumptions, the cross-section in Eq. 5.2 becomes

$$\Big(\frac{d\sigma}{dT_{\rm nr}}\Big)^{\nu_\ell\text{-}\mathcal{N}}_{\rm B-L}(E,T_{\rm nr}) = \frac{G_F^2 M}{\pi}\Big(1-\frac{MT_{\rm nr}}{2E^2}\Big)\times \Big[Q_{\ell,\,\rm SM} - \frac{(g_{Z'})^2}{\sqrt{2}G_F}\frac{ZF_Z(|\vec{q}|^2)+NF_N(|\vec{q}|^2)}{|\vec{q}|^2+M_{Z'}^2}\Big]^2. \tag{6.5}$$

The last scenario that we consider is a model with gauged $L_\mu - L_\tau$ symmetry [232]. In this case, the new Z' boson can couple directly only to muonic or tauonic flavor and there is no tree-level coupling to the quark sector. Thus, this model can be studied through the CEνNS process by considering the interaction between the new boson and quarks via kinetic loops of muons and tauons involving photons. Under these assumptions, the cross section for this process becomes [232]

$$\Big(\frac{d\sigma}{dT_{\rm nr}}\Big)^{\nu_\ell\text{-}\mathcal{N}}_{L_\mu-L_\tau}(E,T_{\rm nr}) = \frac{G_F^2 M}{\pi}\Big(1-\frac{MT_{\rm nr}}{2E^2}\Big)\times \left\{\left[g_V^p(\nu_\ell) - \frac{\alpha_{\rm EM}\,(g_{Z'})^2}{3\sqrt{2}\pi G_F}\log\Big(\frac{m_\tau^2}{m_\mu^2}\Big)\frac{1}{|\vec{q}|^2+M_{Z'}^2}\right] ZF_Z(|\vec{q}|^2) + g_V^n NF_N(|\vec{q}|^2)\right\}^2, \tag{6.6}$$

where $\alpha_{\rm EM}$ is the electromagnetic fine-structure constant and m_τ is the tau lepton mass. As visible, only protons interact with the new boson due to the presence of the photon in the loop, and only the proton coupling is modified with a term that is proportional to the electric charge. As far as the CEνNS process in COHERENT is concerned, this last model modifies only the muonic neutrino and antineutrino cross sections, leaving the electronic neutrino cross section unchanged, since there is no direct coupling to the electronic flavor. It is worth to specify that in the case of antineutrinos, the term induced by the introduction of the light vector mediator changes sign as well as the other vector couplings.

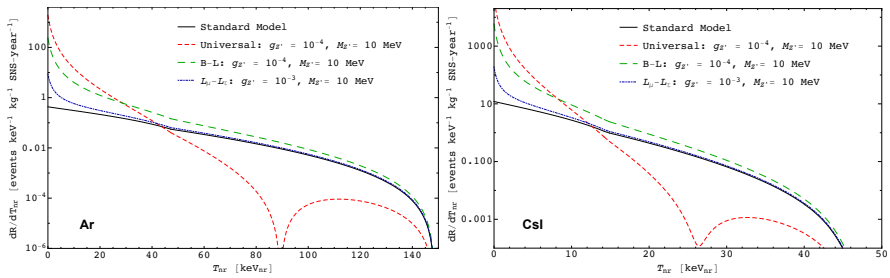

Figure 6.1: Differential predicted CEνNS event rates for Ar (*left*) and CsI (*right*) in the Standard Model (solid black), and universal (thin dashed red), $B - L$ (dashed green) and $L_\mu - L_\tau$ (dashed-dotted blue) models with $M_{Z'} = 10$ MeV and different couplings $g_{Z'}$ specified in the figure label.

6.2 Constraints on light vector mediator models

In this section we derive the constraints that can be obtained using CsI and Ar COHERENT data on the mass, $M_{Z'}$, and the coupling, $g_{Z'}$, of a light vector mediator that couples with the SM particles according to the models described in Sec. 6.1. Some of these constraints have been already derived in CsI for the universal model, see Ref. [149,151,195,226,231] and for the $L_\mu - L_\tau$ model [242]. Here we derive the limits for CsI using the more recent Chicago-3 quenching factor measurement [212], then we derive the same limits in the recently released Ar dataset and we also perform for the first time their combination.

First of all, in Fig. 6.1 we compare the SM differential CEνNS event rate for Ar (*left*) and CsI (*right*) to those obtained for the universal, $B - L$ and $L_\mu - L_\tau$ light vector mediator models. For illustrative purposes, we fixed the mass of the light vector mediator to $M_{Z'} = 10$ MeV and we use different values of the couplings $g_{Z'}$ depending on the model. The latter have been chosen close to the current lower limits determined by other experiments.

It is possible to see that all the light vector mediator models cause an increment of the differential event rate for small recoil energies, i.e., less than about 40 $\mathrm{keV_{nr}}$ for Ar and less than about 15 $\mathrm{keV_{nr}}$ for CsI, respectively. Interestingly, the universal model also shows a dip in the event rate due to the fact that in Eq. 6.4 the contribution of the light vector mediator enters with opposite sign with respect to the SM one. In CsI the cancellation between the two contributions is not perfect due to the presence of two different atomic species that compensate slightly each other.

When the experimental COHERENT response is taken into account for the

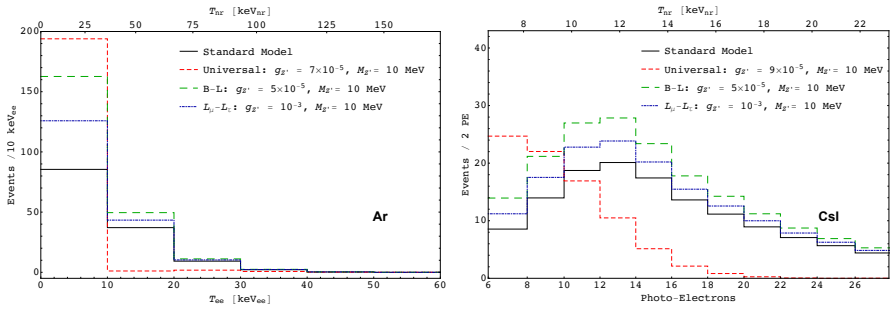

Figure 6.2: Binned experimental CEνNS event distributions for Ar (*left*) and CsI (*right*) predicted in the Standard Model (solid black), and universal (thin dashed red), $B - L$ (dashed green) and $L_\mu - L_\tau$ (dashed-dotted blue) models with $M_{Z'} = 10$ MeV and the different values of the couplings $g_{Z'}$ specified in the figure label.

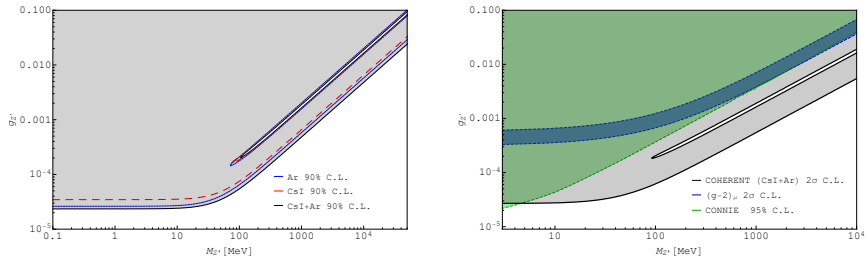

Figure 6.3: *Left*: Excluded regions in the $M_{Z'} - g_{Z'}$ plane for the universal model at 90% C.L. using COHERENT Ar (limited by the dotted blue line), CsI (limited by the dashed red) data sets and their combination (solid black-grey shaded area). *Right*: Comparison of the combined CsI+Ar COHERENT limits at 2σ C.L. with the experimental bounds at 95% C.L. from the CONNIE experiment using the Lindhard quenching factor [243] (green area) and with the $(g-2)_\mu$ 2σ region indicated by the explanation of the anomalous magnetic moment of the muon [233, 235] (blue region).

recoil energy bins, the theoretical event rates transform into the experimental spectral distributions shown in Fig. 6.2 for Ar (*left*) and CsI (*right*). The same mass but slightly different couplings of the light vector mediator for the different models as in the previous figure have been assumed for illustrative purposes.

In Fig. 6.3 we report the 90% C.L. limits obtained using Ar and CsI COHERENT data for the universal Z' model, where the grey shaded area represents the region excluded by the combination of the Ar and CsI datasets. The limits obtained from the separate Ar and CsI analyses are similar, with the Ar limit being slightly more stringent for $M_{Z'} \lesssim 100$ MeV. Note that there is a thin diagonal strip that is allowed because it corresponds to values of $g_{Z'}$ and $M_{Z'}$ for which the universal Z' cross section in Eq. 6.4 is almost degenerate with the SM cross section in Eq. 5.2 that fits well the data. This happens for values

of $M_{Z'}$ much larger than the typical momentum transfer of the order of few tens of MeV. Neglecting the $|\vec{q}|^2$ in the denominator of the Z' contribution, the small proton contribution to the SM cross section, and all the form factors, and considering $g_V^n \simeq -1/2$, we obtain the approximate degeneracy condition

$$-\frac{N}{2} + \frac{3g_{Z'}^2}{\sqrt{2}G_F}\frac{Z+N}{M_{Z'}^2} \simeq \frac{N}{2}. \tag{6.7}$$

Taking into account that $N/(Z+N)$ is about 0.55 for ^{40}Ar and about 0.58 for ^{127}I and ^{133}Cs, we can write the approximate degeneracy condition as

$$g_{Z'} \simeq 2 \times 10^{-6}\,\frac{M_{Z'}}{\text{MeV}}. \tag{6.8}$$

One can easily see that the thin diagonal allowed strip in Fig. 6.3 corresponds to this approximate relation.

In Fig. 6.3 the combined Ar and CsI result is shown at 2σ C.L. to allow a better comparison with the constraints at 95% C.L. obtained in the CONNIE reactor CEνNS experiment [243] using the Lindhard quenching factor and with the $(g-2)_\mu$ 2σ region in order to explain in this model the anomalous magnetic moment of the muon [233, 235]. As one can see, the CONNIE bound is the most stringent in the very low mass region of the mediator, namely for $M_{Z'} \lesssim 5$ MeV. In the region above, our limits obtained from the COHERENT data improve the CONNIE limits and allow us to exclude with much higher confidence level the $(g-2)_\mu$ region (the χ^2 difference with the minimum is more than 120, with two degrees of freedom, that means a practical certainty of exclusion). The high sensitivity to this model is due to the fact that the CEνNS cross section is strongly modified with respect to the SM one by the introduction of the universal Z' mediator with sufficiently large coupling, as visible in Fig. 6.1.

Let us also compare the limits that we obtain for CsI with those obtained in Ref. [226], that have been derived using the same quenching factor as in this work, but considering only the total number of events in the COHERENT CsI experiment. Comparing our Fig. 6.3 with Fig. 8 of Ref. [226], one can see the impact of performing a spectral analysis of the COHERENT data instead of using only the total event number. Indeed, in Fig. 8 of Ref. [226] the degeneracy region extends down to very low Z' masses, while the spectral information allows us to restrict it to a very narrow island only present for values of $M_{Z'}$ larger than about 100 MeV. Moreover, also the overall limit becomes more stringent by including the spectral information. A comparable behaviour was also found in Ref. [149], that similarly to us used the spectral information, but employed the constant quenching factor in the COHERENT publication [144], that has a larger uncertainty than that in Ref. [212] used

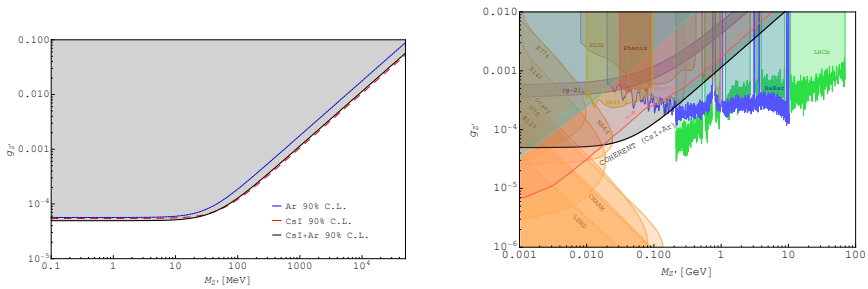

Figure 6.4: *Left*: Excluded regions in the $M_{Z'} - g_{Z'}$ plane for the $B - L$ model at 90% C.L. using the COHERENT Ar (above the dotted blue line), CsI (above the dashed red line) data sets and their combination (solid black-grey shaded area). *Right*: Comparison of the combined COHERENT CsI+Ar 90% C.L. excluded area with those obtained from the BaBar [244] (violet region), LHCb [245] (green region), KLOE [246] (brown region), Phenix [247] (dark orange region), NA48/2 [248] (yellow region), A1/MAMI in Mainz [249,250] (pink region) and different fixed target [251] (orange regions) experiments (E774 [252], E141 [253], Orsay [254], U70 [255], E137 [256], CHARM [257] and LSND [258]). The area excluded by neutrino-electron scattering experiments [259] (red region) is also indicated. The $(g-2)_\mu$ 90% C.L. region needed to explain the anomalous magnetic moment of the muon [233,235] (purple region) and the $(g-2)_\mathrm{e}$ 90% C.L. limit [260] (cyan line) from the searches of an anomalous magnetic moment of the electron are also shown.

by ourselves. Comparing our Fig. 6.3 to Fig. 2 of Ref. [149], one can see that our limits are much more stringent (for example, for $M_{Z'} \lesssim 10\,\mathrm{MeV}$, we obtain $g_{Z'} \gtrsim 3\times10^{-5}$ at 2σ, whereas the 2σ limit in Ref. [149] is $g_{Z'} \gtrsim 6\times10^{-5}$).

In Fig. 6.4 we show the 90% C.L. limits obtained using the Ar and CsI COHERENT data for the $B-L$ Z' model, together with their combination. In this case, the CsI limit is more stringent than that obtained with Ar for $M_{Z'} \gtrsim 10$ MeV and dominates the combined bound. The combination of the two data sets produces only a slight improvement of the separate limits for $M_{Z'} \lesssim 10$ MeV. In Fig. 6.4 the combined CsI and Ar bound is shown together with the regions excluded at 90% C.L. obtained by interpreting the BaBar [244] and LHCb [245] dark photon constraints in terms of the $B-L$ Z' model [261]. Moreover, the regions excluded at 90% C.L. by KLOE [246], Phenix [247], NA48/2 [248], Mainz [249,250] are also indicated. The areas excluded at 90% C.L. by fixed target experiments [251] (E774 [252], E141 [253], Orsay [254], U70 [255], E137 [256], CHARM [257] and LSND [258]) are also shown. The area excluded by neutrino-electron scattering experiments [259] is also indicated. For completeness, also the $(g-2)_\mu$ 90% C.L. region needed to explain the anomalous magnetic moment of the muon [233, 235] and the $(g-2)_\mathrm{e}$ 90% C.L. limit [260] from the searches of an anomalous magnetic moment of the electron are depicted. The COHERENT limit obtained in this work allows us to improve the coverage between accelerator and fixed target experiment

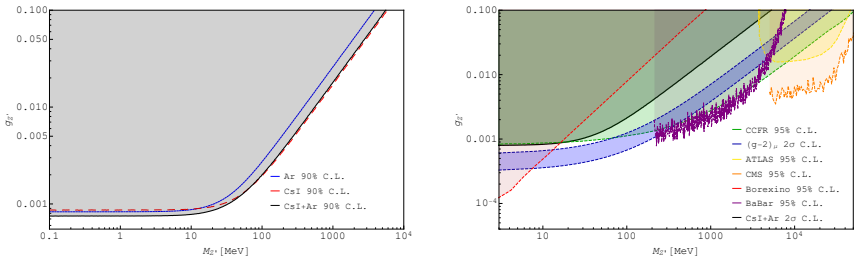

Figure 6.5: *Left*: Excluded regions in the $M_{Z'} - g_{Z'}$ plane for the $L_\mu - L_\tau$ model at 90% C.L. using COHERENT Ar (above the dotted blue line) and CsI (above the dashed red) data sets, and their combination (solid black-grey shaded area). *Right*: Comparison of the combined COHERENT CsI and Ar bound at 2σ with the existing experimental bounds at 95% C.L. from the CCFR experiment [263] (green area) and from LHC searches in ATLAS [264, 265] (yellow area) and CMS [266] (orange area), and the rescaled bounds at 95% C.L. from the BaBar [267] (purple area) and the Borexino [232, 251, 268, 269] (red area) experiments. The $(g-2)_\mu$ 2σ region needed to explain the anomalous magnetic moment of the muon [233, 235] (blue region) is also shown.

limits.

Our limits for the $B - L$ Z' model are similar to those obtained in Ref. [262], that have been derived using only the total number of events. In particular, it is difficult to compare our analysis of the COHERENT Ar dataset with that in Ref. [262], that used the fitted number of CEνNS events derived by the COHERENT Collaboration [156] instead of the experimental data.

Finally, in Fig. 6.5 we report the the 90% C.L. limits obtained using the Ar and CsI COHERENT data for the $L_\mu - L_\tau$ Z' model and the combined bound. In this framework, as in the $B - L$ Z' case, the CsI limit is more stringent than that obtained with Ar for $M_{Z'} \gtrsim 10$ MeV and dominates the combined bound. However, the combination of the two data sets allows us to improve the separate limits for $M_{Z'} \lesssim 10$ MeV slightly more than in the $B - L$ Z' case. In Fig. 6.5 the combined CsI and Ar bound is shown together with the constraints at 95% C.L. obtained with the CCFR measurement [263] of the neutrino trident cross section, with the search of SM Z boson decay to four leptons in ATLAS [264, 265] and CMS [266] reinterpreted under the hypothesis $Z \to Z'\mu\mu$ and with the search for $e^+e^- \to \mu^+\mu^- Z'$, $Z' \to \mu^+\mu^-$ from BaBar [267]. The constraints at 90% C.L. for the Borexino [232,251,268,269] experiment and the $(g-2)_\mu$ 2σ band, related to the anomalous magnetic moment of the muon [233, 235], are also shown. For the $L_\mu - L_\tau$ model, the present COHERENT dataset is unfortunately unable to improve the current existing limits and it is not sensitive to the $(g-2)_\mu$ band, most of which is already excluded by other data, except for $10 \lesssim M_{Z'} \lesssim 400$ MeV. However, the shape of the COHERENT combined CsI and Ar bound shows good potentiality

to extend the sensitivity in the region $10 \lesssim M_{Z'} \lesssim 400$ MeV when further data now being collected by the COHERENT experiment will be released.

Our results for the $L_\mu - L_\tau$ Z' model are more stringent than those obtained recently in Ref. [270] by fitting the number of CEνNS events obtained by the COHERENT Collaboration from the fit of the data [156]. Since this is not a real fit of the COHERENT data, the result is questionable.

The results discussed in this part of the thesis have been published on JHEP in the paper in Ref. [236].

6.3 COHERENT+APV analysis

In this section, we present improved measurements of the average neutron rms radius of ^{133}Cs and ^{127}I obtained analyzing the updated COHERENT CsI data [204]. In combination with the APV experimental result, we derive the most precise measurement of R_n of ^{133}Cs and ^{127}I, disentangling for the first time the contributions of the two nuclei. Moreover, for the first time, we obtain a data-driven measurement of the low-energy weak mixing angle with a percent uncertainty, independent of the value of the average neutron rms radius of ^{133}Cs and ^{127}I (that is allowed to vary freely in the analysis), from a simultaneous fit of the COHERENT and APV experimental results.

6.3.1 COHERENT 2020 results with CsI

At the conference "Magnificent CEνNS 2020" two talks regarding the new results of COHERENT with CsI have been given [204,271]. A big experimental work has been done in order to reduce some systematic uncertainties affecting the first detection of CEνNS, namely the prediction of the quenching factor for CsI, the light yield determination, and, even though with lower impact, a little improvement on the efficiency contribution. The overall systematic uncertainty dropped from 28% (2017) to 13% (2020), along with the reduction of the statistical error from $\sim 17\%$ to $\sim 11\%$ due to the increased sample size.

Taking into account the improvements in this new data-set we calculate the CEνNS event number $N_i^{\rm CE\nu NS}$ in each nuclear recoil energy bin i with

$$N_i^{\rm CE\nu NS} = N_{\rm CsI} \int_{T_{\rm nr}^i}^{T_{\rm nr}^{i+1}} dT_{\rm nr}\, A(T_{\rm nr}) \times \int_0^{T_{\rm nr}^{\prime \rm max}} dT'_{\rm nr}\, R(T_{\rm nr}, T'_{\rm nr}) \times \int_{E_{\rm min}(T'_{\rm nr})}^{E_{\rm max}} dE \sum_{\nu=\nu_e,\nu_\mu,\overline{\nu}_\mu} \frac{dN_\nu}{dE}(E)\, \frac{d\sigma_{\nu\text{-CsI}}}{dT'_{\rm nr}}(E, T'_{\rm nr}), \tag{6.9}$$

where $T_{\rm nr}$ is the reconstructed nuclear recoil energy, $A(T_{\rm nr})$ is the energy-dependent detector efficiency, $T_{\rm nr}^{\prime \rm max} = 2E_{\rm max}^2/M$, $E_{\rm max} = m_\mu/2 \sim 52.8$ MeV, m_μ being the muon mass, $E_{\rm min}(T'_{\rm nr}) = \sqrt{MT'_{\rm nr}/2}$, dN_ν/dE is the neutrino flux integrated over the experiment lifetime and $N_{\rm CsI}$ is the number of ^{133}Cs and ^{127}I atoms in the detector. The latter is given by $N_{\rm A}\, M_{\rm det}/M_{\rm CsI}$, where $N_{\rm A}$ is the Avogadro number, $M_{\rm det}$ is the detector active mass equal to 14.6 kg and $M_{\rm CsI}$ is the molar mass of CsI. The neutrino flux from the spallation neutron source, dN_ν/dE, is given by the sum of the prompt ν_μ component and the delayed ν_e and $\bar{\nu}_\mu$ components, considering 8.48×10^{-2} as the number of neutrinos per flavor that are produced for each proton-on-target. A number of POT equal to 3.20×10^{23} and a distance of 19.3 m between the source and the COHERENT detector are used. The energy resolution function, $R(T_{\rm nr}, T'_{\rm nr})$, is parametrized in terms of the number of photoelectrons following Ref. [271]

$$R(N_{\rm PE}, N'_{\rm PE}) = \frac{[a_R(1+b_R)]^{1+b_R}}{\Gamma(1+b_R)} N_{\rm PE}^{b_R} e^{-a_R(1+b_R)N_{\rm PE}}, \tag{6.10}$$

where $a_R = 1/N'_{\rm PE}$ and $b_R = 0.7157 N'_{\rm PE}$. The number of PE is related to the nuclear recoil kinetic energy thanks to the light yield $13.348\, N_{\rm PE}$/keV [271] and the quenching factor, $f_{\rm Q}(T_{\rm nr})$, that is parametrized as a fourth order polynomial as in Ref. [271].

In order to exploit also the arrival time information, we calculate the CEνNS event number, $N_{ij}^{\rm CE\nu NS}$, in each nuclear recoil energy bin i and time interval j with

$$N_{ij}^{\rm CE\nu NS} = (N_i^{\rm CE\nu NS})_{\nu_\mu} P_j^{(\nu_\mu)} + (N_i^{\rm CE\nu NS})_{\nu_e,\bar{\nu}_\mu} P_j^{(\nu_e,\bar{\nu}_\mu)}, \tag{6.11}$$

where $P_j^{(\nu_\mu)}$ and $P_j^{(\nu_e,\bar{\nu}_\mu)}$ are obtained by integrating the arrival time distributions in the corresponding time intervals with the time-dependent efficiency function [204, 271]. Using the SM inputs, the experimental values of $R_p(^{133}\text{Cs}) = 4.821 \pm 0.005$ fm and $R_p(^{127}\text{I}) = 4.766 \pm 0.008$ fm and the expected values of $R_n^{\rm EFT}(^{133}\text{Cs}) \simeq 5.09$ fm and $R_n^{\rm EFT}(^{127}\text{I}) \simeq 5.03$ fm [272], the total number of predicted events is found to be $N^{\rm CE\nu NS} = 311.8$.

The analysis of COHERENT data is performed in each nuclear recoil energy bin i and time interval j with the least-squares function

$$\chi^2_{\rm C} = \sum_{i=2}^{9}\sum_{j=1}^{11}\left(\frac{N_{ij}^{\rm exp} - \sum_{z=1}^{3}(1+\eta_z)N_{ij}^{z}}{\sigma_{ij}}\right)^2 + \sum_{z=1}^{3}\left(\frac{\eta_z}{\sigma_z}\right)^2, \tag{6.12}$$

where $z = 1, 2, 3$ stands for CEνNS, Beam-Related Neutron (BRN) and Steady-State (SS) backgrounds. $N_{ij}^{\rm exp}$ is the experimental event number, $N_{ij}^{\rm CE\nu NS}$ is the predicted number of CEνNS events, described in Eqs. 6.11 and 6.9, $N_{ij}^{\rm BRN}$ and $N_{ij}^{\rm SS}$ are the estimated number of BRN and SS background events, respectively, and σ_{ij} is the statistical uncertainty, all taken from Ref. [204]. We omitted the first energy bin because its value and uncertainty cannot be obtained from Ref. [204]. In any case, its contribution is negligible, because of the very low efficiency. The uncertainties of the η_z nuisance parameters, which quantify the systematic uncertainty of the signal rate, of the BRN and of the SS background rates, are $\sigma_{\rm CE\nu NS} = 13\%$, $\sigma_{\rm BRN} = 0.9\%$ and $\sigma_{\rm SS} = 3\%$ [204].

We fitted the COHERENT CsI data to get information on the average neutron rms radius of ^{133}Cs and ^{127}I, $R_n({\rm CsI})$, obtaining[ii]

$$R_n({\rm CsI}) = 5.55 \pm 0.44\,{\rm fm}. \tag{6.13}$$

This result is almost a factor of 2.5 more precise than previous determinations [146] using the 2017 COHERENT dataset [144, 145]. The average of the EFT expected values $R_n^{\rm EFT}({\rm CsI}) \simeq 5.06\,{\rm fm}$, is compatible with the determination in Eq. 6.13 at 1.1σ.

6.3.2 Atomic Parity Violation

The COHERENT data do not allow us to disentangle the contributions of the two nuclei, but only to constrain their average. A separation of the two contributions can be achieved in combination with the low-energy measurement of the weak charge, Q_W, of ^{133}Cs in APV experiments, also known as parity nonconservation (PNC) experiments. PNC interaction mixes S states with P states. In cesium, this feature allows for the transition 6S→7S between Zeeman sub-levels [273]. The probability of the effect is related to the weak mixing

[ii] We considered also a fit with equal ^{133}Cs and ^{127}I neutron skins, which gave the almost equivalent result $R_n({\rm Cs}) = 5.56^{+0.45}_{-0.43}$ fm and $R_n({\rm I}) = 5.51^{+0.45}_{-0.43}$ fm.

angle through the relation

$$Q_W^{\rm th}(\sin^2\vartheta_W) = -2[Z(g_{AV}^{ep}(\sin^2\vartheta_W) + 0.00005) + N(g_{AV}^{en} + 0.00006)]\left(1 - \frac{\alpha}{2\pi}\right), \tag{6.14}$$

where α is the fine-structure constant and the couplings of electrons to nucleons, g_{AV}^{ep} and g_{AV}^{en}, using $\sin^2\vartheta_W^{\rm SM}$ and taking into account radiative corrections in the SM [169, 274, 275], are given by

$$g_{AV,\rm SM}^{ep} = 2g_{AV,\rm SM}^{eu} + g_{AV,\rm SM}^{ed} = -0.0357, \tag{6.15}$$

$$g_{AV,\rm SM}^{en} = g_{AV,\rm SM}^{eu} + 2g_{AV,\rm SM}^{ed} = 0.495, \tag{6.16}$$

where $g_{AV,\rm SM}^{eu} = -0.1888$ and $g_{AV,\rm SM}^{ed} = 0.3419$. In App. A.1 the details on the radiative correction are explained. These values give$Q_W^{\rm SM} = -73.23 \pm 0.01$. Experimentally, the weak charge of a nucleus is extracted from the ratio of the parity violating amplitude, $E_{\rm PNC}$, to the Stark vector transition polarizability, β, and by calculating theoretically $E_{\rm PNC}$ in terms of

$$Q_W = N\left(\frac{{\rm Im}\, E_{\rm PNC}}{\beta}\right)_{\rm exp.}\left(\frac{Q_W}{N\,{\rm Im}\, E_{\rm PNC}}\right)_{\rm th.}\beta_{\rm exp.+th.}\,, \tag{6.17}$$

where $\beta_{\rm exp.+th}$ and $({\rm Im}\, E_{\rm PNC})_{\rm th.}$ are determined from atomic theory, and Im stands for imaginary part [274]. We use $({\rm Im}\, E_{\rm PNC}/\beta)_{\rm exp} = (-3.0967 \pm 0.0107) \times 10^{-13}|e|/a_B^2$ [274], where a_B is the Bohr radius and $|e|$ is the absolute value of the electric charge, and $\beta_{\rm exp.+th.} = (27.064 \pm 0.033)\, a_B^3$ [274]. For the imaginary part of $E_{\rm PNC}$ we use $({\rm Im}\, E_{\rm PNC})_{\rm th.}^{\rm w.n.s.} = (0.8995 \pm 0.0040) \times 10^{-11}|e|a_B\frac{Q_W}{N}$ [214], where we subtracted the correction called "neutron skin", introduced in Ref. [276] to take into account the difference between R_n and R_p that is not considered in the nominal atomic theory derivation. Here we remove this correction in order to be able to directly evaluate R_n from a combined fit with the COHERENT data. The neutron skin corrected value of the weak charge, $Q_W^{\rm n.s.}(R_n)$, is thus retrieved by summing to $({\rm Im}\, E_{\rm PNC})_{\rm th.}^{\rm w.n.s.}$ the correcting term $\delta E_{\rm PNC}^{\rm n.s.}(R_n) = [(N/Q_W)\,(1 - (q_n(R_n)/q_p))\, E_{\rm PNC}^{\rm w.n.s.}]$ [185, 277, 278]. The factors q_p and q_n incorporate the radial dependence of the electron axial transition matrix element by considering the proton and the neutron spatial distribution, respectively [277, 279–282]. Our calculation of q_p and q_n is explained in details in App. A.2.

6.3.3 Updates on nuclear physics and electroweak theory

We performed the combined APV and COHERENT analysis with the least-squares function

$$\chi^2 = \chi^2_{\rm C} + \left(\frac{Q_W^{\rm Cs\,n.s.}(R_n) - Q_W^{\rm th}(\sin^2\vartheta_W)}{\sigma_{\rm APV}(R_n, \sin^2\vartheta_W)} \right)^2 , \tag{6.18}$$

where the first term is defined in Eq. 6.12 and the second term represents the contribution of the APV measurement, where $\sigma_{\rm APV}$ is the total uncertainty. Considering that COHERENT data depends separately on $R_n(^{133}{\rm Cs})$ and $R_n(^{127}{\rm I})$, while APV depends only on $R_n(^{133}{\rm Cs})$, we disentangle for the first time the two nuclear contributions. Assuming $\sin^2\vartheta_W = \sin^2\vartheta_W^{\rm SM}$, we obtained

$$R_n(^{133}{\rm Cs}) = 5.27^{+0.33}_{-0.33}\,{\rm fm}\,,\; R_n(^{127}{\rm I}) = 5.9^{+1.0}_{-0.9}\,{\rm fm}. \tag{6.19}$$

The contours at different confidence levels (C.L.) of the allowed regions in the plane of $R_n(^{133}{\rm Cs})$ and $R_n(^{127}{\rm I})$ are shown in Figure 6.6, from which one can see that EFT expected values $R_n^{\rm EFT}(^{133}{\rm Cs}) \simeq 5.09\,{\rm fm}$ and $R_n^{\rm EFT}(^{127}{\rm I}) \simeq 5.03\,{\rm fm}$ lie in the 1σ allowed region. Thanks to the combination with APV, $R_n(^{133}{\rm Cs})$ is well constrained and practically uncorrelated with $R_n(^{127}{\rm I})$. The value in Eq. 6.19 represents the most precise determination of $R_n(^{133}{\rm Cs})$ and implies a value of the neutron skin

$$\Delta R_{np}(^{133}{\rm Cs}) = R_n(^{133}{\rm Cs}) - R_p(^{133}{\rm Cs}) = 0.45^{+0.33}_{-0.33}\,{\rm fm}, \tag{6.20}$$

that tends to be larger than those predicted by nuclear models. This value can be translated in terms of the proton and neutron point radii to allow a direct comparison with $\Delta R_{np}^{\rm point}$ measured with parity-violating electron scattering on ^{208}Pb in the PREX experiments [181, 283–285]. The comparison is shown in Figure 6.7, together with the neutron skin predictions that have been obtained with nonrelativistic Skyrme-Hartree-Fock models (red circles) and relativistic mean-field models (blue squares). A clear model-independent linear correlation is present between the neutron skin of ^{208}Pb and ^{133}Cs within the nonrelativistic and relativistic models with different interactions. This has been already discussed in the literature [286–290], but here for the first time we are able to compare different experimental determinations of the neutron skin of two nuclei obtained exploiting three electroweak processes, namely atomic parity violation, CEνNS, and parity-violating electron scattering. The combination of the precise PREX results with the unique determination of $\Delta R_{np}(^{133}{\rm Cs})$ from APV and COHERENT prefers models that predict large

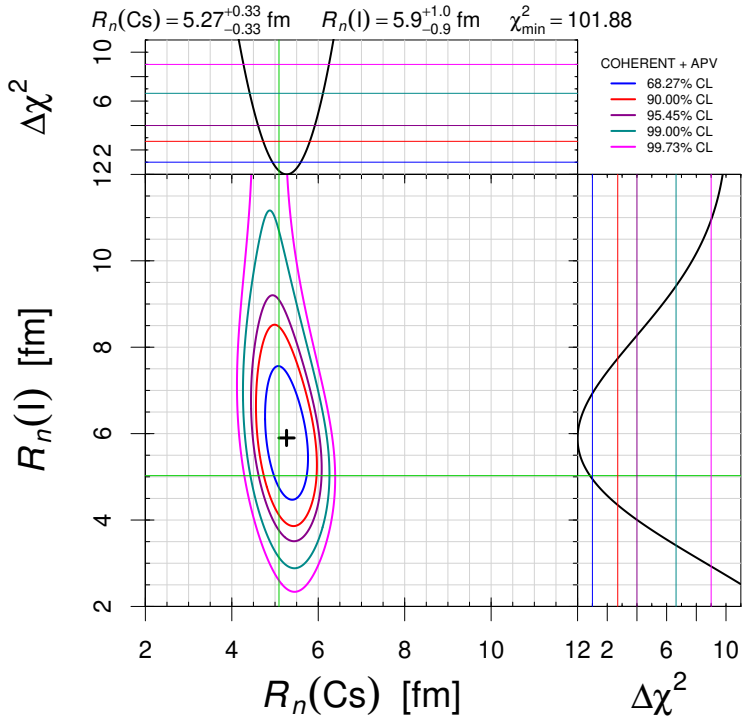

Figure 6.6: Contours at different C.L. of the allowed regions in the plane of $R_n(^{133}\mathrm{Cs})$ and $R_n(^{127}\mathrm{I})$, together with their marginalizations, obtained from the combined fit of the COHERENT and APV data. The green lines indicate the EFT expected values $R_n^{\mathrm{EFT}}(^{133}\mathrm{Cs}) \simeq 5.09\,\mathrm{fm}$ and $R_n^{\mathrm{EFT}}(^{127}\mathrm{I}) \simeq 5.03\,\mathrm{fm}$.

neutron skins. The neutron skin of a neutron-rich nucleus is the result of the competition between the Coulomb repulsion between the protons, the surface tension, that decreases when the excess neutrons are pushed to the surface, and the symmetry energy [291]. The latter reflects the variation in binding energy of the nucleons as a function of the neutron to proton ratio. Its density dependence, that is a fundamental ingredient of the EOS, is expressed in terms of the slope parameter, L, that depends on the derivative of the symmetry energy with respect to density at saturation. Theoretical calculations show a strong correlation [292–295] between ΔR_{np} and L, namely larger neutron skins translate into larger values of L. Thus, an experimental measurement of ΔR_{np} represents the most reliable way to determine L, which in turn provides critical inputs to a wide range of problems in physics. Among others, it would greatly improve the modeling of matter inside the cores of neutron stars [160, 161], despite a difference in size with the nucleus of 18 orders of magnitude. Specifically, given that L is directly proportional to the pressure of pure neutron matter at saturation density, larger values of ΔR_{np} imply a larger size of neutron stars [296]. In Fig. 6.7 we indicated the lower

limit for L suggested by the combined COHERENT and APV result, namely $L > 38.5$ MeV. Interestingly, these findings are not in contrast with laboratory experiments or astrophysical observations [290,297,298]. Indeed, our bound is compatible with the constraints on the slope parameter L derived in Ref. [299, 300] from a combined analysis of a variety of experimental and theoretical approaches, comprising heavy ion collisions [301], neutron skin-thickness of tin isotopes [302], giant dipole resonances [303], the dipole polarizability of ^{208}Pb [304,305], and nuclear masses [306]. All these constraints indicate an allowed region of L corresponding to $40 \lesssim L \lesssim 65$. However, the central value of the averaged PREX result as well as of the combined COHERENT and APV determination presented in this paper suggest rather large neutron skin-thicknesses that would imply a fairly stiff EOS at the typical densities found in atomic nuclei. This finding is in contrast with the current understanding of the neutron star parameters coming from the observation of gravitational waves from GW170817 [307, 308]. If both are correct, it would imply the softening of the EOS at intermediate densities, followed by a stiffening at higher densities [297], that may be indicative of a phase transition in the stellar core [309].

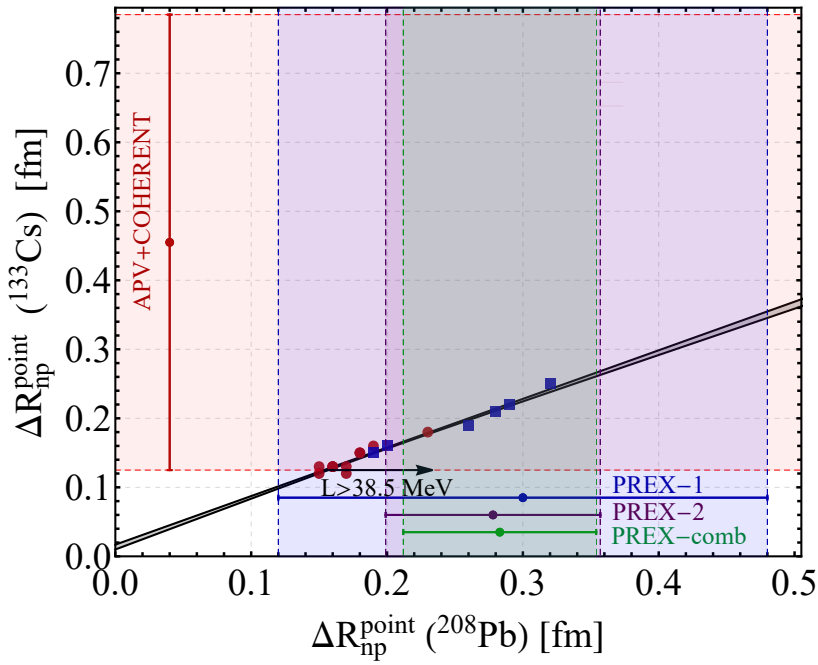

Figure 6.7: Point neutron skin predictions for ^{208}Pb and ^{133}Cs according to different models (blue squares and red circles, see text for details). Constraints set by PREX-1 [181,283], PREX-2 and their combination [284,285] and the constraint derived in this work using COHERENT+APV data are also shown by the blue, purple, green, and light red bands, respectively.

For completeness, using the result in Eq. 6.19 we are also able to measure for the first time the neutron skin of ^{127}I, $\Delta R_{np}(^{127}\mathrm{I}) = 1.1^{+1}_{-0.9}$ fm, even though with large uncertainty.

Finally, leaving $\sin^2\vartheta_W$ free to vary in the χ^2 in Eq. 6.18 and assuming that $R_n(^{133}\mathrm{Cs}) \simeq R_n(^{127}\mathrm{I}) \simeq R_n(\mathrm{CsI})$, it is possible to constrain simultaneously R_n and $\sin^2\vartheta_W$. We obtained[iii]

$$R_n(\mathrm{CsI}) = 5.60^{+0.47}_{-0.50}\,\mathrm{fm},\ \sin^2\vartheta_W = 0.2406 \pm 0.0035. \tag{6.21}$$

The choice to fit the average radius is motivated by the similar nuclear structure of the Cs and I nuclei. It is important to specify that the same value of $\sin^2\vartheta_W$ is used for APV and COHERENT, since both experiments work at a low-energy scale, where the SM prediction for the running of $\sin^2\vartheta_W$ is constant. The contours at different C.L. in the plane of $R_n(\mathrm{CsI})$ and $\sin^2\vartheta_W$ are shown in Figure 6.8. One can see that the EFT expected value for $R_n(\mathrm{CsI})$ and the SM value of $\sin^2\vartheta_W$ lie in the 1σ allowed region. The inclusion of the experimental input of $R_n(\mathrm{CsI})$ has the effect of shifting the measurement of $\sin^2\vartheta_W$ towards larger values with respect to the Particle Data Group (PDG) APV value $\sin^2\vartheta_W^{\mathrm{PDG}} = 0.2367 \pm 0.0018$ [274], while keeping the uncertainty at the percent level. Our result is depicted by the red data point in Figure 6.9, where a summary of the weak mixing angle measurements as a function of the energy scale μ is shown along with the SM predicted running calculated in the $\overline{\mathrm{MS}}$ scheme [170, 310, 311]. It is important to remark that, before this paper, the value of $R_n(^{133}\mathrm{Cs})$ used in the APV result was extrapolated from hadronic experiments using antiprotonic atoms [238], that are known to be affected, unlike electroweak measurements, by considerable model dependencies and uncontrolled approximations that may be underestimated in the nuclear uncertainty [312]. Among others, antiprotonic atoms test the neutron distribution in the nuclear periphery, where the density drops exponentially, under the strong assumption that a two-parameter Fermi distribution can be safely used to extrapolate the information on the nuclear interior. Thus, it is legit to question if the uncertainty of the official APV result is realistic. On the contrary, the measurement of $\sin^2\vartheta_{\mathrm{W}}$ presented in this paper in Eq. 6.21 keeps into account the correlation with the value of R_n determined simultaneously using two electroweak probes, that are known to be practically model independent. In this regard, the precise determination of R_n for different nuclei from electroweak measurements, as shown in this paper in Eq. 6.19 for ^{133}Cs, provides a valuable benchmark to calibrate the result of experiments involving hadronic probes, that are fundamental to map the large neutron skins of

[iii] Considering a fit with equal ^{133}Cs and ^{127}I neutron skins, we obtained the almost equivalent result $R_n(\mathrm{Cs}) = 5.63^{+0.47}_{-0.50}$ fm, $R_n(\mathrm{I}) = 5.58^{+0.47}_{-0.50}$ fm, and $\sin^2\vartheta_W = 0.2407 \pm 0.0035$.

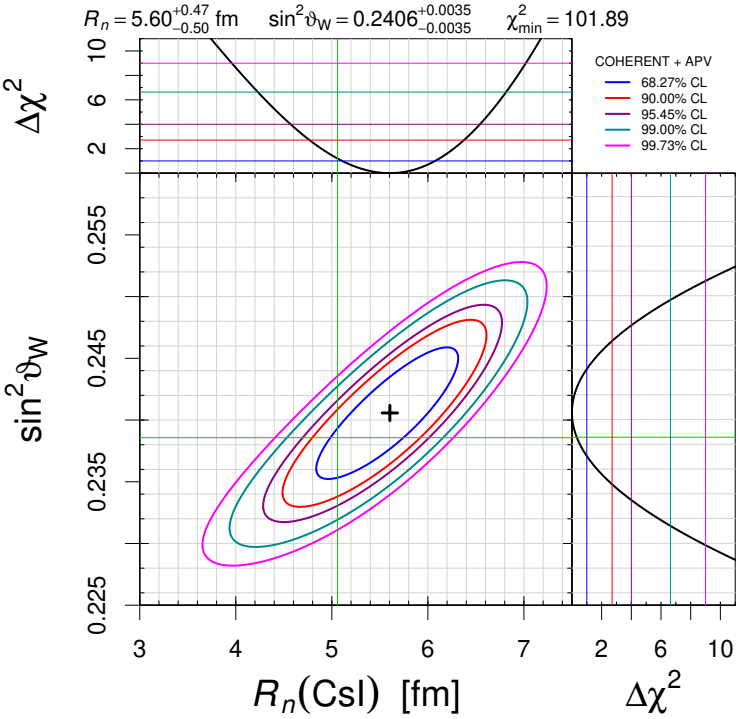

Figure 6.8: Contours at different C.L. of the allowed regions in the plane of $R_n(^{133}\mathrm{Cs})$ and $\sin^2\vartheta_W$, together with their marginalizations, obtained from the combined fit of the COHERENT and APV data. The green lines indicate the average of the EFT expected values in Eq. **??**, $R_n^{\mathrm{EFT}}(\mathrm{CsI}) \simeq 5.06\,\mathrm{fm}$, and $\sin^2\vartheta_W = \sin^2\vartheta_W^{\mathrm{SM}} \simeq 0.23857$.

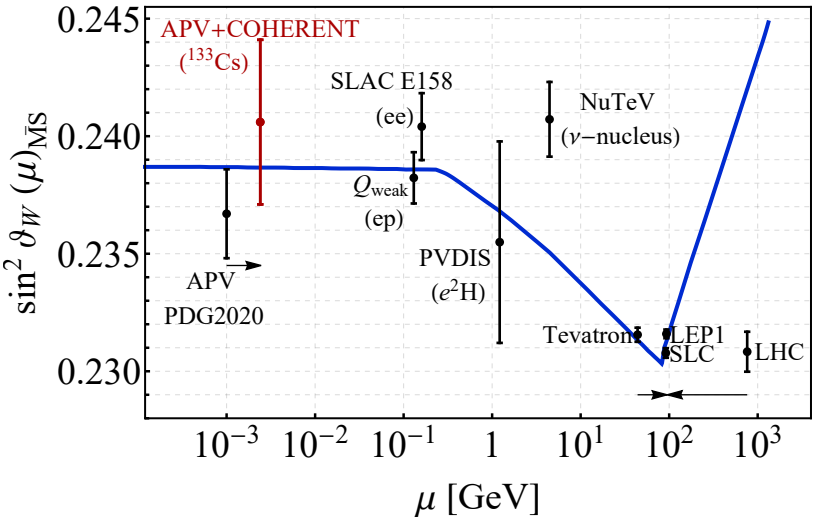

Figure 6.9: Variation of $\sin^2\vartheta_W$ with energy scale μ. The SM prediction is shown as the solid curve, together with experimental determinations in black [170, 213–215, 215–218]. The result derived in this paper is shown in red.

exotic nuclei. In the future, the COHERENT program [313] will include more detectors, each based on a different material allowing more determinations of R_n. Besides more data that will be available using a single-phase liquid argon detector, that so far allowed a first constrain on $R_n(\mathrm{Ar})$ [157], there will be two future experiments that are still being developed: a germanium detector, that is also the target used by the CONUS experiment [314], and an array of NaI crystals.

It is also important to note that the central value of the $\sin^2\vartheta_{\mathrm{W}}$ measurement presented in Eq. 6.21 is slightly larger with respect to the SM prediction. Combined with the other low-energy measurements, it could be interpreted in terms of a presence of a new dark boson [315–318]. Further measurements of $\sin^2\vartheta_{\mathrm{W}}$ in the low energy sector should come from the P2 [319] and MOLLER [320] experiments, from the near DUNE detector [321] and the exploitation of coherent elastic neutrino scattering in atoms [228] and nuclei [157, 322, 323].

We obtained the most precise measurement of the neutron rms radius and neutron-skin values of ^{133}Cs and ^{127}I, disentangling for the first time the two nuclear contributions. Moreover, for the first time, we derived a data-driven APV+COHERENT measurement of the low-energy weak mixing angle with a percent uncertainty fully determined from electroweak processes and independent of the average neutron rms radius of CsI that was allowed to vary freely in the fit.

All the results obtained through the combination of APV and COHERENT are reported in Ref. [239].

7

THE COHERENT NEUTRINO ATOM SCATTERING

In the seventh chapter the physics involving neutrino scattering is discussed, especially focusing on the case with energy scale as low as that the neutrino scatters with the whole target atom elastically. Future detectors made of superfluid ^{4}He, developed for low-mass dark matter, may be the path to observe such a phenomenon.

Contents

In the previous chapters we presented and explored the potentialities of CEνNS as a low-energy process. Indeed, it is a great way to test the electroweak theory of the Standard Model by measuring, for instance, the Weinberg angle. In addition, the need of pushing the search of dark matter particles towards lower masses is leading the community to the development of new technologies and detectors techniques pointing at the capability of detect lower and lower recoil energy signals. A new technology based on the evaporation of superfluid ^{4}He looks very promising in exploring physics at energy scale of $\mathcal{O}$(meV).

Recalling that the experimental challenge related to the CEνNS observation is due to the fact that in order to meet the coherence requirement $qR \ll 1$ [165], where $q = |\vec{q}|$ is the three-momentum transfer and R is the nuclear radius, one has to detect very small nuclear recoil energies $T_{\rm nr}$, lower than a few keV. At even lower momentum transfers, such that $qR_{\rm atom} \ll 1$, where $R_{\rm atom}$ is the radius of the target atom including the electron shells, the reaction can be viewed as taking place on the atom as a whole [324]. This effect should be visible for $qR_{\rm atom} \sim 1$, i.e. for momentum transfers $q \sim 2\,{\rm keV}/R_{\rm atom}[\text{Å}]$, where $R_{\rm atom}[\text{Å}]$ is the atomic radius in angstroms. The corresponding atomic recoil energy is $T_{\rm ar} \sim 2\,{\rm meV}/(AR^2_{\rm atom}[\text{Å}])$, where A is the atomic mass number of the recoiling atom. In the following we consider helium atoms that have an atomic radius of about 0.5 Å, for which the effect is expected to be observable at $T_{\rm ar} \sim 2\,{\rm meV}$. For much larger recoil energies of $\mathcal{O}(100\,{\rm meV})$ the atomic effect becomes completely negligible.

The small recoils needed for the observation of coherent elastic neutrino-atom scattering are well below the thresholds of detectability of currently available detectors, making it very difficult to observe this effect. However, in Ref. [325] a new technology based on the evaporation of helium atoms from a cold surface and their subsequent detection using field ionization has been proposed for the detection of low-mass dark matter particles. In this configuration, the nuclear recoils induced by dark-matter scattering produce elementary excitations (phonons and rotons) in the target that can result in the evaporation of helium atoms, if the recoil energy is greater than the binding energy of helium to the surface. Given that the latter can be below 1 meV, this proposed technique represents an ideal experimental setup to observe atomic effects in coherent neutrino scattering. The aforementioned low-energy detection technologies have the possibility, in principle, to measure the atomic processes and to test the Standard Model at energies never explored so far.

Here, we propose a future experiment that would allow the observation of coherent elastic neutrino-atom scattering (CEνAS) processes and we investigate its sensitivity. Since this effect could be visible only for extremely small

recoil energies, in order to achieve a sufficient number of low-energy CEνAS events, electron neutrinos with energies of the order of a few keV need to be exploited. Unfortunately, there are not so many available sources of such low-energy neutrinos. In this study, we investigate the possibility to use a tritium β-decay source, that is characterized by a Q-value of 18.58 keV. The PTOLEMY project [326,327], that aims to develop a scalable design to detect cosmic neutrino background, is already planning to use about 100 g of tritium, so we can assume that a similar or even larger amount could be available in the near future. Moreover, we show the potentialities of such a detector to perform the lowest-energy measurement of the weak mixing angle ϑ_W, also known as the Weinberg angle, a fundamental parameter in the theory of Standard Model electroweak interactions, and to reveal a magnetic moment of the electron neutrino below the current limit.

The results presented in this chapter are published on Physical Review D [228].

7.1 Atomic effect in neutrino coherent scattering

In order to derive the cross section for a CEνAS process $\nu_\ell + A \to \nu_\ell + A$, where A is an atom and $\ell = e, \mu, \tau$, we start from the differential cross-section of a CEνNS process as a function of the recoil energy $T_{\rm nr}$ of the nucleus [324,328]

$$\frac{d\sigma^{\rm CE\nu NS}}{dT_{\rm nr}} = \frac{G_F^2}{\pi} M \left(1 - \frac{M T_{\rm nr}}{2E^2}\right) C_V^2 \,, \tag{7.1}$$

where G_F is the Fermi constant, M is the nuclear mass, E is the neutrino energy and C_V[i]. is the q^2-dependent matrix element of the vector neutral-current charge[ii]

$$C_V = \frac{1}{2}[(1 - 4\sin^2\vartheta_W) Z\, F_{\rm Z}(q^2) - N\, F_{\rm N}(q^2)] \,. \tag{7.2}$$

Here, Z and N are the number of protons and neutrons in the atom and $F_{\rm N}(q^2)$ ($F_{\rm Z}(q^2)$) is the nuclear neutron (proton) form factor [146,167,329]. In principle, one should also consider the axial coupling C_A contribution, but for even-even (spin zero) nuclei it is equal to zero. Since in this discussion we take as a target a ^{4}He detector, we have $C_A = 0$.

[i] C_V corresponds to the electroweak charge described in previous chapters, but in here we decided to use this notation to keep the same notation use in [324].

[ii] In this chapter we do not include the radiative correction for the electroweak charge, because at this level their contribution only adds complexity.

As anticipated in the introduction, when the energy of the incoming neutrino is low enough, atomic effects arise. In the case of CEνAS processes, $d\sigma^{\mathrm{CE}\nu\mathrm{AS}}/dT_{\mathrm{ar}}$ can be derived starting from the formula in Eq. (7.1) with the inclusion of the electron contribution to the vector coupling [324,328]

$$C_V^{\mathrm{Atom}} = C_V + \frac{1}{2}(\pm 1 + 4\sin^2\vartheta_W) Z\, F_{\mathrm{e}}(q^2)\,, \tag{7.3}$$

where $F_{\mathrm{e}}(q^2)$ is the electron form factor and the $+$ sign applies to ν_e and $\bar{\nu}_e$, while the $-$ sign applies to all the other neutrino species. As explained in Ref. [324], the $+$ sign is responsible for the destructive interference between the electron and nuclear contributions. In principle, one should add also the axial contribution from the electron cloud, C_A^{Atom}, that however becomes null when the number of spin up and down electrons is the same, which applies to our scenario. Moreover, at the low momentum transfers considered in CEνAS processes, one can safely put $F_{\mathrm{N}}(q^2) = F_{\mathrm{Z}}(q^2) = 1$. This allows one to derive physics properties from the analysis on CEνAS being independent on the knowledge of the neutron distribution that is largely unknown [146,330].

As visible from Eq. 7.3, in CEνAS processes a key role is played by the electron form factor, that is defined as the Fourier transform of the electron density of an atom. In contrast to the case of atomic hydrogen, the He electron density is not known exactly. In our present study we employ the following parameterization of the He electron form factor, that has proved to be particularly effective and accurate (see, for instance, Refs. [331–333])

$$F_{\mathrm{e}}(q^2) = \mathcal{A}\cdot\left(\sum_{i=1}^{4} a_i \cdot e^{-b_i (q/4\pi)^2} + c\right). \tag{7.4}$$

The parameters $a_i = \{0.8734, 0.6309, 0.3112, 0.178\}$, $b_i = \{9.1037, 3.3568, 22.9276, 0.9821\}$ and $c = 0.0064$, extracted from Tab. 6.1.1.4 of Ref. [332], are given by a close fit of the numerical calculations for $F_{\mathrm{e}}(q^2)$ using a well-established theoretical model of the He electron wave function. The normalization $\mathcal{A}$ is a scaling factor such that $F_{\mathrm{e}}(q^2) \to 1$ for $q \to 0$, as in the nuclear form factor definition. This parameterization assumes that the electron density is spherically symmetric so that the value of the Fourier transform only depends on the distance from the origin in reciprocal space. The moment transfer q is related to the atomic recoil energy through $q = \sqrt{2 M_A T_{\mathrm{ar}}}$, where $M_A \sim M$ is the atomic mass.[iii] For various models of the He electron wave function that give an accurate value of the electron binding energy, the numerical results for $F_{\mathrm{e}}(q^2)$ are known to be practically identical in a wide range of q values. To illustrate this feature, we compare in Fig. 7.1

[iii] Here we neglect the binding of the atom in the liquid helium target, since it becomes of relevance only at the energy scale $T_{\mathrm{ar}} \lesssim 1$ meV.

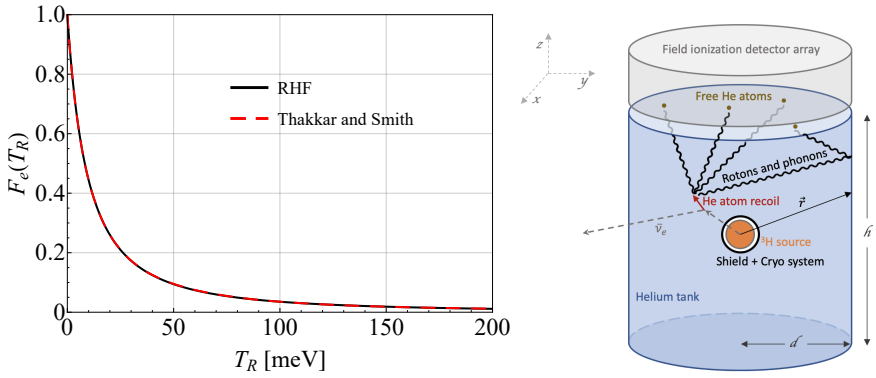

Figure 7.1: *Left:* The He electron form factor as a function of the recoil energy $T_{\rm ar}$. The solid (black) curve represents the RHF model [334] and the dashed (red) curve the strongly correlated model of Thakkar and Smith [335]. *Right*: Schematic representation of the detector proposed to observe CEνAS processes. The recoil of a helium atom after the scattering with an electron antineutrino coming from the tritium source in the center produces phonons and rotons which, upon arrival at the top surface, cause helium atoms to be released by quantum evaporation. A field ionization detector array on the top surface, as proposed in Ref. [325], detects the number of helium atoms evaporated.

(left) two He electron form factors obtained with two different well-known approaches: (i) the Roothaan-Hartree-Fock (RHF) method [334] and (ii) the variational method using a strongly correlated ansatz [335]. Despite the fact that the indicated methods treat electron-electron correlations in an opposite manner (the first completely neglects them, while the second takes them into account explicitly), they yield very close electron form-factor values. This illustration shows a negligible role of the theoretical uncertainties associated with the He electron form factor in the analysis carried out in the next sections.

7.2 Experimental setup for CEνAS detection

As mentioned in the introduction, a tritium source would provide electron antineutrinos in the needed energy range. Indeed, tritium β^- decay produces one electron, one antineutrino and a ^{3}He atom via the decay $^3\mathrm{H} \rightarrow {}^3\mathrm{He} + e^- + \bar{\nu}_e$, with a lifetime $\tau = 17.74$ years. The antineutrino energy spectrum ranges from 0 keV to the Q-value, with a maximum at approximately 15 keV [190]. The number of neutrinos released, N_ν, after a time t follows the simple exponential law

$$N_\nu(t) = N_{^3\mathrm{H}} \left(1 - e^{-t/\tau}\right), \tag{7.5}$$

where $N_{^3\mathrm{H}}$ is the number of tritium atoms in the source at $t = 0$. Given the rather large lifetime, the decay rate is almost linear up to 4-5 years. The number of tritium nuclei decaying in 4 years is approximately 20% of the population at the beginning. Thus, considering 100 g of source, the number of emitted antineutrinos in 4 years is expected to be $\sim 4 \cdot 10^{24}$, which corresponds to an antineutrino rate of about $3.2 \cdot 10^{16}\ \bar{\nu}_e/s$. Given the rather large tritium lifetime, the antineutrino rate is expected to stay almost constant in the first 5 years.

We consider a detector setup such that the tritium source is surrounded with a cylindrical superfluid-helium tank, as depicted in Fig. 7.1. This configuration allows us to maximize the geometrical acceptance, satisfying the request of having a top flat surface where helium atoms could evaporate after a recoil. This surface should be equipped as described in Ref. [325], to detect the small energy deposited by the helium evaporation. In order to shield the helium detector from the electrons produced by the tritium decay, an intermediate thin layer of heavy material has to be inserted between the source and the detector, which also acts as a vessel for the source. Cautions have to be taken such that all the materials used in the detector are extremely radiopure, such that the background contaminations are kept under control. Finally, the energy deposited by the electrons in the shield would cause a significant heating of the surrounding helium. Thus the shield has to be placed inside a cryocooler to keep the source at the desired temperature, surrounded by a vacuum layer to further isolate the source.

The expected CEνAS differential rate $d\mathcal{N}/(dt\, dT_{\mathrm{ar}})$ in such a cylindrical configuration, that represents the number of neutrino-induced events $\mathcal{N}$ that would be observed in the detector each second and per unit of the atomic recoil energy, is

$$\frac{d\mathcal{N}}{dt\, dT_{\mathrm{ar}}} = n \int_V \int_{E^{\mathrm{min}}}^{Q} \frac{1}{4\pi r^2} \frac{dN_\nu}{dt\, dE} \frac{d\sigma^{\mathrm{CE}\nu\mathrm{AS}}}{dT_{\mathrm{ar}}}\, dV\, dE\,, \tag{7.6}$$

where n is the number density of helium atoms in the target, dV is the infinitesimal volume around the position $\overrightarrow{r} \equiv (x, y, z)$ in the detector, $dN_\nu/(dt\, dE)$ is the differential neutrino rate and $E^{\mathrm{min}} \simeq \sqrt{M_A T_{\mathrm{ar}}/2}$ is the minimum antineutrino energy necessary to produce an atom recoil of energy T_{ar}. Note that, if the atomic effect is neglected, the differential number of events $d\mathcal{N}^{\mathrm{CE}\nu\mathrm{NS}}/dT_{\mathrm{nr}}$ could be straightforwardly obtained with the following set of substitutions: $d\sigma^{\mathrm{CE}\nu\mathrm{AS}}/dT_{\mathrm{ar}} \to d\sigma^{\mathrm{CE}\nu\mathrm{NS}}/dT_{\mathrm{nr}}$, $M_A \to M$ and $T_{\mathrm{ar}} \to T_{\mathrm{nr}}$. However, given that $M_A \simeq M$, the atomic and nuclear recoil energies are practically coincident, $T_{\mathrm{ar}} \simeq T_{\mathrm{nr}}$.

To illustrate the consequences of the atomic effect on the expected number

of events, we consider a detector of height $h = 160$ cm, and radius $d = 90$ cm filled with 500 kg of helium, a tritium source of 60 g, and a data-taking period of 5 years. The choice of this particular configuration will be clarified in Sec. 7.3.

The number of neutrino-induced events as a function of the recoil energy $T_{\rm ar}$ is obtained by integrating the differential rate defined in Eq. (7.6) for a time period of 5 years. The result is illustrated in Fig. 7.2, where the CEνNS differential rate is shown by the black solid line, while the CEνAS one is shown by the dashed red line. As stated in the introduction, when atomic effects are considered, electrons screen the weak charge of the nucleus as seen by the antineutrino. The screening is complete for atomic recoil energies $T_{\rm ar}$ such that $C_V^{\rm Atom} = 0$, or, in accordance with Eqs. (7.2) and (7.3), when

$$F_e(T_{\rm ar}) = \frac{\frac{N}{Z} - (1 - 4\sin^2\vartheta_W)}{1 + 4\sin^2\vartheta_W}\,, \tag{7.7}$$

where for ^{4}He atoms $N/Z = 1$. Using the SM prediction of the Weinberg angle at near zero momentum transfer $\sin^2\vartheta_W^{\rm SM} = 0.23857(5)$ [170], calculated in the $\overline{\rm MS}$ scheme, we obtain from Eq. (7.7) the following condition: $F_e(T_{\rm ar}) = 0.4883$. Thus, the screening is complete for $T_{\rm ar} \simeq 9$ meV (see again Fig. 7.1). Due to this destructive interference between the nuclear and the electron contributions, the number of events drops rapidly to zero, as shown by the red dashed line in Fig. 7.2. Note that the value of $T_{\rm ar}$ for which there is complete screening is larger than the value of $T_{\rm ar}$ that we estimated in the Introduction ($T_{\rm ar} \sim 2\,$meV) for neutrino-helium CEνAS, because of the requirement of partial coherence given by $F_e(T_{\rm ar}) = 0.4883$.

Another interesting feature of Fig. 7.2 is that it shows that in practice the atomic effect can be observed only as a suppression of the cross section with respect to that of coherent elastic neutrino-nucleus scattering. Indeed, the CEνAS cross section is smaller than the CEνNS cross section for all values of $T_{\rm ar}$ in Fig. 7.2. The CEνAS cross section can be larger than the CEνNS cross section for very small values of $T_{\rm ar}$, for which $F_e(T_{\rm ar}) \simeq 1$ and $C_V^{\rm Atom} \simeq Z - N/2$. However, since all stable atoms except ^{1}H and ^{3}He have $Z \leq N$, the value of the amplitude of CEνAS is bounded by $C_V^{\rm Atom} \leq N/2$, i.e.[iv]

$$C_V^{\rm Atom} \leq |C_V| + Z\, g_V^p, \tag{7.8}$$

where $g_V^p = 0.5 - 2\sin^2\vartheta_W \simeq 0.023$. It will be practically very difficult to

[iv] The inequality (7.8) applies to ν_e and $\bar{\nu}_e$ CEνAS. For the other neutrino species there is a similar very small and difficult to detect enhancement of the cross section amplitude: $|C_V^{\rm Atom}| = |C_V| + Z\, g_V^p$ for $F_e(T_{\rm ar}) \simeq 1$.

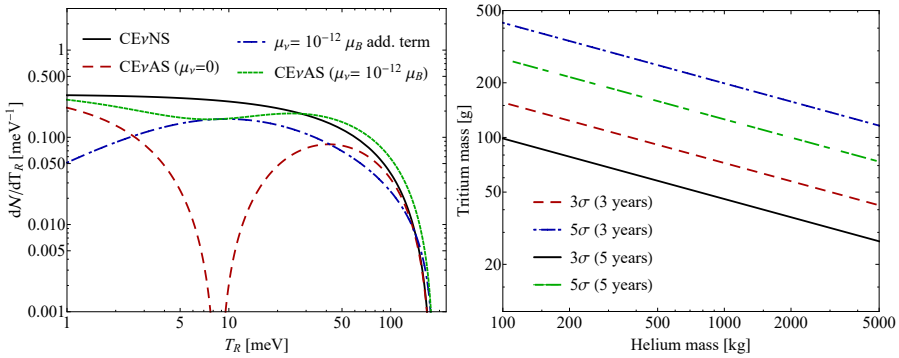

Figure 7.2: *Left*:Differential number of neutrino-induced events as a function of the atomic recoil energy $T_{\rm ar}$ in a logarithmic scale on both axes. The CEνNS differential number is shown by the black solid line while the CEνAS one is shown by the dashed red line. The dashed-dotted blue line represents the additional term appearing in the CEνAS differential number of events assuming a neutrino magnetic moment of $\mu_\nu = 10^{-12}\ \mu_B$ while the dotted green line represents the total differential number of CEνAS for the same value of μ_ν (i.e. using the differential cross section in Eq. 7.12).*Rigth*: Iso-sigma curves to observe (3σ in dashed red and solid black) or discover (5σ in dotted-dashed blue and long dashed green) the atomic effect, as a function of the helium and tritium masses, considering a data taking time of 3 and 5 years, respectively.

measure such a small enhancement of the cross section due to the atomic effect for very low values of the momentum transfer.

7.3 Sensitivity analysis and physics perspectives

We test the feasibility to observe the atomic effect in coherent neutrino scattering using the experimental setup described in Sec. 7.2. For this purpose, we build the following least-squares function

$$\chi^2 = \left(\frac{\mathcal{N}^{\rm CE\nu AS} - \mathcal{N}^{\rm CE\nu NS}}{\sigma} \right)^2 , \tag{7.9}$$

where $\mathcal{N}^{\rm CE\nu AS}$ represents the number of neutrino-induced events observed considering the atomic effect, while $\mathcal{N}^{\rm CE\nu NS}$ is the number of events expected ignoring such an effect, which represents our reference model [336]. These quantities are obtained integrating in time and recoil energy the differential spectrum in Eq. (7.6), considering for the latter the range of 1-184 meV, being the upper limit the maximum recoil energy that a neutrino with energy E can

give to an atom with mass M_A, which is given by

$$T_{\rm ar}^{\rm max} = \frac{2E^2}{M_A + 2E}\,. \tag{7.10}$$

Assuming that the main uncertainty contribution is due to the available statistics, the denominator in Eq. (7.9) is set to be $\sigma = \sqrt{\mathcal{N}^{\rm CE\nu AS}}$.

In order to find the experimental setup that would allow us to reach a sensitivity of at least 3σ, we calculate this least-squares function in terms of three parameters: the amount of helium in the tank, the amount of tritium in the source, and the time of data-taking (the main contributor being the amount of tritium used). We find that a reasonable combination of these parameters that would allow the observation of the atomic effect is 500 kg of helium, 60 g of tritium, and 5 years of data-taking. In this scenario, the expected number of CEνAS events is $\mathcal{N}^{\rm CE\nu AS} = 6.7$, to be compared with the expected number of CEνNS events $\mathcal{N}^{\rm CE\nu NS} = 14.6$.

In order to claim a discovery, i.e. reach a sensitivity of 5σ, the amount of tritium needed increases to 160 g, leaving the other parameters unchanged. The expected number of events in this case becomes $\mathcal{N}^{\rm CE\nu AS} = 17.7$ considering the atomic effect and $\mathcal{N}^{\rm CE\nu NS} = 38.9$ without the atomic effect. One can note that the atomic screening reduces the number of events by almost one half with the particular experimental setup proposed in here. For completeness, in Fig. 7.2 one can see the amount of tritium and helium mass needed to observe (3σ) or discover (5σ) the atomic effect, considering a data taking time of 3 and 5 years.

Clearly, all these estimates are to be refined for a specific experiment by taking into account systematic contributions from backgrounds and detector efficiencies and resolutions. However, neither of the indicated contributions appear to be seriously limiting [337] and, hence, the conclusions drawn in this work should remain valid.

By assuming that CEνAS has been observed we discuss the sensitivity of the determination of the Weinberg angle and the neutrino magnetic moment. Motivated by the studies performed in the previous section, we consider a detector made of 500 kg of helium, 5 years of data-taking, and three different scenarios for the source: 60 g, 160 g, and 500 g of tritium. The last scenario is considered in order to see the potentialities of such a detector if a large quantity of tritium will become available. For completeness, the expected number of events in this optimistic scenario becomes $\mathcal{N}^{\rm CE\nu AS} = 55$ taking into account the atomic effect and $\mathcal{N}^{\rm CE\nu NS} = 122$ without it.

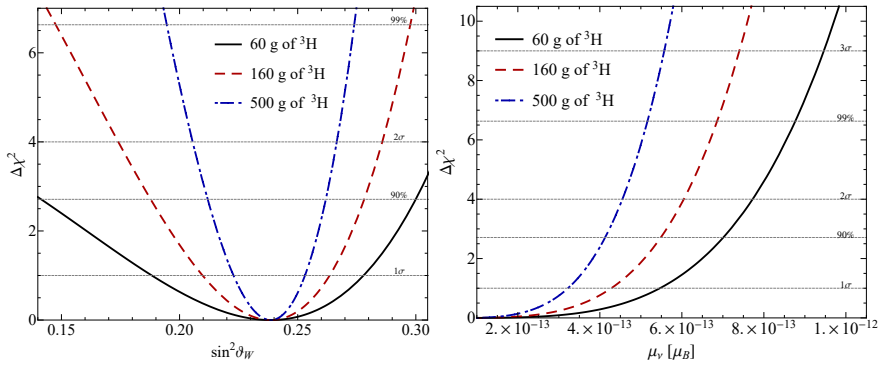

Figure 7.3: With the black solid curve is shown the $\Delta\chi^2 = \chi^2 - \chi^2_{\rm min}$, where the χ^2 is defined in Eq. (7.11), as a function of the Weinberg angle $\sin^2\vartheta_W$ (*left*) and the neutrino magnetic moment μ_ν (*right*), obtained considering a tritium source of 60 g, while with the dashed red line and the dotted-dashed blue line is shown the $\Delta\chi^2$ obtained considering a tritium source of 160 g and 500 g, respectively.

7.3.1 Determination of the Weinber angle

Since the vector coupling $C_V^{\rm Atom}$ in Eq. (7.3) depends on $\sin^2\vartheta_W$, the Weinberg angle can be measured in CEνAS processes. In order to quantify the sensitivity of a measurement of the Weinberg angle with the experimental setup described above, we consider a deviation of $\sin^2\vartheta_W$ from the Standard Model value $\sin^2\vartheta_W^{\rm SM}$ in the least-squares function

$$\chi^2(\sin^2\vartheta_W) = \left(\frac{\mathcal{N}_{\rm SM}^{\rm CE\nu AS} - \mathcal{N}^{\rm CE\nu AS}(\sin^2\vartheta_W)}{\sqrt{\mathcal{N}_{\rm SM}^{\rm CE\nu AS}}}\right)^2 . \tag{7.11}$$

Here, $\mathcal{N}_{\rm SM}^{\rm CE\nu AS}$ represents the expected number of CEνAS events if $\sin^2\vartheta_W = \sin^2\vartheta_W^{\rm SM}$, while $\mathcal{N}^{\rm CE\nu AS}(\sin^2\vartheta_W)$ is the number of events for a given value of the Weinberg angle.

Figure 7.3 shows the $\Delta\chi^2 = \chi^2 - \chi^2_{\rm min}$ profile as a function of $\sin^2\vartheta_W$ for the three different scenarios described above. The black solid, red dashed, and blue dotted-dashed lines refer to 60 g, 160 g, and 500 g of tritium, respectively. The uncertainties achievable in the three scenarios are $^{+0.04}_{-0.05}$, $^{+0.025}_{-0.029}$ and $^{+0.015}_{-0.016}$, respectively.

Figure 7.4 shows a summary of the weak mixing angle measurements at different values of q, together with the SM prediction. The uncertainty that can

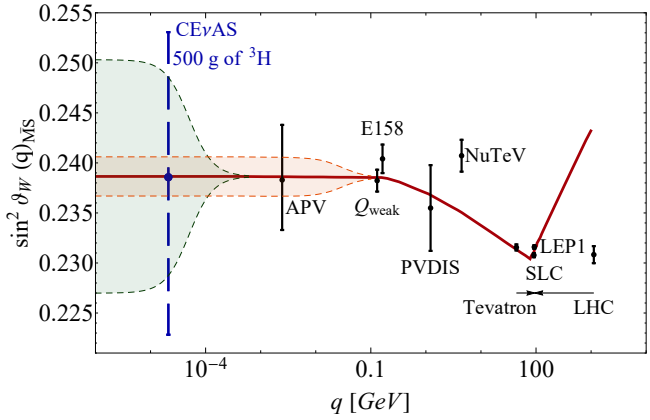

Figure 7.4: Variation of $\sin^2\vartheta_{\rm W}$ with energy scale q. The SM prediction is shown as the red solid curve, together with experimental determinations in black at the Z-pole [170] (Tevatron, LEP1, SLC, LHC), from atomic parity violation on caesium [213,214,278], which has a typical momentum transfer given by $\langle q\rangle \simeq 2.4$ MeV, Møller scattering [215] (E158), deep inelastic scattering of polarized electrons on deuterons **[?]** (e^2H PVDIS) and from neutrino-nucleus scattering [217] (NuTeV) and the result from the proton's weak charge at $q = 0.158$ GeV [218] (Q_{weak}). For clarity the Tevatron and LHC points have been displayed horizontally to the left and to the right, respectively, as indicated by the arrows. In dashed blue is shown the result that could be achieved using the experimental setup proposed in this chapter, obtained exploiting CEνAS effect at very low momentum transfer. The orange and green regions indicate the values of the weak mixing angle that are obtained for particular masses and couplings of a hypothetical Z_d boson, see the text for more details.

be reached with the method proposed in the case of a 500 g tritium source is shown by the dashed blue line. Despite the fact that this uncertainty is rather large, such a measurement would represent a unique opportunity to explore the low-energy sector, since the value $\langle q\rangle \simeq 2\times10^{-5}$ GeV is several orders of magnitude smaller than in all the other measurements. Given that the value of the Weinberg angle provides a direct probe of physics phenomena not included in the SM, such a measurement would give complementary information to those at mid and high-energy. In particular, this measurement would be highly sensitive to an extra dark boson, Z_d, whose existence is predicted by grand unified theories, technicolor models, supersymmetry and string theories [338]. Measurements of the Weinberg angle provide constraints on the properties of this dark boson as its mass, m_{Z_d}, its kinetic coupling to the SM fermions, ε, and its Z-Z_d mass-mixing coupling, δ [339–341]. As an example, the orange and green regions in Fig. 7.4 show the low-q deviations of $\sin^2\vartheta_{\rm W}$ with respect to the SM value predicted for two particular configurations of these parameters: the contours of the orange shadowed region correspond to $m_{Z_d} = 30$ MeV, $\delta = 0.015$, and $\varepsilon = 1\times10^{-3}$, while the contours of the green shadowed region have been obtained using $m_{Z_d} = 0.05$ MeV, $\delta = 0.0015$, and $\varepsilon = 1\times10^{-5}$. These values have been chosen such that $|\varepsilon\,\delta| \leq 8\times10^{-4}$ [341], which allows to

roughly satisfy the existing upper bounds on these quantities[v]. The shadowed regions indicate the values of the weak mixing angle obtained leaving the mass of the Z_d boson invariant, but using smaller values of ε and δ. As it is visible from Fig. 7.4, the impact of the hypothetical Z_d boson starts at values of the transferred momentum equal to its mass and extends to lower values. Thus, a measurement like the one proposed in here would be useful to better constrain even lighter Z_d's. Moreover, given that the atomic electron form factor is considerably better known with respect to the nuclear neutron form factor, such a measurement would be less dependent on the knowledge of nuclear parameters.

7.3.2 Effect of neutrino magnetic moment

The experiment proposed in this work would be highly sensitive to a possible neutrino magnetic moment.

So far, as we described in Chap. 5 the most stringent constraints on the electron neutrino magnetic moment in laboratory experiments have been obtained looking for possible distortions of the recoil electron energy spectrum in neutrino-electron elastic scattering, exploiting solar neutrinos and reactor antineutrinos.

The existence of a neutrino magnetic moment could have a significant effect on the CEνAS cross-section, that acquires an additional term

$$\left.\frac{d\sigma^{\mathrm{CE}\nu\mathrm{AS}}}{dT_{\mathrm{ar}}}\right|_{\mu_\nu\neq 0} \simeq \frac{d\sigma^{\mathrm{CE}\nu\mathrm{AS}}}{dT_{\mathrm{ar}}} + \frac{\pi\alpha^2 Z^2}{m_e^2}\left(\frac{\mu_\nu}{\mu_B}\right)^2 \cdot \left(\frac{1}{T_{\mathrm{ar}}} - \frac{1}{E}\right)\left(1 - F_{\mathrm{e}}(T_{\mathrm{ar}})\right)^2 , \tag{7.12}$$

where α is the fine structure constant and m_e is the electron mass. The atomic effect is included in the term $(1 - F_{\mathrm{e}}(T_{\mathrm{ar}}))^2$. In fact, for high energy neutrinos, the electron form factor goes to zero, obtaining the neutrino magnetic moment contribution for CEνNS process. On the contrary, for low energies, where $F_{\mathrm{e}}(T_{\mathrm{ar}}) \to 1$, neutrinos see the target as a whole neutral object; thus no electromagnetic properties can affect the process. By adding this contribution in Eq. (7.6), integrating for a time period of 5 years, and considering a magnetic moment of $10^{-12}\,\mu_B$, one obtains the expected differential number of CEνAS events as a function of the atomic recoil energy shown by the blue

[v] Note that in Ref. [341] the constraint is expressed in terms of δ', but for our choice of parameters $\delta' \simeq \delta$.

dotted-dashed line in Fig. 7.2. Comparing it to the red dashed curve obtained considering a null magnetic moment, it is clear that there is a large difference between the two cases and this difference could be exploited to put stringent limits on the neutrino magnetic moment.

To estimate the sensitivity, we consider the least-squares function

$$\chi^2(\mu_\nu) = \left(\frac{\mathcal{N}_{\rm SM}^{\rm CE\nu AS} - \mathcal{N}^{\rm CE\nu AS}(\mu_\nu)}{\sqrt{\mathcal{N}_{\rm SM}^{\rm CE\nu AS}}} \right)^2 , \tag{7.13}$$

where $\mathcal{N}_{\rm SM}^{\rm CE\nu AS}$ represents the number of CEνAS events that one would observe if the magnetic moment is zero, while $\mathcal{N}^{\rm CE\nu AS}(\mu_\nu)$ is the number of events for a given value of the magnetic moment.

Figure 7.3 (*right*) shows the $\Delta\chi^2$ profile as a function of the neutrino magnetic moment for the three different experimental scenarios described above: the black solid, red dashed and blue dotted-dashed lines refer to 60 g, 160 g, and 500 g of tritium, respectively. The respective limits that are achievable in these three different scenarios at 90% C.L. are $7.0 \times 10^{-13}\,\mu_B$, $5.5 \times 10^{-13}\,\mu_B$, and $4.1 \times 10^{-13}\,\mu_B$, which are almost two orders of magnitude smaller than the current experimental limits.

It is interesting to make some final remarks on the possibility to detect CEνAS effect using different targets, like those exploited to search for low-mass dark matter particles. The condition for which the atom recoils as a whole is $F_e(q^2) \simeq 1$, or $qR_{\rm atom} \ll 1$, where $R_{\rm atom}$ is determined by the rms radius of the outermost electron shell. From this it follows that, compared to the helium case, the recoil energy for which the coherence condition is realized reads

$$T_{\rm ar} \simeq \frac{4T_{\rm ar}^{\rm He}}{A} \left(\frac{R_{\rm He}}{R_{\rm atom}} \right)^2 , \tag{7.14}$$

where A is the mass number of the target atomic nucleus, $R_{\rm He}$ is the rms atomic He radius, and $T_{\rm ar}^{\rm He}$ is the recoil energy for which the CEνAS process occurs in He. Since only hydrogen has lower A and $R_{\rm atom}$ values than helium, the detection of the CEνAS process with other atoms appears to be difficult if one consider the value $T_R^{\rm He} \sim 2\,$meV estimated in the Introduction. However, as discussed at the end of Section 7.2, the CEνAS effect is observable in practice through the screening of the nucleus by the atomic electrons at a recoil energy given by the condition in Eq. (7.7), that depends on the behavior of the atomic electron form factor $F_e(T_{\rm ar})$ and is less stringent than the requirement of full coherency of neutrino-atom elastic scattering. Among the proposals found in the literature for the detection of low-mass dark matter [342–346], the most

promising seems to be the one exploiting diamonds as a target. Indeed, although carbon atoms have an atomic radius that is almost twice that of helium and Eq. (7.14) gives the very low value $T_{\rm ar}^{\rm C} \sim 0.2\,$meV, in accordance with Eq. (7.7) the screening condition would be realized at about 1.8 meV, which is only slightly below the lower energy threshold currently declared for these detectors. Let us finally note that there is not any limiting uncertainty concerning the knowledge of the electron form factors, that have been calculated accurately for all stable nuclei and have been parameterized in Tab. 6.1.1.4 of Ref. [332] with uncertainties at the level of a few per mille.

CONCLUSIONS

This thesis, with the studies presented therein, points out the low-energy features in particle-physics detectors. The presented features have a crucial impact in the understanding of both background and signal in the detectors.

In the first part, the role of low-energy background as the single-electron in DarkSide-50 is discussed. In LAr TPCs the single-electron signals are the least energetic signals that can be observed. As the dark matter search is moving from GeV-scale to sub-GeV WIMPs, the need to be sensitive to less energetic signals becomes fundamental. This is the reason that pushed us to investigate the characteristics of single-electron background in DarkSide-50. The aim is to understand its cause and behavior in order to suppress it in future dark matter detectors. We found out that the origin of single-electron signals is strongly related to the events occurring right before them. Indeed, we observed that single-electron signals are produced by the photo-ionization of the cathode of DarkSide-50, induced by the 128-nm photons produced during scintillation in the TPC. We have been able to calculate that the photo-ionization efficiency of the DarkSide-50 cathode resulting to be around $0.1‰$. We also deduced a clear correlation between single-electron signals and the number of electronegative impurities in the detector. This was done comparing the rate obtained during a short period of time in which the inline argon purification getter was turned off for maintenance purposes. During that period, the number of single electrons coming from the bulk of the detector increased by $\sim$40%, suggesting that at least part of these events are due to the photoelectric extraction from contaminants that are typically trapped by the getter. These studies will be essential for the design of a future detector specifically thought to look at low-mass WIMPs. The preliminary sensitivity of such a detector has been calculated and it is expected that a 1-tonne LAr TPC could exclude dark matter-nucleon cross-sections of the order of $\sim 10^{-44}$ cm^2 for ~ 1 GeV/c^2 particles and dark matter-electron cross-sections of $\sim 10^{-43}$ cm^2 for ~ 50 MeV/c^2.

The core of the second part of this thesis is the coherent elastic neutrino scattering. This is a Standard Model process that occurs only when the momentum transfer q is much smaller than the inverse of the typical size of the target. This means that the energy of the incoming neutrino involved in the process must be small. This fact turns into low-energy recoils in the detector used to search for these events. So far, COHERENT is the only collaboration that detected coherent scattering of neutrinos with nuclei, using CsI and LAr as targets. We performed several phenomenological analyses with COHERENT data and we highlighted the potentialities and the feasible measurements that this process can permit. First of all, from the analysis of the COHERENT LAr data-set

we put the first experimental upper bounds on the value of ^{40}Ar neutron distribution radius $R_n(^{40}\mathrm{Ar}) < 4.2\,\mathrm{fm}$ but unfortunately too weak to allow us a selection of the preferred nuclear models. In combination with the first COHERENT data-set with CsI, we set bounds on the electromagnetic properties of neutrinos as the neutrino charge radii, the neutrino electric charge, and the neutrino magnetic moment. Moreover, we performed analyses within the sector of non-standard interaction. Indeed, CEνNS is the perfect place to study scenarios including a new MeV-scale vector mediator Z', which has a nature depending on the details of the specific model assumed. We considered only three models: one in which the Z' couples universally to all Standard Model fermions, another corresponding to a $B - L$ extension of the Standard Model, and the third one with a gauged $L_\mu - L_\tau$ symmetry, comparing our results with the limits derived from searches in fixed target, accelerator, solar neutrino, and reactor CEνNS experiments, and with the parameter region that could explain the anomalous magnetic moment of the muon. We show that for the universal and the $B - L$ models, the COHERENT data allow us to put stringent limits in the light vector mediator mass, $M_{Z'}$, and coupling, $g_{Z'}$, parameter space. In addition, using the new COHERENT data-set with CsI, in combination with the atomic parity violation experimental result, we derived the most precise measurement of the neutron rms radii of ^{133}Cs and ^{127}I, namely $R_n(^{133}\mathrm{Cs}) = 5.27^{+0.33}_{-0.33}\,\mathrm{fm}$ and $R_n(^{127}\mathrm{I}) = 5.9^{+1.0}_{-0.9}\,\mathrm{fm}$, disentangling for the first time the contributions of the two nuclei. By exploiting these measurements we determine the corresponding neutron skin values for ^{133}Cs and ^{127}I. These results suggest a preference for models which predict large neutron skin values, as corroborated by the only other electroweak measurements of the neutron skin of ^{208}Pb performed by PREX experiments. Moreover, for the first time, we obtain a data-driven APV+COHERENT measurement of the low-energy weak mixing angle with a percent uncertainty, independent of the value of the average neutron rms radius of ^{133}Cs and ^{127}I, that is allowed to vary freely in the fit. The obtained value of the low-energy weak mixing angle $\sin^2\vartheta_W = 0.2406 \pm 0.0035$ is slightly larger than the Standard Model prediction. The low-energy measurement of the weak mixing angle is a key ingredient to constrain the presence of a new mediator boson. Thinking about even lower energy processes, we propose an experimental setup to observe coherent elastic neutrino-atom scattering using electron antineutrinos from tritium decay and a liquid helium target. In this scattering process with the whole atom, which has not been observed so far, the electrons tend to screen the weak charge of the nucleus as seen by the electron antineutrino probe. We showed that this process would allow us to perform the lowest-energy measurement of $\sin^2\vartheta_W$, with the advantage of being not affected by the uncertainties on the neutron form factor of the nucleus as the current lowest-energy determination. Finally, we also studied the sensitivity of this experiment to a possible electron

neutrino magnetic moment and we find that using 60 g of tritium it is possible to set an upper limit of about $7 \times 10^{-13}\,\mu_B$ at 90% C.L., that is more than one order of magnitude smaller than the current experimental limit.

In the following the contributions of the studies presented in this thesis submitted and published to journals:

- "A study of events with photoelectric emission in the DarkSide-50 liquid argon Time Projection Chamber", submitted to Astroparticle Physics and currently under review.
- "Physics results from the first COHERENT observation of $\mathrm{CE}\nu\mathrm{NS}$ in argon and their combination with cesium-iodide data", published on Physical Review D.
- "Constraints on light vector mediators through coherent elastic neutrino nucleus scattering data from COHERENT" published on Journal of High Energy Physics.
- "New insights into nuclear physics and weak mixing angle using electroweak probes", under review by APS journals.
- "Potentialities of a low-energy detector based on ^{4}He evaporation to observe atomic effects in coherent neutrino scattering and physics perspectives" published on Physical Review D.

Bibliography

[1] David N. Spergel. The dark side of cosmology: Dark matter and dark energy. *Science*, 347(6226):1100–1102, 2015. ↑8, ↑9

[2] P. J. E. Peebles and Bharat Ratra. The cosmological constant and dark energy. *Rev. Mod. Phys.*, 75:559–606, Apr 2003. ↑9

[3] Baron Kelvin, William Thomson. Baltimore lectures on molecular dynamics and the wave theory of light. *Baltimore, Publication agency of the Johns Hopkins university*, 1904. ↑9

[4] Edwin Hubble and Milton L. Humason. The Velocity-Distance Relation among Extra-Galactic Nebulae. , 74:43, July 1931. ↑9

[5] F. Zwicky. Die Rotverschiebung von extragalaktischen Nebeln. *Helv. Phys. Acta*, 6:110–127, 1933. [Gen. Rel. Grav.41,207(2009)]. ↑10

[6] F. Zwicky. On the Masses of Nebulae and of Clusters of Nebulae. , 86:217, October 1937. ↑10

[7] Wong et al. H0LiCOW â XIII. A 2.4 per cent measurement of H0 from lensed quasars: 5.3Ï tension between early- and late-Universe probes. *Monthly Notices of the Royal Astronomical Society*, 498(1):1420–1439, 09 2019. ↑10

[8] V. C. Rubin, N. Thonnard, and W. K. Ford, Jr. Rotational properties of 21 SC galaxies with a large range of luminosities and radii, from NGC 4605 /R = 4kpc/ to UGC 2885 /R = 122 kpc/. *Astrophys. J.*, 238:471, 1980. ↑10, ↑11

[9] K. G. Begeman, A. H. Broeils, and R. H. Sanders. Extended rotation curves of spiral galaxies: Dark haloes and modified dynamics. *Mon. Not. Roy. Astron. Soc.*, 249:523, 1991. ↑11

[10] Albert Bosma. 21-cm line studies of spiral galaxies. i - observations of the galaxies ngc 5033, 3198, 5055, 2841, and 7331. ii - the distribution and kinematics of neutral hydrogen in spiral galaxies of various morphological types. 86:1791–1846, 11 1981. ↑11

[11] Mariangela Lisanti. *Lectures on Dark Matter Physics*, chapter Chapter 7, pages 399–446. ↑11

[12] Pijushpani Bhattacharjee, Soumini Chaudhury, and Susmita Kundu. Rotation Curve of the Milky Way out to $\sim$ 200 kpc. *Astrophys. J.*, 785:63, 2014. ↑11

[13] Esa/hubble. `https://www.spacetelescope.org/`. ↑12, ↑13

[14] Pierre Magain and Virginie Chantry. Gravitational lensing evidence against extended dark matter halos. 2013. ↑11

[15] Anton G. Bergmann, Vahe Petrosian, and Roger Lynds. Gravitational lens models of arcs in clusters. 350, 03 1990. ↑12

[16] Richard Massey et al. Dark matter maps reveal cosmic scaffolding. *Nature*, 445:286, 2007. ↑12

[17] Douglas Clowe, Marusa Bradac, Anthony H. Gonzalez, Maxim Markevitch, Scott W. Randall, Christine Jones, and Dennis Zaritsky. A direct empirical proof of the existence of dark matter. *Astrophys. J.*, 648:L109–L113, 2006. ↑13

[18] P. A. R. Ade et al. Planck 2015 results. XIII. Cosmological parameters. *Astron. Astrophys.*, 594:A13, 2016. ↑13, ↑14

[19] Esa/planck. https://www.esa.int/Our_Activities/Space_Science/Planck/Planck_and_the_cosmic_microwave_background. ↑13

[20] M. Milgrom. A modification of the Newtonian dynamics as a possible alternative to the hidden mass hypothesis. , 270:365–370, July 1983. ↑14

[21] Jacob D. Bekenstein. Relativistic gravitation theory for the modified newtonian dynamics paradigm. *Phys. Rev. D*, 70:083509, Oct 2004. ↑14

[22] C. Skordis, D. F. Mota, P. G. Ferreira, and C. Bœhm. Large scale structure in bekenstein's theory of relativistic modified newtonian dynamics. *Phys. Rev. Lett.*, 96:011301, Jan 2006. ↑14

[23] J. Zuntz, T. G Zlosnik, F. Bourliot, P. G. Ferreira, and G. D. Starkman. Vector field models of modified gravity and the dark sector. *Phys. Rev. D*, 81:104015, May 2010. ↑14

[24] Mariangela Lisanti, Matthew Moschella, Nadav Joseph Outmezguine, and Oren Slone. Testing dark matter and modifications to gravity using local milky way observables. *Phys. Rev. D*, 100:083009, Oct 2019. ↑14

[25] Gianfranco Bertone and Dan Hooper. History of dark matter. *Rev. Mod. Phys.*, 90:045002, Oct 2018. ↑14

[26] Tongyan Lin. Dark matter models and direct detection. *PoS*, 333:009, 2019. ↑15

[27] Riccardo Catena and Piero Ullio. A novel determination of the local dark matter density. *JCAP*, 08:004, 2010. ↑15

[28] Lam Hui, Jeremiah P. Ostriker, Scott Tremaine, and Edward Witten. Ultralight scalars as cosmological dark matter. *Phys. Rev. D*, 95:043541, Feb 2017. ↑16

[29] Georg G. Raffelt. Axions in astrophysics and cosmology. In *30th Rencontres de Moriond: Euroconferences: Dark Matter in Cosmology, Clocks and Tests of Fundamental Laws*, 1995. ↑16

[30] P. Sikivie, D. B. Tanner, and Karl van Bibber. Resonantly enhanced axion-photon regeneration. *Phys. Rev. Lett.*, 98:172002, 2007. ↑16

[31] N. Du et al. A Search for Invisible Axion Dark Matter with the Axion Dark Matter Experiment. *Phys. Rev. Lett.*, 120(15):151301, 2018. ↑16

[32] M. Arik et al. Search for Solar Axions by the CERN Axion Solar Telescope with ^{3}He Buffer Gas: Closing the Hot Dark Matter Gap. *Phys. Rev. Lett.*, 112(9):091302, 2014. ↑16

[33] Peter W. Graham, Igor G. Irastorza, Steven K. Lamoreaux, Axel Lindner, and Karl A. van Bibber. Experimental Searches for the Axion and Axion-Like Particles. *Ann. Rev. Nucl. Part. Sci.*, 65:485–514, 2015. ↑16

[34] Riccardo Murgia, Vid Iršič, and Matteo Viel. Novel constraints on noncold, nonthermal dark matter from lyman-α forest data. *Phys. Rev. D*, 98:083540, Oct 2018. ↑16

[35] Asher Berlin, Pierre Gratia, Dan Hooper, and Samuel D. McDermott. Hidden sector dark matter models for the galactic center gamma-ray excess. *Phys. Rev. D*, 90:015032, Jul 2014. ↑17

[36] Kevork Abazajian and Savvas M. Koushiappas. Constraints on sterile neutrino dark matter. *Phys. Rev. D*, 74:023527, Jul 2006. ↑17

[37] Edward W. Kolb and Michael S. Turner. The Early Universe. *Front. Phys.*, 69:1–547, 1990. ↑18

[38] Gerard Jungman, Marc Kamionkowski, and Kim Griest. Supersymmetric dark matter. *Phys. Rept.*, 267:195–373, 1996. ↑19

[39] Michael Dine. Naturalness under stress. *Annual Review of Nuclear and Particle Science*, 65(1):43–62, 2015. ↑19

[40] Stephen P. Martin. A Supersymmetry primer. pages 1–98, 1997. [Adv. Ser. Direct. High Energy Phys.18,1(1998)]. ↑19

[41] John Ellis, J.S. Hagelin, D.V. Nanopoulos, K. Olive, and M. Srednicki. Supersymmetric relics from the big bang. *Nuclear Physics B*, 238(2):453 – 476, 1984. ↑19

[42] G. C. Branco, P. M. Ferreira, L. Lavoura, M. N. Rebelo, Marc Sher, and Joao P. Silva. Theory and phenomenology of two-Higgs-doublet models. *Phys. Rept.*, 516:1–102, 2012. ↑19

[43] Martin Schmaltz and David Tucker-Smith. Little Higgs review. *Ann. Rev. Nucl. Part. Sci.*, 55:229–270, 2005. ↑19

[44] Z. Chacko, Hock-Seng Goh, and Roni Harnik. The Twin Higgs: Natural electroweak breaking from mirror symmetry. *Phys. Rev. Lett.*, 96:231802, 2006. ↑19

[45] Toby Falk, Keith A. Olive, and Mark Srednicki. Heavy sneutrinos as dark matter. *Phys. Lett.*, B339:248–251, 1994. ↑19

[46] Daniel J. H. Chung, Patrick Crotty, Edward W. Kolb, and Antonio Riotto. Gravitational production of superheavy dark matter. *Phys. Rev. D*, 64:043503, Jul 2001. ↑20

[47] Alexander Kusenko and Mikhail Shaposhnikov. Supersymmetric q-balls as dark matter. *Physics Letters B*, 418(1):46–54, 1998. ↑20

[48] Yang Bai, Andrew J. Long, and Sida Lu. Dark quark nuggets. *Phys. Rev. D*, 99:055047, Mar 2019. ↑20

[49] Yacine Ali-Haïmoud and Marc Kamionkowski. Cosmic microwave background limits on accreting primordial black holes. *Phys. Rev. D*, 95:043534, Feb 2017. ↑20

[50] Mark W. Goodman and Edward Witten. Detectability of Certain Dark Matter Candidates. *Phys. Rev.*, D31:3059, 1985. [,325(1984)]. ↑21

[51] A. K. Drukier, Katherine Freese, and D. N. Spergel. Detecting Cold Dark Matter Candidates. *Phys. Rev.*, D33:3495–3508, 1986. ↑21

[52] F. J. Kerr and Donald Lynden-Bell. Review of galactic constants. *Mon. Not. Roy. Astron. Soc.*, 221:1023, 1986. ↑22

[53] Richard H. Helm. Inelastic and Elastic Scattering of 187-Mev Electrons from Selected Even-Even Nuclei. *Phys. Rev.*, 104:1466–1475, 1956. ↑24, ↑78, ↑94, ↑97, ↑172

[54] M. Cannoni. Reanalysis of nuclear spin matrix elements for dark matter spin-dependent scattering. *Phys. Rev.*, D87(7):075014, 2013. ↑24

[55] Matteo Cadeddu. *DarkSide-20k sensitivity, directional dark matter detection and the role of coherent elastic neutrino-nucleus scattering background*. PhD dissertation, University of Cagliari, 2017. ↑24

[56] Guillaume Plante. *The XENON100 Dark Matter Experiment: Design, Construction, Calibration and 2010 Search Results with Improved Measurement of the Scintillation Response of Liquid Xenon to Low-Energy Nuclear Recoils*. PhD dissertation, Columbia University, 2012. ↑25

[57] R. Bernabei et al. Final model independent result of DAMA/LIBRA-phase1. *Eur. Phys. J.*, C73:2648, 2013. ↑24, ↑25

[58] R. Bernabei et al. First model independent results from DAMA/LIBRA-phase2. 2018. ↑24, ↑25

[59] R. Agnese et al. First Dark Matter Constraints from a SuperCDMS Single-Charge Sensitive Detector. *Submitted to: Phys. Rev. Lett.*, 2018. ↑24

[60] F. Petricca et al. First results on low-mass dark matter from the CRESST-III experiment. In *15th International Conference on Topics in Astroparticle and Underground Physics (TAUP 2017) Sudbury, Ontario, Canada, July 24-28, 2017*, 2017. ↑24

[61] C. E. Aalseth et al. CoGeNT: A Search for Low-Mass Dark Matter using p-type Point Contact Germanium Detectors. *Phys. Rev.*, D88:012002, 2013. ↑24

[62] E. Armengaud et al. Performance of the EDELWEISS-III experiment for direct dark matter searches. *JINST*, 12(08):P08010, 2017. ↑24

[63] E. Behnke et al. First Dark Matter Search Results from a 4-kg CF_3I Bubble Chamber Operated in a Deep Underground Site. *Phys. Rev.*, D86(5):052001, 2012. [Erratum: Phys. Rev.D90,no.7,079902(2014)]. ↑25

[64] M. Felizardo et al. The SIMPLE Phase II Dark Matter Search. *Phys. Rev.*, D89(7):072013, 2014. ↑25

[65] S. Archambault et al. Constraints on Low-Mass WIMP Interactions on ^{19}F from PICASSO. *Phys. Lett.*, B711:153–161, 2012. ↑25

[66] P. Agnes et al. First results from the darkside-50 dark matter experiment at laboratori nazionali del gran sasso. *Physics Letters B*, 743:456–466, 2015. ↑25, ↑33

[67] Amaudruz et al. First results from the deap-3600 dark matter search with argon at snolab. *Phys. Rev. Lett.*, 121:071801, Aug 2018. ↑25

[68] E. Aprile et al. The XENON1T Dark Matter Experiment. *Eur. Phys. J.*, C77(12):881, 2017. ↑25

[69] D. S. Akerib et al. First results from the LUX dark matter experiment at the Sanford Underground Research Facility. *Phys. Rev. Lett.*, 112:091303, 2014. ↑25

[70] Xiangyi Cui et al. Dark Matter Results From 54-Ton-Day Exposure of PandaX-II Experiment. *Phys. Rev. Lett.*, 119(18):181302, 2017. ↑25

[71] Tarek Saab. An Introduction to Dark Matter Direct Detection Searches & Techniques. In *The Dark Secrets of the Terascale: Proceedings, TASI 2011, Boulder, Colorado, USA, Jun 6 - Jul 11, 2011*, pages 711–738, 2013. ↑25

[72] E. Aprile et al. Dark Matter Search Results from a One Tonne$\times$Year Exposure of XENON1T. 2018. ↑25

[73] D. S. Akerib et al. Results from a search for dark matter in the complete LUX exposure. *Phys. Rev. Lett.*, 118(2):021303, 2017. ↑25

[74] R. Agnese, T. Aramaki, I. J. Arnquist, W. Baker, D. Balakishiyeva, S. Banik, D. Barker, R. Basu Thakur, D. A. Bauer, T. Binder, M. A. Bowles, P. L. Brink, R. Bunker, B. Cabrera, D. O. Caldwell, R. Calkins, C. Cartaro, D. G. Cerdeño, Y. Chang, Y. Chen, J. Cooley, B. Cornell, P. Cushman, M. Daal, P. C. F. Di Stefano, T. Doughty, E. Fascione, E. Figueroa-Feliciano, M. Fritts, G. Gerbier, R. Germond, M. Ghaith, G. L. Godfrey, S. R. Golwala, J. Hall, H. R. Harris, Z. Hong, E. W. Hoppe, L. Hsu, M. E. Huber, V. Iyer, D. Jardin, A. Jastram, C. Jena, M. H. Kelsey, A. Kennedy, A. Kubik, N. A. Kurinsky, B. Loer, E. Lopez Asamar, P. Lukens, D. MacDonell, R. Mahapatra, V. Mandic, N. Mast, E. H. Miller, N. Mirabolfathi, B. Mohanty, J. D. Morales Mendoza, J. Nelson, J. L. Orrell, S. M. Oser, K. Page, W. A. Page, R. Partridge, M. Penalver Martinez, M. Pepin, A. Phipps, S. Poudel, M. Pyle, H. Qiu, W. Rau, P. Redl, A. Reisetter, T. Reynolds, A. Roberts, A. E. Robinson, H. E. Rogers, T. Saab, B. Sadoulet, J. Sander, K. Schneck, R. W. Schnee, S. Scorza, K. Senapati, B. Serfass, D. Speller, M. Stein, J. Street, H. A. Tanaka, D. Toback, R. Underwood, A. N. Villano, B. von Krosigk, B. Welliver, J. S. Wilson, M. J. Wilson, D. H. Wright, S. Yellin, J. J. Yen, B. A. Young, X. Zhang, and X. Zhao. Results from the super cryogenic dark matter search experiment at soudan. *Phys. Rev. Lett.*, 120:061802, Feb 2018. ↑25

[75] P. Agnes et al. Darkside-50 532-day dark matter search with low-radioactivity argon. *Phys. Rev. D*, 98:102006, Nov 2018. ↑25, ↑31, ↑35, ↑36, ↑37, ↑39, ↑45

[76] E. Aprile et al. Physics reach of the XENON1T dark matter experiment. *JCAP*, 1604(04):027, 2016. ↑26

[77] J. Aalbers et al. DARWIN: towards the ultimate dark matter detector. *JCAP*, 1611:017, 2016. ↑26

[78] C. E. Aalseth et al. DarkSide-20k: A 20 tonne two-phase LAr TPC for direct dark matter detection at LNGS. *Eur. Phys. J. Plus*, 133:131, 2018. ↑26

[79] J. Billard, L. Strigari, and E. Figueroa-Feliciano. Implication of neutrino backgrounds on the reach of next generation dark matter direct detection experiments. *Phys. Rev. D*, 89(2):023524, 2014. ↑26, ↑85

[80] M Cadeddu and E Picciau. Impact of neutrino background prediction for next generation dark matter xenon detector. *Journal of Physics: Conference Series*, 956(1):012014, 2018. ↑26

[81] M. Cadeddu et al. Potential for an argon directional dark matter detector. 2017. ↑26

[82] M. Ackermann et al. Fermi LAT Search for Dark Matter in Gamma-ray Lines and the Inclusive Photon Spectrum. *Phys. Rev.*, D86:022002, 2012. ↑27

[83] P. Picozza et al. PAMELA: A Payload for Antimatter Matter Exploration and Light-nuclei Astrophysics. *Astropart. Phys.*, 27:296–315, 2007. ↑27

[84] M. Aguilar et al. Electron and Positron Fluxes in Primary Cosmic Rays Measured with the Alpha Magnetic Spectrometer on the International Space Station. *Phys. Rev. Lett.*, 113:121102, 2014. ↑27

[85] Oscar Adriani et al. An anomalous positron abundance in cosmic rays with energies 1.5-100 GeV. *Nature*, 458:607–609, 2009. ↑27

[86] M. Ackermann et al. Fermi LAT observations of cosmic-ray electrons from 7 GeV to 1 TeV. *Phys. Rev.*, D82:092004, 2010. ↑27

[87] Dan Hooper, Pasquale Blasi, and Pasquale Dario Serpico. Pulsars as the Sources of High Energy Cosmic Ray Positrons. *JCAP*, 01:025, 2009. ↑27

[88] M. Di Mauro, F. Donato, N. Fornengo, R. Lineros, and A. Vittino. Interpretation of AMS-02 electrons and positrons data. *JCAP*, 04:006, 2014. ↑27

[89] Yutaka Fujita, Kazunori Kohri, Ryo Yamazaki, and Kunihito Ioka. Is the PAMELA anomaly caused by the supernova explosions near the Earth? *Phys. Rev. D*, 80:063003, 2009. ↑27

[90] Howard Baer, Eun-Kyung Park, and Xerxes Tata. Collider, direct and indirect detection of supersymmetric dark matter. *New J. Phys.*, 11:105024, 2009. ↑28

[91] Steven Lowette. Search for dark matter at cms. *Nuclear and Particle Physics Proceedings*, 273-275:503 – 508, 2016. 37th International Conference on High Energy Physics (ICHEP). ↑28

[92] J. H. J. Poole and C. F. G. Delaney. Origin of atmospheric argon and the radioactive decay constants of potassium-40. *Nature*, 167(4252):680–681, 1951. ↑30

[93] P. Benetti et al. Measurement of the specific activity of ar-39 in natural argon. *Nucl. Instrum. Meth. A*, 574:83–88, 2007. ↑30

[94] H.H. Loosli and H. Oeschger. Detection of 39ar in atmospheric argon. *Earth and Planetary Science Letters*, 5:191–198, 1968. ↑30

[95] R. Saldanha, H. O. Back, R. H. M. Tsang, T. Alexander, S. R. Elliott, S. Ferrara, E. Mace, C. Overman, and M. Zalavadia. Cosmogenic production of ^{39}Ar and ^{37}Ar in argon. *Phys. Rev. C*, 100(2):024608, 2019. ↑30

[96] C. Galbiati et al. Discovery of underground argon with a low level of radioactive39ar and possible applications to WIMP dark matter detectors. *Journal of Physics: Conference Series*, 120(4):042015, jul 2008. ↑30

[97] P. Agnes et al. Results From the First Use of Low Radioactivity Argon in a Dark Matter Search. *Phys.Rev.D*, 93(8):081101, 2016. ↑31

[98] P. Agnes et al. Low-mass dark matter search with the darkside-50 experiment. *Phys. Rev. Lett.*, 121:081307, Aug 2018. ↑31, ↑36, ↑37, ↑46, ↑48, ↑56, ↑63, ↑68

[99] P. Agnes et al. Separating ^{39}Ar from ^{40}Ar by cryogenic distillation with Aria for dark-matter searches. *Eur. Phys. J. C*, 81(4):359, 2021. ↑31

[100] J. A. Cameron, J. Chen, Balraj Singh, and N. Nica. Nuclear data sheets for a = 37. *Nuclear Data Sheets*, 113:365–514, 2012. ↑31

[101] A. S. Barabash, R. R. Saakyan, and V. I. Umatov. On concentration of ^{42}Ar in liquid argon. *J. Phys. Conf. Ser.*, 718(6):062004, 2016. ↑31

[102] V. Chepel and H. Araujo. Liquid noble gas detectors for low energy particle physics. *JINST*, 8:R04001, 2013. ↑32

[103] Tadayoshi Doke, Kimiaki Masuda, and Eido Shibamura. Estimation of absolute photon yields in liquid argon and xenon for relativistic (1 mev) electrons. *Nuclear Instruments and Methods in Physics Research Section A: Accelerators, Spectrometers, Detectors and Associated Equipment*, 291(3):617–620, 1990. ↑32

[104] Akira Hitachi, Tan Takahashi, Nobutaka Funayama, Kimiaki Masuda, Jun Kikuchi, and Tadayoshi Doke. Effect of ionization density on the time dependence of luminescence from liquid argon and xenon. *Phys. Rev. B*, 27:5279–5285, May 1983. ↑33

[105] G. Bellini et al. Cosmogenic backgrounds in borexino at 3800 m water-equivalent depth. *Journal of Cosmology and Astroparticle Physics*, 2013(08):049, 2013. ↑33

[106] P. Agnes et al. The veto system of the DarkSide-50 experiment. *JINST*, 11(03):P03016, 2016. ↑34

[107] A. Bondar, A. Buzulutskov, A. Grebenuk, D. Pavlyuchenko, and Y. Tikhonov. Electron emission properties of two-phase argon and argon-nitrogen avalanche detectors. *JINST*, 4:P09013, 2009. ↑34

[108] M. G. Boulay and A. Hime. Technique for direct detection of weakly interacting massive particles using scintillation time discrimination in liquid argon. *Astropart. Phys.*, 25:179–182, 2006. ↑36

[109] P. Agnes et al. Constraints on Sub-GeV Dark Matter-Electron Scattering from the DarkSide-50 Experiment. 2018. ↑36, ↑37, ↑41, ↑63

[110] Shayne Reichard, Rafael F. Lang, Christopher McCabe, Marco Selvi, and Irene Tamborra. Supernova Neutrino Physics with Xenon Dark Matter Detectors. *J. Phys. Conf. Ser.*, 888(1):012260, 2017. ↑37

[111] Peter Sorensen. Electron train backgrounds in liquid xenon dark matter search detectors are indeed due to thermalization and trapping. 2017. ↑37, ↑44

[112] P. Sorensen and K. Kamdin. Two distinct components of the delayed single electron noise in liquid xenon emission detectors. *JINST*, 13(02):P02032, 2018. ↑37, ↑44

[113] J. Angle et al. Search for light dark matter in xenon10 data. *Phys. Rev. Lett.*, 107:051301, Jul 2011. ↑37, ↑44

[114] E. Aprile et al. Light Dark Matter Search with Ionization Signals in XENON1T. *Phys. Rev. Lett.*, 123(25):251801, 2019. ↑37, ↑44

[115] P. Agnes et al. Low-Mass Dark Matter Search with the DarkSide-50 Experiment. 2018. ↑39

[116] P. Agnes et al. Measurement of the liquid argon energy response to nuclear and electronic recoils. *Phys. Rev. D*, 97(11):112005, 2018. ↑40

[117] E. Aprile et al. Light Dark Matter Search with Ionization Signals in XENON1T. *Phys. Rev. Lett.*, 123(25):251801, 2019. ↑40, ↑42, ↑68

[118] Rouven Essig, Aaron Manalaysay, Jeremy Mardon, Peter Sorensen, and Tomer Volansky. First direct detection limits on sub-gev dark matter from xenon10. *Phys. Rev. Lett.*, 109:021301, Jul 2012. ↑41

[119] Rouven Essig, Tomer Volansky, and Tien-Tien Yu. New Constraints and Prospects for sub-GeV Dark Matter Scattering off Electrons in Xenon. *Phys. Rev. D*, 96(4):043017, 2017. ↑41

[120] D.Yu. Akimov et al. Observation of delayed electron emission in a two-phase liquid xenon detector. *Journal of Instrumentation*, 11(03):C03007–C03007, mar 2016. ↑44

[121] E Aprile et al. Observation and applications of single-electron charge signals in the XENON100 experiment. *Journal of Physics G: Nuclear and Particle Physics*, 41(3):035201, feb 2014. ↑44

[122] B. Edwards et al. Measurement of single electron emission in two-phase xenon. *Astroparticle Physics*, 30(2):54 – 57, 2008. ↑44, ↑55

[123] E. Santos et al. Single electron emission in two-phase xenon with application to the detection of coherent neutrino-nucleus scattering. *JHEP*, 12:115, 2011. ↑44

[124] E. Santos et al. Single electron emission in two-phase xenon with application to the detection of coherent neutrino-nucleus scattering. *Journal of High Energy Physics*, 2011(12):115, 2011. ↑44

[125] P. Agnes et al. Simulation of argon response and light detection in the DarkSide-50 dual phase TPC. *JINST*, 12(10):P10015, 2017. ↑51

[126] Christopher Benson, Gabriel Orebi Gann, and Victor Gehman. Measurements of the intrinsic quantum efficiency and absorption length of tetraphenyl butadiene thin films in the vacuum ultraviolet regime. *Eur. Phys. J. C*, 78(4):329, 2018. ↑52

[127] D.S. Akerib et al. Investigation of background electron emission in the LUX detector. *Phys. Rev. D*, 102(9):092004, 2020. ↑55

[128] E. Aprile et al. Observation and applications of single-electron charge signals in the XENON100 experiment. *J. Phys. G*, 41:035201, 2014. ↑55

[129] P. Agnes et al. A study of events with photoelectric emission in the DarkSide-50 liquid argon Time Projection Chamber. 7 2021. ↑56

[130] Abigail Kopec, Amanda L. Baxter, Michael Clark, Rafael F. Lang, Shengchao Li, Juehang Qin, and Riya Singh. Correlated single- and few-electron backgrounds milliseconds after interactions in dual-phase liquid xenon time projection chambers. *JINST*, 16(07):P07014, 2021. ↑59

[131] Jim Alexander et al. Dark Sectors 2016 Workshop: Community Report. 8 2016. ↑62

[132] Marco Battaglieri et al. US Cosmic Visions: New Ideas in Dark Matter 2017: Community Report. In *U.S. Cosmic Visions: New Ideas in Dark Matter*, 7 2017. ↑62

[133] H. Cao et al. Measurement of Scintillation and Ionization Yield and Scintillation Pulse Shape from Nuclear Recoils in Liquid Argon. *Phys. Rev. D*, 91:092007, 2015. ↑63

[134] P. Agnes et al. Calibration of the liquid argon ionization response to low energy electronic and nuclear recoils with DarkSide-50. 7 2021. ↑63

[135] R Ajaj et al. Electromagnetic Backgrounds and Potassium-42 Activity in the DEAP-3600 Dark Matter Detector. *arXiv*, May 2019. ↑64

[136] T. Doke, A. Hitachi, S. Kubota, A. Nakamoto, and T. Takahashi. Estimation of Fano factors in liquid argon, krypton, xenon and xenon-doped liquid argon. *Nucl. Inst. Meth.*, 134(2):353–357, April 1976. ↑67

[137] S. Kubota, A. Nakamoto, T. Takahashi, S. Konno, T. Hamada, M. Miyajima, A. Hitachi, H. Shibamura, and T. Doke. Ionization yield in xenon-doped liquid argon. *Phys. Lett. A*, 49(5):393–394, October 1974. ↑67

[138] Jay A. LaVerne, Akira Hitachi, J. J. Kolata, and Tadayoshi Doke. Scintillation and ionization in allene-doped liquid argon irradiated with $^{18}\mathrm{O}$ and $^{36}\mathrm{Ar}$ ions of 30 MeV/u. *Phys. Rev. B*, 54(22):15724–15729, December 1996. ↑67

[139] H. Ichinose et al. Energy resolution for 1 mev electrons in liquid argon doped with allene. *Nucl. Inst. Meth A*, 295(3):354 – 358, 1990. ↑67

[140] Michael Clark. Lbeca: A low-mass dark matter search with xenon. Aug. 2019. ↑69

[141] G. S. Hurst and T. E. Bortner. Capture of electrons in molecular oxygen. Technical Report ORNL-2670, Oak Ridge National Lab., Tenn., July 1959. ↑69

[142] George Bakale, Ulrich Sowada, and Werner F. Schmidt. Negative ion–molecule reactions in liquid argon following electron capture by N2o. *Can. J Chem.*, 55(11):2220–2224, June 1977. ↑69

[143] Jingke Xu, Sergey Pereverzev, Brian Lenardo, James Kingston, Daniel Naim, Adam Bernstein, Kareem Kazkaz, and Mani Tripathi. Electron extraction efficiency study for dual-phase xenon dark matter experiments. *Phys. Rev. D*, 99(10):103024, May 2019. arXiv: 1904.02885. ↑69

[144] D. Akimov et al. Observation of Coherent Elastic Neutrino-Nucleus Scattering. *Science*, 357:1123–1126, 2017. ↑74, ↑76, ↑88, ↑89, ↑90, ↑91, ↑97, ↑98, ↑100, ↑110, ↑116, ↑121

[145] D. Akimov et al. COHERENT Collaboration data release from the first observation of coherent elastic neutrino-nucleus scattering, 2018. ↑74, ↑97, ↑110, ↑121

[146] M. Cadeddu, C. Giunti, Y. F. Li, and Y. Y. Zhang. Average CsI neutron density distribution from COHERENT data. *Phys.Rev.Lett.*, 120:072501, 2018. ↑74, ↑78, ↑92, ↑95, ↑110, ↑121, ↑131, ↑132

[147] D.K. Papoulias, T.S. Kosmas, R. Sahu, V.K.B. Kota, and M. Hota. Constraining nuclear physics parameters with current and future coherent data. *Physics Letters B*, 800:135133, Jan 2020. ↑74, ↑95, ↑110

[148] Pilar Coloma, M. C. Gonzalez-Garcia, Michele Maltoni, and Thomas Schwetz. A COHERENT enlightenment of the neutrino Dark Side. *Phys.Rev.*, D96:115007, 2017. ↑74, ↑110

[149] Jiajun Liao and Danny Marfatia. COHERENT constraints on nonstandard neutrino interactions. *Phys. Lett. B*, 775:54–57, 2017. ↑74, ↑110, ↑112, ↑114, ↑116, ↑117

[150] D. K. Papoulias and T. S. Kosmas. COHERENT constraints to conventional and exotic neutrino physics. *Phys.Rev.*, D97:033003, 2018. ↑74, ↑83, ↑110

[151] Peter B. Denton, Yasaman Farzan, and Ian M. Shoemaker. Testing large non-standard neutrino interactions with arbitrary mediator mass after COHERENT data. *JHEP*, 07:037, 2018. ↑74, ↑110, ↑114

[152] D. Aristizabal Sierra, Valentina De Romeri, and N. Rojas. COHERENT analysis of neutrino generalized interactions. *Phys.Rev.*, D98:075018, 2018. ↑74, ↑110

[153] M. Cadeddu, C. Giunti, K.A. Kouzakov, Y. F. Li, A.I. Studenikin, and Y. Y. Zhang. Neutrino Charge Radii from COHERENT Elastic Neutrino-Nucleus Scattering. *Phys.Rev.*, D98:113010, 2018. ↑74, ↑80, ↑82, ↑100, ↑102, ↑110

[154] Bhaskar Dutta, Shu Liao, Samiran Sinha, and Louis E. Strigari. Searching for Beyond the Standard Model Physics with COHERENT Energy and Timing Data. *Phys.Rev.Lett.*, 123:061801, 2019. ↑74, ↑110

[155] Bhaskar Dutta, Doojin Kim, Shu Liao, Jong-Chul Park, Seodong Shin, and Louis E. Strigari. Dark matter signals from timing spectra at neutrino experiments. *Phys.Rev.Lett.*, 124:121802, 2020. ↑74, ↑110

[156] D. Akimov et al. First Measurement of Coherent Elastic Neutrino-Nucleus Scattering on Argon. *Phys. Rev. Lett.*, 126(1):012002, 2021. ↑74, ↑88, ↑92, ↑93, ↑94, ↑95, ↑100, ↑103, ↑110, ↑118, ↑119

[157] M. Cadeddu, F. Dordei, C. Giunti, Y.F. Li, E. Picciau, and Y.Y. Zhang. Physics results from the first COHERENT observation of CEνNS in argon and their combination with cesium-iodide data. *Phys. Rev. D*, 102(1):015030, 2020. ↑74, ↑75, ↑97, ↑110, ↑128

[158] O.G. Miranda, D.K. Papoulias, G. Sanchez Garcia, O. Sanders, M. Tórtola, and J.W.F. Valle. Implications of the first detection of coherent elastic neutrino-nucleus scattering (cevns) with liquid argon. *Journal of High Energy Physics*, 2020(5), May 2020. ↑74

[159] J. M. Lattimer and M. Prakash. The physics of neutron stars. *Science*, 304:536–542, 2004. ↑74

[160] Andrew W. Steiner, Madappa Prakash, James M. Lattimer, and Paul J. Ellis. Isospin asymmetry in nuclei and neutron stars. *Phys. Rept.*, 411:325–375, 2005. ↑74, ↑124

[161] B. Alex Brown. Neutron radii in nuclei and the neutron equation of state. *Phys. Rev. Lett.*, 85:5296–5299, Dec 2000. ↑74, ↑124

[162] S. Typel and B. Alex Brown. Neutron radii and the neutron equation of state in relativistic models. *Phys. Rev. C*, 64:027302, Jun 2001. ↑74

[163] Daniel Z. Freedman. Coherent Neutrino Nucleus Scattering as a Probe of the Weak Neutral Current. *Phys. Rev.*, D9:1389–1392, 1974. ↑75

[164] F. J. Hasert et al. Observation of Neutrino Like Interactions Without Muon Or Electron in the Gargamelle Neutrino Experiment. *Phys. Lett. B*, 46:138–140, 1973. ↑75

[165] Vadim A. Bednyakov and Dmitry V. Naumov. Coherency and incoherency in neutrino-nucleus elastic and inelastic scattering. *Phys. Rev. D*, 98(5):053004, 2018. ↑75, ↑130

[166] A. Drukier and Leo Stodolsky. Principles and Applications of a Neutral Current Detector for Neutrino Physics and Astronomy. *Phys. Rev.*, D30:2295, 1984. ↑76

[167] J. Barranco, O. G. Miranda, and T. I. Rashba. Probing new physics with coherent neutrino scattering off nuclei. *JHEP*, 12:021, 2005. ↑76, ↑112, ↑131

[168] Kelly Patton, Jonathan Engel, Gail C. McLaughlin, and Nicolas Schunck. Neutrino-nucleus coherent scattering as a probe of neutron density distributions. *Phys. Rev.*, C86:024612, 2012. ↑76, ↑95

[169] Jens Erler and Shufang Su. The Weak Neutral Current. *Prog. Part. Nucl. Phys.*, 71:119–149, 2013. ↑77, ↑122, ↑168, ↑169

[170] M. Tanabashi et al. Review of Particle Physics. *Phys. Rev.*, D98(3):030001, 2018. ↑77, ↑79, ↑81, ↑96, ↑98, ↑99, ↑106, ↑108, ↑126, ↑127, ↑135, ↑139

[171] J. Alitti et al. A Determination of the strong coupling constant α_s from W production at the CERN $p\bar{p}$ collider. *Phys. Lett. B*, 263:563–572, 1991. ↑77

[172] J. Bernabeu, L. G. Cabral-Rosetti, J. Papavassiliou, and J. Vidal. On the charge radius of the neutrino. *Phys. Rev.*, D62:113012, 2000. ↑77, ↑80

[173] J. Bernabeu, J. Papavassiliou, and J. Vidal. On the observability of the neutrino charge radius. *Phys. Rev. Lett.*, 89:101802, 2002. ↑77, ↑80

[174] J. Bernabeu, J. Papavassiliou, and J. Vidal. The neutrino charge radius is a physical observable. *Nucl. Phys.*, B680:450, 2004. ↑77, ↑80

[175] J. Piekarewicz, A. R. Linero, P. Giuliani, and E. Chicken. Power of two: Assessing the impact of a second measurement of the weak-charge form factor of ^{208}Pb. *Phys. Rev.*, C94(3):034316, 2016. ↑78, ↑94, ↑97

[176] Spencer Klein and Joakim Nystrand. Exclusive vector meson production in relativistic heavy ion collisions. *Phys. Rev.*, C60:014903, 1999. ↑78, ↑94, ↑97

[177] Amir N. Khan and Werner Rodejohann. New physics from COHERENT data with improved Quenching Factors. ↑78, ↑83

[178] Dimitrios K. Papoulias. COHERENT constraints after the COHERENT-2020 quenching factor measurement. *Phys. Rev. D*, 102(11):113004, 2020. ↑78, ↑83

[179] J. Friedrich and N. Voegler. The salient features of charge density distributions of medium and heavy even-even nuclei determined from a systematic analysis of elastic electron scattering form factors. *Nucl. Phys.*, A373:192–224, 1982. ↑78

[180] A. Ong, J. C. Berengut, and V. V. Flambaum. The Effect of spin-orbit nuclear charge density corrections due to the anomalous magnetic moment on halonuclei. *Phys. Rev. C*, 82:014320, 2010. ↑78

[181] C. J. Horowitz et al. Weak charge form factor and radius of 208Pb through parity violation in electron scattering. *Phys. Rev. C*, 85:032501, 2012. ↑78, ↑123, ↑125

[182] Hans-Werner Hammer and Ulf-G Meißner. The proton radius: From a puzzle to precision. *Sci. Bull.*, 65:257–258, 2020. ↑79, ↑96

[183] M.S. Safronova, D. Budker, D. DeMille, Derek F. Jackson Kimball, A. Derevianko, and Charles W. Clark. Search for new physics with atoms and molecules. *Reviews of Modern Physics*, 90(2), 2018. ↑79, ↑98

[184] Carlo Giunti and Alexander Studenikin. Neutrino electromagnetic interactions: a window to new physics. *Rev. Mod. Phys.*, 87:531, 2015. ↑80, ↑82, ↑83, ↑106, ↑108

[185] M. Cadeddu, F. Dordei, C. Giunti, Y. F. Li, and Y. Y. Zhang. Neutrino, electroweak, and nuclear physics from COHERENT elastic neutrino-nucleus scattering with refined quenching factor. *Phys. Rev. D*, 101(3):033004, 2020. ↑80, ↑83, ↑97, ↑98, ↑100, ↑103, ↑106, ↑107, ↑110, ↑122

[186] Konstantin A. Kouzakov and Alexander I. Studenikin. Electromagnetic properties of massive neutrinos in low-energy elastic neutrino-electron scattering. *Phys. Rev. D*, 95(5):055013, 2017. [Erratum: Phys.Rev.D 96, 099904 (2017)]. ↑81, ↑82

[187] A. Grau and J.A. Grifols. Neutrino charge radius and substructure. *Phys.Lett.*, B166:233, 1986. ↑81

[188] G. Degrassi, A. Sirlin, and W. J. Marciano. Effective electromagnetic form-factor of the neutrino. *Phys. Rev.*, D39:287–294, 1989. ↑81

[189] P. Vogel and J. Engel. Neutrino electromagnetic form-factors. *Phys. Rev.*, D39:3378, 1989. ↑81

[190] C. Giunti and C. W. Kim. *Fundamentals of Neutrino Physics and Astrophysics*. Oxford University Press, Oxford, UK, 2007. ↑81, ↑133

[191] Carlo Giunti, Konstantin A. Kouzakov, Yu-Feng Li, Alexey V. Lokhov, Alexander I. Studenikin, and Shun Zhou. Electromagnetic neutrinos in laboratory experiments and astrophysics. *Annalen Phys.*, 528:198–215, 2016. ↑83

[192] D. K. Papoulias and T. S. Kosmas. COHERENT constraints to conventional and exotic neutrino physics. *Phys. Rev. D*, 97(3):033003, 2018. ↑83

[193] Amir N. Khan and Werner Rodejohann. New physics from COHERENT data with an improved quenching factor. *Phys. Rev. D*, 100(11):113003, 2019. ↑83

[194] O. G. Miranda, D. K. Papoulias, M. Tórtola, and J. W. F. Valle. Probing neutrino transition magnetic moments with coherent elastic neutrino-nucleus scattering. *JHEP*, 07:103, 2019. ↑83

[195] D. K. Papoulias, T. S. Kosmas, and Y. Kuno. Recent probes of standard and non-standard neutrino physics with nuclei. *Front. in Phys.*, 7:191, 2019. ↑83, ↑114

[196] John N. Bahcall, Aldo M. Serenelli, and Sarbani Basu. New solar opacities, abundances, helioseismology, and neutrino fluxes. *Astrophys. J. Lett.*, 621:L85–L88, 2005. ↑84

[197] John F. Beacom. The Diffuse Supernova Neutrino Background. *Ann. Rev. Nucl. Part. Sci.*, 60:439–462, 2010. ↑84

[198] M. Honda, T. Kajita, K. Kasahara, and S. Midorikawa. Improvement of low energy atmospheric neutrino flux calculation using the jam nuclear interaction model. *Phys. Rev. D*, 83:123001, Jun 2011. ↑84

[199] D. S. Akerib et al. Projected WIMP sensitivity of the LUX-ZEPLIN dark matter experiment. *Phys. Rev. D*, 101(5):052002, 2020. ↑86

[200] J. Aalbers et al. DARWIN: towards the ultimate dark matter detector. *JCAP*, 11:017, 2016. ↑86

[201] O. Moreno and T. W. Donnelly. Unified approach to electron and neutrino elastic scattering off nuclei with an application to the study of the axial structure. *Phys. Rev. C*, 92(5):055504, 2015. ↑88

[202] D Akimov et al. COHERENT Collaboration data release from the first observation of coherent elastic neutrino-nucleus scattering, April 2018. ↑88

[203] D. Akimov et al. COHERENT Collaboration data release from the first detection of coherent elastic neutrino-nucleus scattering on argon. 6 2020. ↑88

[204] D. Pershey. New coherent results, 2020. Talk presented at Magnificent CEνNS 2020, 16-20 November 2020. ↑89, ↑111, ↑119, ↑120, ↑121

[205] J. Engel, S. Pittel, and P. Vogel. Capture of solar and higher-energy neutrinos by ^{127}I. *Phys. Rev. C*, 50:1702–1708, Sep 1994. ↑89

[206] Rebecca Rapp. COHERENT Plans for D_2O at the Spallation Neutron Source. In *Meeting of the Division of Particles and Fields of the American Physical Society*, 10 2019. ↑89

[207] S. Abrahamyan et al. Measurement of the Neutron Radius of 208Pb Through Parity-Violation in Electron Scattering. *Phys. Rev. Lett.*, 108:112502, 2012. ↑92

[208] D. Akimov et al. First Constraint on Coherent Elastic Neutrino-Nucleus Scattering in Argon. *Phys. Rev. D*, 100(11):115020, 2019. ↑93

[209] Emilio Ciuffoli, Jarah Evslin, Qiang Fu, and Jian Tang. Extracting nuclear form factors with coherent neutrino scattering. *Phys. Rev.*, D97(11):113003, 2018. ↑95

[210] J. A. Maruhn, P. G. Reinhard, P. D. Stevenson, and A. S. Umar. The TDHF Code Sky3D. *Comput. Phys. Commun.*, 185:2195–2216, 2014. ↑96

[211] T. Niksic, N. Paar, D. Vretenar, and P. Ring. DIRHB - A relativistic self-consistent mean-field framework for atomic nuclei. *Comput. Phys. Commun.*, 185:1808–1821, 2014. ↑96

[212] J. I. Collar, A. R. L. Kavner, and C. M. Lewis. Response of CsI[Na] to Nuclear Recoils: Impact on Coherent Elastic Neutrino-Nucleus Scattering (CEνNS). *Phys. Rev. D*, 100(3):033003, 2019. ↑97, ↑100, ↑114, ↑116

[213] C. S. Wood, S. C. Bennett, D. Cho, B. P. Masterson, J. L. Roberts, C. E. Tanner, and Carl E. Wieman. Measurement of parity nonconservation and an anapole moment in cesium. *Science*, 275:1759–1763, 1997. ↑99, ↑111, ↑127, ↑139

[214] V. A. Dzuba, J. C. Berengut, V. V. Flambaum, and B. Roberts. Revisiting parity nonconservation in cesium. *Phys. Rev. Lett.*, 109:203003, 2012. ↑99, ↑111, ↑122, ↑127, ↑139

[215] P. L. Anthony et al. Precision measurement of the weak mixing angle in Moller scattering. *Phys. Rev. Lett.*, 95:081601, 2005. ↑99, ↑127, ↑139

[216] D. Wang et al. Measurement of parity violation in electron–quark scattering. *Nature*, 506(7486):67–70, 2014. ↑99, ↑127

[217] G. P. Zeller et al. A precise determination of electroweak parameters in neutrino nucleon scattering. *Phys. Rev. Lett.*, 88:091802, 2002. ↑99, ↑127, ↑139

[218] D. Androic et al. Precision measurement of the weak charge of the proton. *Nature*, 557(7704):207–211, 2018. ↑99, ↑127, ↑139

[219] M. Bender, K. Rutz, P.-G. Reinhard, J. A. Maruhn, and W. Greiner. Shell structure of superheavy nuclei in self-consistent mean-field models. *Physical Review C*, 60(3), 1999. ↑98

[220] M. Deniz et al. Measurement of Nu(e)-bar -Electron Scattering Cross-Section with a CsI(Tl) Scintillating Crystal Array at the Kuo-Sheng Nuclear Power Reactor. *Phys. Rev. D*, 81:072001, 2010. ↑101, ↑102, ↑103

[221] L. A. Ahrens et al. Determination of electroweak parameters from the elastic scattering of muon neutrinos and antineutrinos on electrons. *Phys. Rev. D*, 41:3297–3316, Jun 1990. ↑101, ↑102, ↑103

[222] Alexander Studenikin. New bounds on neutrino electric millicharge from limits on neutrino magnetic moment. *EPL*, 107(2):21001, 2014. [Erratum: EPL 107, 39901 (2014), Erratum: Europhys.Lett. 107, 39901 (2014)]. ↑106

[223] Jiunn-Wei Chen, Hsin-Chang Chi, Hau-Bin Li, C. P. Liu, Lakhwinder Singh, Henry T. Wong, Chih-Liang Wu, and Chih-Pan Wu. Constraints on millicharged neutrinos via analysis of data from atomic ionizations with germanium detectors at sub-keV sensitivities. *Phys. Rev. D*, 90(1):011301, 2014. ↑106

[224] L. B. Auerbach et al. Measurement of electron-neutrino electron elastic scattering. *Phys. Rev.*, D63:112001, 2001. ↑107, ↑108

[225] A.G. Beda, V.B. Brudanin, V.G. Egorov, D.V. Medvedev, V.S. Pogosov, et al. The results of search for the neutrino magnetic moment in GEMMA experiment. *Adv.High Energy Phys.*, 2012:350150, 2012. ↑108

[226] Dimitrios K. Papoulias. COHERENT constraints after the Chicago-3 quenching factor measurement. 7 2019. ↑110, ↑114, ↑116

[227] Amir N. Khan and Werner Rodejohann. New physics from coherent data with an improved quenching factor. *Physical Review D*, 100(11), Dec 2019. ↑110

[228] M. Cadeddu, F. Dordei, C. Giunti, K.A. Kouzakov, E. Picciau, and A.I. Studenikin. Potentialities of a low-energy detector based on he4 evaporation to observe atomic effects in coherent neutrino scattering and physics perspectives. *Physical Review D*, 100(7), Oct 2019. ↑110, ↑128, ↑131

[229] C. Giunti. General COHERENT constraints on neutrino nonstandard interactions. *Phys. Rev. D*, 101(3):035039, 2020. ↑110

[230] Julien Billard, Joseph Johnston, and Bradley J. Kavanagh. Prospects for exploring new physics in coherent elastic neutrino-nucleus scattering. *Journal of Cosmology and Astroparticle Physics*, 2018(11):016–016, Nov 2018. ↑110, ↑112, ↑113

[231] Tao Han, Jiajun Liao, Hongkai Liu, and Danny Marfatia. Nonstandard neutrino interactions at coherent, dune, t2hk and lhc. *Journal of High Energy Physics*, 2019(11), Nov 2019. ↑110, ↑113, ↑114

[232] Wolfgang Altmannshofer, Stefania Gori, Justo Martín-Albo, Alexandre Sousa, and Michael Wallbank. Neutrino Tridents at DUNE. *Phys. Rev. D*, 100(11):115029, 2019. ↑110, ↑113, ↑118

[233] G. W. Bennett, B. Bousquet, H. N. Brown, G. Bunce, R. M. Carey, P. Cushman, G. T. Danby, P. T. Debevec, M. Deile, H. Deng, and et al. Final report of the e821 muon anomalous magnetic moment measurement at bnl. *Physical Review D*, 73(7), Apr 2006. ↑110, ↑115, ↑116, ↑117, ↑118

[234] B. Abi et al. Measurement of the Positive Muon Anomalous Magnetic Moment to 0.46 ppm. *Phys. Rev. Lett.*, 126(14):141801, 2021. ↑110

[235] T. Aoyama et al. The anomalous magnetic moment of the muon in the standard model, 2020. ↑110, ↑115, ↑116, ↑117, ↑118

[236] M. Cadeddu, N. Cargioli, F. Dordei, C. Giunti, Y. F. Li, E. Picciau, and Y. Y. Zhang. Constraints on light vector mediators through coherent elastic neutrino nucleus scattering data from COHERENT. *JHEP*, 01:116, 2021. ↑110, ↑119

[237] J. Guena, M. Lintz, and M. A. Bouchiat. Measurement of the parity violating 6S-7S transition amplitude in cesium achieved within 2 x 10(-13) atomic-unit accuracy by stimulated-emission detection. *Phys. Rev. A*, 71:042108, 2005. ↑111

[238] A. Trzcińska, J. Jastrzębski, P. Lubiński, F. J. Hartmann, R. Schmidt, T. von Egidy, and B. Kłos. Neutron density distributions deduced from antiprotonic atoms. *Phys. Rev. Lett.*, 87:082501, Aug 2001. ↑111, ↑126

[239] M. Cadeddu, N. Cargioli, F. Dordei, C. Giunti, Y. F. Li, E. Picciau, C. A. Ternes, and Y. Y. Zhang. New insights into nuclear physics and weak mixing angle using electroweak probes. 2 2021. ↑111, ↑128

[240] *Neutrino Non-Standard Interactions: A Status Report*, volume 2, 2019. ↑111

[241] C. Giunti. General coherent constraints on neutrino nonstandard interactions. *Physical Review D*, 101(3), Feb 2020. ↑111

[242] Mohammad Abdullah, James B. Dent, Bhaskar Dutta, Gordon L. Kane, Shu Liao, and Louis E. Strigari. Coherent elastic neutrino nucleus scattering as a probe of a Z through kinetic and mass mixing effects. *Phys. Rev. D*, 98(1):015005, 2018. ↑114

[243] Alexis Aguilar-Arevalo, Xavier Bertou, Carla Bonifazi, Gustavo Cancelo, Brenda Aurea Cervantes-Vergara, Claudio Chavez, Juan C. D'Olivo, João C. dos Anjos, Juan Estrada, and et al. Search for light mediators in the low-energy data of the connie reactor neutrino experiment. *Journal of High Energy Physics*, 2020(4), Apr 2020. ↑115, ↑116

[244] J.P. Lees, V. Poireau, V. Tisserand, E. Grauges, A. Palano, G. Eigen, B. Stugu, D.N. Brown, M. Feng, L.T. Kerth, and et al. Search for a dark photon ine+ecollisions atbabar. *Physical Review Letters*, 113(20), Nov 2014. ↑117

[245] Roel Aaij et al. Search for $A' \to \mu^+\mu^-$ Decays. *Phys. Rev. Lett.*, 124(4):041801, 2020. ↑117

[246] Betty Abelev et al. Centrality Dependence of Charged Particle Production at Large Transverse Momentum in Pb–Pb Collisions at $\sqrt{s_{\rm NN}} = 2.76$ TeV. *Phys. Lett. B*, 720:52–62, 2013. ↑117

[247] A. Adare et al. Search for dark photons from neutral meson decays in $p + p$ and $d + \mathrm{Au}$ collisions at $\sqrt{s_{NN}} = 200\mathrm{GeV}$. *Phys. Rev. C*, 91:031901, Mar 2015. ↑117

[248] J.R. Batley et al. Search for the dark photon in π^0 decays. *Phys. Lett. B*, 746:178–185, 2015. ↑117

[249] H. Merkel et al. Search for light gauge bosons of the dark sector at the mainz microtron. *Phys. Rev. Lett.*, 106:251802, Jun 2011. ↑117

[250] H. Merkel et al. Search at the Mainz Microtron for Light Massive Gauge Bosons Relevant for the Muon g-2 Anomaly. *Phys. Rev. Lett.*, 112(22):221802, 2014. ↑117

[251] Roni Harnik, Joachim Kopp, and Pedro A.N. Machado. Exploring nu Signals in Dark Matter Detectors. *JCAP*, 07:026, 2012. ↑117, ↑118

[252] A. Bross, M. Crisler, S. Pordes, J. Volk, S. Errede, and J. Wrbanek. Search for short-lived particles produced in an electron beam dump. *Phys. Rev. Lett.*, 67:2942–2945, Nov 1991. ↑117

[253] E. M. Riordan et al. Search for short-lived axions in an electron-beam-dump experiment. *Phys. Rev. Lett.*, 59:755–758, Aug 1987. ↑117

[254] M. Davier and H. Nguyen Ngoc. An unambiguous search for a light higgs boson. *Physics Letters B*, 229(1):150 – 155, 1989. ↑117

[255] Johannes Blumlein and Jurgen Brunner. New Exclusion Limits for Dark Gauge Forces from Beam-Dump Data. *Phys. Lett. B*, 701:155–159, 2011. ↑117

[256] J. D. Bjorken, S. Ecklund, W. R. Nelson, A. Abashian, C. Church, B. Lu, L. W. Mo, T. A. Nunamaker, and P. Rassmann. Search for neutral metastable penetrating particles produced in the slac beam dump. *Phys. Rev. D*, 38:3375–3386, Dec 1988. ↑117

[257] Search for axion-like particle production in 400 GeV proton-copper interactions. *Physics Letters B*, 157(5):458 – 462, 1985. ↑117

[258] C. Athanassopoulos et al. Evidence for $\nu_\mu \to \nu_e$ oscillations from pion decay in flight neutrinos. *Phys. Rev. C*, 58:2489–2511, 1998. ↑117

[259] Manfred Lindner, Farinaldo S. Queiroz, Werner Rodejohann, and Xun-Jie Xu. Neutrino-electron scattering: general constraints on Z' and dark photon models. *JHEP*, 05:098, 2018. ↑117

[260] Hooman Davoudiasl and William J. Marciano. Tale of two anomalies. *Phys. Rev. D*, 98(7):075011, 2018. ↑117

[261] Philip Ilten, Yotam Soreq, Mike Williams, and Wei Xue. Serendipity in dark photon searches. *JHEP*, 06:004, 2018. ↑117

[262] O.G. Miranda, D.K. Papoulias, G. Sanchez Garcia, O. Sanders, M. Tórtola, and J.W.F. Valle. Implications of the first detection of coherent elastic neutrino-nucleus scattering (CEvNS) with Liquid Argon. *JHEP*, 05:130, 2020. ↑118

[263] Wolfgang Altmannshofer, Stefania Gori, Maxim Pospelov, and Itay Yavin. Neutrino trident production: A powerful probe of new physics with neutrino beams. *Physical Review Letters*, 113(9), Aug 2014. ↑118

[264] Wolfgang Altmannshofer, Stefania Gori, Stefano Profumo, and Farinaldo S. Queiroz. Explaining dark matter and B decay anomalies with an $L_\mu - L_\tau$ model. *JHEP*, 12:106, 2016. ↑118

[265] Georges Aad et al. Measurements of Four-Lepton Production at the Z Resonance in pp Collisions at $\sqrt{s}$ =7 and 8 TeV with ATLAS. *Phys. Rev. Lett.*, 112(23):231806, 2014. ↑118

[266] A.M. Sirunyan, A. Tumasyan, W. Adam, F. Ambrogi, E. Asilar, T. Bergauer, J. Brandstetter, M. Dragicevic, J. Erö, A. Escalante Del Valle, and et al. Search for an ll gauge boson using z→4 events in proton-proton collisions at s=13 tev. *Physics Letters B*, 792:345–368, May 2019. ↑118

[267] J.P. Lees et al. Search for a muonic dark force at BABAR. *Phys. Rev. D*, 94(1):011102, 2016. ↑118

[268] Ayuki Kamada and Hai-Bo Yu. Coherent Propagation of PeV Neutrinos and the Dip in the Neutrino Spectrum at IceCube. *Phys. Rev. D*, 92(11):113004, 2015. ↑118

[269] Sergei Gninenko and Dmitry Gorbunov. Refining constraints from Borexino measurements on a light Z'-boson coupled to L_μ-L_τ current. 7 2020. ↑118

[270] do. Amaral, Dorian Warren Praia, David G. Cerdeno, Patrick Foldenauer, and Elliott Reid. Solar neutrino probes of the muon anomalous magnetic moment in the gauged $U(1)_{L_\mu - L_\tau}$. 6 2020. ↑119

[271] A. Konovalov. COHERENT, 2020. Talk presented at Magnificent CEνNS 2020, 16-20 November 2020. ↑119, ↑120

[272] Martin Hoferichter, Javier Menéndez, and Achim Schwenk. Coherent elastic neutrino-nucleus scattering: Eft analysis and nuclear responses. *Physical Review D*, 102(7), Oct 2020. ↑120

[273] S. L. Gilbert, M. C. Noecker, R. N. Watts, and C. E. Wieman. Measurement of parity nonconservation in atomic cesium. *Phys. Rev. Lett.*, 55:2680–2683, Dec 1985. ↑121

[274] P.A. Zyla et al. Review of Particle Physics. *PTEP*, 2020(8):083C01, 2020. ↑122, ↑126, ↑169

[275] Jens Erler, Charles J. Horowitz, Sonny Mantry, and Paul A. Souder. Weak Polarized Electron Scattering. *Ann. Rev. Nucl. Part. Sci.*, 64:269–298, 2014. ↑122, ↑168, ↑169

[276] Andrei Derevianko. Correlated many-body treatment of the breit interaction with application to cesium atomic properties and parity violation. *Phys. Rev. A*, 65:012106, Dec 2001. ↑122

[277] A. V. Viatkina, D. Antypas, M. G. Kozlov, D. Budker, and V. V. Flambaum. Dependence of atomic parity-violation effects on neutron skins and new physics. *Phys. Rev. C*, 100:034318, Sep 2019. ↑122, ↑170

[278] Matteo Cadeddu and Francesca Dordei. Reinterpreting the weak mixing angle from atomic parity violation in view of the Cs neutron rms radius measurement from COHERENT. *Phys. Rev. D*, 99(3):033010, 2019. ↑122, ↑139

[279] S. J. Pollock, E. N. Fortson, and L. Wilets. Atomic parity nonconservation: Electroweak parameters and nuclear structure. *Phys. Rev. C*, 46:2587–2600, Dec 1992. ↑122

[280] S.J Pollock and M.C Welliver. Effects of neutron spatial distributions on atomic parity nonconservation in cesium. *Physics Letters B*, 464(3-4):177–182, Oct 1999. ↑122

[281] J James and P G H Sandars. A parametric approach to nuclear size and shape in atomic parity nonconservation. *Journal of Physics B: Atomic, Molecular and Optical Physics*, 32(14):3295–3307, jul 1999. ↑122, ↑170

[282] C. J. Horowitz, S. J. Pollock, P. A. Souder, and R. Michaels. Parity violating measurements of neutron densities. *Physical Review C*, 63(2), Jan 2001. ↑122

[283] S. Abrahamyan, Z. Ahmed, H. Albataineh, K. Aniol, D. S. Armstrong, W. Armstrong, T. Averett, B. Babineau, A. Barbieri, V. Bellini, and et al. Measurement of the neutron radius of ^{208}Pb through parity violation in electron scattering. *Physical Review Letters*, 108(11), Mar 2012. ↑123, ↑125

[284] D. Adhikari et al. An Accurate Determination of the Neutron Skin Thickness of ^{208}Pb through Parity-Violation in Electron Scattering, 2 2021. ↑123, ↑125

[285] B. Reed. Measuring the weak charge radius of ^{208}Pb with prex-ii. *Presentation on behalf of the PREX-II Collaboration at the Magnificent CEvNS 2020 workshop*, 2020. ↑123, ↑125

[286] Junjie Yang, Jesse A. Hernandez, and J. Piekarewicz. Electroweak probes of ground state densities. *Phys. Rev. C*, 100(5):054301, 2019. ↑123

[287] Hao Zheng, Zhen Zhang, and Lie-Wen Chen. Form Factor Effects in the Direct Detection of Isospin-Violating Dark Matter. *JCAP*, 08:011, 2014. ↑123

[288] Tapas Sil, M. Centelles, X. Vinas, and J. Piekarewicz. Atomic parity non-conservation, neutron radii, and effective field theories of nuclei. *Phys. Rev. C*, 71:045502, 2005. ↑123

[289] J. Piekarewicz, B. K. Agrawal, G. Colò, W. Nazarewicz, N. Paar, P.-G. Reinhard, X. Roca-Maza, and D. Vretenar. Electric dipole polarizability and the neutron skin. *Phys. Rev. C*, 85:041302, Apr 2012. ↑123

[290] Tong-Gang Yue, Lie-Wen Chen, Zhen Zhang, and Ying Zhou. Constraints on the Symmetry Energy from PREX-II in the Multimessenger Era, 2 2021. ↑123, ↑125

[291] M. Baldo and G. F. Burgio. The nuclear symmetry energy. *Prog. Part. Nucl. Phys.*, 91:203–258, 2016. ↑124

[292] Zhen Zhang and Lie-Wen Chen. Constraining the symmetry energy at subsaturation densities using isotope binding energy difference and neutron skin thickness. *Phys. Lett. B*, 726:234–238, 2013. ↑124

[293] R. J. Furnstahl. Neutron radii in mean field models. *Nucl. Phys. A*, 706:85–110, 2002. ↑124

[294] X. Roca-Maza, M. Centelles, X. Viñas, and M. Warda. Neutron skin of ^{208}Pb, nuclear symmetry energy, and the parity radius experiment. *Phys. Rev. Lett.*, 106:252501, Jun 2011. ↑124

[295] M. Warda, X. Vinas, X. Roca-Maza, and M. Centelles. Neutron skin thickness in droplet model with surface width dependence: Indications of softness of the nuclear symmetry energy. *Phys. Rev. C*, 80:024316, 2009. ↑124

[296] C. J. Horowitz and J. Piekarewicz. Neutron star structure and the neutron radius of ^{208}pb. *Phys. Rev. Lett.*, 86:5647–5650, Jun 2001. ↑124

[297] Brendan T. Reed, F. J. Fattoyev, C. J. Horowitz, and J. Piekarewicz. Implications of PREX-II on the equation of state of neutron-rich matter, 2021. ↑125

[298] F. J. Fattoyev and J. Piekarewicz. Has a thick neutron skin in ^{208}Pb been ruled out? *Phys. Rev. Lett.*, 111:162501, Oct 2013. ↑125

[299] C. Drischler, R. J. Furnstahl, J. A. Melendez, and D. R. Phillips. How well do we know the neutron-matter equation of state at the densities inside neutron stars? a bayesian approach with correlated uncertainties. *Phys. Rev. Lett.*, 125:202702, Nov 2020. ↑125

[300] Ingo Tews, James M. Lattimer, Akira Ohnishi, and Evgeni E. Kolomeitsev. Symmetry parameter constraints from a lower bound on neutron-matter energy. *The Astrophysical Journal*, 848(2):105, Oct 2017. ↑125

[301] M. B. Tsang, Yingxun Zhang, P. Danielewicz, M. Famiano, Zhuxia Li, W. G. Lynch, and A. W. Steiner. Constraints on the density dependence of the symmetry energy. *Phys. Rev. Lett.*, 102:122701, Mar 2009. ↑125

[302] Lie-Wen Chen, Che Ming Ko, Bao-An Li, and Jun Xu. Density slope of the nuclear symmetry energy from the neutron skin thickness of heavy nuclei. *Phys. Rev. C*, 82:024321, Aug 2010. ↑125

[303] Luca Trippa, Gianluca Colò, and Enrico Vigezzi. Giant dipole resonance as a quantitative constraint on the symmetry energy. *Phys. Rev. C*, 77:061304, Jun 2008. ↑125

[304] A. Tamii et al. Complete electric dipole response and the neutron skin in ^{208}Pb. *Phys. Rev. Lett.*, 107:062502, Aug 2011. ↑125

[305] X. Roca-Maza et al. Electric dipole polarizability in ^{208}pb: Insights from the droplet model. *Phys. Rev. C*, 88:024316, Aug 2013. ↑125

[306] M. Kortelainen et al. Nuclear energy density optimization. *Phys. Rev. C*, 82:024313, Aug 2010. ↑125

[307] B.P. Abbott, R. Abbott, T.D. Abbott, F. Acernese, K. Ackley, C. Adams, T. Adams, P. Addesso, R.X. Adhikari, V.B. Adya, and et al. Gw170817: Observation of gravitational waves from a binary neutron star inspiral. *Physical Review Letters*, 119(16), Oct 2017. ↑125

[308] B.P. Abbott, R. Abbott, T.D. Abbott, F. Acernese, K. Ackley, C. Adams, T. Adams, P. Addesso, R.X. Adhikari, V.B. Adya, and et al. Gw170817: Measurements of neutron star radii and equation of state. *Physical Review Letters*, 121(16), Oct 2018. ↑125

[309] F. J. Fattoyev, J. Piekarewicz, and C. J. Horowitz. Neutron skins and neutron stars in the multimessenger era. *Phys. Rev. Lett.*, 120:172702, Apr 2018. ↑125

[310] Jens Erler and Michael J. Ramsey-Musolf. The Weak mixing angle at low energies. *Phys. Rev.*, D72:073003, 2005. ↑126

[311] Jens Erler and Rodolfo Ferro-Hernández. Weak Mixing Angle in the Thomson Limit. *JHEP*, 03:196, 2018. ↑126

[312] M. Thiel, C. Sfienti, J. Piekarewicz, C. J. Horowitz, and M. Vanderhaeghen. Neutron skins of atomic nuclei: per aspera ad astra. *J. Phys. G*, 46(9):093003, 2019. ↑126

[313] D. Akimov et al. Coherent 2018 at the spallation neutron source, 2018. ↑128

[314] H. Bonet, A. Bonhomme, C. Buck, K. Fülber, J. Hakenmüller, G. Heusser, T. Hugle, M. Lindner, W. Maneschg, T. Rink, and et al. Constraints on elastic neutrino nucleus scattering in the fully coherent regime from the conus experiment. *Physical Review Letters*, 126(4), Jan 2021. ↑128

[315] Hooman Davoudiasl, Hye-Sung Lee, and William J. Marciano. Muon anomaly and dark parity violation. *Phys. Rev. Lett.*, 109:031802, Jul 2012. ↑128

[316] Hooman Davoudiasl, Hye-Sung Lee, and William J. Marciano. Muon $g2$, rare kaon decays, and parity violation from dark bosons. *Phys. Rev. D*, 89(9):095006, 2014. ↑128

[317] Hooman Davoudiasl, Hye-Sung Lee, and William J. Marciano. Low Q^2 weak mixing angle measurements and rare higgs decays. *Phys. Rev. D*, 92:055005, Sep 2015. ↑128

[318] M. Cadeddu, N. Cargioli, F. Dordei, C. Giunti, and E. Picciau. Muon and electron g-2 and proton and cesium weak charges implications on dark Zd models. *Phys. Rev. D*, 104(1):011701, 2021. ↑128

[319] Dominik Becker et al. The P2 experiment. *Eur. Phys. J. A*, 54(11):208, 2018. ↑128

[320] J. Benesch et al. The MOLLER Experiment: An Ultra-Precise Measurement of the Weak Mixing Angle Using M\oller Scattering, 2014. ↑128

[321] Andre de Gouvea, Pedro A. N. Machado, Yuber F. Perez-Gonzalez, and Zahra Tabrizi. Measuring the Weak Mixing Angle in the DUNE Near Detector Complex. *Phys. Rev. Lett.*, 125(5):051803, 2020. ↑128

[322] Guillermo Fernandez-Moroni, Pedro A. N. Machado, Ivan Martinez-Soler, Yuber F. Perez-Gonzalez, Dario Rodrigues, and Salvador Rosauro-Alcaraz. The physics potential of a reactor neutrino experiment with skipper ccds: measuring the weak mixing angle. *Journal of High Energy Physics*, 2021(3), Mar 2021. ↑128

[323] B.C. Cañas, E.A. Garcés, O.G. Miranda, and A. Parada. Future perspectives for a weak mixing angle measurement in coherent elastic neutrino nucleus scattering experiments. *Physics Letters B*, 784:159–162, Sep 2018. ↑128

[324] L. M. Sehgal and M. Wanninger. Atomic effects in coherent neutrino scattering. *Physics Letters B*, 171(1):107–112, apr 1986. ↑130, ↑131, ↑132

[325] Humphrey J. Maris, George M. Seidel, and Derek Stein. Dark Matter Detection Using Helium Evaporation and Field Ionization. *Phys. Rev. Lett.*, 119(18):181303, 2017. ↑130, ↑133, ↑134

[326] S. Betts et al. Development of a Relic Neutrino Detection Experiment at PTOLEMY: Princeton Tritium Observatory for Light, Early-Universe, Massive-Neutrino Yield. In *Proceedings, 2013 Community Summer Study on the Future of U.S. Particle Physics: Snowmass on the Mississippi (CSS2013): Minneapolis, MN, USA, July 29-August 6, 2013*, 2013. ↑131

[327] M. G. Betti et al. Neutrino physics with the PTOLEMY project: active neutrino properties and the light sterile case. *JCAP*, 1907:047, 2019. ↑131

[328] Yu. V. Gaponov and V.N. Tikhonov. Elastic scattering of low energy neutrinos by atomic systems. *Yadernaya Fizika*, 26(9):594–600, 1977. ↑131, ↑132

[329] Kelly Patton, Jonathan Engel, Gail C. McLaughlin, and Nicolas Schunck. Neutrino-nucleus coherent scattering as a probe of neutron density distributions. *Phys. Rev. C*, 86:024612, Aug 2012. ↑131

[330] D. Aristizabal Sierra, Jiajun Liao, and D. Marfatia. Impact of form factor uncertainties on interpretations of coherent elastic neutrino-nucleus scattering data. *JHEP*, 06:141, 2019. ↑132

[331] P. A. Doyle and P. S. Turner. Relativistic Hartree–Fock X-ray and electron scattering factors. *Acta Crystallographica Section A*, 24(3):390–397, May 1968. ↑132

[332] P. J. Brown et al. Intensity of diffracted intensities. *International Tables for Crystallography*, C ch. 6.1(ch. 6.1):554–595, 2006. ↑132, ↑142

[333] A. J. Thakkar and V. H. Smith, Jnr. High-accuracy *ab initio* form factors for the hydride anion and isoelectronic species. *Acta Crystallographica Section A*, 48(1):70–71, Jan 1992. ↑132

[334] M A Coulthard. A relativistic hartree-fock atomic field calculation. *Proceedings of the Physical Society*, 91(1):44–49, may 1967. ↑133

[335] Ajit J. Thakkar and Vedene H. Smith. Compact and accurate integral-transform wave functions. i. the 1^1s state of the helium-like ions from h^- through mg^{10+}. *Phys. Rev. A*, 15:1–15, Jan 1977. ↑133

[336] Glen Cowan, Kyle Cranmer, Eilam Gross, and Ofer Vitells. Asymptotic formulae for likelihood-based tests of new physics. *Eur. Phys. J.*, C71:1554, 2011. [Erratum: Eur. Phys. J.C73,2501(2013)]. ↑136

[337] S. A. Hertel, A. Biekert, J. Lin, V. Velan, and D. N. McKinsey. A Path to the Direct Detection of sub-GeV Dark Matter Using Calorimetric Readout of a Superfluid ^{4}He Target. 2018. ↑137

[338] M. S. Safronova, D. Budker, D. DeMille, Derek F. Jackson Kimball, A. Derevianko, and C. W. Clark. Search for New Physics with Atoms and Molecules. *Rev. Mod. Phys.*, 90(2):025008, 2018. ↑139

[339] Hooman Davoudiasl, Hye-Sung Lee, and William J. Marciano. 'Dark' Z implications for Parity Violation, Rare Meson Decays, and Higgs Physics. *Phys. Rev.*, D85:115019, 2012. ↑139

[340] Hooman Davoudiasl, Hye-Sung Lee, and William J. Marciano. Muon Anomaly and Dark Parity Violation. *Phys. Rev. Lett.*, 109:031802, 2012. ↑139

[341] Hooman Davoudiasl, Hye-Sung Lee, and William J. Marciano. Low Q^2 weak mixing angle measurements and rare Higgs decays. *Phys. Rev.*, D92(5):055005, 2015. ↑139, ↑140

[342] Yonit Hochberg, Yue Zhao, and Kathryn M. Zurek. Superconducting Detectors for Superlight Dark Matter. *Phys. Rev. Lett.*, 116(1):011301, 2016. ↑141

[343] Philip C. Bunting, Giorgio Gratta, Tom Melia, and Surjeet Rajendran. Magnetic Bubble Chambers and Sub-GeV Dark Matter Direct Detection. *Phys. Rev.*, D95(9):095001, 2017. ↑141

[344] Simon Knapen, Tongyan Lin, Matt Pyle, and Kathryn M. Zurek. Detection of Light Dark Matter With Optical Phonons in Polar Materials. *Phys. Lett.*, B785:386–390, 2018. ↑141

[345] Yonit Hochberg, Yonatan Kahn, Mariangela Lisanti, Kathryn M. Zurek, Adolfo G. Grushin, Roni Ilan, Sinéad M. Griffin, Zhen-Fei Liu, Sophie F. Weber, and Jeffrey B. Neaton. Detection of sub-MeV Dark Matter with Three-Dimensional Dirac Materials. *Phys. Rev.*, D97(1):015004, 2018. ↑141

[346] Noah Alexander Kurinsky, To Chin Yu, Yonit Hochberg, and Blas Cabrera. Diamond Detectors for Direct Detection of Sub-GeV Dark Matter. *Phys. Rev.*, D99(12):123005, 2019. ↑141

[347] W. J. Marciano and A. Sirlin. Radiative corrections to atomic parity violation. *Phys. Rev. D*, 27:552–556, Feb 1983. ↑168

[348] W. J. Marciano and A. Sirlin. Some general properties of the $o(\alpha)$ corrections to parity violation in atoms. *Phys. Rev. D*, 29:75–88, Jan 1984. ↑168

[349] J. Alitti, Giovanna Ambrosini, Reza Ansari, D. Autiero, P. Bareyre, Iain Bertram, G. Blaylock, P. Bonamy, Maurizio Bonesini, K. Borer, M. Bourliaud, D. Buskulic, G. Carboni, D. Cavalli, V. Cavasinni, Patrizia Cenci, J.C. Chollet, C. Conta, Giliano Costa, and Enrico Iacopini. A determination of the strong coupling constant s from w production at the cern pp collider. *Physics Letters B*, 263:563–572, 07 1991. ↑169

A

APV CALCULATION DETAILS

In the following appendices we provide additional details of Chap. 6. We present the APV weak charge calculation and we describe the calculation of the nuclear integrals q_p and q_n that determine the neutron skin correction to the weak charge in APV experiments.

A.1 APV Weak Charge Calculation

In order to determine the APV weak charge, $Q_W^{\rm th}$, it is necessary to study in detail the calculation of the couplings, taking into account the radiative corrections. Following Refs. [169,275,347,348] the lepton-fermion couplings are

$$\begin{aligned} g_{AV}^{\ell f} &= \rho\Big[-\frac{1}{2}+2Q_f\hat{s}_0^2-2Q_f\varnothing_{\ell Z}+\boxtimes_{ZZ}^{\ell f}+\boxtimes_{\gamma Z}^{\ell f}\Big] \\ &- 2Q_f\varnothing_{\ell W}+\square_{WW}, \quad \text{for } f=u, \end{aligned} \tag{A.1}$$

$$\begin{aligned} g_{AV}^{\ell f} &= \rho\Big[\frac{1}{2}+2Q_f\hat{s}_0^2-2Q_f\varnothing_{\ell Z}+\boxtimes_{ZZ}^{\ell f}+\boxtimes_{\gamma Z}^{\ell f}\Big] \\ &- 2Q_f\varnothing_{\ell W+WW}, \quad \text{for } f=d. \end{aligned} \tag{A.2}$$

In these relations for up and down quarks, $\rho = 1.00063$ represents a low-energy correction for neutral-current processes and Q_f is the fermion charge. Here $\hat{s}_0^2 = \sin^2\vartheta_W^{\rm SM}$, which keeps the same value for $\mu < \mathcal{O}(0.1\ \text{GeV})$. The other corrections inserted in equations (A.1)-(A.2) come from different contributions, such as electron charge radii ($\varnothing_{eW}$,$\varnothing_{eZ}$), EW box diagrams ($\boxtimes_{ZZ}^{\ell f}$, $\square_{WW}$, $_{WW}$) and vacuum polarization of γZ diagrams ($\boxtimes_{\gamma Z}^{\ell f}$) [275]. They can be expressed as

$$\varnothing_{\ell W} = \frac{2\alpha}{9\pi}, \tag{A.3a}$$

$$\varnothing_{\ell Z} = \frac{\alpha}{6\pi}Q_\ell g_{VA}^{\ell\ell}\Big(\ln\frac{M_Z^2}{m_\ell^2}+\frac{1}{6}\Big), \tag{A.3b}$$

$$\begin{aligned} \boxtimes_{ZZ}^{\ell f} &= -\frac{3\hat{\alpha}_Z}{16\pi\hat{s}_Z^2\hat{c}_Z^2}\Big(g_{VA}^{\ell f}g_{VV}^{\ell f}+g_{AV}^{\ell f}g_{AA}^{\ell f}\Big)\times \\ &\quad \Big[1-\frac{\hat{\alpha}_s(M_Z)}{\pi}\Big], \end{aligned} \tag{A.3c}$$

$$\boxtimes_{\gamma Z}^{\ell f} = \frac{3\hat{\alpha}_{fZ}}{2\pi}Q_f g_{VA}^{\ell f}\Big(\ln\frac{M_Z^2}{m_f^2}+\frac{3}{2}\Big), \tag{A.3d}$$

$$\square_{WW} = -\frac{\hat{\alpha}_Z}{2\pi\hat{s}_Z^2}\Big[1-\frac{\hat{\alpha}_s(M_W)}{2\pi}\Big], \tag{A.3e}$$

$$_{WW} = \frac{\hat{\alpha}_Z}{8\pi\hat{s}_Z^2}\Big[1+\frac{\hat{\alpha}_s(M_W)}{\pi}\Big]. \tag{A.3f}$$

In the expressions above, ℓ indicates the lepton involved in the interaction (in our case $\ell = e$), while f indicates the quarks (in our case $f = u, d$).
For the electromagnetic-running coupling we adopt the abbreviation $\hat{\alpha}_{ij} \equiv \hat{\alpha}(\sqrt{m_i M_j})$ and $\hat{\alpha}_Z \equiv \alpha(M_Z)$. In particular, $\hat{\alpha}_{fZ}$, that is present in the $\boxtimes_{\gamma Z}^{\ell f}$

contribution in Eq. (A.3d), is evaluated considering the quark masses equal to the proton one, and inside the logarithmic term the same value ($m_q = m_p$) is used. For the strong coupling, we use the values $\hat{\alpha}_s(M_Z) = 0.1185$ [274] and $\hat{\alpha}_s(M_W) = 0.123$ [349].

Inside the correction diagrams in Eqs. (A.3b), (A.3c), (A.3d), the neutral-current couplings enter at tree level and can be written as [169]

$$g_V^f \equiv \sqrt{2}\frac{T_f^3 - 2Q_f \sin^2\vartheta_W(\mu)}{\cos\vartheta_W(\mu)}, \tag{A.4}$$

$$g_A^f \equiv \sqrt{2}\frac{T_f^3}{\cos\vartheta_W(\mu)}. \tag{A.5}$$

Their products are defined as

$$g_{\alpha\beta}^{\ell f} = \cos^2\vartheta_W(\mu) g_\alpha^\ell g_\beta^f \quad \text{for } \alpha,\beta = V,A. \tag{A.6}$$

It is important to remark, as reported in Ref. [275], that for the EW box corrections (Eqs. (A.3c), (A.3e), (A.3f)) the sine is evaluated at the value of the Z mass, $\hat{s}_Z^2 \equiv \sin^2\hat{\theta}_W(M_Z) = 0.23121$ [274], while in the $\boxtimes_{\gamma Z}^{\ell f}$ term (Eq. (A.3d)) the sine is evaluated at scale $\mu = \sqrt{m_p M_Z}$. Finally, inside the $\oslash_{\ell Z}$ term (Eq. (A.3b)) the coupling $g_{VA}^{\ell\ell}$ is obtained using the value $\sin^2\theta_W(\sqrt{m_\ell M_Z})$ as discussed in Ref. [275].
In order to determine the couplings to the proton and to the neutron it is sufficient to use the fact that

$$g_{AV}^{ep} = 2g_{AV}^{eu} + g_{AV}^{ed}, \tag{A.7}$$

$$g_{AV}^{en} = g_{AV}^{eu} + 2g_{AV}^{ed}. \tag{A.8}$$

However, as pointed out in Refs. [169, 275], it is necessary to take into account also a correction relative to the $\boxtimes_{\gamma Z}^{\ell f}$ contribution, and this is obtained by adding to the proton and neutron couplings some small constants such that

$$g_{AV}^{ep} \to g_{AV}^{ep} + 0.00005, \tag{A.9}$$

$$g_{AV}^{en} \to g_{AV}^{en} + 0.00006, \tag{A.10}$$

obtaining the theoretical expression for the APV weak charge written in Eq. (7).

A.2 Nuclear integrals calculation

The approach used to model the nuclear size and shape of the nucleus in APV experiments is based on Refs. [277, 281], where the interaction matrix is proportional to the electroweak couplings to protons and neutrons

$$\mathcal{M} \propto G_{\mathrm{F}} \widetilde{Q}_W . \tag{A.11}$$

Here G_{F} is the Fermi constant and

$$\widetilde{Q}_W \equiv Z q_p (1 - 4 \sin^2 \vartheta_W) - N q_n . \tag{A.12}$$

This coupling depends on the integrals

$$q_{p,n} = 4\pi \int_0^\infty \rho_{p,n}(r) f(r) r^2 \mathrm{d}r, \tag{A.13}$$

where $\rho_{p,n}(r)$ are the proton and neutron densities in the nucleus as functions of the radius r and $f(r)$ is the matrix element of the electron axial current between the atomic $s_{1/2}$ and $p_{1/2}$ wave functions inside the nucleus normalized to $f(0) = 1$. The function $f(r)$ can be expressed as a series in power of $(Z\alpha)$, and for most of the atoms of interest, in particular for $(Z\alpha)$ up to ~ 0.7, cutting off the series at $(Z\alpha)^2$ is more than adequate to fulfil the requirements of precision for the comparison with experimental observation. According to Eq. (13) of Ref. [281], at order $(Z\alpha)^2$, for any nucleus, $f(r)$ is given by

$$f(r) = 1 - 2 \int_0^r \frac{V(r')}{r'^2} \int_0^{r'} V(r'') r''^2 \mathrm{d}r'' \mathrm{d}r' + \left(\frac{1}{r} \int_0^r V(r') r'^2 \mathrm{d}r' \right)^2 , \tag{A.14}$$

where $V(r)$ represents the radial electric potential determined uniquely by the charge distribution $\rho_c(r)$ of the nucleus. One can obtain the potential through the Poisson equation

$$\frac{1}{r} \frac{d^2}{dr^2} [r V(r)] = -4\pi Z \alpha \rho_c(r), \tag{A.15}$$

whose general solution is

$$V(r) = 4\pi Z \alpha \left[\frac{1}{r} \int_0^r \rho_c(r') r'^2 \mathrm{d}r' + \int_r^\infty \rho_c(r') r' \mathrm{d}r' \right] . \tag{A.16}$$

At this point one has to choose how to parametrize the charge density in order to perform the calculation. The easiest choice is to imagine the nucleus as a sphere of radius R_c and constant density

$$\rho_c^{\mathrm{cd}}(r) = \frac{3}{4\pi R_c^3}\,\Theta(R_c - r), \tag{A.17}$$

$\Theta(R_c - r)$ is the Heaviside function, and the potential, using Eq. (A.16) turns out to be

$$V^{\mathrm{cd}}(r) = \begin{cases} \frac{Z\alpha}{2R_c}\left(3 - \frac{r^2}{R_c^2}\right) & \text{for } r < R_c \\ \frac{Z\alpha}{r} & \text{for } r > R_c \end{cases}. \tag{A.18}$$

By using Eq. (A.14), it is possible to derive the analytical form of $f^{\mathrm{cd}}(r)$ for $r < R_c$

$$f^{\mathrm{cd}}(r) = 1 - \frac{(Z\alpha)^2}{2}\left(\frac{r^2}{R_c^2} - \frac{r^4}{5R_c^4} + \frac{r^6}{75R_c^6}\right), \tag{A.19}$$

and for $r > R_c$

$$f^{\mathrm{cd}}(r) = 1 - \frac{(Z\alpha)^2}{2}\left(\frac{13}{30} + \frac{2R_c^2}{5r^2} - \frac{R_c^4}{50r^4} + 2\ln\left(\frac{r}{R_c}\right)\right). \tag{A.20}$$

Using the above results and Eq. (A.13), one can calculate the proton and neutron integrals. It is worth to notice that in the case of constant density, the integrals in Eq. (A.13) have a cut-off at the value of the proton distribution radius R_p, and the neutron distribution radius R_n. Since both R_p and R_n are larger than R_c, one has to use both forms for $f(r)$, depending on the region of integration. These considerations lead to

$$\begin{aligned} q_{p,n}^{\mathrm{cd}} = 1 - (Z\alpha)^2 \Bigg(&-\frac{7}{60} + \frac{3}{5}\frac{R_c^2}{R_{p,n}^2} - \frac{16}{63}\frac{R_c^3}{R_{p,n}^3} \\ &+\frac{3}{100}\frac{R_c^4}{R_{p,n}^4} + \ln\frac{R_{p,n}}{R_c}\Bigg). \end{aligned} \tag{A.21}$$

Under the approximation $R_c \simeq R_p$ and for $R_n^2/R_p^2 - 1 \ll 1$, it is possible to obtain the typically used forms of $q_{p,n}$

$$q_p^{\mathrm{cd}} \simeq 1 - \frac{817}{3150}(Z\alpha)^2, \tag{A.22}$$

$$q_n^{\mathrm{cd}} \simeq 1 - (Z\alpha)^2\left[\frac{817}{3150} + \frac{116}{525}\left(\frac{R_n^2}{R_p^2} - 1\right)\right]. \tag{A.23}$$

In this manuscript we performed the calculations considering the more accurate charge, proton and neutron distribution densities that correspond to

the form factors in the cross section. Therefore, we evaluated numerically the quantities in Eqs. (A.13), (A.14), and (A.16). In practice, we used the Helm parametrization [53] with $R_c(^{133}\mathrm{Cs}) = 4.8041$ fm and $R_p(^{133}\mathrm{Cs}) = 4.8212$ fm which, for reference, give as a result $q_p(^{133}\mathrm{Cs}) = 0.9567$.